

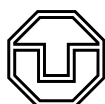
Institut für Luftfahrt und Logistik  
Professur Technologie und Logistik des Luftverkehrs  
Fakultät Verkehrswissenschaften "Friedrich List"  
Technische Universität Dresden

# Optical Properties of Condensation Trails

Dissertation  
zur Erlangung des  
akademischen Grades  
Doktor-Ingenieur,  
(Dr.-Ing.)

vorgelegt von  
**Judith Rosenow**  
geboren am 14.11.1983 in Berlin

Dresden 10.06.2016



**TECHNISCHE  
UNIVERSITÄT  
DRESDEN**

Eingereicht am 29.01.2016

1. Gutachter: Prof. Dr. Hartmut Fricke
2. Gutachter: Prof. Dr. Ulrich Schumann

Verteidigt am 10.06.2016

# Contents

<b>1</b>	<b>Introduction .....</b>	<b>3</b>
1.1	Motivation . . . . .	3
1.2	State of the art . . . . .	5
1.3	Approach . . . . .	6
<b>2</b>	<b>Theoretical background .....</b>	<b>9</b>
2.1	The Earth's atmosphere . . . . .	9
2.1.1	The mean vertical structure of the atmosphere . . . . .	12
2.1.2	Standard atmospheres . . . . .	14
2.2	Radiation . . . . .	15
2.2.1	Nature of radiation . . . . .	15
2.2.2	Important metrics describing radiation . . . . .	17
2.2.3	Relevant spectra and principles of radiation . . . . .	19
2.2.4	Solar radiation . . . . .	20
2.2.5	Terrestrial radiation . . . . .	21
2.2.6	Radiative transfer and extinction . . . . .	22
2.2.7	Radiative transfer equation . . . . .	30
2.2.8	Energy budget of the Earth-atmosphere system . . . . .	32
2.3	Thermodynamics . . . . .	33
2.3.1	Atmospheric stability . . . . .	33
2.3.2	Turbulence . . . . .	36
2.3.3	Conditions of contrail formation . . . . .	41
<b>3</b>	<b>Development of a radiative forcing model .....</b>	<b>45</b>
3.1	Model atmosphere . . . . .	45
3.2	Flight performance model . . . . .	46
3.3	Atmospheric radiative transfer model . . . . .	49
3.3.1	Two Stream Approximation . . . . .	51
3.3.2	Discrete ordinate radiative transfer solver . . . . .	52
3.3.3	Methods to calculate broadband radiances and irradiances . . . . .	53
3.4	Contrail life cycle model . . . . .	57
3.4.1	Dissipation regime . . . . .	58

3.4.2	Diffusion regime . . . . .	63
3.5	Contrail radiative forcing model . . . . .	74
3.5.1	Consideration of multiple scattering using a Monte Carlo simulation . . . . .	74
3.5.2	Geometry of the Monte Carlo simulation . . . . .	75
3.5.3	Interpretation of Beer's law . . . . .	76
3.5.4	Procedure of the Monte Carlo simulation . . . . .	79
3.5.5	The extinguished power per unit length contrail . . . . .	87
3.5.6	Scattering and absorption efficiencies $Q_s$ , $Q_a$ and asymmetry parameters $g_{HG}$ . . . . .	89
3.5.7	Calibration of the Monte Carlo simulation . . . . .	94
<b>4</b>	<b>Calculations . . . . .</b>	<b>99</b>
4.1	Contrail properties . . . . .	99
4.1.1	Conditions of contrail formation . . . . .	100
4.1.2	Initial dimensions at the end of the dissipation regime . . . . .	101
4.1.3	Microphysical properties during the diffusion regime . . . . .	103
4.2	Radiative transport up to the contrail . . . . .	105
4.2.1	Solar direct and diffuse radiance . . . . .	106
4.2.2	Terrestrial irradiance . . . . .	107
4.3	Scattering and absorption properties of radiation within the contrail . . . . .	109
4.3.1	Monte Carlo simulation for solar radiation . . . . .	109
4.3.2	Monte Carlo simulation for terrestrial irradiances . . . . .	112
4.3.3	Relevance of multiple scattering . . . . .	116
4.4	Radiative extinction . . . . .	116
4.4.1	Solar zenith and azimuthal angle . . . . .	118
4.4.2	Flight path . . . . .	120
4.4.3	Contrail evolution . . . . .	122
4.4.4	Turbulence . . . . .	126
4.4.5	Wavelength specific extinction . . . . .	129
4.5	Terrestrial energy forcing of a contrail . . . . .	133
4.6	Verification . . . . .	135
<b>5</b>	<b>Conclusion and outlook . . . . .</b>	<b>141</b>
5.1	Conclusion . . . . .	141
5.2	Outlook . . . . .	144
	<b>List of Figures . . . . .</b>	<b>147</b>
	<b>List of Tables . . . . .</b>	<b>151</b>
	<b>Abbreviations and Symbols . . . . .</b>	<b>153</b>

---

<b>Glossary.....</b>	<b>161</b>
<b>Bibliography.....</b>	<b>169</b>
<b>Acknowledgements.....</b>	<b>183</b>



## Abstract

Persistent condensation trails are clouds, induced by the exhaust of an aircraft engine in a cold and ice-supersaturated environment. These artificial ice clouds can both cool and heat the atmosphere by scattering solar radiation and absorbing terrestrial radiation, respectively.

The influence of condensation trails on the Earth-atmosphere energy balance and therefore the answer to the question of the dominating process had been mostly approximated on a global scale by treating the condensation trail as plane parallel layer with constant optical properties. Individual condensation trails and the influence of the solar angle had been analyzed, always using a coarse spatial grid and never under consideration of the aircraft performance, generating the condensation trail. For a trajectory optimization, highly precise results of the impact of condensation trails on the radiation budget and the influence of the aircraft performance on this impact is needed, so that future air traffic may consider the main factors of flight performance on the environmental impact of condensation trails. That's why, a model is developed in this thesis to continuously estimate the scattering and absorption properties and their dependence on the aircraft performance.

The initial microphysical properties of realistic condensation trails are calculated using a sophisticated flight performance model yielding precise information about fuel flow, thrust, true air speed, as well as the emission of water vapor and heat. The evolution of the microphysical properties of the condensation trail during the diffusion regime is calculated with the help of a Gaussian plume model. Likewise, the ice particle number density within the condensation trail is defined by a two-dimensional Gaussian distribution function. The radiation field near the aircraft induced ice cloud is calculated with the radiative transfer library libRadtran using a discrete ordinate radiative transfer solver for solar radiation and a Two Stream Approximation for terrestrial radiation.

Radiative extinction due to the condensation trail is calculated by following individual photons, whose extinguishing events are determined utilizing a Monte Carlo simulation. These radiative extinction model was calibrated and tested for a wide range of realistic parameter settings. The extinction increases with growing particle radius, which is found to be the parameter with the major impact on radiative extinction. In comparison, the particle number density and condensation trail cross section have a minor impact. Radiative extinction strongly depends on the angle of irradiation and on the geographical orientation of the condensation trail both determining the distance photons travel through the condensation trail. Furthermore, strong forward scattering, defined

by the particle shape and wavelength, cause a reduced cooling effect at noon, when the main part of solar direct radiation is irradiating perpendicular to the condensation trail axis.

The terrestrial extinction on the Earth-atmosphere system is calculated for the whole life cycle of the condensation trail and integrated over the terrestrial spectrum. The energy forcing is compared for five classes of turbulence. Weaker turbulence will lead to a longer contrail life time and an increased energy forcing.

For the trajectory optimization several conclusions can be drawn. The results indicate, that research is needed to reduce the size of the ice particles, even if it increases the number density of these particles. This requires further research regarding the formation of soot particles in the combustion chamber. Furthermore, flying in a slightly stronger turbulent environment would reduce the radiation impact of the condensation trail. Not least advices regarding the flight path can be given, proposing that flying around ice-supersaturated regions and, if not possible, flying along the North-South axis preferably during sunrise and sunset would be best for the environment.



# 1 Introduction

In 44 BC Marcus Tullius Cicero described the work of the Augurs who put a great deal into the prediction of human's success by examining the aviation of birds [1]. Today humans try to predict aviation. In 1505 Leonardo da Vinci studied flight characteristics of birds [2], though not yet with condensation trails. Today, the response of the Earth to aviation is in investigation and still not clear [3]. This work attends to the impact of a single well defined condensation trail on the Earth-atmosphere energy budget.

## 1.1 Motivation

In 1999 the European Commission founded the Single European Sky (SES) program to restructure the European air space with the objective of an air traffic optimization to increase the efficiency of the European air traffic [4]. The SES legislative framework is positioned in four Basic Regulations (No. 549/2004, 550/2004, 551/2004 and 552/2004). One of the main instruments to satisfy the SES task is the elimination of national frontiers and country-specific interests and therefore the introduction of a few Functional Airspace Blocks [4]. A research program belongs to the SES program. The Single European Sky ATM Research (SESAR) program, which should harmonize the interests of all air traffic stakeholders and develop the implementation of the SES objectives [5]. In the SES Basic Regulation No 549/2004 [4] the objectives of SESAR are published aiming a warranty of a sustainable development of the European air traffic sector. Beside the tripling of capacity, the increase of safety by a factor of 10 and the decrease of air traffic management costs by 50 %, the environmental compatibility of each flight should be reduced by 10 %. For these targets, the air traffic performance is measured and validated with the help of key performance indicators (KPI) [6], defining special target values of the performance of the air traffic system.

In 2012, the basic concept for the design of the future air traffic management (ATM) had been established by EUROCONTROL as ATM Master Plan [6]. According to the ATM Master Plan a premise to meet the SESAR targets is the introduction of an optimized

flight trajectory, the 4D Business Trajectory [6]. Using four-dimensional trajectories, requires a four-dimensional air traffic management and the introduction of Functional Airspace Blocks. This facilitates the generation of free trajectories without any constraint waypoints given by the air traffic control or by any other administration. Hence, optimized trajectories with specific target functions can be used. Their performance can be validated with the help of the KPIs. Albeit without a previously defined special KPI, one of the optimization functions will be the generation of trajectories with a minimum radiative forcing, induced by the condensation trail behind the aircraft. This is the aim of this thesis.

Plenty of research studies concerning other target functions of an optimized trajectory or parts of it had been published, identifying the complexity of trajectory optimization and the conflicts between individual target functions. Fricke et al. [7] analyzed current continuous descent operation (CDO) procedures and compared the maximum possible fuel savings with the achieved fuel savings. He found out, that the design of the aircraft specific and environment specific optimal CDO profile is sometimes not within the pre-set corridor defined in the appropriate legislative regulation, the ICAO Doc. 9931/AN/476 [8]. Günther et al. analyzed special key performance indicators along the SES Performance Scheme for efficiency improvements to modernize the air traffic management system and found, that not only the average horizontal en route flight efficiency, but also the vertical en route flight efficiency and the speed profile should be considered as key performance indicator [9]. He considered both fuel and time related costs by using the cost index (CI) concept which quantifies additional costs caused by any trajectory restrictions. Kaiser et al. [10] developed the Enhanced Trajectory Prediction Model (ETPM) with dynamical adaptations of the required nodes within the grid. Therewith, he predicted four-dimensional trajectories with the ability to satisfy the SESAR objectives considering constraints by the air traffic management and control system. This model had been applied to automated four-dimensional descent path optimization considering the target function of minimum fuel and the constraints by existing standard arrival routes[10]. Furthermore, Kaiser et al. [11] did an application of the ETPM to calculate optimized trajectories with respect to minimum fuel flow on the condition of stringent avoidance of condensation trail formation.

From the ATM point of view, the avoidance of condensation trail formation on global scale had been analyzed several times, often resulting in a change of the cruising altitude. For example, Sausen et al. [12] and Fichter et al. [13] analyzed increased and decreased cruising altitudes for the total air traffic on a global scale and identified a strongly latitude dependent formation of condensation trails. Furthermore, Williams et al. [14], [15] analyzed the effect of a reduced cruising altitude to avoid condensation trail formation on additional fuel burn and time of flight. Investigations had been done within the European airspace and North-East American and transatlantic airspace. Mannstein et al. [16] explained, that only flight paths through ice supersaturated regions

have to be changed to avoid condensation trail formation. Due to the small vertical extent of ice-supersaturated regions, small changes in cruising altitude are sufficient [16]. However, the detection of ice-supersaturated regions is nontrivial and sometimes flying through these regions is unavoidable due to other constraints concerning the target functions of the trajectory optimization. That is why this thesis focuses on condensation trails behind individual flight paths and gives advises on how to optimize the trajectory with respect to minimum condensation trail radiative forcing.

Condensation trails (short: contrails) are ice particles at flight level developed from condensed water vapor emitted by an aircraft [17]. The water condenses at soot particles, which are in the exhaust of the aircraft. For contrail formation, the ambient atmosphere has to be cold enough to counterbalance the exhaust heat, which works against condensation [18, 19]. The threshold temperature can be derived from the Schmidt-Appelman-criterion [18, 19]. Under these conditions contrails will live for about 100 s until the complete evaporation of the ice particles [17, 20]. However, in an ice-supersaturated ambient atmosphere (that means a relative humidity with respect to ice over 100 %, which is possible due to missing activated ice nuclei at flight level), contrails will survive the dispersion regime of the wake vortex evolution and form into long living artificial cirrus clouds, which are also called persistent contrails [20–22].

In the Earth-atmosphere energy budget, contrails act like a barrier [3, 23, 24]. They scatter incoming shortwave solar radiation back to the sky and they absorb and emit the outgoing longwave terrestrial radiation back to the Earth's surface [3, 25–27]. The impact of a single contrail on this extinction of radiation (radiative forcing,  $RF$ ) will be calculated in this thesis.

Ice particles within contrails are non-spherically shaped and differ in crystal size and shape from natural cirrus clouds [28–31]. Furthermore, the condensation nuclei within contrails are soot cores [32]. Therefore, absorption is increased in comparison to natural cirrus clouds [32–34]. Hence, the radiative forcing of contrails is different from that of natural cirrus clouds.

## 1.2 State of the art

The radiative forcing of contrails has been estimated several times. For example, using a global climate model, differences between the radiative transport in a cloud free atmosphere with and without an artificial line shaped cirrus cloud layer results in the estimation of a global contrail radiative forcing as done by Burkhardt and Kärcher [27]. Observing contrails and interpreting the incoming and outgoing radiation with the help of satellite data allows the estimation of microphysical and optical contrail properties

above a particular flight corridor and its diurnal variation as shown by Graf et al. [35] and Schumann et al. [36] and Vázquez-Navarro et al. [37].

The influence of contrails on the Earth-atmosphere energy balance at the top of the atmosphere has been first approximated by Hansen et al. [38, 39], Meerkötter et al. [23], Myhre et al. [40], Petty [41], Marquart et al. [42], Ponater et al. [43], Solomon et al. [44] and Corti et al. [45] treating contrails as plane parallel layer with constant properties to overcome computational costs. Meerkötter et al. [23] and Schumann et al. [46] parameterized the radiative forcing of contrails for thin layers in a horizontally homogenous atmosphere considering the solar zenith and azimuthal angle. However, considering the contrail as horizontally homogenous layer, ignores the realistic three-dimensional structure of a contrail [47, 48]. A detailed study of angular dependent photon transport through a three-dimensional defined realistic condensation trail by Gounou et al. [48] and Forster et al. [49] demonstrated the importance of considering large solar zenith angles. Due to an application of a Monte Carlo code for photon transport as used by Forster et al. [49] effects like multiple scattering are already considered.

However, the latest estimations of realistic contrails are still based on a radiative transport calculation of the whole atmosphere with an additional contrail using a coarse spatial grid within the contrail. With this approach it is not possible to calculate the radiative extinction of the contrail separately from atmospheric radiative extinction. Furthermore, the spatial resolution will always limit the accuracy of the results. From a meteorological point of view, which is the estimation of the contrail influence on the energy budget, the latest results are very useful and the extinction properties of the contrail without an atmospheric environment are not of interest. However, for an optimization of a single flight with respect to the contrail optical properties those calculations are insufficient. In this work, the contrail is treated as a continuous object. The photon transport through the contrail is estimated separately from the radiative transfer processes through the atmosphere. Hence, a feedback of the flight performance on the contrail radiative forcing is possible.

An advantage of the here developed approach is the combination of complex photon extinction calculations within the contrail (Monte Carlo simulations) with the results of the radiative transport calculations of the atmosphere so that changes in day time or flight direction can be realized easily and without high computational costs.

### 1.3 Approach

The influence of a condensation trail on the energy budget of the Earth-atmosphere system strongly depends on the properties of the contrail. These properties range from

macroscopic scales like the location and the dimensions of the contrail, up to microscopic characteristics like the ice particle size and shape. Many of these features are influenced by the aircraft generating the contrail [50, 51].

In a first step, the Schmidt-Appleman criterion is applied to a flight performance model estimating the conditions of contrail formation within a model atmosphere [52]. Having a dedicated time step within the flight profile with secure persistent contrail formation, the characteristics of the flight profile and the atmosphere allow the calculation of the initial dimensions and microphysical properties of the contrail. Because the exhaust is captured in the wake vortices of the aircraft, the initial characteristics of the contrail are defined at the beginning of the dispersion regime of the wake vortices with the help of the “Probabilistic Two-Phase Wake Vortex Decay and Transport Model” (P2P) by [53]. This idea is taken from Schumann [54], who already developed the “Contrail cirrus prediction tool” (CoCiP) describing the whole contrail life cycle and parameterized its impact on the Earth-atmosphere energy budget [46] by simplifying the contrail to a horizontally homogenous layer. The calculation of the contrail life cycle is also based on CoCiP [54] except for some unpublished parameters, like the parameters describing the change in number of particles due to agglomeration and break up of ice particles. The life cycle of the contrail is described by a Gaussian plume model resulting in a continuous calculation of the contrail microphysics at every position within the contrail. Hence, for every point in space, the radiative extinction properties can be calculated using parameterizations depending on ice particle radius and ice water content [55, 56]. For radiative extinction due to the contrail the “fate” of photons is traced in a Monte Carlo simulation. Solar and terrestrial radiation at contrail height are calculated utilizing the radiative transfer model LibRadtran [57]. Considering the corresponding hemispheres of the entering and leaving photons, a calculation of the impact of a contrail formed behind an aircraft with specific flight performance characteristics on the Earth’s energy system is possible.



## 2 Theoretical background

*This chapter provides an introduction into meteorological, optical and thermodynamical basics applied in this work. After some fundamentals on the Earth's atmosphere, an elaboration of radiation relevant for meteorology is given. Therein, several characteristics of atmospheric radiation like measures, directions, extinction, and the global energy budget are demonstrated. Finally, some thermodynamical principles are established, allowing the understanding of the conditions of condensation trail formation and the assumptions made regarding atmospheric extinction.*

### 2.1 The Earth's atmosphere

The Earth is covered by a gaseous layer, which gravitates to the Earth. This cover is called atmosphere and contains on average by volume 78 % nitrogen, 21 % oxygen, 1 % argon, and 0.4 % carbon dioxide [58]. The gas within the atmosphere can be treated as ideal gas, because the boiling points of the ingredients of the atmosphere are low enough and interactions between the gas molecules can be neglected [58]. The three state variables of every gas are pressure  $p$  [Pa], temperature  $T$  [K] and density  $\rho$  [ $\text{kg m}^{-3}$ ]. The correlation between these variables is called the ideal gas law

$$p = \rho R_L T. \quad (2.1)$$

In Equation 2.1,  $R_L = 287 \text{ J}(\text{kg K})^{-1}$  denotes the individual gas constant of dry air.

The pressure gradient with height is defined by the barometric formula, which is the consequence of the ideal gas law and the hydrostatic formula describing the decreasing pressure  $p$  with height  $z$  due to gravity  $g = 9.81 \text{ m s}^{-2}$

$$\frac{\partial p}{\partial z} = -\rho g. \quad (2.2)$$

Equations 2.1 and 2.2 lead to the change of pressure  $p$  with height  $z$ , the barometric formula:

$$p = p_0 \exp \left[ -\frac{g(z - z_0)}{R_L T} \right], \quad (2.3)$$

where  $p_0 = p(z_0)$  denotes the pressure at the reference level. According to Equation 2.1, the density  $\rho$  and its gradient with height is proportional to the pressure  $p$ .

Because the assumption of air being an ideal gas is valid, no interactions between individual gas molecules are assumed [58]. Hence, every single gas molecule acts as if it was by itself. In a gas mixture like the atmosphere the ideal gas law can be applied for every single ingredient or for the whole mixture. This is described by Dalton's law

$$\sum p_i = p. \quad (2.4)$$

The pressure  $p$  of a gas mixture is equal to the sum of the partial pressures  $p_i$  of the gas components [58]. Daltons law is also valid for volumes  $V$  or numbers of moles  $n$ :

$$\frac{p_i}{p} = \frac{V_i}{V} = \frac{n_i}{n}. \quad (2.5)$$

Following Dalton's law the amount of water vapor in the atmosphere can be understood as partial pressure of water vapor (or vapor pressure)  $p_{\text{water}} = e$  with  $0 \leq e \leq 40$  hPa in the atmosphere [58]. A saturated volume with respect to water under atmospheric conditions (at 300 K) contains approximately a partial pressure of  $e = 40$  hPa [58]. There is a maximum value of water vapor in a volume, called the saturation vapor pressure  $e^*$  [Pa], which exponentially depends on temperature  $T$ . An empiric formula for the calculation of  $e^*_{\text{water}}$  [hPa] over a flat water surface is given by Sonntag [59]

$$e^*_{\text{water}} = 100 \exp \left[ \frac{-6096.938}{T} - 2.711 \cdot 10^{-2} T + 1.673 \cdot 10^{-5} T^2 + 2.433 \log(T) \right] \quad (2.6)$$

where  $T$  [K] denotes the temperature.



If a volume is saturated with respect to water or ice, the water or the ice will be able to condensate. However, this process needs surface energy, which must be overcome. If the bond forces between the molecules or crystals exceed the surface energy, a condensation will only be possible in case of existing condensation nuclei with ideal properties for condensation. Because the bonding forces within an ice particle are larger than the bonding forces in water molecules, the saturation vapor pressure above ice is smaller than above water [58]. The larger the bond force, the larger the force of capturing ambient particles or molecules. Figure 2.1 shows the differences of  $e_{\text{water}}^*$  and  $e_{\text{ice}}^*$  with the empirical formulas according to Sonntag [59].

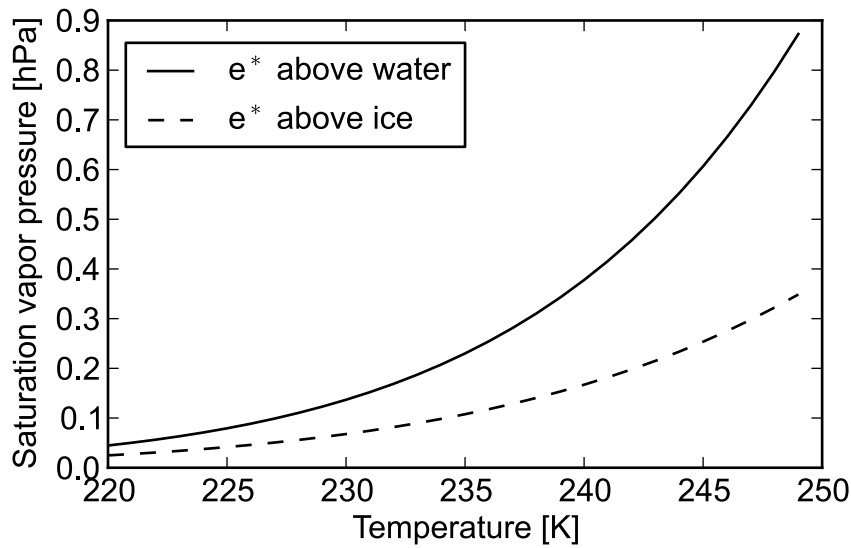


**Figure 2.1:** Saturation vapor pressure curves above water (straight) and above ice (dashed). Empirical exponential relations depending on temperature  $T$  according to Sonntag 1994 [59]. Above water, the air is able to capture more water vapor than above ice, because of larger bonding forces within an ice particle.

The quotient between vapor pressure  $e$  and saturation vapor pressure  $e^*$  is defined as relative humidity  $rH$ :

$$rH = \frac{e}{e^*}. \quad (2.7)$$

### 2.1.1 The mean vertical structure of the atmosphere

There are different layers of the atmosphere above the Earth's surface, which are defined by the temperature gradient with height (also called lapse rate). From this follows, that the individual layers of the atmosphere depend on latitude of the Earth's surface. The differences evolve from the development of thermal buoyant processes. These are the consequence of the distribution of energy coming from the sun to the Earth's surface. The temperature gradient corresponds to individual main processes within the atmospheric layer. For example, processes, which result in high absorption of radiation cause a higher temperature in this layer. In the following the layers of the atmosphere will be described. The elevations originate from the U.S. Standard-Atmosphere. Figure 2.2 shows the gradient of temperature and pressure of the lowest 250 km within the U.S. Standard-Atmosphere.

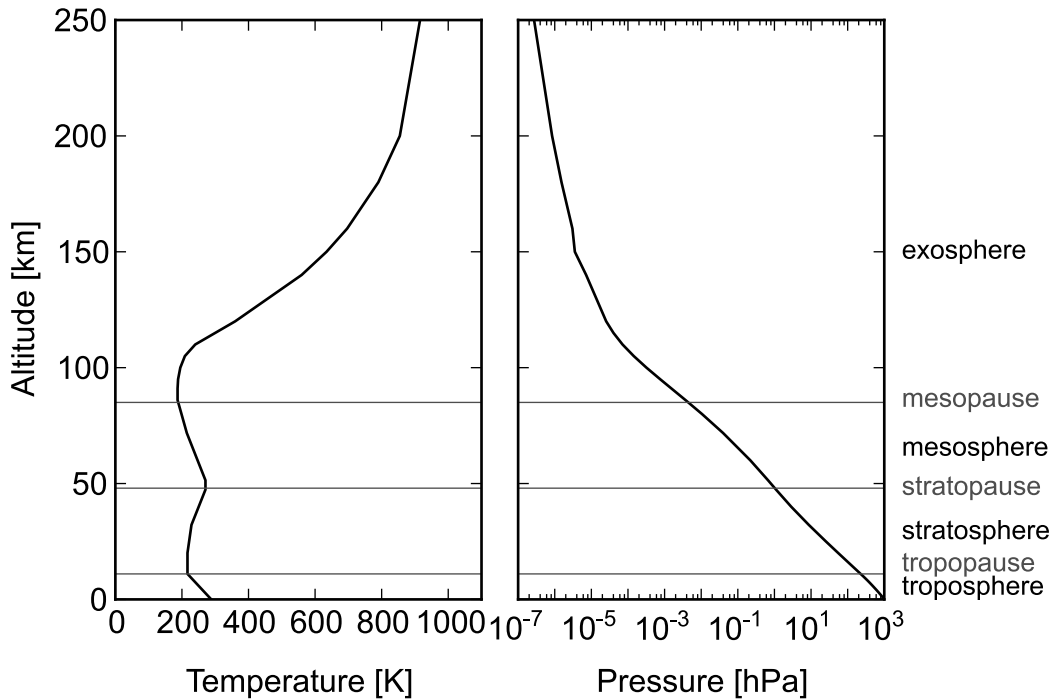


**Figure 2.2:** Atmospheric temperature gradient and pressure gradient defined by the U.S. Standard Atmosphere [60].

At the very bottom (0 to 11 km) is the troposphere with a decreasing temperature gradient with height (lapse rate). The most important characteristic of the troposphere is a strong horizontal and vertical mixing due to absorption and emission of radiation at the surface, radiative transfer processes within the atmosphere and due to turbulent energy fluxes. Furthermore, the troposphere contains nearly the entire atmospheric water va-

por and weather events. At approximately (latitude averaged) 11 km (226 hPa) is the tropopause, as the upper boundary of the troposphere, located. This layer has a constant temperature with height and determines a very weak vertical mixing and acts like a barrier for water vapor. Above the tropopause follows the stratosphere, an expanded layer between 11 km and about 47 km (or 226 hPa to 1 hPa). The characteristic of the stratosphere is a temperature gradient with height. The temperature is constant in the lower part of the stratosphere and increases at about 20 km (55 hPa) at first weakly and at approximately 32 km (8.7 hPa) strongly. An important role considering the radiation budget of the Earth-atmosphere system plays the stratospheric ozone, which absorbs a large part of solar radiation, which otherwise would destroy the cells of any living creature on Earth. The concentration of stratospheric ozone is 300 times higher than the ozone level at the surface [58]. This high ozone level is the result of the photochemical balance between the following processes: First, the dissociation of molecular oxygen  $O_2$  to atomic oxygen  $O$  by absorption of radiation with wavelengths  $\lambda \leq 0.24 \mu\text{m}$  and the recombination of molecular and atomic oxygen to ozone  $O_3$ . Second, the decay of ozone by dissociation due to absorption of radiation with wavelengths  $\lambda \leq 0.3 \mu\text{m}$ . Both processes lead to an absorption of radiation in the UV spectrum and to a warming of the stratosphere [58]. Between 47 km and 51 km (1.1 hPa and 0.67 hPa) appears again a constant temperature gradient in the stratopause, which is the boundary layer between the stratosphere (with decreasing temperature gradient) and the mesosphere (with increasing temperature gradient). In the above existing mesosphere (51 km to 85 km or 0.067 hPa to 0.0037 hPa) the temperature is increasing again. This heating is caused by absorption of radiation in the ultra violet spectrum by oxygen [61]. Up to the mesopause in 85 km altitude the air can be assumed to be well mixed with constant ingredients [58].

From all these different temperature gradients (mostly due to the absorption of radiation with specific wavelengths) follows a distinct wavelength specific radiative extinction due to the atmosphere itself, even without existing condensation trails or other clouds. This radiative extinction will be solved with the radiative transfer equation, where the following sections are leading to.

The upper layer of the atmosphere, called the exosphere (or magnetosphere) is located above 800 km. The upper boundary of the magnetosphere, the magnetopause, at approximately 60000 km is called the top of the atmosphere (TOA) [58]. It is the upper boundary of the Earth's atmosphere and is defined as the layer, where escaping charged particles are captured by the magnetic field of the atmosphere [58].

### 2.1.2 Standard atmospheres

Standard atmospheres are models describing the change of the state variables temperature  $T$ , pressure  $p$ , density  $\rho$  of the atmosphere with altitude.

The International Standard Atmosphere (ISA) describes annual averaged values (tables and formulas for calculation of the values) for the temperate zone of the Earth's atmosphere and is derived for a reference. The ISA is published by the International Organization for Standardization (ISO) as ISO 2533:1975.

The ICAO (International Civil Aviation Organization) Standard Atmosphere was published in 1993 as Doc 7488-CD [62]. The atmosphere does not contain water vapor and is defined up to 80 km. It is a kind of improvement of the ISA for aviation and has the same lapse rate as the ISA. For example, the ICAO Standard Atmosphere additionally contains aviation standard units like feet and knots.

The U.S. Standard Atmosphere (Figure 2.2) contains several models for different latitudes and seasons. It was first published in 1958 by the U.S. Committee as extension to the ISA and is defined up to 1000 km. Up to 32 km the U.S. Standard Atmosphere is equal to the ISA. Its last update was in 1976.

The Air force Geophysics Laboratory (AFGL) published their Atmospheric Constituent Profile between 0 and 200 km in 1986 [52]. It is specially made for the use in spectral radiance transmittance modeling and contains six atmospheres for different latitudes and seasonal conditions: Subarctic Winter, Subarctic Summer, Midlat Winter, Midlat Summer, Tropical and U.S. Standard. Differences between these six model atmospheres are significant only in temperature profiles. In the tropopause region the warmer atmospheres show higher values of temperature and a smaller extend of constant temperature. Furthermore, the altitude of the tropopause region increases with surface temperature, because of higher amounts of internal energy and therefore larger adiabatic buoyant forces in summer and near the equator. The lapse rate between surface and tropopause is similar for all atmospheres.

For the sake of completeness it should be mentioned that the Committee on Space Research (CIRA or COSPAR) defined an International Reference atmosphere between 25 and 2000 km with additional wind information and seasonal consideration. It also distinguishes between different geographical latitudes and sun activity.

Model atmospheres numerically describe the variation of the physical variables of the atmosphere. These quantities are achieved by assuming a continuous spectrum of radiation which causes profiles in temperature and radiative active molecules. These profiles are compared with measured ones and manipulated until the modeled values are consistent with the measurements. Model atmospheres assume homogenous plane

parallel layers (no changes in physical parameters in the horizontal direction) with a constant acceleration of gravity  $g$ . Furthermore, a hydrostatic equilibrium is assumed, which means pressure stratification (compare Equation 2.2) and no movements of the ingredients of the atmosphere such as winds. The parameters of model atmospheres do not depend on time. Hence, daily or seasonal variations are ignored. Steady state parameters with a constant population in each level are defined. Thereby, the rotation of the Earth and the atmosphere and fluctuations in magnetic fields are neglected. Further, a radiative equilibrium is adopted. This means that all energy is transported by radiative processes. Hence, no convection (the movement of molecules within fluids due to advection or diffusion or both) and no hydrodynamic effects are considered. And of course, a thermodynamic equilibrium is expected, which means that all properties of a small volume in the atmosphere are equal to their thermodynamic equilibrium values at the local values of temperature  $T$  and pressure  $p$ . All these assumptions are valid for estimations of radiative transfer processes within the lower atmosphere, where a constant gravity and a hydrostatic equilibrium are satisfied for acceptable short time spans. However, the model atmosphere does not represent a realistic composition of the atmosphere in detail.

## 2.2 Radiation

Contrails seem like a restriction in the radiation budget between the Earth's surface and the atmosphere. They scatter incoming shortwave solar radiation partly back to the sky and they absorb and emit outgoing longwave terrestrial radiation partly back to the Earth's surface [3]. Before the calculation of this radiative extinction is possible, a short introduction into the optics, a branch of physics considering the propagation of light and its interactions with matter is necessary. This outline contains a definition of electromagnetic radiation, atmospheric radiative extinction and the radiation budget is. Furthermore, sources, units and metrics of radiation are described. Subsequent to the definitions, radiative transfer through the atmosphere up or down to contrail altitude is introduced considering all possible types of atmospheric radiative extinction.

### 2.2.1 Nature of radiation

Radiation can be described either as particles or as electromagnetic waves propagating through space [63]. Depending on the problem either model is used.

### The wave model of light

In electrodynamics radiation is treated as a high frequency planar electromagnetic wave, described by its frequency  $\nu$  [ $\text{Hz} = \text{s}^{-1}$ ]. Light is the visible part of the electromagnetic radiation with wavelengths between 380 nm and 780 nm [63] or frequencies between  $7.8 \cdot 10^{14} \text{ s}^{-1}$  and  $3.8 \cdot 10^{14} \text{ s}^{-1}$ . The frequency defines the spectral color of light. Different frequencies of light travel with the same velocity in vacuum. This velocity is one of the fundamental constants of nature, the speed of light in vacuum  $c$ :

$$c = 2.98 \cdot 10^8 \text{ ms}^{-1}.$$

From this follows the dispersion model, a conversion between frequency  $\nu$  [ $\text{s}^{-1}$ ] and wavelength  $\lambda$  [m] in vacuum:

$$\lambda = \frac{c}{\nu}. \quad (2.8)$$

The basic equations of electrodynamics by James Clerk Maxwell [64] written in 1864 allow the forecast of free electromagnetic waves and their propagation speed. The propagation speed is equal to the speed of light in vacuum  $c$ , which is why Maxwell already assumed light to be a wave. Electromagnetic waves are propagating oscillations of electric and magnetic fields. These fields oscillate to one another, because a time variant electric field induces a magnetic field and vice versa [64]. In Figure 2.3 the relevant wavelength region of electromagnetic waves for meteorology are shown. Electromagnetic waves with wavelengths  $10^{-1} \mu\text{m} \leq \lambda \leq 10^2 \mu\text{m}$  have a significant contribution to the radiation balance of the Earth-atmosphere system. This includes ultra violet ( $10^{-2} \mu\text{m} \leq \lambda \leq 4 \mu\text{m}$ ), visible ( $4 \mu\text{m} \leq \lambda \leq 8 \mu\text{m}$ ) and infrared radiation ( $8 \mu\text{m} \leq \lambda \leq 10^2 \mu\text{m}$ ).

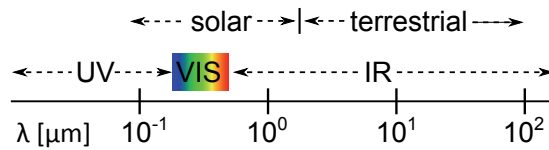


**Figure 2.3:** Meteorologically relevant wavelengths of electromagnetic waves.

### The particle model of light

The theory by Maxwell is able to describe propagation, diffraction, refraction and interference. However, there are phenomenons and characteristics of light, such as in-

interactions between light and material, which can not be described by the theory of Maxwell. For example, the photoelectric effect. A negatively charged metal is irradiated with light. Electrons get ejected from the metal and are measurable as voltage. The electrical current is the number of ejected electrons per time unit and per area unit and is proportional to the intensity  $I$  of the irradiating light. The intensity  $I$  [ $\text{Js}^{-1}\text{m}^{-2}$ ] describes the energy  $E$  per time unit  $dt$  and area  $dA$

$$I = \frac{E}{dt dA} \quad (2.9)$$

where the energy  $E$  is defined with the help of Planck's constant  $h = 6.626 \cdot 10^{-34}$  Js and the frequency  $\nu$

$$E = h \nu. \quad (2.10)$$

For the photoelectric effect high frequency light is necessary. It is not sufficient to enhance the irradiance or the irradiation time. To describe this phenomenon, in 1901 Albert Einstein defined light as an energy flux from which energy gets absorbed in terms of light quanta (photons) with the energy  $E = h\nu$  [65]. He found the measure of absorbed photons being proportional to the irradiated frequency  $\nu$  of light. While an increased intensity  $I$  only corresponds to an increased number of absorbed photons per time and area. Apparently, a single electron absorbs the energy of a single photon. If the photon energy does not exceed the electron affinity of the metal, no current will be measurable. Hence, light has both wave and particle characteristics. A specialty of this wave-particle duality is the possibility of both models to complement one another.

### 2.2.2 Important metrics describing radiation

Because radiation is defined as transport of energy either by photons or electromagnetic waves, the unit of radiation has to be Joule per second (because radiation is a continuous flow) and unit area (for the distribution of radiation) [ $\text{Js}^{-1}\text{m}^{-2}$ ].  $\text{Js}^{-1}\text{m}^{-2} = \text{Wm}^{-2}$  is the common unit of the irradiance  $F$ . Irradiance denotes irradiance incident on a plane, while exitance means irradiance emerging from a surface [66]. Irradiance refers to the rate of radiation incident on or pass through a flat surface.  $F$  [ $\text{Wm}^{-2}$ ] contributes energy with all wavelengths between specified limits (e.g.  $\lambda_1$  to  $\lambda_2$ ). A monochromatic irradiance (also called spectral irradiance)  $F_\lambda(\lambda)$  [ $\text{Wm}^{-2}\mu\text{m}^{-1}$ ] refers to a single wavelength.

The irradiance and the spectral irradiance determine neither the direction of incident

light nor the direction of exitance. For this further information, another measure of radiation including additional parameters is necessary. The radiance  $I$  [ $\text{Wm}^{-2}\text{sr}^{-1}$ ] contains both the strength and the direction of radiation. Formerly, radiance  $I$  [ $\text{Wm}^{-2}\text{sr}^{-1}$ ] was called intensity  $I$  [ $\text{Wm}^{-2}\text{sr}^{-1}$ ] (compare Section 2.2.1 and Equation 2.9). Technically speaking, for obtaining an irradiance incident on a surface, the contributing intensities from all possible directions must be integrated. The direction may be expressed by a unit vector  $\Omega$ . For example  $\Omega$  can be used as  $\Omega(x, y, z)$  in Cartesian coordinates or  $\Omega(\theta, \phi)$  in spherical polar coordinates, when the radius of the unit vector is one (compare Figure 2.4).

### Directions of radiation

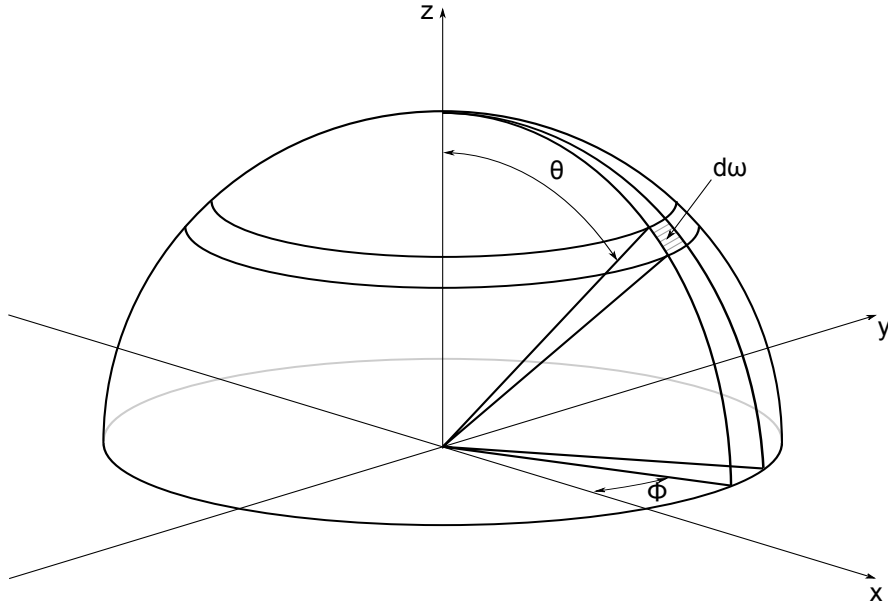


**Figure 2.4:** Angles and orientation of polar coordinates.

Figure 2.4 gives an impression of the geometry. The zenith angle  $\theta$  measures the angle of radiation from the vertical plane. The azimuthal angle  $\phi$  measures the angle counterclockwise from a defined longitude, (e.g. South) on the horizon with values from  $0 < \phi < 2\pi$ . Using  $\theta$  and  $\phi$  the solid angle  $\omega$  defines the surface area of a sphere in an arbitrarily distance around an observer in units of steradian [sr]. An infinitesimal increment of the solid angle  $d\omega$  is defined as

$$d\omega = \sin \theta \, d\theta \, d\phi. \quad (2.11)$$

$\sin \theta$  defines the meridian convergence, where lines of equal azimuthal angle  $\phi$  con-



verge at the pole. A whole sphere has a solid angle of  $\omega = 4\pi$ . Having defined solid angle  $d\omega$  and unit vector  $\Omega$ , the radiance  $I$  can be understood as the irradiance  $dF$  (on a surface normal to the beam) per unit solid angle  $d\omega$  traveling in a particular direction  $\Omega$ :

$$I(\Omega) = \frac{dF}{d\omega}. \quad (2.12)$$

Equation 2.12 is valid only for small angles of  $\theta$  and  $\phi$  (approximately  $5^\circ$  [66]) for uniform radiance within this solid angle  $d\omega$ . Equation 2.12 defines the radiance  $I$  in units of  $\text{Wm}^{-2}\text{sr}^{-1}$ .

### 2.2.3 Relevant spectra and principles of radiation

In meteorology and for the calculation of the impact of contrails on the radiation budget, radiation emitted by both the sun and the Earth shall be considered. The sun's contribution to the radiation budget is referred to as solar radiation with wavelengths  $10^{-1} \mu\text{m} \leq \lambda \leq 4 \mu\text{m}$ . The Earth emits terrestrial radiation with wavelengths between  $3 \mu\text{m} \leq \lambda \approx 10^2 \mu\text{m}$ .

Both the sun and any liquid or solid terrestrial surface can be treated as a blackbody, because the Earth's surface has an absorption capacity  $\alpha_\lambda$  close to 1 ( $0 \leq \alpha_\lambda \leq 1$ ) [61]. A blackbody is a model describing an idealized thermal radiant source assuming a complete absorption of the total irradiating electromagnetic radiation [61]. This radiant source can be calculated with the help of Planck's function  $B_\lambda(T)$  [67].

The energy of terrestrial radiation depends on the Earth's surface temperature  $T_{\text{Earth}}$ . The Stefan-Boltzmann Law describes the total radiated energy  $E$  of a blackbody depending on its temperature  $T$ :

$$E = \varepsilon_\lambda \sigma T^4, \quad (2.13)$$

where  $\sigma = 5.67 \cdot 10^{-8} \text{ Jm}^{-2}\text{K}^{-4}$  is the Stefan-Boltzmann constant and  $\varepsilon_\lambda$  with  $0 \leq \varepsilon_\lambda \leq 1$  denotes the emission capacity of the matter. For a blackbody with an absorption capacity  $\alpha_\lambda = 1$ ,  $\varepsilon_\lambda = 1$  is valid. The function of  $\varepsilon_\lambda$  is a consequence of the second law of thermodynamics and is used in Kirchhoff's law

$$\varepsilon_\lambda = \alpha_\lambda \quad (2.14)$$

which says, that a blackbody emits radiation in the same magnitude and in the similar spectral region as it absorbs electromagnetic waves [61].

The spectral radiance of radiation emitted by a blackbody can be calculated with the help of Planck's function  $B_\lambda(T)$  [ $\text{Wm}^{-2}\mu\text{m}^{-1}\text{sr}^{-1}$ ] [67] [68]:

$$B_\lambda(T) = \frac{2hc^2}{\lambda^5} \frac{1}{\exp[hc/(k_B\lambda T)] - 1}, \quad (2.15)$$

where  $c$  is the speed of light in vacuum,  $h$  is Planck's constant, and  $k_B = 1.381 \cdot 10^{-23} \text{JK}^{-1}$  is Boltzmann's constant. Figure 2.5 shows the spectral radiance of emitted radiation by a blackbody with mean temperatures of the sun (5750 K) and the Earth (288 K).

The wavelength  $\lambda_{\max}$  of the maximum peak of the Planck's function, which describes the maximum emission of a blackbody of the temperature  $T$  [K] is given by Wien's displacement law

$$\lambda_{\max} = \frac{k_W}{T}, \quad (2.16)$$

where  $k_W$  equals  $2897 \mu\text{mK}$ . Considering a mean surface temperature of the sun  $T_{\text{Sun}} = 5750 \text{ K}$ , Equation 2.16 calculates a maximum radiance at  $\lambda_{\max, \text{Sun}} = 0.503 \mu\text{m}$ . For the Earth's mean temperature  $T_{\text{Earth}} = 288 \text{ K}$ , a maximum wavelength of  $\lambda_{\max, \text{Earth}} = 10.06 \mu\text{m}$  is estimated.

Terrestrial radiation originating from a matter of the Earth's surface (with temperatures between 200 and 300 K) is called thermal radiation, because following Wien's displacement law, the maximum peak of radiance of that radiation is located in the infrared spectrum ( $\approx 10 \mu\text{m}$ ).

## 2.2.4 Solar radiation

Figure 2.5 shows the spectrum of a blackbody with the mean sun's temperature of 5750 K. Based on a radiant power of the sun of  $W_{\text{Sun}} = 3.8 \cdot 10^{23} \text{ kW}$  and assuming isotropic radiation, a distance between Earth and sun of  $r = 149 \cdot 10^6 \text{ km}$  and the Earth's radius  $r_{\text{Earth}} = 6378 \text{ km}$ , the total power of solar radiation per unit area of the Earth and second amounts  $S_0 = 1361 \text{ W m}^{-2}$  [69].  $S_0$  is called solar constant and defines the theoretically maximum value of solar radiation reaching the projected circular area of the Earth ( $\pi \cdot r_{\text{Earth}}^2$ ) [58]. The amount of solar radiation relating to the Earth's spherical

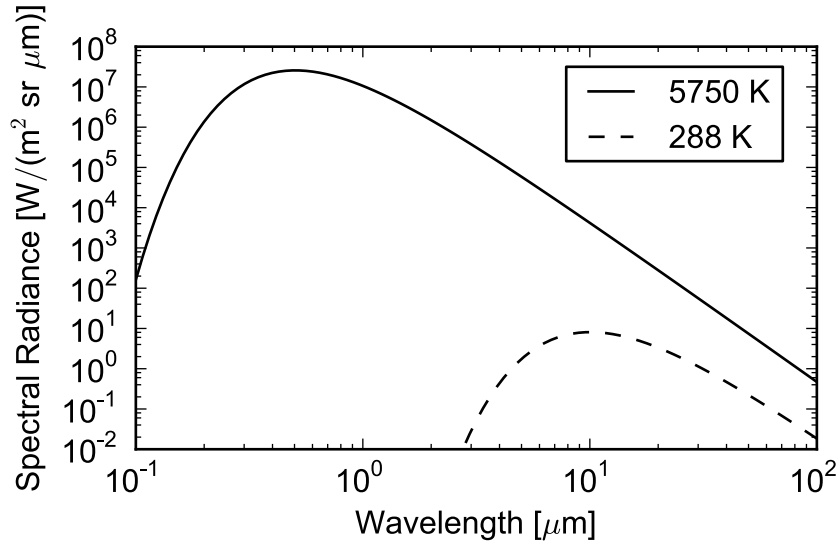


**Figure 2.5:** Spectral radiance of blackbodies with different temperatures. The solid line represents the surface of the sun with assumed temperature of 5750 K, the dotted line shows the Earth's surface with mean temperature of 288 K.

surface area denotes  $S_0$  relating to  $4\pi r_{\text{Earth}}^2$ , which is estimated to  $I_0 = 342 \text{ W m}^{-2}$ .  $I_0$  refers to as solar irradiance neglecting any interactions between radiation and the atmosphere. On the Earth's surface the mean amount of solar radiation is much smaller (approximately 50 % of  $I_0$  [70]), because solar radiation is attenuated due to absorption and reemission by molecules and particles within the atmosphere. Hence, two different types of solar radiation can be detected on the Earth's surface: First, direct solar radiation  $I_{\text{dir}}$ , which is the amount of solar radiation without interactions with the atmosphere, originating from one single direction  $\Omega$ . And second, diffuse solar radiation  $I_{\text{diff}}$  originating from emission and scattering of solar radiation by molecules and particles within the atmosphere. Diffuse radiation is isotropic, which means it is constant within a finite solid angle  $d\omega$ . In contrast to the angular dependence of direct solar radiation. This distinctive feature has to be considered in the present calculations by always respecting both the solar zenith  $\theta$  and azimuthal angle  $\phi$ .

### 2.2.5 Terrestrial radiation

The amount of solar radiation measurable on the Earth's surface is either reflected (back scattered) or absorbed by the Earth and emitted according to Stefan-Boltzmann law leaving the Earth's surface as longwave terrestrial radiation. It's spectrum and total

amount of energy can be estimated with the help of the blackbody model and Planck's function  $B_\lambda(T)$ . Considering a mean Earth temperature of  $T_{Earth} = 288$  K, blackbody radiation results in the spectrum shown in Figure 2.5.

Terrestrial radiation only contains diffuse radiation, because there is no point source of radiation. From this follows an independence on direction. In calculations, terrestrial radiation can be treated as irradiance with different contributions depending on the originating hemisphere (above or beneath the contrail).

### 2.2.6 Radiative transfer and extinction

Absorption, emission and scattering of electromagnetic radiation are taking place on every atmospheric ingredient. Diffraction and refraction are optical phenomena, which can be described by absorption, emission and scattering. Absorption is the conversion of photons into intrinsic energy and emission is the conversion of intrinsic energy into photons. Scattering (elastic scattering, to be precisely) is a redirection of radiation without a change of the intrinsic energy. For the sake of convenience, only elastic scattering is considered in this thesis. Reflection is a special case of scattering, it is also called backscattering. The reflectivity of a surface is called albedo  $a$ .  $a$  describes the reflectance of a surface with  $0 \leq a \leq 1$  and depends on wavelength and the structure of the surface. On the Earth's surface and in solar spectral region  $a$  varies between  $a = 0.9$  for fresh fallen snow and  $a = 0.06$  above the ocean [58].

Scattering redirects radiation from  $\Omega$  to a new direction  $\Omega'$ . This is a kind of extinction of radiation, its amount can be described by a volume extinction coefficient  $\beta_e$ , which is the sum of the absorption coefficient  $\beta_a$  and the scattering coefficient  $\beta_s$  [66]:

$$\beta_e = \beta_a + \beta_s. \quad (2.17)$$

The coefficients  $\beta_e$ ,  $\beta_a$  and  $\beta_s$  [ $\text{m}^{-1}$ ] define the attenuation of an electromagnetic wave per unit distance through the extinguishing material. They depend on wavelength and material. A medium can be characterized by the single scatter albedo  $\tilde{\omega}$

$$\tilde{\omega} = \frac{\beta_s}{\beta_e} = \frac{\beta_s}{\beta_s + \beta_a}. \quad (2.18)$$

$\tilde{\omega}$  is called single scatter albedo, because only a single scattering event per photon passing the medium is considered.  $\tilde{\omega} = 1$  describes a fully scattering medium,  $\tilde{\omega} = 0$  defines a totally absorbing material.

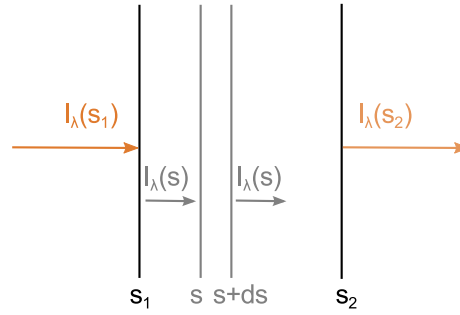


**Figure 2.6:** Extinction of radiation from the original value  $I_\lambda(s_1)$  to  $I_\lambda(s_2)$  due to passing along an infinitesimal path  $ds$  from location  $s_1$  to  $s_2$  through an extinguishing matter.

In a homogenous medium the infinitesimal decrease of radiance after passing a medium over an infinitesimal distance  $ds$  between locations  $s$  and  $s + d$  is [66]

$$dI_\lambda = I_\lambda(s + d) - I_\lambda(s) = -I_\lambda(s) \beta_e(s) ds. \quad (2.19)$$

The negative sign in front of  $I_\lambda(s)$  is a convention for having a positive extinction coefficient. The geometry is shown in Figure 2.6. Using separation of variables of Equation 2.19, the fraction of the infinitesimal decrease of radiance  $dI_\lambda$  to the incident radiance  $I_\lambda(s)$  can be formulated as

$$\frac{dI_\lambda}{I_\lambda(s)} = -\beta_e ds. \quad (2.20)$$

Within the infinitesimal path  $ds$ , the extinction coefficient  $\beta_e$  is assumed constant. To consider an extended path between locations  $s_1$  and  $s_2$  where  $\beta_e(s)$  is a function of location  $s$  within the path, an integration over several  $\beta_e(s)$

$$\int_{I_\lambda(s_1)}^{I_\lambda(s_2)} \frac{dI_\lambda}{I_\lambda(s_1)} = - \int_{s_1}^{s_2} \beta_e(s) ds \quad (2.21)$$

is necessary. Solving the integral results in

$$\ln I_\lambda(s_2) - \ln I_\lambda(s_1) = \ln \left( \frac{I_\lambda(s_2)}{I_\lambda(s_1)} \right) = - \int_{s_1}^{s_2} \beta_e(s) ds \quad (2.22)$$

and rearranging for the unknown extenuated radiance  $I_\lambda(s_2)$ , Equation 2.22 becomes

$$I_\lambda(s_2) = I_\lambda(s_1) \exp \left[ - \int_{s_1}^{s_2} \beta_e(s) ds \right]. \quad (2.23)$$

In other words, in a homogenous medium (i.e.  $\beta(s)$  is constant over the finite path  $ds$ ), the radiance  $I_\lambda$  decreases exponentially with the distance  $ds$ . Equation 2.23 is called Beer's law and is a fundamental model for calculating radiative extinction.

The integral

$$\tau = \int_{s_1}^{s_2} \beta_e(s) ds \quad (2.24)$$

defines the optical depth (if vertically quantified: optical thickness) [66]. Following the naming of  $\tau$ , it describes the extinction of light which is traveling through matter, e.g. the atmosphere.  $\tau$  is defined as  $\tau \geq 0$ , where  $\tau = 0$  represents  $\beta_e = 0$  or  $s_1 = s_2$  and  $\tau = 1$  denotes an extinction of radiation by  $e^{-1}$  of its original value. To understand the last sentence,  $\tau = 1$  can be inserted in Equation 2.23:

$$I_\lambda(s_i) \stackrel{!}{=} I_\lambda(s_1) e^{-1}. \quad (2.25)$$

From

$$\tau = \int_{s_1}^{s_2} \beta_e(s) ds = 1 \quad (2.26)$$

follows for a constant  $\beta_e$  over the path  $ds$ :

$$\beta_e ds = 1 \quad (2.27)$$

and

$$ds = \frac{1}{\beta_e} \quad (2.28)$$

Hence, after a distance  $ds = \frac{1}{\beta_e}$  the incident radiance  $I_\lambda(s_1)$  is decreased to

$$I_\lambda(s_2) = I_\lambda(s_1)e^{-1}. \quad (2.29)$$

The optical depth depends on wavelength, on the extinguishing matter and on the distance between  $s_1$  and  $s_2$ .

As mentioned, the volume extinction coefficient  $\beta_e$  is a measure of radiation extinction after passing a given distance  $s$ . The mass extinction coefficient  $k_e$  [ $\text{m}^2\text{kg}^{-1}$ ]

$$k_e = \frac{\beta_e}{\rho} \quad (2.30)$$

with  $\rho$  as density of the material [ $\text{kg m}^{-3}$ ] describes radiation extinction per mass of extinguishing material [71]. If only the number density of particles  $n_p$  [ $\text{m}^{-3}$ ] within the medium is relevant, the extinction cross section  $\sigma_e$  [ $\text{m}^2$ ]

$$\sigma_e = \frac{\beta_e}{n_p} \quad (2.31)$$

is used [66] for the calculation of radiation extinction. Equations 2.30 and 2.31 permit the calculation of extinction per single particle

$$\sigma_e = k_e m_p, \quad (2.32)$$

where  $m_p$  denotes the mass per particle [kg] [66]. For the application of  $\sigma_e$ , the extinction efficiency  $Q_e$

$$Q_e = \frac{\sigma_e}{A_{\text{proj.}}} \quad (2.33)$$

is used in Beer's law (Equation 2.23) [66], where  $A_{\text{proj.}}$  denotes the projected area of cloud droplets or ice particles and can be calculated according to Wyser et al. [55] for the shortwave spectrum and by Yang et al. [56] for longwave spectral region. In the visible and infrared spectrum  $Q_e \approx 2$  is often assumed for cloud droplets when the particle diameter is large, compared to the wavelength [66]. However the range of  $Q_e$  varies strongly, depending on wavelength and droplet radius. Analog to the definition

of the extinction coefficients, the absorption and scattering coefficients can be written as

$$\beta_a = \rho k_a = n_p \sigma_a \quad \sigma_a = Q_a A_{\text{proj.}} \quad (2.34)$$

$$\beta_s = \rho k_s = n_p \sigma_s \quad \sigma_s = Q_s A_{\text{proj.}} \quad (2.35)$$

and the single scatter albedo can be understood as

$$\tilde{\omega} = \frac{\beta_s}{\beta_e} = \frac{k_s}{k_e} = \frac{\sigma_s}{\sigma_e}. \quad (2.36)$$

The extinction coefficient  $\beta_e$  can be derived using the scattering and absorption efficiencies  $Q_s$  and  $Q_a$ , the projected area of the particle  $A_{\text{proj.}}$  [ $\text{m}^2$ ] and the number density of particles per volume  $N$  [ $\text{m}^{-3}$ ]. For non spherical particles (as considered in this thesis) using the particle cross section  $A_p$  of the particles for the estimation of the extinction coefficient doesn't make sense. More important is the projected area  $A_{\text{proj.}}$  of the particles.  $A_{\text{proj.}}$  can be calculated for various typical ice particle habits according to Yang et al. [55].

Exemplary results of atmospheric extinction are given in Figure 2.7 and Figure 2.8. Here, the theoretical spectrum of radiation without any extinction (blackbody radiation as already shown in Figure 2.5 ) is compared with a modeled spectrum after passing the modified model atmosphere Midlat Winter (modified with an ice-supersaturated layer at flight level). Figure 2.7 and Figure 2.8 are shown here only for the demonstration of the consequences of natural radiation extinction by the atmosphere itself. The simulations are done with the radiative transfer model LibRadtran using a Two Stream Approximation under consideration of a solid angle of  $\omega = 6.8 \cdot 10^{-5}$  sr of the Earth radiated by the sun [68]. Extinguished terrestrial irradiances are calculated at the top of the atmosphere after traveling through the atmosphere from the Earth's surface up to the top of the atmosphere. Extinguished solar irradiances are calculated at the Earth's surface after passing the atmosphere from the top of the atmosphere down to the Earth's surface.

Figure 2.7 shows the atmospheric extinction in the solar spectrum, which is partly absorbed by individual molecules of the atmosphere. Four ranges of wavelengths with very strong absorption (absorption bands) are defined. For example ozone absorbs large



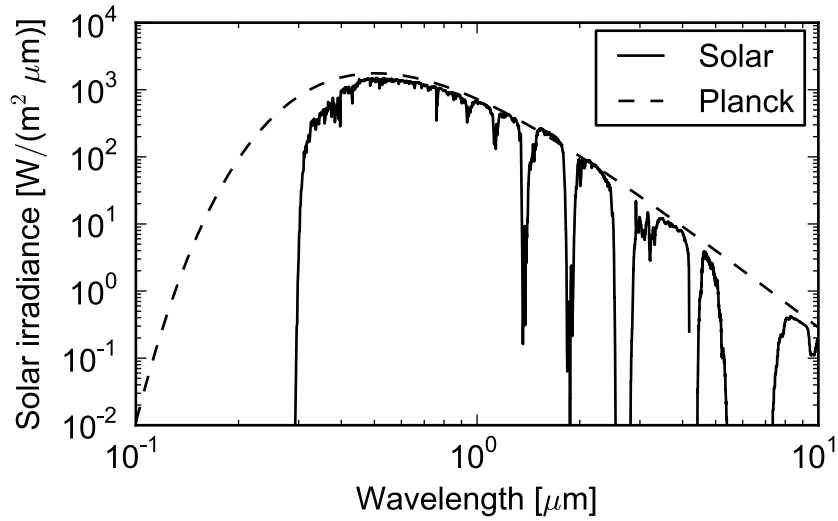


**Figure 2.7:** Radiant emittance of a blackbody with a temperature of 5750 K (dotted line) and simulated solar radiation at the Earth's surface after atmospheric extinction (solid line).

amounts of radiation within the Hartley band between  $0.22 \mu\text{m}$  and  $0.31 \mu\text{m}$  and for wavelengths  $\lambda \leq 0.24 \mu\text{m}$ , within the Huggins band at  $\approx 0.35 \mu\text{m}$  and within the Chapuis band at  $\approx 0.55 \mu\text{m}$ . Water vapor weakly absorbs at  $0.72 \mu\text{m}$ ,  $0.81 \mu\text{m}$ ,  $0.93 \mu\text{m}$ ,  $1.13 \mu\text{m}$ ,  $1.37 \mu\text{m}$ , and  $1.85 \mu\text{m}$ . Additionally, there is a continuous extinction over the whole spectrum due to scattering in the atmosphere, increasing with  $\lambda^{-1}$  [61].

The terrestrial extinction is demonstrated in Figure 2.8. Here, absorption of radiation by molecules in the atmosphere is a highly complex and important fact. Except of radiation with wavelengths between  $8 \mu\text{m}$  and  $12 \mu\text{m}$  (where the atmosphere is quite opaque and satellites can measure terrestrial radiation originating from the Earth's surface) the whole spectrum is extinguished by absorption. Especially radiation with wavelengths longer than  $15 \mu\text{m}$  and between  $5 \mu\text{m}$  and  $8 \mu\text{m}$  is absorbed by water vapor. Around  $15 \mu\text{m}$  absorption by carbon dioxide takes place. This is not a continuous absorption over many wavelengths. It is rather a partial absorption, where several wavelengths get fully absorbed and others (between the strongly extinguished ones) get transmitted through the atmosphere. Hence, calculations of the terrestrial spectrum at any point within the Earth-atmosphere system are very complex. Nearly monochromatic irradiances over a range of nearly  $100 \mu\text{m}$  (at least between  $\lambda = 4.7 \mu\text{m}$  and  $\lambda = 21 \mu\text{m}$ , where the contribution of irradiances to the terrestrial wavelength spectrum is significant) have to be considered separately.

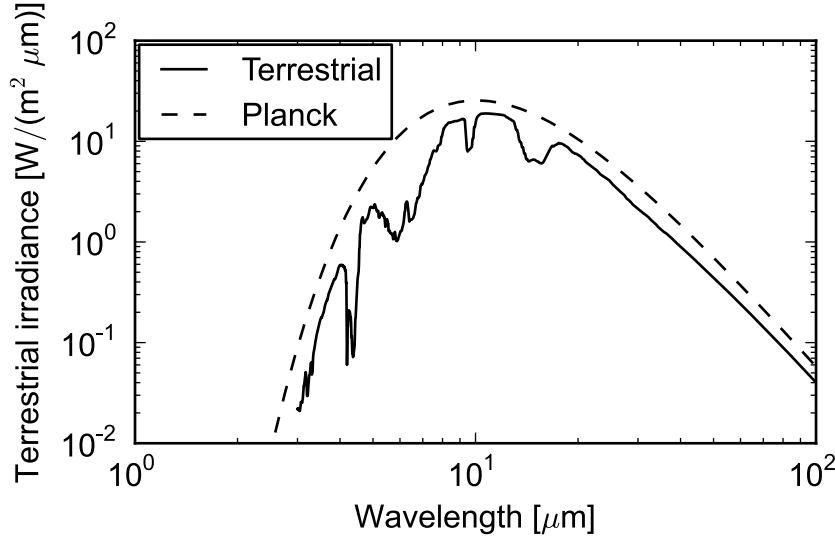


**Figure 2.8:** Radiant emittance of a blackbody with a temperature of 288 K representing the surface of the Earth (dotted line) and simulated terrestrial radiation at the top of the atmosphere after atmospheric extinction (solid line). The simulations are done with LibRadtran (compare Section 3.3) using a Two Stream Approximation.

### The scattering phase function

Radiative transfer calculations are used for the estimation of a radiation budget between two different levels of the atmosphere. Scattering is the redirection of radiation coming from the original direction  $\Omega$  to  $\Omega'$ . In radiative transfer calculations, scattering is often considered into a solid angle  $d\omega$  in the direction of  $\Omega'$ . Most scattering events occur due to interactions with particles [66]. The scattering angles are defined as  $\vartheta$  between  $\Omega$  and  $\Omega'$  relative to the propagation direction and  $\phi$  as polar angle around  $\Omega$  measured from an arbitrary point. The geometry of the scattering angles is visualized in Figure 2.9. If the particles are randomly orientated (like ice particles in a condensation trail), the polar angle will be uniformly distributed [55].

$$\cos \vartheta = \Omega' \Omega. \quad (2.37)$$

The probability of a photon getting scattered by the angle  $\vartheta$  relative to the original direction  $\Omega$  is given by the scattering phase function  $P(\cos \vartheta)$  [66].

To ensure energy conservation, a normalization condition

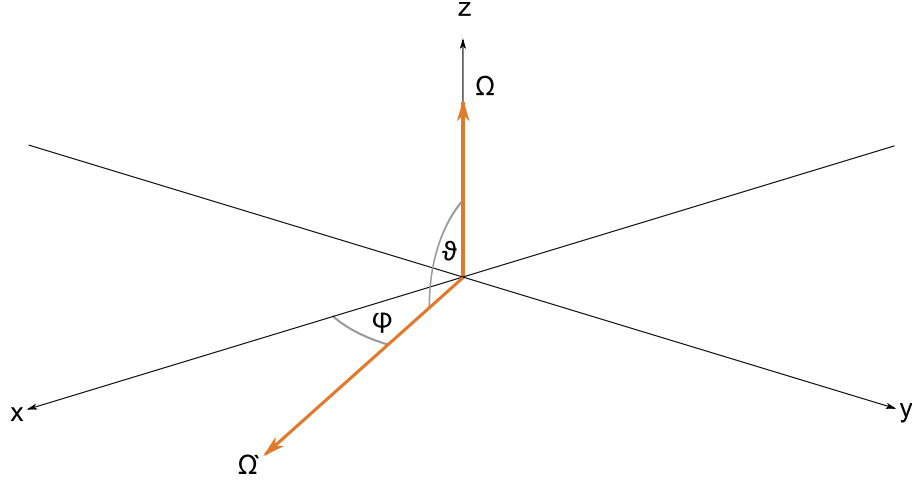


**Figure 2.9:** Geometry of a scattering event (orange) from propagation direction  $\Omega$  to  $\Omega'$  defining the angles  $\vartheta$  relative to the  $\Omega$  and the polar angle  $\phi$ .

$$\frac{1}{2} \int_{-1}^1 P(\cos \vartheta) d\cos \vartheta = 1 \quad (2.38)$$

must be valid. A constant phase function

$$P(\cos \vartheta) = 1 \quad (2.39)$$

describes isotropic scattering with a uniformly distributed scattering angle  $\vartheta$ . In this case, the source term only depends on scattering efficiency  $\beta_s$ . For the calculation of irradiances the asymmetry parameter  $-1 \leq g_{\text{HG}} \leq 1$  [a.u.] describes the proportion of scattered photons in the forward versus backward direction. According to Equation 2.38,  $g_{\text{HG}}$  is the averaged value of  $\cos \vartheta$ . For  $g_{\text{HG}} = 1$  photons are scattered in the forward direction,  $g_{\text{HG}} = -1$  describes scattering events in the backward direction and isotropic scattering is reached by  $g_{\text{HG}} = 0$ . In the solar wavelength spectrum, atmospheric scattering events at ice particles dominate in the forward direction with  $0.8 \leq g_{\text{HG}} \leq 0.9$  [66]. The estimation of a scattering phase function is complicated, because scattering properties depend on wavelength and on particle characteristics like size, shape, density and surface structure.

The Henyey-Greenstein phase function  $P_{\text{HG}}(\cos \vartheta)$  is a model phase function depending on the asymmetry parameter  $g_{\text{HG}}$ :

$$P_{\text{HG}}(\cos \vartheta) = \frac{1}{4\pi} \frac{1 - g_{\text{HG}}^2}{(1 + g_{\text{HG}}^2 - 2g_{\text{HG}} \cos \vartheta)^{3/2}} \quad (2.40)$$

The Henyey-Greenstein phase function satisfies isotropic scattering for  $g_{\text{HG}} = 0$ , as well as forward and backward scattering for  $g_{\text{HG}} = 1$  and  $g_{\text{HG}} = -1$ , respectively. It calculates a smooth phase function (compare Figure 2.10) with a loss of some particle and wavelength specific details. The Henyey-Greenstein phase function does not include a backscattering peak, which is typical for ice clouds [66]. However, it constitutes a possibility to consider scattering in the radiative transfer with acceptable effort.

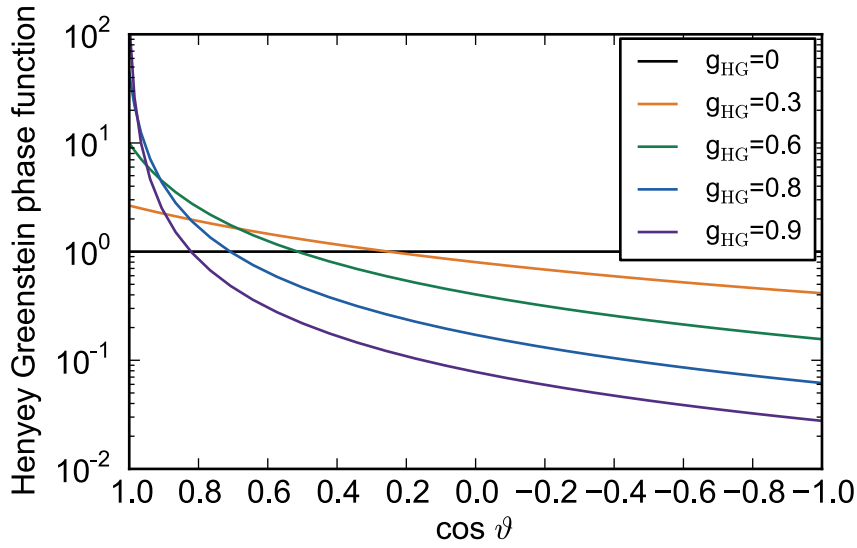


**Figure 2.10:** Henyey-Greenstein phase function  $P_{\text{HG}}(\cos \vartheta)$  with various values of asymmetry parameter  $g_{\text{HG}}$ .

## 2.2.7 Radiative transfer equation

According to Section 2.2.6, absorption, emission and scattering have to be considered for a quantification of radiative extinction. Beer's law (Equation 2.23) with the extinction coefficient  $\beta_e = \beta_a + \beta_s$  considers extinction of radiation due to absorption and scattering. Neither the source of radiation due to emission, nor the source of radiation due to light scattered into the beam are taken into account. Hence, the change of radiance  $I$  along an infinitesimal path  $ds$  must be understood as the sum of sources and losses of radiation. In general, this can be expressed as

$$dI = dI_{ext} + dI_{emit} + dI_{scat}, \quad (2.41)$$

where  $dI_{ext}$  denotes the loss due to extinction (compare Equation 2.19) and can be written as

$$dI_{ext} = -\beta_e I ds. \quad (2.42)$$

The amount of radiation emitted by the atmosphere  $dI_{emit}$

$$dI_{emit} = \beta_a B(T) ds \quad (2.43)$$

can be understood as blackbody emission  $B(T)$  according to the temperature  $T$  of the layer, using Kirchhoff's law ( $\epsilon_\lambda = \alpha_\lambda$ ) for the estimation of the amount of emitted radiation.

$dI_{scat}$  describes the source of radiation coming from an arbitrary direction  $\Omega'$  getting scattered into direction  $\Omega$  of interest.

$$dI_{scat} = \frac{\beta_s}{4\pi} \int_{4\pi} P(\Omega', \Omega) I(\Omega') d\omega' ds. \quad (2.44)$$

Both processes, the source term and the loss term are considered by the normalization condition (the integral over the whole solid angle  $4\pi$  of  $d\omega'$ ) and the scattering phase function  $P(\Omega', \Omega)$ . Considering Equations 2.42 to 2.44 the radiative transfer equation can be written as

$$dI = -\beta_e I ds + \beta_a B(T) ds + \frac{\beta_s}{4\pi} \int_{4\pi} p(\Omega', \Omega) I(\Omega') d\omega' ds. \quad (2.45)$$

Often, Equation 2.45 is divided by  $d\tau = -\beta_e ds$ . Furthermore, the single scatter albedo  $\tilde{\omega} = \beta_s(\beta_s + \beta_a)^{-1}$  is used resulting in

$$\frac{dI}{I} = I(\Omega) - (1 - \tilde{\omega})B - \frac{\tilde{\omega}}{4\pi} \int_{4\pi} p(\Omega', \Omega) I(\Omega') d\omega'. \quad (2.46)$$

Equation 2.46 is the radiative transfer equation giving the depletion of radiation due to atmospheric extinction for a single wavelength and a single direction.

### 2.2.8 Energy budget of the Earth-atmosphere system

Two sources of radiation and several radiative transfer processes result in an energy budget. The result of the radiative transfer equation (Equation 2.46) can be quantified at any altitude in the Earth-atmosphere system.

If there is no balance between the incoming and outgoing radiation, the system will heat or cool. The radiative forcing  $RR$  is defined as the net change in the energy balance of the Earth-atmosphere system due to a perturbation [3]. Such a perturbation could be a condensation trail scattering the incoming radiation and absorbing the outgoing energy.

To get a feel for the magnitude of irradiances, irradiating the Earth's surface, getting scattered, absorbed and emitted by either the atmosphere or the surface, Figure 2.11 introduces the annual global mean energy budget of the Earth-atmosphere system according to Kiehl et al. 1997 [72]. For this demonstrative purpose, the values originate from modeling of the U.S. Standard Atmosphere. From Figure 2.11 the importance of the natural greenhouse effect should be taken, emphasized by the large amount of terrestrial irradiances emitted by the Earth's surface ( $350 \text{ W m}^{-2} + 40 \text{ W m}^{-2}$ ) and by the atmosphere ( $324 \text{ W m}^{-2}$ ) back to the Earth's surface. This absorption and reemission is taking place even without any radiation barrier (like a contrail) in the atmosphere. Furthermore, the magnitude of radiative extinction of irradiances coming from different hemispheres to an arbitrary altitude within the atmosphere shall be taken into account. The radiative extinction due to a contrail shall be in the same order of magnitude.

Hence, the contrail will absorb more terrestrial radiation (here  $350 \text{ W m}^{-2}$ ), than solar radiation ( $67 \text{ W m}^{-2}$ ). On the contrary, more solar radiation ( $77 \text{ W m}^{-2}$ ) will be scattered, instead of absorbed. Moreover, the small amount of transmitted terrestrial radiation through the atmosphere shall be emphasized: only  $40 \text{ W m}^{-2}$  are coming through the atmospheric window.

For a closure of the energy balance in lower altitudes of the atmosphere, turbulent energy fluxes have to be considered. Energy transfer due to dry rising air parcels is called sensible heat flux. Furthermore, energy is transported from the surface to the lower part of the atmosphere by latent heat, released by condensation of water-saturated air parcels. This process is called latent heat flux. Turbulent fluxes will be discussed in the following section.

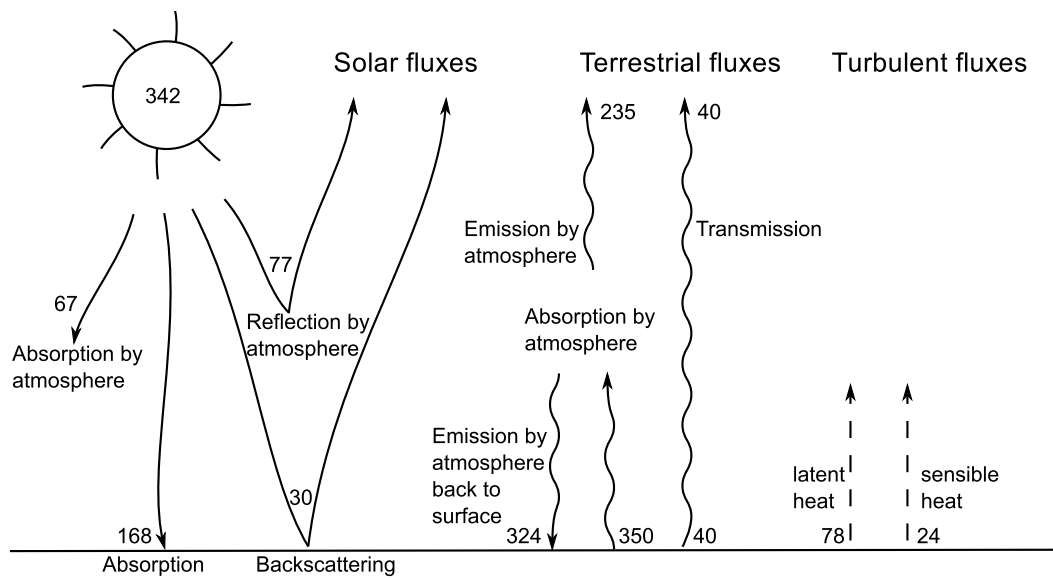


**Figure 2.11:** Energy budget in irradiances [ $\text{W m}^{-2}$ ] of the Earth-atmosphere system including incoming and outgoing solar, terrestrial irradiances and turbulent heat fluxes. Numerical quantity values are taken from Kiehl et al. 1997 [72].

## 2.3 Thermodynamics

### 2.3.1 Atmospheric stability

Both the life time of the contrail and its initial dimensions depend on atmospheric turbulence. Atmospheric turbulence in turn, is controlled by atmospheric stability, which defines the ability of an air parcel to move vertically within the atmosphere. Hence, atmospheric stability has to be introduced to understand the measures of atmospheric turbulence, which is described thereafter.

Atmospheric stability is controlled by the temperature gradient with altitude. The negative temperature gradient in the troposphere is controlled by the transport of latent and sensible heat from the surface to the atmosphere. Sensible and latent heat flux have been introduced in the last section. With increasing altitude the impact of turbulent heat fluxes on the temperature gradient decreases. In the stratosphere the temperature is dominated by the radiation balance [61].

In the lower parts of the troposphere the thermal energy is transformed into potential energy by the following process [61]: A warm air parcel rises due to decreasing ambient pressure with height. At the same time the air parcel expands and executes work against

the ambient pressure. The energy for this work has to come from the internal energy. Hence, the air parcel cools down according to the dry adiabatic lapse rate  $\gamma_d$ , typically in  $[\text{K}(100 \text{ m})^{-1}]$  [58]

$$\gamma_d = -\frac{dT}{dz} = -\frac{g}{c_p} = -0.00981 \frac{\text{K}}{\text{m}}. \quad (2.47)$$

Heat transfer from the surface to the lower part of the atmosphere with the help of the dry adiabatic lapse rate describes the turbulent sensible heat flux mentioned in Section 2.2.8. If the air parcel is saturated with respect to water vapor and cools down further, liquid water will condensate and the evaporation heat of  $L = 2500 \text{ J(g)}^{-1}$  per gram water will be set free at a temperature of  $T \approx 300 \text{ K}$ . This heat warms the air parcel and partly compensates the cooling rate. The saturated lapse rate is not constant over altitude. It depends on temperature and pressure, because the amount of condensed water and thereby the amount of released evaporation heat  $L$  depends on temperature according to Figure 2.1. The saturated adiabatic lapse rate can be approximated by [58]

$$\gamma_s = -\frac{dT}{dz} = -\frac{g}{c_p} \frac{1 + \frac{Lm^*}{R_L T}}{\frac{Lm^*}{c_p e^*} \frac{de^*}{dT}}, \quad (2.48)$$

where

$$m^* = \frac{0.622 e^*(T)}{p - e^*(T)} \quad (2.49)$$

denotes the saturation mixing ratio,  $c_p = 1004 \text{ J(kg K)}^{-1}$  the specific heat capacity for constant pressure,  $R_L = 287 \text{ J(kg K)}^{-1}$  the individual gas constant for dry air and  $de^* dT^{-1}$  the derivation of saturation vapor pressure with respect to temperature  $T$ . The heat transport along the saturated adiabatic lapse rate is also called the turbulent latent heat flux as described in Section 2.2.8.

However, the temperature gradient with altitude is not only defined by the moisture content of the atmosphere. External influences, like cold or hot air streaming in the atmosphere, are causing changes in the temperature gradient with altitude. Even the sign of the temperature gradient with altitude can change. Hence, the temperature gradient of the ambient atmosphere allows the prediction of the vertical movement of an air parcel within the ambient atmosphere, with different temperature or pressure and therefore the stability of the atmosphere. If an air parcel is vertically moved, it heats or cools adiabatically. If the ambient lapse rate causes positive or negative buoyancy



on the air parcel and the parcel drifts to its original altitude, the ambient atmosphere is stable stratified and the mixing of air parcels of different altitudes is weak. The atmosphere is unstable stratified and vertical mixing is likely if the air parcel removes from its original altitude. In a neutral stratified atmosphere, the air parcel can stay at any level.

A stable stratification occurs if the ambient lapse rate is smaller than the adiabatic lapse rate of the air parcel. In this case the rising air parcel will cool down faster than the environment, its density will be higher than the ambient density and it will fall down to its original altitude. In the other case with the ambient lapse rate is higher than the adiabatic lapse rate of the air parcel, the rising parcel will be warmer than the environment and will rise further.

For a quantification of atmospheric stability two measures are necessary. On the one hand the potential temperature  $T_\Theta$  is the temperature, that an air parcel would reach, if it is adiabatically moved from an arbitrary altitude, defined by the pressure  $p$ , to the surface with  $p_0 = 1000$  hPa.  $T_\Theta$  [K] can be quantified with the help of the Poisson equation [61]

$$T_\Theta = T \left( \frac{p_0}{p} \right)^{\frac{\gamma}{\gamma-1}}, \quad (2.50)$$

where  $T$  [K] denotes the current absolute temperature.  $T_\Theta$  is a conserved quantity, because it doesn't change during an adiabatic change [61]. With the help of  $T_\Theta$  the Brunt Väisälä frequency  $N$  [ $s^{-1}$ ] can be defined according to Etling 2008 [73]

$$N = \sqrt{\frac{g}{T_\Theta} \frac{dT_\Theta}{dz}}. \quad (2.51)$$

$N$  denotes the buoyancy frequency and represents the frequency of oscillation of an air parcel around its equilibrium level. The three mentioned cases of stratification can be quantified using the fraction  $\frac{dT_\Theta}{dz}$ . For unstable stratification with

$$\frac{dT_\Theta}{dz} < 0$$

$N$  gets imaginary values. The air parcel does not oscillate and removes from its original level. For neutral stratification with

$$\frac{dT_{\Theta}}{dz} = 0$$

$N = 0$  and the air parcel will not change its level. In stable stratification, where

$$\frac{dT_{\Theta}}{dz} > 0$$

$N$  gets a real number [73]. In stable stratification  $N$  denotes the frequency of an oscillating air parcel trying to achieve the atmospheric conditions. The larger the temperature difference between air parcel and environment the faster the frequency  $N$  [73].

**Table 2.1:** Values of the Brunt Väisälä frequency  $N$  [ $s^{-1}$ ] depending on stratification  $dT_{\Theta} dz^{-1}$  [ $K(100\text{ m})^{-1}$ ] for atmospheric conditions. Values are taken from Etling [73].

lapse rate	$dT_{\Theta} dz^{-1}$ [ $K(100\text{ m})^{-1}$ ]	Brunt Väisälä frequency $N$ [ $s^{-1}$ ]
saturated adiabatic	0.4	0.011
dry adiabatic	1.0	0.018
very stable stratification	4.0	0.036

With the introduction and discussion of the Brunt Väisälä frequency  $N$ , this quantity can be calculated for any given atmosphere, described by the change of it's state variables and it's moisture content with altitude. The Brunt Väisälä frequency  $N$  is necessary for the estimation of the initial dimensions of the contrail, because atmospheric stability significantly influences the evolution of the wake vortices behind an aircraft, wherein the emissions are captured at the beginning.

### 2.3.2 Turbulence

For the calculation of the the contrail life cycle and the initial contrail dimensions, atmospheric turbulence has to be introduced and discussed. An analytical calculation of turbulence is not possible [74] and only possible with the help of models, describing single phenomenons of atmospheric turbulence. Because the contrail diffusion (it's mixing with the ambient atmosphere until complete dilution) and the evolution of the wake vortices depend on different aspects of atmospheric turbulence, two measures of

atmospheric turbulence have to be quantified to achieve the aim of this thesis. Therefore, a correlation between two different models of turbulence has to be developed. But first of all, an introduction of both atmospheric turbulence models is necessary. In meteorology, turbulence is defined as an irregular movement of air parcels around a mean state [75]. These movements are called turbulent elements or eddies. They have dimensions between millimeters and kilometers and lifetimes between seconds and days [75]. Turbulent elements are able to transport energy by their proper motion over a large distance. Thereby they transport heat (this is the so called sensible heat flux in Section 2.2.8) or water vapor (this is the latent heat flux) or kinetic energy, originating from the emission of terrestrial radiation by the Earth's surface. Eddies develop due to inertial forces in a stream. Large eddies receive their energy out of the mean flow and pass the energy to smaller eddies. Small turbulent elements decay releasing heat to the flow. This process is known as dissipation and is described by the eddy dissipation rate  $\varepsilon$ . Eddy dissipation  $\varepsilon$  is defined as the conversion of kinetic energy due to molecular friction per unit mass and per time into thermal energy. Hence the unit of  $\varepsilon$  is

$$\left[ \frac{\text{kg m}^2}{\text{kg s s}^2} \right] = \left[ \frac{\text{m}^2}{\text{s}^3} \right]. \quad (2.52)$$

In the lower troposphere, turbulence develops due to the exchange of state variables and ingredients of the atmosphere. In the boundary layer (the lowest 1000 m of the atmosphere) turbulences occur because of buoyant processes either due to differences in surface temperatures, because of friction on the surface, or because of enforced lifting due to altitude differences of the surface. Above the boundary layer, turbulences develop by shear stress between atmospheric layers with different flow velocities (so called clear air turbulences). Strong turbulences develop in the vicinity of jet streams, within convective buoyant processes. Beyond these occurrences, in the free atmosphere, turbulence is weak due to stable atmospheric stratification [76].

In this thesis, two different measures of turbulence are required. For the calculation of the initial dimensions of the contrail, the eddy-dissipation rate  $\varepsilon$  influences the sinking rate of the wake vortex due to the circulation within the vortices. The diffusion of the contrail into the environment after the circulation is decayed depends on horizontal and vertical turbulent diffusivities  $D_h$  and  $D_v$ . These turbulence measures can not be calculated without specific information about turbulence in the atmosphere. These specific measures are not available for this thesis. Hence, turbulence has to be assumed as parameter influencing the contrail life time and its initial dimensions. For this assumption, a correlation between both mentioned turbulence measures is necessary. This correlation is non trivial and needs a deeper look into turbulence and into both required turbulence measures.

### General considerations of turbulence

The following paragraphs will not give a complete description of turbulence, but concentrates on the correlation of the above mentioned parameters. This estimation depends on dimensional analysis, which allow quantitative assessments. Therefore, a model together with its parameters has to be introduced. The true velocity  $v$  is defined as the sum of the mean flow velocity  $u$  and irregular fluctuations  $u'$  around the mean velocity  $u$

$$v = u + u'. \quad (2.53)$$

The term  $u'$  denotes an overlay of movements (turbulent elements) with different dimensions and lifetimes. By analogy with water waves  $u'$  is like an overlay of waves with different frequencies and amplitudes.  $u$  is the time-averaged flow velocity of the velocity field  $v$ . Within the distance  $l$ , the flow velocity  $u$  changes significantly. The change of the mean velocity  $u$  over a distance  $l$  is called  $\Delta u$ . Additionally,  $l$  describes the external size of the turbulent elements.

### Eddy-dissipation rate $\varepsilon$

Small turbulent elements are detectable in the vertical coordinate of the wind velocity in stable stratification [73]. Measurements by [77] and dimensional analysis by [74] show, that the eddy dissipation rate  $\varepsilon$  becomes more important in turbulences dominated by small eddies. Hence, the eddy dissipation rate describes the possibility of an air parcel moving vertically within small scales. That's why,  $\varepsilon$  influences the sinking rate of the wake vortices in the first minute after vortex generation.

According to dimensional analyses [74] the dimension of the eddy dissipation rate  $\varepsilon$  has to be proportional to

$$\varepsilon \sim \frac{(\Delta u)^3}{l}. \quad (2.54)$$

However, characteristics as  $\Delta u$  and  $l$  are not quantifiable in this thesis.

The introduction of the turbulent viscosity  $\nu_{\text{turb}}$  [ $\text{m}^2\text{s}^{-1}$ ]

$$\nu_{\text{turb}} \sim l\Delta u \quad (2.55)$$

allows the estimation of the dimension of the eddy dissipation rate  $\varepsilon$ , proportional to the gradient of the mean flow velocity  $u$  over the distance  $l$  which is more concrete:

$$\varepsilon \sim \nu_{\text{turb}} \left[ \frac{\Delta u}{l} \right]^2. \quad (2.56)$$

Finally, the replacement of the turbulent viscosity  $\nu_{\text{turb}}$  by the molecular viscosity  $\nu$  [ $\text{m}^2\text{s}^{-1}$ ], which describes the molecular diffusivity of momentum, allows the quantification of the eddy dissipation rate  $\varepsilon$  [73]

$$\varepsilon = \nu \overline{\left( \frac{\partial u'_i}{\partial x_k} \right)^2}, \quad (2.57)$$

where

$$\overline{\left( \frac{\partial u'_i}{\partial x_k} \right)^2} = \overline{\left[ \left( \frac{\partial u'}{\partial x} \right) + \left( \frac{\partial u'}{\partial y} \right) + \left( \frac{\partial u'}{\partial z} \right) \right]^2} \quad (2.58)$$

denotes the mean squared changes of fluctuations  $u'$  around the mean wind velocity  $u$  in space. In the atmosphere at  $T = 20^\circ\text{C}$ , molecular viscosity amounts  $\nu = 0.15 \text{ cm}^2\text{s}^{-1}$  [73]. Molecular friction aspires an uniform distribution of the velocity field. This effect increases with an increasing gradient of the velocity field [73]. Hence, considering Equation 2.57, large differences between horizontal and vertical velocities (the terms in Equation 2.58) cause large values of the eddy dissipation rate.

However, in this work it is not possible to estimate the changes of fluctuations of the mean wind velocity in three directions in space. For this purpose turbulent measurements would be necessary. Such measurements at flight level are very difficult, because the measuring aircraft would cause turbulences by itself [76]. Fortunately a few turbulence measurements have been done [76] and values of  $10^{-6} \leq \varepsilon \leq 10^{-4} \text{ m}^2\text{s}^{-3}$  have been measured for stable stratification (compare Section 2.3.1) at cruise flight level ( $\approx 11 \text{ km}$  altitude). Anyhow, it is still not clear, how  $\varepsilon$  describes turbulence and how  $\varepsilon$  correlates with strong and weak turbulence. Therefore, the turbulent Reynolds number  $Re_{\text{turb}}$  characterizes turbulence by describing the change of the mean flow velocity  $\Delta u$  within a distance  $l$  [74],

$$Re_{\text{turb}} = \frac{\Delta u l}{\nu}. \quad (2.59)$$

For a turbulent flow, the turbulent Reynolds number is  $Re_{\text{turb}} \leq 1$  and grows with increasing turbulence [73]. Now, a correlation between  $Re_{\text{turb}}$  and  $\varepsilon$  would be helpful. Equation 2.59 indicates for increasing turbulence either an increasing of the fluctuations of the mean velocity  $\Delta u$  or of the dimensions of the turbulent elements  $l$  [73]. Large turbulent elements (i.e. strong turbulence, according to Equation 2.59) exist in flows with high flow velocities. On the other hand, the eddy dissipation rate depends on the changes of fluctuations  $u'$  around the mean flow velocity  $u$  (compare Equation 2.57). A correlation between  $u$  and  $u'$  can not be generalized. However, large turbulent elements indicate much kinetic energy, which can be converted to thermal energy, after the kinetic energy had been transported to small turbulent elements. Hence, strong turbulence indicate large values of the eddy dissipation rate.

Now, the eddy dissipation rate can be quantified, or at least it can be implicated with strong or weak turbulence. The second turbulence metric, the diffusion coefficients  $D_h$  and  $D_v$ , necessary for the estimation of the contrail diffusion in the ambient atmosphere, is easier to understand and will be discussed in the following.

### Turbulent diffusion coefficients $D_h$ and $D_v$

Diffusion is a thermally determined process. Differences in concentration of different matters within a fluid get aligned by random motions of the substance (molecules, ions or atoms within the fluid). This time dependent process can be characterized by Fick's law [78]

$$J = -D \frac{\partial c}{\partial x}, \quad (2.60)$$

where  $J$  denotes the diffusion flux, which is a particle current density [ $\text{mol m}^{-2} \text{s}^{-1}$ ] as number of particles per unit area and time,  $D$  describes the diffusion coefficient [ $\text{m}^2 \text{s}^{-1}$ ] and the fraction  $\partial c(\partial x)^{-1}$  denotes the molar concentration gradient [ $\text{mol m}^{-3}$ ] along the distance  $x$  [m] resulting in units of  $\text{mol m}^{-4}$ .  $D$  measures the proper motion of particles and depends on matter, pressure and temperature [79]. This movement originates either from Brownian motion (in this case molecular diffusion is described) or the movement is externally driven. If the fluid itself is in motion, the motion of the particles (and the adjustment of concentration) will be accelerated. This process is described by turbulent diffusion [79]. Hence, strong turbulence results in large values of  $D_v$  and  $D_h$ .<sup>1</sup>

---

<sup>1</sup>The difference between molecular and turbulent diffusion can be shown by a glass of water, where someone put in a drop of ink. The mixing would take hours (in case of molecular diffusion), unless someone stirs the fluid and causes an accelerated motion within the matter (turbulent diffusion).

Now, both turbulence measures can be correlated with weak or strong turbulence. Typical values for both metrics can be taken from measurements [76].

### 2.3.3 Conditions of contrail formation

Another thermodynamically describable procedure is the formation of a condensation trail. The contrail forms within the exhaust plume of the aircraft. For convenience, the following wording is used: As long as the conditions of contrail formation are to be estimated, the aircraft exhaust gases will be called "plume", until a contrail formation is sure. For contrail formation, the ambient atmosphere has to satisfy two criteria: On the one hand, the ambient temperature  $T_E$ <sup>2</sup> of the atmosphere must be lower than a threshold temperature  $T_{LC}$ , which can be determined by the Schmidt-Appleman criterion. On the other hand, the ambient atmosphere must be ice-supersaturated  $rH_{ice} > 100\%$ . Otherwise, the contrail will sublime within a short time resulting in a negligible impact on the energy budget of the Earth-atmosphere system.

The thermodynamical formulation of conditions of contrail formation has been done by Appleman and first published by Schmidt [18] in 1940. Hence, the estimation of the threshold temperature  $T_{LC}$  for contrail formation is called Schmidt-Appleman criterion. A derivation of the criterion and a solution is given by Schumann [22]. The following assumptions are made in [22]: 1. All thermal energy coming from the jet engine is converted to internal energy of the exhaust plume. 2. Heat is mixing instantaneously and uniformly within the plume. 3. A complete combustion is considered. 4. Adiabatic (no heat exchange with the ambience) and isobaric (no differences in pressure between environment and exhaust plume) conditions are assumed. Initially neglecting water vapor and enthalpy of the environment in comparison to water vapor and enthalpy of the exhaust gases, the mixing of the engine emissions with the ambient air follows a straight line in an enthalpy-mass diagram with the slope  $G$

$$G = \frac{Q(1 - \eta)}{EI_{\text{water}}}, \quad (2.61)$$

where  $Q = 43 \text{ MJ kg}^{-1}$  denotes the specific combustion heat of the kerosene.  $EI_{\text{water}}$  describes the emission index of water vapor [ $\text{kg kg}^{-1}$ ],  $\eta$  defines the overall propulsion efficiency as the fraction between resulting energy (Thrust  $F$  [N] times true air speed  $v_{\text{TAS}}$  [ $\text{m s}^{-1}$ ]) and required energy (specific combustion heat  $Q$  and fuel flow  $\dot{m}_f$  [ $\text{kg s}^{-1}$ ])

---

<sup>2</sup>the index E refers to "environment"

$$\eta = \frac{F v_{TAS}}{Q \dot{m}_f}. \quad (2.62)$$

Considering the overall definition of the static enthalpy  $h$

$$h = \int c_p dT \quad (2.63)$$

and the emitted mass of water vapor  $m_P$ <sup>3</sup>, which can be understood as a fraction of the vapor pressure in the plume  $e_P$  [Pa] and the air pressure  $p$  [Pa] weighted by the ratio  $\epsilon_{mol} = 0.622$  between molar masses of dry air and water vapor

$$m_P = \epsilon_{mol} \frac{e_P}{p}. \quad (2.64)$$

Equation 2.61 delivers a straight line in a vapor pressure- temperature diagram with the slope  $G$ , already introduced in Equation 2.61

$$G = \frac{EI_{water} c_p p}{\epsilon_{mol} Q (1 - \eta)} = \frac{\Delta e}{\Delta T} = \frac{e_P - e_E}{T_P - T_E} \quad (2.65)$$

characterizing the mixing of the plume with the environment. In Equation 2.12 the slope of the mixing line is defined between the conditions in the plume ( $e_P, T_P$ ) and the environment ( $e_E, T_E$ ). Hence, the line with slope  $G$  describes the mixing process between aircraft emissions and environment from the beginning (the emission) to the end (the complete mixture). If the mixture is saturated with respect to water, condensation will take place and condensation trails will form. An example mixing line with slope  $G$  and the function of the saturation pressure above water are plotted in Figure 2.12.

An intersection between the mixing line and the saturation vapor pressure curve results in a saturation of the mixture. It represents contrail formation. However, in general, only the slope of the mixing line is known not the point of origin, which is necessary for finding the intersection point with the saturation vapor pressure curve, if there is one. On threshold condition both graphs will intersect in the point ( $e^*(T_{LM})$ ) where

$$\frac{de^*(T_{LM})}{dT} \stackrel{!}{=} G \quad (2.66)$$

---

<sup>3</sup>the index P refers to "plume"



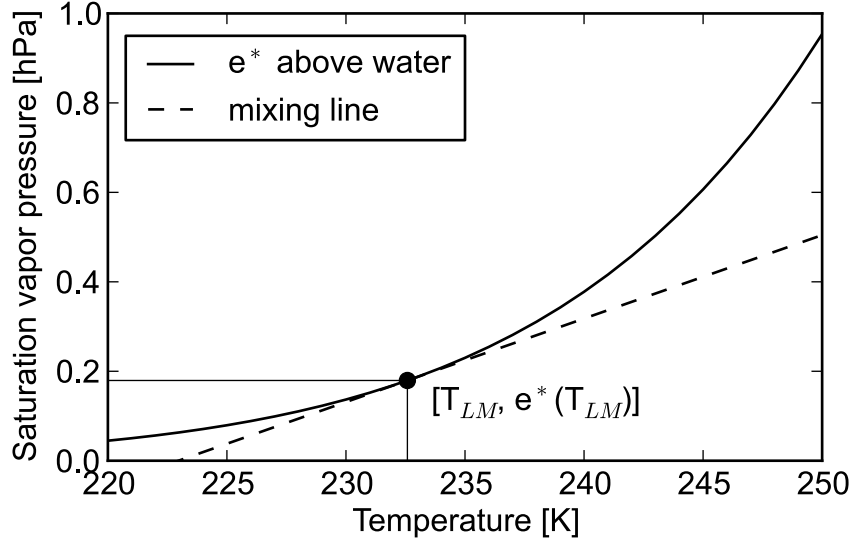


**Figure 2.12:** Saturation vapor pressure above water (solid) and an example mixing line of exhaust emissions with the atmosphere (dashed). The slope of the mixing line is  $G = 1.86 \text{ PaK}^{-1}$ .  $G$  is calculated for an A320 aircraft at 10.37 km altitude and pressure  $p = 243 \text{ hPa}$  with the following flight performance characteristics: true air speed  $v_{\text{TAS}} = 244.36 \text{ m s}^{-1}$ , fuel flow  $\dot{m}_f = 0.72 \text{ kg s}^{-1}$ , Thrust  $F = 50.72 \text{ kN}$  and overall propulsion efficiency  $\eta = 0.4$ . Calculations according to Schumann 1996 [22] using the standard atmosphere for mid latitudes in winter by Anderson et al. [52] with a relative humidity at 10.37 km altitude of  $rH_{\text{water}} = 0.78$  result in a threshold temperature  $T_{\text{LC}} = 227.24 \text{ K}$  and  $T_{\text{LM}} = 232.58 \text{ K}$ .

has to be fulfilled. Interpreting  $G$  as difference in vapor pressure over difference in temperature between saturation ( $e^*(T_{\text{LM}})$ ) and ambient conditions ( $e_E$ ), the derived temperature  $T_{\text{LM}}$  is the threshold temperature for contrail formation in a saturated environment. In undersaturated conditions, the mixing would not be complete at the state  $e^*(T_{\text{LM}})$  the exhaust plume would further mix with the environment, until the ambient relative humidity  $rH_E$

$$rH_E = \frac{e_E}{e^*(T_{\text{LC}})} \quad (2.67)$$

is reached.  $rH_E$  can be used to calculate the corresponding vapor pressure of the environment by  $e_E = rH_E e^*(T_{\text{LC}})$  which is then used as lower boundary in the difference of vapor pressure  $\Delta e$  for the mixing line (compare Equation 2.65) in the following way:

$$G = \frac{\Delta e}{\Delta T} = \frac{e^*(T_{LM}) - rH_E e^*(T_{LC})}{T_{LM} - T_{LC}}. \quad (2.68)$$

Finally, the threshold temperature for contrail formation  $T_{LC}$  can be calculated iteratively.

$$T_{LC} = T_{LM} - \frac{e^*(T_{LM}) - rH_E e^*(T_{LC})}{G}. \quad (2.69)$$

According to Schumann 1996 [22] a good starting value for the iteration for  $T_{LM}$  [°C] denotes

$$T_{LM} = -46.46 + 9.43 \ln(G - 0.053) + 0.720(\ln(G - 0.053))^2. \quad (2.70)$$

Equation 2.70 is valid for values of  $G$  between  $0.24 \leq G \leq 23 \text{ Pa K}^{-1}$ . Measurements with LIDAR and numerical simulations of contrails behind different aircrafts yield an estimation of the influence of the ambient humidity on the contrail life time [20]. Behind an Airbus A320 aircraft two different types of contrails can be observed. Either the contrails sublimates after approximatively four seconds, or the condensation trail develops into a long living artificial ice cloud. The reason for this differences could be found in the relative humidity with respect to ice  $rH_{ice}$ . In an ice-supersaturated environment the ice particles in the contrail may grow on, while in comparatively dry air the ice particles sublime quickly. Hence, for persistent contrail formation the ambient air has to be supersaturated with respect to ice. According to differences in saturation vapor pressure over ice and over water an ice-supersaturated environment  $rH_{ice} = 1.0$  at flight level (with temperatures around  $T = 230 \text{ K}$ ) occurs at approximatively  $rH_{water} = 0.7$ .

## 3 Development of a radiative forcing model

*Within this chapter the development of a model calculating the radiative extinction properties of a condensation trail takes place. Therefore, a model atmosphere Mid-Latitude Winter and a flight performance model are introduced. These models combined, offer the possibility of precisely calculating the life cycle of the condensation trail formed within the model atmosphere behind the aircraft of this particular modeled flight. This provides the opportunity of estimating the radiative extinction of this individual contrail. After introducing radiative transfer solvers, a radiative extinction model is developed and calibrated to determine the expected solar and terrestrial radiation in the vicinity of the contrail, which is to be extinguished by the contrail.*

### 3.1 Model atmosphere

An overview over the common standard atmospheres was given in Section 2.1.2. For the reason of comparability, a variation of the atmospheric reference model Mid-Latitude Winter provided by the AFGL [52] will be used. This atmosphere represents mean values of temperature, pressure and density as functions of altitude. Furthermore, concentrations in terms of volume mixing ratios [ppm] of water vapor  $\text{H}_2\text{O}$ , ozone  $\text{O}_3$ , nitrous oxide  $\text{N}_2\text{O}$ , carbon monoxide  $\text{CO}$  and methane  $\text{CH}_4$  as functions of altitude are provided. The information about concentrations of water vapor and trace gases distinguishes the AFGL atmospheres from other standard atmospheres. The humidity is necessary for the criterion of contrail formation and the concentrations of all ingredients of the atmosphere are required for the precisely calculation of the radiative transfer.

This type of atmosphere is already cold enough to satisfy the Schmidt-Appleman criterion but not ice-supersaturated ( $rH_{\text{ice}} < 1$ ) to allow the formation of persistent contrails

(compare section 2.3.3) at altitudes where air traffic operations take place. To further model the potential of the appearance of persistent contrails in accordance with realistic heterogeneous atmospheric conditions, the relative humidity with respect to ice ( $rH_{ice}$ ) is manipulated following a Gaussian distribution function with a mean value of 10.5 km and a standard deviation of 1 km. The Gaussian distribution function is simply used to model smooth transition between the original values of relative humidity and the manipulated ones. These transitions are taking place at 7 km and 15 km. Due to this manipulation, contrails may become persistent, but natural clouds are still unlikely to appear because of a weak ice-supersaturation within the added ice-supersaturated layer (compare Figure 3.1). This manipulation quadruples the relative humidity with respect to ice of this model atmosphere at flight level. In comparison with the study of measurements of relative humidity profiles recorded by radiosonde data, this manipulation is within a realistic frame. Additionally, studies regarding the distribution and magnitude of ice-supersaturated layers in the upper troposphere [80] confirm the realistic nature of the manipulated model atmosphere.

The temperature gradient in the model atmosphere (compare Figure 3.1) is small and defines a stable atmospheric stratification (compare section 2.3.1). Due to constant temperature near the tropopause, in the vicinity of the air traffic relevant flight level, the atmospheric stability increases with altitude. The negative temperature gradient implicates colder atmospheric layers with increasing altitude. Remembering the Schmidt-Appelmann criterion, which predicts a higher probability of contrail formation in colder atmospheric layers, concludes: the higher the aircraft flies, the higher the probability of contrail formation.

This model atmosphere, interacting with virtual air traffic, modeled by the Enhanced Jet Performance Model EJPM of Kaiser [81], allows the estimation of the required parameters for the Schmidt-Appelmann criterion to decide on those particular time steps where contrail formation takes place.

## 3.2 Flight performance model

Air traffic may be optimized with respect to minimum radiative contrail impact on several different ways. Ice-supersaturated regions could be flown round or aircrafts could fly below the ice-supersaturated regions in general. Anyhow, the aircraft performance itself is suspected of influencing the contrail optical properties. Furthermore, considering the Schmidt-Appelmann criterion, the aircraft performance decides, whether contrails will form or not. Hence, for an elaborately study of the contrail optical properties, an aircraft performance model is necessary, providing information about Thrust  $F$ , fuel flow  $\dot{m}_f$ , and true air speed  $v_{TAS}$  for each time step of a flight path from origin to

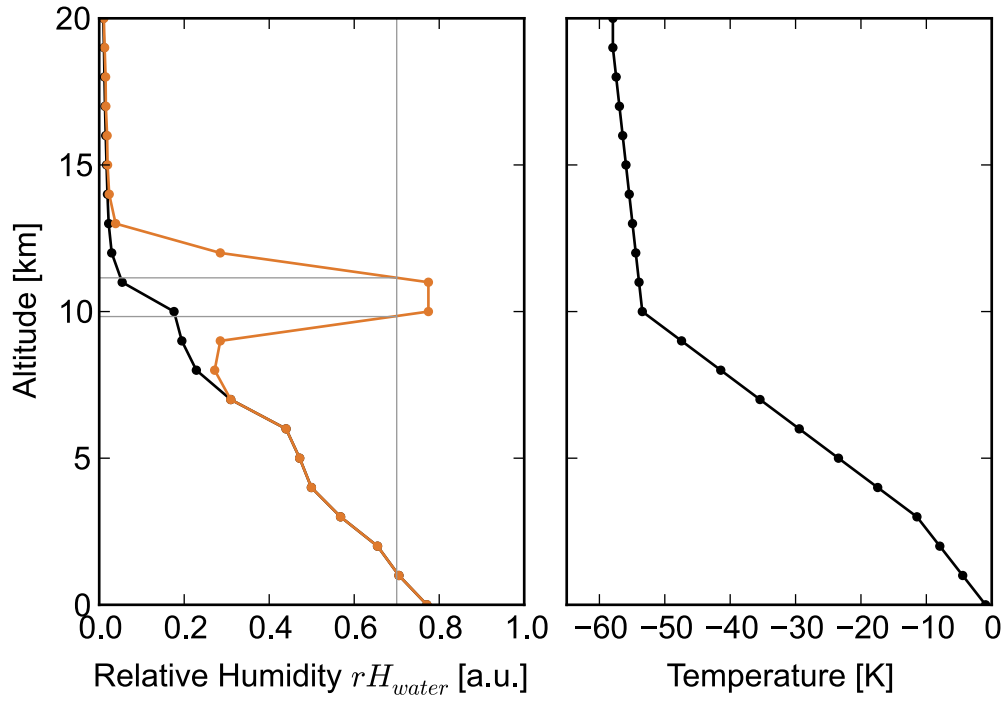


**Figure 3.1:** The model atmosphere Mid-Latitude Winter according to Anderson *et al.* [52]. Profiles of original (black) and manipulated (orange) relative humidity and temperature. The horizontal grey lines emphasize the vertical extent of the ice-supersaturated layer. The vertical grey line in the humidity plot demonstrates the boundary of ice-supersaturation, because  $rH_{ice} = 1$  for  $rH_{water} \approx 0.7$  for temperatures at flight level. Differences between relative humidity above water and ice are due to different saturation water vapors (compare section 2.1, Figure 2.1).

destination. Therewith, the emission principles, necessary for contrail formation, are determined. The Enhance Jet Performance Model of Kaiser (EJPM) [81] generates the required data for an optimized flight profile with respect to minimum fuel flow. Here, an application of the EJPM resulting in a short distance flight profile of an Airbus A320 is used. This flight path includes common cruising altitudes and is suitable for contrail formation. Four-dimensional information about the lateral and vertical position of the aircraft are provided for each time step by the EJPM. The most important characteristics of the aircraft Airbus A320 are listed in Table 3.1, information is taken from the Airbus Aircraft characteristics 2014 [82].

**Table 3.1:** Main characteristics of the aircraft Airbus A320.

Characterisitic	value
Length	37.57 m
Wingspan	34.1 m
Operating empty mass	42600 kg
Maximum landing mass	66000 kg
Maximum take-off mass	78000 kg
Maximum range (fully loaded)	5700 km
Engines	2 x CFM56-5
Thrust	2 x 111 – 120 kN

The EJPM optimizes fuel consumption and the lift to drag ratio using a maximum specific range [81]. It uses analytical methods for both the aerodynamic modeling and the aircraft propulsion system. EJPM is able to implement stochastic parameter functions for the consideration of dynamic input parameters. Furthermore, the EJPM can respond to time variant changes of atmospheric state variables [83]. Within EJPM the Enhanced Trajectory Prediction Model (ETPM) calculates precise four-dimensional trajectories [10]. The input parameters of the ETPM are state variables like speed  $v_{TAS}$  and orientation, initial aircraft mass  $m$  and selected thrust  $F$ . The selected thrust is calculated within an optimization module of the EJPM according to the target function. Additional, environment parameters like state variables of the atmosphere, the wind vector and the relative humidity  $rH_{water}$  (influencing the required engine thrust) are considered [83]. Furthermore, airframe parameters, for example the wing reference area, the wing span and factors describing the parasitic drag and the lift induced thrust are taken into account. The aircraft engine parameters are based on empiric formulas of EUROCONTROL's Base of Aircraft Data (BADA) [84] including fuel flow coefficients and thrust coefficients describing the efficiency of the engine [83]. With the help of these input parameters the EJPM calculates all flight mechanical basics and flight

performance properties. A speed determination module and a lift to drag module are included. Furthermore, operational limits of the current conditions are considered. For this thesis, the following engine parameters are calculated: required Thrust  $F$ , fuel flow  $m_f$ , and true air speed  $v_{TAS}$ . Furthermore, mass  $m$ , altitude  $z$  and distance  $s$  are taken from the flight profile. Figure 3.2 demonstrates the overall change of the given engine parameters with distance and the altitude of the flight profile.

### 3.3 Atmospheric radiative transfer model

For the calculation of the influence of a contrail on the Earth's energy budget, the angular dependent spectral radiances at the position of the contrail in the Earth-atmosphere system have to be known. For this purpose the radiative transfer software package libRadtran [85] is used for solving the radiative transfer equation (Equation 2.46, Section 2.2.7).

Solving the radiative transfer equation requires the knowledge of the extinction coefficient  $\beta_e$  and the absorption coefficient  $\beta_a$  or the single scatter albedo  $\tilde{\omega}$  between the top of the atmosphere and the Earth's surface. However,  $\beta_e$  and  $\beta_a$  depend on wavelength and particle characteristics. Hence, every molecule of the atmosphere holds its proper wavelength value of  $\beta_e$  and  $\beta_a$ . Furthermore, the emission of radiation by atmospheric molecules in the terrestrial wavelength region constitutes an important source term in the radiation budget. This source term equals the absorption coefficient  $\beta_a$  (compare Section 2.2.3, Kirchhoff's law) and further depends on temperature  $T$  and structure of the molecule. Furthermore, the amount of emission is partly the result of scattering. Hence, the radiative transfer equation is a integrodifferential equation, which must be solved numerically.

libRadtran is a library of several radiative transfer solvers for different applications [85]. Within libRadtran, the manipulated model atmosphere Mid-Latitude Winter with the added ice-supersaturated layer is used. The model considers the solar and the terrestrial spectrum with wavelengths between  $120 \text{ nm} \leq \lambda \leq 100 \text{ }\mu\text{m}$ . The tool includes ten radiative transfer solvers [85]. The composition of the atmosphere can be influenced, for example by adding molecules, clouds with specific properties and aerosol particles. The Earth's surface as lower boundary can be manipulated by specifying the reflectivity and the orography. Furthermore, libRadtran contains several libraries with specific information about the Earth's surface at any dedicated point on Earth. For example, the surface library of the International Geosphere Biosphere (IGBP) from the NASA CERES/SARB Surface Properties Project [86] can be used for surface reflectance  $a$  [57]. libRadtran includes several tools for the preparation of the radiative transfer calculation. For example, the position of the sun at a dedicated time and day

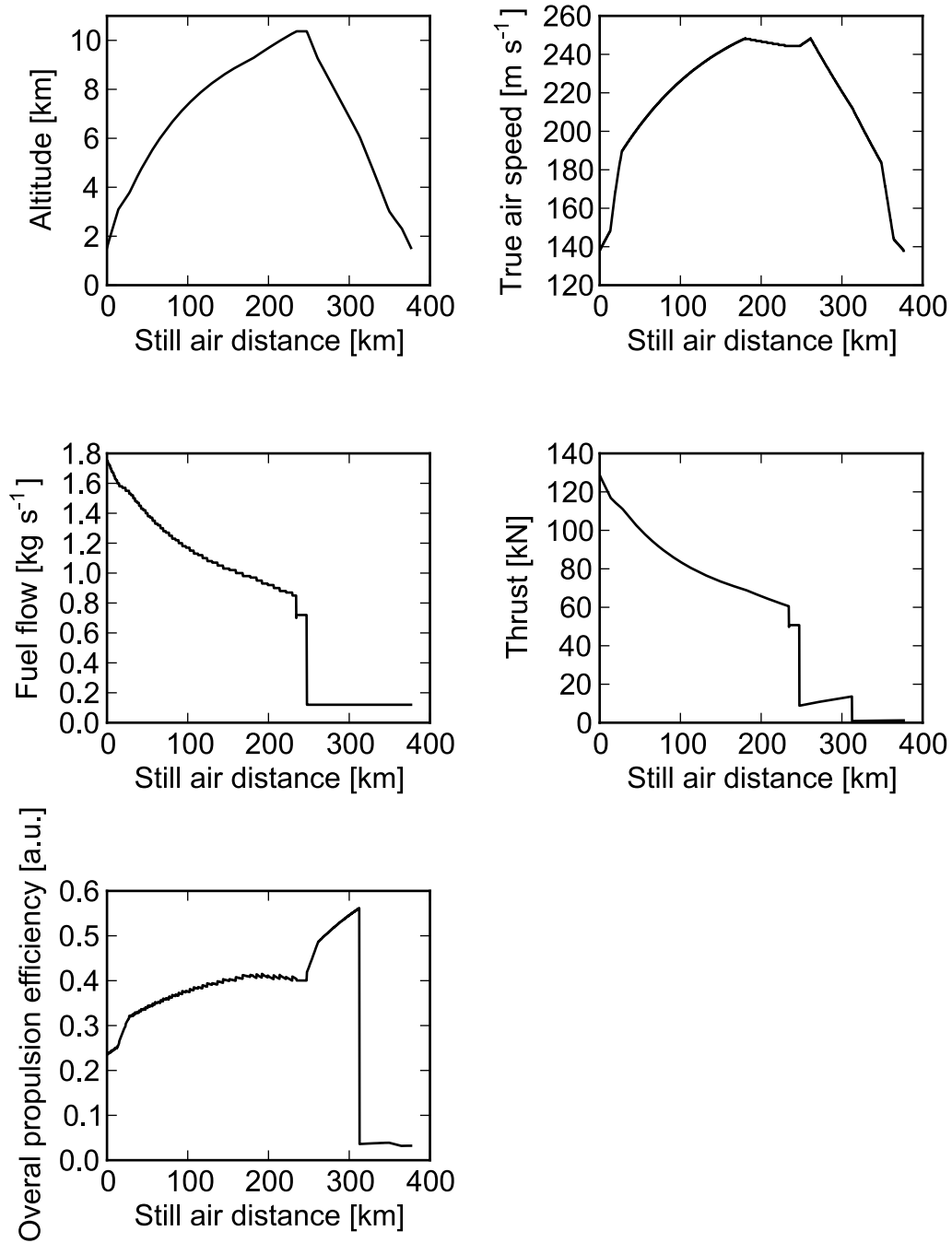


**Figure 3.2:** Engine parameters of the short distance flight of an Airbus A320, calculated with the Enhance Jet Performance Model (EJPM) [81] assuming the international standard atmosphere ISA. For the application of the Schmidt-Appleemann criterion, the overall propulsion efficiency (compare Equation 2.62) is shown.



of year can be calculated. Furthermore, some post processing of the output like integration over several wavelengths or interpolation between wavelengths, which are not calculated, are enabled [85]. Due to different properties of solar and terrestrial extinction in the atmosphere, different radiative transfer solvers have to be used. Both solvers will be introduced in the following.

### 3.3.1 Two Stream Approximation

In the thermal wavelength spectrum, absorption by atmospheric molecules is an important process. The magnitude of absorption strongly depends on wavelength and varies between neighboring wavelengths. These narrow absorption bands require a high spectral resolution in the radiative transfer calculation and therefore a high computational effort. However, a weak angular dependence of radiation due to a missing part of direct irradiance is expected. A solution of the radiative transfer equation using a Two Stream Approximation (TSA) takes advantage of the weak angular dependence and reduces the computational effort [87]. Here, all radiances  $I$  coming from one hemisphere are averaged over the half space and are treated as a single irradiance  $F$  without specific information about the angular direction. The Two Stream Approximation is often used for computing photodissociation rates and surface irradiances. Even clouds and aerosols within a vertically inhomogenous atmosphere and spherical geometry can be considered [87].

As mentioned, the Two Stream Approximation is characterized by an azimuthally averaged radiative transfer equation. From this follows an azimuthally isotropic scattering medium is assumed. Furthermore, an approximately constant radiance  $I(\theta)$  in each hemisphere is assumed. Hence, two irradiances at any altitude remain:  $F_{\text{up}}$  and  $F_{\text{down}}$ . The two remaining irradiances are demonstrated in Figure 3.3.

This assumption is valid above uniform flat surfaces [66]. Often, a linear gradient of the brightness between horizon and zenith is detectable. In this case, the Two Stream Approximation is also a possible solution, assuming a mean value of brightness [66]. Due to the necessary assumption of isotropic scattering the results will be most accurate for an isotropic radiation field, for example, inside a homogenous medium, or far away from boundaries, sinks or sources [71]. The accuracy of the solution of the TSA compared with accurate computations for a homogenous slab is very high (errors smaller than 2.5%) for solar zenith angles  $\cos \theta \geq 0.4$  [71]. As for every numerical problem, the accuracy depends on the solution algorithm and necessary assumptions made in the solver [71]. These assumptions will be discussed in the following and in Section 3.3.3 in more detail.

The general idea of solving the radiative transfer equation (Equation 2.46) is a replace-

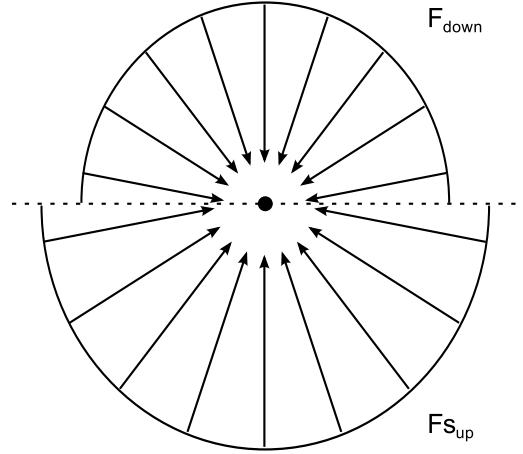


**Figure 3.3:** *Geometry of the Two Stream Approximation. The azimuthally averaged irradiances  $F_{\text{up}}$  and  $F_{\text{down}}$  correspond to two considered streams and are mean values of each hemisphere.*

ment of the integrals of the zenith angle by summations [71]. In the solution of Kylling et al. [87] the summations are done over quadrature points and weights. Often, the Gaussian quadrature based on Legendre Polynomial is used [71] for this purpose. For the estimation of the quadrature points and weights, a polynomial in the indeterminate  $\cos \theta$  of degree  $(2n - 1)$  is required [87]. The degree of the polynomial defines the number of streams of radiances, each representing a different direction of radiances [66]. Hence, the Two Stream Approximation holds for  $n = 1$  [71], resulting in a degree of polynomial of 2, corresponding to 2 streams  $F_{\text{up}}$  and  $F_{\text{down}}$ . Within the streams the radiances do not depend on zenith angle  $\theta$  or azimuthal angle  $\phi$  [66].

For terrestrial radiative transfer calculations the solver twostr by Kylling et al. [87] is used. Here, the scattering phase function can be described by the asymmetry parameter  $g_{\text{HG}}$ . Hence, the downward and upward irradiances are weighted by the fraction of forward to backward scattering [71]. Due to the backscattering phenomena,  $F_{\text{up}}$  and  $F_{\text{down}}$  depend on each other and a coupled pair of ordinary linear differential equations has to be solved [71].

### 3.3.2 Discrete ordinate radiative transfer solver

In the solar wavelength region a Two Stream Approximation is out of question, because of a large influence of the direct beam on the radiation field. This influence causes a strong angular radiative dependence which cannot be described by a Two Stream Approximation. The radiative transfer solver DISORT (DIScrete Ordinate Radiative Transfer solver) is used for the calculation of direct and diffuse solar radiances  $I_{\text{dir}}$  and

$I_{\text{diff}}$ . DISORT was developed by Stamnes et al. [88] and solves the radiative transfer in a one-dimensional geometry. Spherical effects may be considered using the pseudo spherical solver by Dahlback et al. [89]. DISORT is the most used, recommended and most updated solver for angular depending radiative transfer in the shortwave spectrum [57]. Processes like thermal emission, scattering, absorption, bidirectional reflection and emission at the lower boundary are considered [88]. The DISORT solver is a generalization of the Two Stream Approximation to a large number of discrete streams of radiation, each representing a different direction [66]. DISORT can handle a maximum number of 256 streams [90], which are used in this thesis for an optimized angular dependent calculation of the direct beam. As explained above, the number of streams is defined by the degree of the polynomial, which defines the quadrature points and weights of the quadratures replacing the integral over  $\cos \theta$ . The higher the degree of the polynomial, the higher the accuracy of the adaption to the real function  $I(\cos \theta)$ , because the more different radiances coming from different directions are considered. Because of the fact, that the single scatter albedo  $\tilde{\omega}(\tau)$  and the scattering phase function  $P(\tau, \cos \theta, \varphi, \cos \theta', \varphi')$  are functions of the optical path  $\tau$  in a vertical homogeneous medium, a parallel laminated stack of homogeneous layers with constant  $\tilde{\omega}$  and  $P$  for each layer is used in DISORT. This enhances the efficiency of the algorithm [90]. The procedure is demonstrated in Figure 3.4.

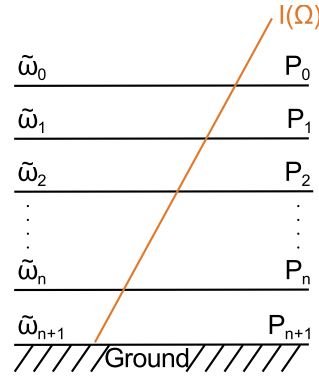


**Figure 3.4:** Geometry of the Discrete Ordinate Radiative Transfer solver (DISORT) considering homogenous plane parallel layers with constant values of single scatter albedo  $\tilde{\omega}$  and scattering phase functions  $P$  for each layer.

### 3.3.3 Methods to calculate broadband radiances and irradiances

As mentioned, absorption, emission and scattering are highly wavelength specific processes. For radiative transfer calculations, the radiative transfer equation (Equation 2.46) has to be solved for each wavelength one by one or at least for a very narrow wavelength

range of  $\Delta\lambda \leq 5$  nm. Furthermore, for each wavelength the absorption and scattering coefficients have to be known. To calculate monochromatic radiances  $I_{\text{dir}}$  and  $I_{\text{diff}}$  or irradiances  $F_{\text{up}}$  and  $F_{\text{down}}$  at a given altitude the sum of the contributions of all important absorption lines (of all present molecules) would define the absorption coefficient  $\beta_a$ . These calculations require a large computational effort. Especially in the thermal wavelength region, absorption bands are quite narrow. For this purpose tables of such line positions and strengths of important absorption bands in the atmosphere are available (for example the HIRTRAN database). However, the computational effort is still intractable. Due to the fact, that emission of molecules (after they absorbed radiation) takes place in a wavelength according to their temperature and not according to the wavelength of the absorbed radiation, the absorption coefficient has to be determined for all wavelengths and for all points along the path from a given boundary up to the point of interest. If scattering is considered, calculations of all directions within the globe are necessary. These calculations are called line-by-line calculations.

There are different approaches reducing the computational time. The general idea of these models is an analytical treatment of the absorption spectrum by replacing the original spectrum with an analytically solvable function. For this purpose, band models and k-distribution models divide the thermal spectrum into intervals, each being large enough to reduce computational effort and small enough to assume a constant Planck function  $B_{\tilde{\nu}}(T)$  [66]. The wavenumber  $\tilde{\nu}$  [ $\text{cm}^{-1}$ ] is the reciprocal of the wavelength [66]

$$\tilde{\nu} = \frac{1}{\lambda}. \quad (3.1)$$

Band models like the Elsasser band model or the Random/Molkmus band model try to find analytical approximations to the band averaged transmittance over a finite mass path  $v$  [71]. Following Dalton's law (compare section 2.1) the mass path  $v$  [ $\text{kgm}^{-2}$ ]

$$v = \int_{s_1}^{s_2} \rho(s) ds \quad (3.2)$$

can be used for a single constituent or a mixture of different ingredients. For the analytical approximation to the band averaged transmittance, band models assume a statistical distribution of the line positions and strengths within the spectral band [71]. Hence, band models only consider absorption and emission, scattering is neglected [66].

The so called k-distribution method additionally considers scattering and replaces the integration over frequency with an equivalent integration over a smoother function  $k(\zeta)$ , which allows for large discretization steps and reduces computational effort [71]. There

are two approaches of the k-distribution method available: The first one only considers homogenous paths, the second one includes inhomogenous paths. The difference between a homogenous and an inhomogenous path is difficult to explain and will be discussed as disadvantage of the homogenous path method.

The homogenous path method averages a spectrum between the wavenumbers  $\tilde{\nu}_1$  and  $\tilde{\nu}_2$  and numerically evaluates the integral of transmittance T

$$T(\nu) = \frac{1}{\tilde{\nu}_1 - \tilde{\nu}_2} \int_{\tilde{\nu}_1}^{\tilde{\nu}_2} \exp[-k(\tilde{\nu})\nu] d\tilde{\nu} \quad (3.3)$$

with  $k(\tilde{\nu})$  as absorption spectrum. Therefore, the integral (Equation 3.3) is replaced with summations, characterized by the number  $N_{\tilde{\nu}}$  of wavenumbers  $\tilde{\nu}_i$ , the mean values of  $k(\tilde{\nu})$  and weights. Sorting all  $N_{\tilde{\nu}}$  values of  $k(\tilde{\nu})$  ascendingly, yields a definition of a new function  $k(\varsigma)$  with  $0 \leq \varsigma \leq 1$  ( $\varsigma = 0$  and  $\varsigma = 1$  correspond to the smallest and the largest values of  $k(\tilde{\nu})$ , respectively), which is a simple monotonic increasing function and allows the replacement of the integral over the original spectrum by a simpler integral.

$$T(\nu) = \int_0^1 \exp[-k(\varsigma)\nu] d\varsigma \quad (3.4)$$

All information is preserved, just the order of the absorptions lines within a small range of wavenumbers  $\tilde{\nu}_i$  is lost. This method is recommended by [71], if the transmittance of different mass paths  $\nu$  for equal temperature and pressure are required, because the derivation of the new function  $k(\varsigma)$  is as complicated as a line-by-line calculation. If  $k(\tilde{\nu})$  is constant over the path, no significant changes in the constitution of the atmosphere along the path will take place. This is defined as the homogenous path. This is satisfied along short horizontal paths [71].

Unfortunately, the changes of pressure and temperature with altitude are not negligible and a phenomenon called pressure broadening dominates the spectrum. Pressure broadening is the spreading of frequencies of a spectral line due to interactions between the molecules [71]. The number density of gas molecules is proportional to the pressure at a constant temperature. The smaller the number density of gas molecules, the higher the potential energy of intermolecular interactions. Hence, pressure broadening leads to a smoother spectrum with reduced peaks [66].

The inhomogenous path method (so called correlated-k) computes for every value of  $\varsigma$  the transmittance over the path  $\nu'$  for a range of mass path  $\nu$  between  $\nu_1$  and  $\nu_2$  and averages the derived transmittance over the interval  $0 \leq \varsigma \leq 1$  [66]. Therefore,

Equation 3.4 is replaced by

$$T(\nu) = \int_0^1 \exp\left[-\int_0^u k(\zeta, \nu') d\nu'\right] d\zeta. \quad (3.5)$$

This approach will only be valid, if a value of  $\zeta$  corresponds to the same wavenumber  $\tilde{\nu}$  along the inhomogenous path [71]. In this case, pressure broadening would not take place. Hence, calculated irradiances with Equation 3.5 are in general defective, yet the errors are smaller than 1% [71]. Because line-by-line calculations are not an alternative, the correlated-k method is used in this thesis. Compared to line-by-line methods, the correlated-k approach saves computational efforts by factors of 1000 [71]. Furthermore, correlated-k models are able to solve multiple scattering problems accurately [71]. They are recommended for one-dimensional radiative calculations, because the computational effort is still too large for three-dimensional calculations. Because the angular dependence of the direct solar radiation is very important in this study, the computational time is accepted for the sake of nearly accurate radiative transfer calculations.

The radiative transfer library libRadtran offers several types of correlated-k schemes depending on the aim of the calculations. Special schemes for terrestrial wavelengths above  $2.5 \mu\text{m}$  by Kato et al. [91] or for a specific extraterrestrial solar spectrum Kato et al. [91], Fu et al. [92] and Kratz et al. [93] are available. An approach called LOW-TRAN of Ricciazzi et al. [94] considers both solar and terrestrial wavelengths, interacts with any given solar spectrum and is used in this thesis.

With this last explanation, all required parameters for the radiative transfer calculations are defined. Now, the solar and terrestrial wavelength spectrum at the position of the contrail can be calculated. The solar wavelength spectrum can be estimated for all directions in space considering diffuse and direct radiances  $I_{\text{diff}}$  and  $I_{\text{dir}}$  [ $\text{W m}^{-2}\text{nm}^{-1}\text{sr}^{-1}$ ]. The terrestrial wavelength spectrum can be calculated as averaged irradiances, integrated over one hemisphere  $F_{\text{down}}$  and  $F_{\text{up}}$  [ $\text{W m}^{-2}\text{nm}$ ] coming from above or below the contrail. In the calculated quantities, radiative extinction due to molecules within the atmosphere depending on contrail altitude, longitude and latitude, as well as time of the day and time of the year is considered accurately. This precision is necessary for the optimization of the aircraft trajectory with respect to a minimum influence of the contrail on the radiation budget, because not only the radiative extinction due to the contrail differs with altitude, longitude, latitude, time of the day and time of the year, but also the background radiances and irradiances at the position of the contrail are variables of those parameters.

In the following, the radiative extinction due to the contrail will be calculated. This phenomenon depends on the microphysical properties of the contrail, which in turn are

functions of the flight performance, which is to be optimized in this thesis. Hence, first of all, the microphysical properties of the contrail have to be modeled from the beginning, right after contrail formation, until the end, when the contrail is completely mixed with the ambient atmosphere. The approach has been already published by Rosenow et al. 2012 [95].

### 3.4 Contrail life cycle model

Right after aircraft engine emission, the emissions are captured in the wake vortices behind the aircraft due to a circulation within the wake vortices. That's why, the dimension of the wake vortices defines the initial dimension of the contrail. Not until the circulation is decayed, the emissions are released to the atmosphere and start to mix with the ambient atmosphere. Hence, to estimate the initial dimensions of the contrail, a wake vortex calculation, e.g. according to Holzäpfel et al. [53] have to be performed.

Wake vortex generation and decay are divided into four regimes [96]:

1. The jet regime.  
In the first seconds after emission, the development of two counter rotating vortices (the primary wake) takes place.
2. The vortex regime.  
During the next few minutes the vortices fall down due to the strong circulation within the vortices, which induces a strong downward velocity. The gradient of ambient density generates a secondary wake at flight level, which remains at flight level.
3. The dissipation regime.  
After about 100 s (in the following specified with the time  $t$  [s], estimated according to Holzäpfel et al. [53]) turbulence and exhaust gases leave the primary wake in the dissipation regime and both the primary and the secondary wake begin to decay. Only in an ice-supersaturated atmosphere the ice particles are big enough to survive the dissipation regime.
4. The diffusion regime.  
In the last hours to days, the diffusion of the exhaust takes place in the diffusion regime. The mixing of the emissions with the ambient atmosphere starts.

The time data depend on turbulence and on the circulation within the vortices, i.e. the aircraft mass  $m$ , true air speed  $v_{TAS}$ , and aircraft wing span  $l_s$ . Hence, precise



declarations of the duration of each regime can not be generated. For example, as calculated in this thesis, behind an aircraft Airbus A320 the time  $t$  while the wake vortices are falling down is only 40 to 58 s, depending on turbulence.

### 3.4.1 Dissipation regime

Following the above description of wake vortex generation and decay, the emissions are released to the ambient atmosphere at the end of the dissipation regime. Hence, this state is taken for the calculation of the initial dimensions of the contrail. The dimensions at the end of the dissipation regime are calculated with the help of wake vortex calculations according to Holzäpfel et al. [53]. At the beginning of the dissipation regime the vortices begin to descent with a descent speed  $v_s$  [ $\text{m s}^{-1}$ ] (Equation 3.6) for a time  $t$  once fully established [53]. The descent speed  $v_s$  is normalized to the initial tangential velocity  $v_{t,0}$  and can be calculated according to Holzäpfel et al. [53]

$$v_s = v_{t,0} \left( 1 - \exp \left[ \frac{-1.257 b^2}{r_c^2} \right] \right), \quad (3.6)$$

where  $b = 0.4 b_0$  [m] denotes the effective horizontal vortex spacing.  $b_0$  [m] describes the initial horizontal vortex spacing  $b_0 = \frac{\pi}{4} l_s$  with the aircraft wing span  $l_s$  [m], between left and right vortex assuming an elliptical wing loading [97]. The elliptical wing loading leads to the smallest induced drag and is a rather good assumption for modern aircraft design [98]. The radius of the vortex core  $r_c = 0.09 l_s$  is estimated iteratively aiming an equally calculated initial contrail height compared to measurements by Sussmann and Gierens [20]. Hence, the value of  $r_c$  is not derived following any physical law, but experimentally shown. The initial tangential velocity  $v_{t,0}$  [ $\text{m s}^{-1}$ ] within the vortices follows

$$v_{t,0} = \frac{\Gamma_0}{2\pi b_0}. \quad (3.7)$$

$\Gamma_0$  [ $\text{m}^2 \text{s}^{-1}$ ] denotes the initial circulation of the wake vortex as integral of the velocity along the circular path around the wing:

$$\Gamma_0 = \oint v \, ds. \quad (3.8)$$

Equation 3.8 shows, that circulation occurs for a divergence of the velocity around the wing greater than zero. In this case, a lifting force  $F_A$  [N] develops within the



flow. According to the Kutta-Joukowski theorem [99] this lift can be described by the circulation  $\Gamma_0$

$$F_A = \rho v_{\text{TAS}} b_0 \Gamma_0, \quad (3.9)$$

where  $v_{\text{TAS}}$  [ $\text{m s}^{-1}$ ] is the true air speed of the aircraft and  $b_0$  [m] denotes the initial horizontal vortex spacing. Assuming the aircraft in a vertical equilibrium where lift compensates weight ( $F_A = F_G$ ) with  $F_G = mg$  [N] with mass  $m$  [kg] and gravity  $g = 9.81 \text{ m s}^{-2}$ , the initial circulation can be understood as

$$\Gamma_0 = \frac{mg}{\rho b_0 v_{\text{TAS}}}. \quad (3.10)$$

The time  $t$  while the wake vortices descent during the dissipation regime depends on stratification ( $N$ ) and turbulence ( $\epsilon$ ). The impact of stratification is considered by

$$t = \frac{t_n(N_n = 0) \exp[-0.185 t_n(N_n = 0) N_n]}{t_n}, \quad (3.11)$$

where  $N_n$  [a.u.] denotes the normalized Brunt-Väisälä frequency  $N_n = N t_n$  and  $t_n$  [s]

$$t_n = \frac{b_0}{v_{t,0}} \quad (3.12)$$

describes the normalized time scale. Every normalized time can be calculated back to aircraft specific times by multiplication with  $t_n^1$ . The time  $t_n(N_n = 0)$  represents the time of descent in a neutrally stratified atmosphere.  $t_n(N_n = 0)$  depends on a normalized eddy dissipation rate  $\epsilon_n$

$$\epsilon_n = \frac{(\epsilon b_0)^{1/3}}{v_{t,0}} \quad (3.13)$$

with  $\epsilon$  [ $\text{m}^2 \text{s}^{-3}$ ] as eddy dissipation rate,  $b_0$  [m] as initial vortex spacing, and  $v_{t,0}$  [ $\text{m s}^{-1}$ ] the initial tangential velocity.

$t_n(N_n = 0)$  can be derived considering another normalized time  $t_{n,2}$  [53]

---

<sup>1</sup>the index n refers to normalized parameters

$$t_n(N_n = 0) = t_{n,2} - 1, \quad (3.14)$$

for  $\varepsilon_n > 0.2535$ ,  $t_{n,2}$  can be calculated by a model of Sarpkaya [100], modified by Holzäpfel et al. [53]

$$t_{n,2} = 0.804 \varepsilon_n^{-3/4}. \quad (3.15)$$

For  $0.02535 < \varepsilon_n < 0.2535$ , the original formula of Sarpkaya [100] can be used:

$$\varepsilon_n = t_{n,2}^{-1/4} \exp[-0.70 t_{n,2}]. \quad (3.16)$$

For  $\varepsilon_n \leq 0.0235$ , Holzäpfel et al. [53] defined:

$$t_n(N_n = 0) = 5. \quad (3.17)$$

With this explanations the initial vertical dimension of the contrail  $c_v$  can be estimated (Equation 3.18). Initially, the contrail reaches from emission altitude plus vortex radius  $r$  [m] down to the altitude the vortex fall during the time  $t$  with descent speed  $v_s$  again plus the vortex radius  $r$ . Figure 3.5 and Equation 3.18 demonstrate the initial vertical contrail height.

$$c_v(t) = v_s t + 2r. \quad (3.18)$$

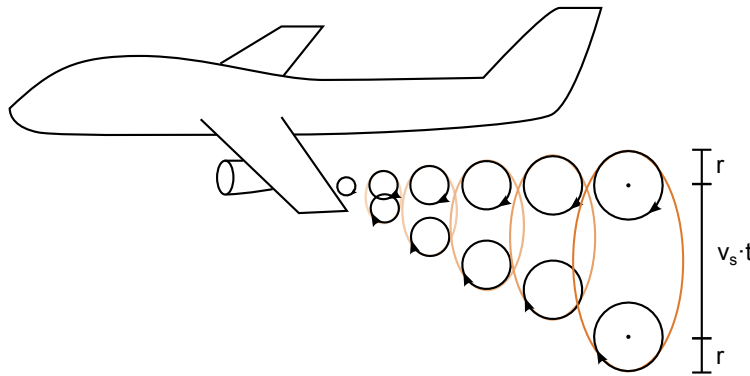


**Figure 3.5:** Initial vertical contrail extension estimated with the help of wake vortex characteristics [53] at the end of the dissipation regime for one wake vortex behind a single jet engine.

However, the wake vortex  $r$  has not been quantified, yet. The vortex radius  $r$  is determined considering the correlation between tangential velocity  $v_t(r')$  [ $\text{m s}^{-1}$ ], as a measure of the ability of ice particles to follow the circular path within the wake vortices. The circular path is defined by the circulation. The tangential velocity is defined as the cross product of the angular velocity  $\vec{\omega}$  and the radius  $\vec{r}'$ . Figure 3.6 demonstrates the geometry.

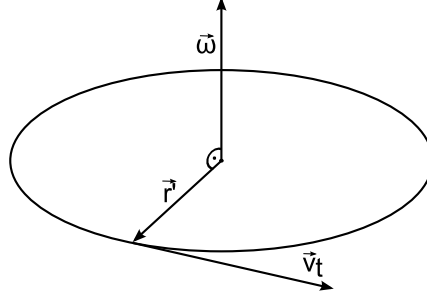


**Figure 3.6:** Geometry of circular velocities. The tangential velocity  $\vec{v}_t$  is the cross product of angular velocity  $\vec{\omega}$  and radius  $\vec{r}'$ .

The tangential velocity  $v_t(r')$  can be calculated using a vortex model. According to Burnham et al. [101]

$$v_t(r') = \frac{\Gamma}{2\pi} \left( \frac{r'}{r'^2 + r_c^2} \right) \quad (3.19)$$

is maximal in the vortex core  $r_c$  and decelerates with increasing radius  $r'$ . For the estimation of the contrail mixing with the ambient atmosphere, a Gaussian plume model is used, assuming that during the diffusion regime the change of the contrail cross section can be described by a growing ellipse. By treating the contrail as a Gaussian plume, an exact definition of the contrail boundaries is impossible, because the number of ice particles within the ellipse is only described by a Gaussian probability density function. However, the standard deviation  $\sigma$  describes the considered fraction. Furthermore, at one standard deviation  $1\sigma$  the distribution function reaches a value  $(\sqrt{e})^{-1}$  of the maximum value of the function. The vortex radius  $r$  is defined, where tangential velocity  $v_t(r')$  reaches that value  $(\sqrt{e})^{-1}$ . Consequently, tangential velocity  $v_t$  is maximum at location  $r_c$

$$v_t(r_c) = \frac{\Gamma}{4\pi r_c}. \quad (3.20)$$

Hence,  $(\sqrt{e})^{-1}$  of  $v_t(r_c)$  is

$$v_t(r) = \frac{1}{\sqrt{e}} \frac{\Gamma}{4\pi r_c} = \frac{\Gamma}{2\pi} \left( \frac{r}{r^2 + r_c^2} \right). \quad (3.21)$$

The radius  $r$  is the larger value of the quadratic equation

$$r^2 - \sqrt{e} 2 r_c r + r_c^2 = 0, \quad (3.22)$$

which is

$$r = (\sqrt{e} + \sqrt{e-1}) r_c. \quad (3.23)$$

The estimation of  $r$  is demonstrated in Figure 3.7.

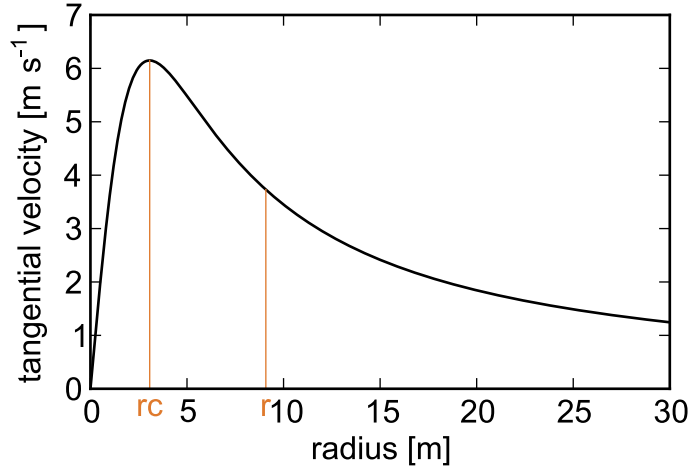


**Figure 3.7:** Dispersion model of the tangential velocity  $v_t(r')$  as function of radius  $r'$  within a vortex according to Burnham et al. [101] and estimation of the vortex radius  $r$  as radius of the vortex for further calculations. The vortex radius  $r$  is defined, where  $v_t(r')$  is  $(\sqrt{e})^{-1}$  times the maximum value  $v_t(r_c)$ .

Now, the horizontal dimension, the contrail width will be estimated. In the horizontal plane, the contrail begins within the initial horizontal vortex spacing  $b_0$  plus two times the vortex radius  $r$  (Figure 3.8).

$$c_h = b_0 + 2r. \quad (3.24)$$

Within the time span  $t$  until the end of the dissipation regime a horizontal spreading of the two vortices can be neglected in a weakly stably stratified environment (with a small Brunt-Väisälä frequency  $N$ ) and weak turbulence [102].



**Figure 3.8:** Contrail horizontal extension estimated with the help of wake vortex characteristics [53] at the end of the dissipation regime.

### 3.4.2 Diffusion regime

#### The Gaussian plume model describing the diffusion

During the diffusion regime, the contrail grows and sediments, until the end of the contrail life time, which is when the air within the contrail is no longer ice-supersaturated or the ice particles are far away from each other, so that radiative extinction due to the ice particles becomes unlikely. The process of diffusion has been introduced in Section 2.3.2 as thermally determined process for the reduction of differences in concentration of particles and turbulent diffusion has been described by turbulent diffusivities. For the turbulent diffusion of the contrail up to complete mixing with the atmosphere, a Gaussian plume model is used. The application of a Gaussian plume model to contrails is demonstrated by Schumann et al. [76]. This model compares the contrail with an arbitrary exhaust plume and describes the contrail as a sheared Gaussian distribution of ice particles. Hence, this model, originally developed for exhaust plumes is applied to the contrail. The Gaussian plume model is often used for calculating the spreading of atmospheric pollution, e.g. exhaust plumes from any industry burning fossil fuels [75]. Hence, the contrail is no longer defined by the wake vortices, because the circulation, which captures the emissions within the wake vortices, is decayed. Now the contrail is treated as an accumulation of ice particles, slowly mixing with the ambient atmosphere and thereby growing with a symmetrically elliptical cross section.

The Gaussian plume model assumes a diffusion of the artificial cloud with a growing elliptical cross section with time and a decreasing concentration of ice mass with distance from the center. This assumption results in vortex centric ellipses of constant ice mass.

The total amount of ice mass per volume contrail is expressed as the ice water content  $IWC$  [ $\text{kg m}^{-3}$ ]. Following the definition of a Gaussian distribution, one standard deviation defines the location along the vertical and horizontal axes, with a concentration of  $(\sqrt{e})^{-1}$  of its maximum value in the middle of the cross section. Figure 3.9 shows the application of a two dimensional Gaussian distribution and defines the axes, used in this thesis.

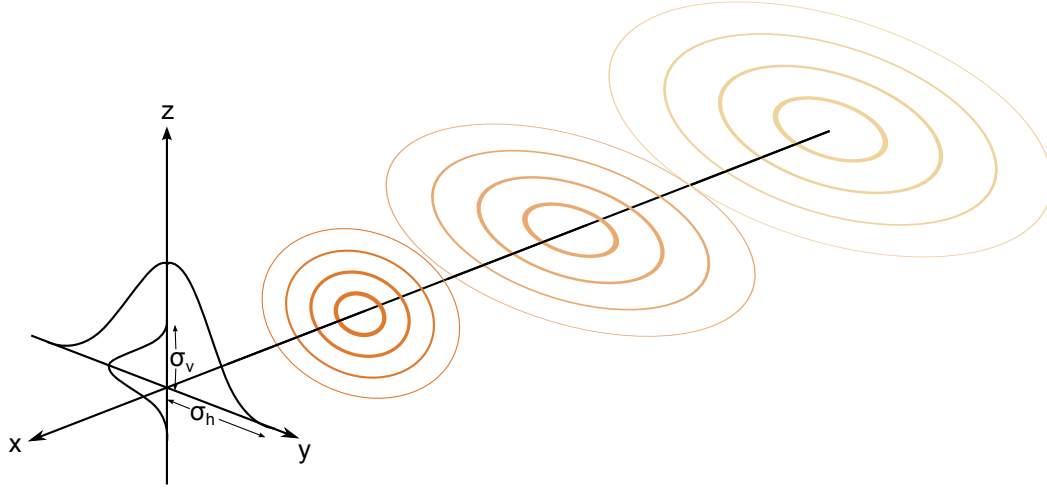


**Figure 3.9:** Two-dimensional Gaussian plume model. The  $x$ -axis follows the flight path and considers the time. Hence, light orange ellipses represent an older state of the contrail.

The two-dimensional probability density function, which estimates the number density of ice particles  $n_p$  at arbitrary time and location within the contrail, is:

$$f(\vec{x}, t) = \frac{1}{2\pi\sqrt{\det \hat{\sigma}(t)}} \exp \left[ -\frac{1}{2} \vec{x}^T \hat{\sigma}(t)^{-1} \vec{x} \right]. \quad (3.25)$$

Where  $\vec{x}$  describes the position vector

$$\vec{x} = \begin{pmatrix} y \\ z \end{pmatrix} \quad (3.26)$$

and  $t$  [s] denotes the time. The contrail life time is defined by two limiting parameters [54]: either  $IWC < 10^{-8} \text{ kg m}^{-3}$  or  $rH_{\text{ice}} < 100\%$ . The first case is an arbitrary limit describing the situation of a contrail becoming optically too thin to be perceived as contrail. In the second case the contrail drifts out of the ice-supersaturated environment and the ice particles sublime.

The variance  $\hat{\sigma}(t)$  is described by a matrix of horizontal  $\hat{\sigma}_h(t)$ , vertical  $\hat{\sigma}_v(t)$  and sheared  $\hat{\sigma}_s(t)$  components of the contrail's diffusion.

$$\hat{\sigma}(t) = \begin{pmatrix} \hat{\sigma}_h(t) & \hat{\sigma}_s(t) \\ \hat{\sigma}_s(t) & \hat{\sigma}_v(t) \end{pmatrix} \quad (3.27)$$

Following the definition of an area of an ellipse [103] and [54], the contrail cross section  $A$  can be calculated to

$$A = 2\pi\sqrt{\det \sigma}. \quad (3.28)$$

As starting values at the beginning of the simulation, the initial standard deviations  $\sigma_{0v}$  and  $\sigma_{0h}$  are defined in the following manner:  $\sigma_{0h} = 2.2$  times contrail width  $c_h$  and  $\sigma_{0v} = 2.2$  times contrail height  $c_v$  [76].

The development of the variances  $\hat{\sigma}_i(t)$  is defined by Schumann et al. [76] as

$$\hat{\sigma}_h(t) = \frac{2}{3}s^2 D_v t^3 + (2D_s + s\sigma_{0v}^2)t^2 + 2D_h t + \sigma_{0h}^2 \quad (3.29)$$

$$\hat{\sigma}_s(t) = sD_v t^2 + (2D_s + s\sigma_{0v}^2)t \quad (3.30)$$

$$\hat{\sigma}_v(t) = sD_v t + \sigma_{0v}^2, \quad (3.31)$$

where  $s$  [ $s^{-1}$ ]

$$s = \frac{\Delta v}{\Delta z} \quad (3.32)$$

denotes the constant wind shear as difference in wind velocity  $\Delta v$  [ $m s^{-1}$ ] between two altitudes  $\Delta z$  [m]. In Equations 3.29 to 3.31,  $D_v$ ,  $D_h$  and  $D_s$  are the components of a asymmetric and anisotropic diffusivity tensor:

$$\hat{D} = \begin{pmatrix} D_h & D_s \\ D_s & D_v \end{pmatrix}. \quad (3.33)$$

For the application of the Gaussian plume model, the diffusivities  $D_v$ ,  $D_h$  and  $D_s$  have to be estimated. However, the determination of these measures of turbulence is nontrivial (compare Section 2.3.2) Schumann et al. [76] estimated typical values of  $D_v$ ,  $D_h$  and  $D_s$  at flight level measuring the diffusion of nitric oxide in a stably stratified atmosphere and assumed a similar diffusion of ice particles, compared to the diffusion of nitric oxides. These values are used in this thesis:

$$0 \leq D_v \leq 0.6 \text{ m}^2\text{s}^{-2} \quad (3.34)$$

$$5 \leq D_h \leq 20 \text{ m}^2\text{s}^{-2} \quad (3.35)$$

$$0 \leq |D_s| \leq 2 \text{ m}^2\text{s}^{-2} \quad (3.36)$$

$$|s| \approx 0.002 \text{ s}^{-1} \quad (3.37)$$

The sheared components of both the variance matrix  $\hat{\sigma}(t)$  and the skewed diffusivity  $D_s$  can be neglected, because Schumann et al. [76] recommended  $D_s = 0$  for stable stratification, which is given by the used model atmosphere (see Section 2.3.1 for the explanation of atmospheric stratification). To verify this assumption, the influence of both wind shear  $s$  and skewed diffusivity  $D_s$  on the contrail life cycle is estimated and shown in Figure 3.10. Here, the contrail life cycle is calculated for  $D_s = 0 \text{ m}^2\text{s}^{-2}$  and  $D_s = 0.3 \text{ m}^2\text{s}^{-2}$ .  $D_s$  influences the horizontal diffusivity  $D_h$  and vertical diffusivity  $D_v$ . According to a two-dimensional Fick's law  $D_s \neq 0$  causes a composition of  $D_h$  and  $D_v$  influencing each other. Differences are small, but for  $D_s = 0.3 \text{ m}^2\text{s}^{-2}$  the contrail lives approximately five hours longer. Differences in wind shear are more significant. For a constant wind shear of  $s = 0.002 \text{ s}^{-1}$  particles grow faster and get larger, than for  $s = 0 \text{ s}^{-1}$ . The same phenomena can be estimated for the contrail cross section, which also grows faster and gets larger in a sheared environment. The wind shear causes a faster dilution of the contrail with the ambient atmosphere. Following Equations 3.29 to 3.31, the wind shear  $s$  constitutes the vertical and horizontal components of the variance matrix  $\hat{\sigma}(t)$  and therefore the diffusivity tensor  $\hat{D}$ . However, the Gaussian plume model is very sensitive to sheared components. For values of  $D_s \approx \sqrt{D_v D_h}$  the two-dimensional Gaussian distribution function results in a contrail cross section converging to zero, until for  $D_s = \sqrt{D_v D_h}$  the Gaussian function describes no longer an ellipse, but a pair of parallel straight lines. In this case the determinant  $\det \hat{\sigma} = 0$  and the area  $A$  is also zero [103]. For  $D_s > \sqrt{D_v D_h}$ , the determinant  $\det \hat{\sigma}$  becomes an imaginary number, the area is not computable, the ice water content is not defined and the simulation of the life cycle aborts.

Following the achievements of Section 2.3.2 a linear correlation between  $\varepsilon$  and  $D_v$ ,  $D_h$  is assumed and summarized in Table 3.2. Therefore, the eddy dissipation rate is categorized into five turbulence classes covering the total range of eddy dissipation rate  $\varepsilon$ , measured by Schumann et al. [76] in a stably stratified atmosphere at cruising



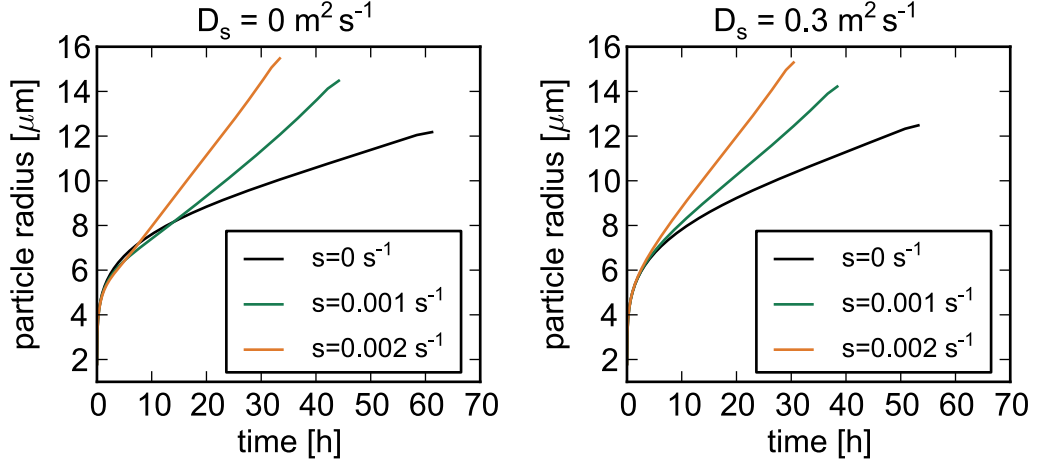


**Figure 3.10:** Evolution of particle radius for  $D_s = 0$  (left) and  $D_s = 0.3 \text{ m}^2 \text{ s}^{-2}$  (right). A mean turbulence indicating  $\varepsilon = 5 \cdot 10^{-5} \text{ m}^2 \text{ s}^{-1}$  and a horizontal diffusivity  $D_h = 16.25 \text{ m}^2 \text{ s}^{-2}$  and a vertical wind drift of  $v_z = 0.01 \text{ m s}^{-1}$  are assumed. Each plot further contains a variation of constant wind shear  $s$  (compare Equation 3.32).

altitudes.

Furthermore, Schumann et al. [76] used the following correlation between  $\varepsilon$  and the vertical diffusion coefficient  $D_v$ , which is taken over this thesis:

$$D_v = c \frac{\varepsilon}{N^2}, \quad (3.38)$$

where  $N$  denotes the Brunt-Väisälä frequency (compare Section 2.3.1) and the constant factor  $c = 0.1$  holds for good results for strongly stratified situations [76].

With these last explanations, Equation 3.25 can finally be applied:

$$f(y, z, t, D_v, D_h, D_s) = \frac{1}{2\pi\sqrt{\det\hat{\sigma}(t)}} \exp \left[ -\frac{1}{2\det\hat{\sigma}(t)} (\hat{\sigma}_v(t)y^2 + \hat{\sigma}_h(t)z^2) \right]. \quad (3.39)$$

Both assumptions, the elliptical cross section and the monotonically decreasing concentration of ice mass with distance from the center are rather rough. In reality, large and heavy ice particles are depositing faster than small and light ones, causing an enhanced concentration of ice mass at the bottom of the contrail. Some ice particle habits,

**Table 3.2:** Used measures of turbulence and assumed correlation between Eddy dissipation rate  $\varepsilon$  and horizontal diffusivity  $D_h$  indicating the diffusion of the contrail in horizontal direction. Values are taken from measurements by Schumann et al. [76].

Eddy dissipation rate $\varepsilon$ [ $\text{m}^2\text{s}^{-3}$ ]	Horizontal diffusivity $D_h$ [ $\text{m}^2\text{s}^{-2}$ ]
$1 \cdot 10^{-6}$	5.00
$5 \cdot 10^{-6}$	8.75
$1 \cdot 10^{-5}$	12.50
$5 \cdot 10^{-5}$	16.254
$1 \cdot 10^{-4}$	20.00

like long columns are vertically orientated and lifted up causing an enhanced concentration at the top of the contrail. This inhomogenous distribution of ice particles within a contrail cross section causes a different optical path and therefore a different change of the extinction coefficient along the optical path than assumed in this thesis. Especially at the beginning of the simulation (the end of the dissipation regime), the elliptical cross section is a weak assumption and does not agree with realistic cross sections of young contrails as simulated by Sussmann et al. [104], [20], Naimann et al. [105] and Paugam et al. [96]. Furthermore, the maximum values of  $IWC$  will be in the cores of the vortices and therefore not exactly in the center of the contrail. However, exact estimations of the early contrail require extensive simulations of the turbulence pattern within the wake vortex, such as been done by Sussmann et al. [104], [20], Paugam et al. [96] or Chlond [106] and would exceed the possibilities of this thesis by far. For more precise estimations of an atmospheric diffusion, detailed turbulence information, including highly spatial resolved values of the Brunt-Väisälä frequency and diffusivity coefficients, are necessary.

### Vertical displacement of the contrail during the diffusion regime

Mainly due to the weight of the ice particles within the contrail, the ice particles are accelerated vertically in the downward direction, i.e. they sediment. Because the contrail is defined as ice particles developed from condensed water vapor, emitted by aircrafts, the initial position of the contrail is defined by the position of the ice particles. Hence, the entire contrail moves vertically. The sedimentation of the contrail is counteracted by the vertical wind velocity  $v_z$ , which causes an upward movement of small ice particles. Now, the balance between both directions of vertical movement will be calculated.

According to Stokes, a drag force  $F_{W,p}$ , which acts on every particle within the contrail due to viscous friction

$$F_{W,p} = 6\pi\eta_{\text{dyn}}v_{s,p}r_p \quad (3.40)$$

is equal to the weight  $F_{G,p}$  of the particle

$$F_{G,p} = \frac{4}{3}\pi r_p^3 \rho_p g. \quad (3.41)$$

In Equations 3.40 and 3.41,  $v_{s,p}$  [ $\text{ms}^{-1}$ ] denotes the ice particle sedimentation speed,  $r_p$  [m] the ice particle radius,  $\rho_p$  [ $\text{kg m}^{-3}$ ] the ice particle density, and  $\eta$  [ $\text{kg m}^{-1}\text{s}^{-1}$ ] the dynamical viscosity. Equating Equations 3.40 and 3.41, the ice particles sediment according to Stokes law [61] with the sedimentation speed  $v_{s,p}$

$$v_{s,p} = \frac{2r_p^2\rho_p g}{9\eta_{\text{dyn}}}. \quad (3.42)$$

The dynamical viscosity  $\eta_{\text{dyn}}$  is the product of density of the atmosphere  $\rho$  [ $\text{kg m}^{-3}$ ] and the kinematical viscosity  $\nu_{\text{kin}}$  [ $\text{m}^2\text{s}^{-1}$ ], which was already introduced in Section 2.3.2

$$\nu_{\text{kin}} = \rho \eta_{\text{dyn}}. \quad (3.43)$$

The kinematical viscosity  $\nu_{\text{kin}}$  can be calculated according to Sutherland [107].

This sedimentation speed  $v_{s,p}$  would cause a sedimentation of the entire contrail. Anyhow, this sedimentation is counteracted by an upward motion due to wind drift. Because the vertical wind velocity is two orders of magnitudes smaller than the horizontal wind velocity [61], a vertical upwind velocity of  $v_z = 0.005 \text{ ms}^{-1}$  is realistic in stable stratification [61] and assumed in this thesis. Assuming this vertical upward speed, Equation 3.42 shows, that by exceeding values of the ice particle radius  $r_p \approx 6 \mu\text{m}$ , the contrail sediments and reaches warmer and dryer altitudes in the atmosphere (compare Section 4.1.3, Figure 4.2). During this sedimentation the contrail heats adiabatically according to Equation 2.48, resulting in subliming ice particles and in decreasing relative humidity within the contrail and in total in a shorter contrail life time. As mentioned in Section 3.4.2, the contrail life time is defined by either  $IWC < 10^{-8} \text{ kg m}^{-3}$  or  $rH_{\text{ice}} < 100\%$ .

Figure 3.11 shows the influence of the vertical wind velocity  $v_z$  on the development of the particle radius  $r_p$  and on the contrail life time (x-axis). For  $v_z > 0.01 \text{ ms}^{-1}$ , the contrail lives unrealistically long. The lifetime and the development of the particle radius saturate at the level of  $v_z = 0.001 \text{ ms}$ .

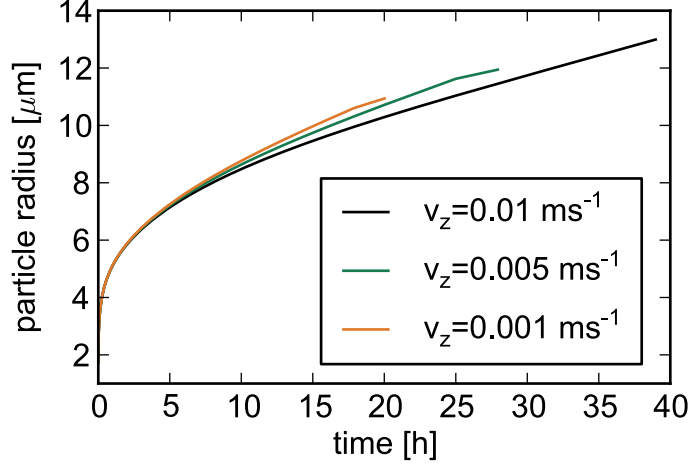


**Figure 3.11:** Influence of the vertical wind drift  $v_z$  on particle radius  $r_p$  and contrail life time (x-axis). The stronger the vertical upward wind, the longer the contrail stays in the ice saturated region and the longer the contrail lives. The calculations are done for a mean turbulent environment with  $\varepsilon = 5 \cdot 10^{-5} \text{ m}^2 \text{ s}^{-3}$ .

Stokes law is valid for large particles or for small sedimentation speeds [61]. It is valid up to

$$Re = \frac{2 r_p v_{s,p}}{v_{\text{kin}}} = 0.1 \quad (3.44)$$

which is satisfied for all calculations presented within this thesis (compare Figure 3.12).

The growth of the cross section due to diffusion causes a reduction of its ice water content  $IWC [\text{kg m}^{-3}]$ , as soon as the contrail leaves the ice-supersaturated altitude.

### Contrail microphysics in the diffusion regime

The decisive characteristics of the contrail for radiative extinction are the microphysical properties like ice particle number density and ice particle size, because these two

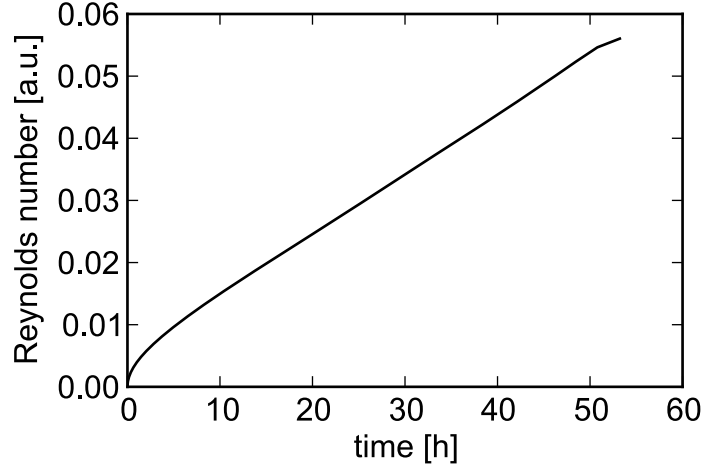
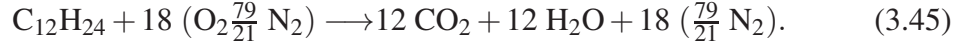


**Figure 3.12:** Reynolds number  $Re = 2r_p v_{s,p} v_{\text{kin}}^{-1}$  over a contrail's lifecycle with no wind shear  $s = 0 \text{ s}^{-1}$ , no sheared diffusivities  $D_s = 0 \text{ m}^2 \text{ s}^{-2}$  and a vertical upward wind component of  $v_z = 0.005 \text{ m s}^{-1}$ . A mean turbulence indicating  $\varepsilon = 5 \cdot 10^{-5} \text{ m}^2 \text{ s}^{-1}$  and a horizontal diffusivity  $D_h = 16.25 \text{ m}^2 \text{ s}^{-2}$  is assumed. Values of  $Re$  do not exceed  $Re = 0.1$ , which allows using Stokes law for contrail sedimentation.

measures are determining the probability of an interaction between radiation and ice particle, which is formulated in the extinction efficiency  $\beta_e$ . That's why, a closer look on the change of the available ice water content and the number of ice particles during the contrail life cycle is given in the following. The initial composition of the contrail is determined by the amount of emitted water and soot, captured in the wake vortices. The number of ice particles corresponds to the number of emitted (hydrophilic) soot particles. Assuming an emission index of soot  $EI_{\text{soot}} = 0.04 \text{ g kg}^{-1}$  kerosene [108], a density of soot  $\rho_{\text{soot}} = 2 \text{ g cm}^{-3}$  and a mean soot particle diameter  $d_{\text{soot}} = 60 \text{ nm}$  [109], the specific number of emitted soot particles is  $N_{\text{ice}} = 10^{15}$  per kg of combusted kerosene [104]. For the whole contrail life cycle, a constant number of ice particles is assumed. The process of the breakup of ice particles and providing several ideal ice nuclei (called secondary nucleation) is possible, but not easily to quantify. Furthermore, the process of large ice particles capturing smaller ones by falling faster (agglomeration [110]) is also possible but its estimation highly complex. Hence, it is impossible to quantify the error made by an assumption of a constant number of ice particles.

Assuming complete combustion conditions, the emission index of water vapor  $EI_{\text{water}}$  is the result of Equation 3.45 using molar masses of carbon  $M_C: 12.0110 \text{ g mol}^{-1}$ , hydrogen  $M_H: 1.0079 \text{ g mol}^{-1}$ , oxygen  $M_O: 15.9994 \text{ g mol}^{-1}$  and nitrogen  $M_N: 14.0067 \text{ g mol}^{-1}$



Following Equation 3.45, the ratio between the molar masses of 12 molecules  $\text{H}_2\text{O}$  and one molecule  $\text{C}_{12}\text{H}_{24}$  is

$$\frac{12 M_{\text{H}_2\text{O}}}{C_{12}\text{H}_{24}} = \frac{216.18 \text{ g mol}^{-1}}{169.46 \text{ g mol}^{-1}} = 1.29. \quad (3.46)$$

Equation 3.46 implies an emission index of water of yields  $EI_{\text{water, compl.}} = 1.29 \text{ kg kg}^{-1}$ . Anyhow, complete combustion does not typically occur during cruise in a jet engine. Here, a lean combustion with more oxygen than necessary is more realistic. That's why, an emission index of  $EI_{\text{water}} = 1.24 \text{ kg kg}^{-1}$  is assumed [3].

Assuming a constant vapor pressure above ice and water, the relative humidity above ice is (following Equation 2.7)

$$rH_{\text{ice}} = rH_{\text{water}} \frac{e_{\text{water}}^*}{e_{\text{ice}}^*}, \quad (3.47)$$

while  $rH_{\text{water}}$  is given by the model atmosphere Midlat Winter. The ratio  $\Delta e$  above saturation is assumed to be captured by the ice particles

$$\Delta e = e_{\text{ice}}^* \left( \frac{rH_{\text{ice}}}{100} - 1 \right). \quad (3.48)$$

Hence, the amount of water vapor  $IWC_s$  contributing to the ice particle size is

$$IWC_s = \frac{\Delta e}{R_v T}, \quad (3.49)$$

where  $R_v = 461.5 \text{ J}(\text{kg K})^{-1}$  denotes the specific gas constant of water vapor.  $IWC_s$  distinguishes from the total ice water content  $IWC$ , because  $IWC_s$  is the humidity, which is not necessary for saturation of the air within contrail and therefore can be used for ice particle growth. The total ice water content  $IWC$  of the ice particles for a section of the contrail is defined by the distance  $s$  flown by the aircraft in one second, estimated with the help of true air speed  $v_{\text{TAS}} [\text{m s}^{-1}]$  and the amount of combusted kerosine (the fuel flow  $\dot{m}_f [\text{kg s}^{-1}]$ )

$$IWC = IWC_s + EI_{\text{water}} \frac{m_f}{v_{\text{TAS}} A}. \quad (3.50)$$

The amount of available ice mass  $m_{\text{ice}}$  [kg] within the volume defined by the contrail cross section  $A$  and a contrail length  $s = 1$  m

$$m_{\text{ice}} = IWC \cdot A \cdot s \quad (3.51)$$

allows the calculation of the volume  $V_p$  [m<sup>3</sup>] of a spherical ice particle

$$V_p = \frac{IWC}{N_{\text{ice}} \rho_{\text{ice}}}, \quad (3.52)$$

where  $\rho_{\text{ice}} = 917 \text{ kg m}^{-3}$  denotes the density of ice [58] and the volume of a sphere is

$$V_p = \frac{\pi}{6} d_{\text{ice}}^3. \quad (3.53)$$

Consequently, the initial mean crystal diameter equals

$$d_{\text{ice}} = \sqrt[3]{\frac{6 m_{\text{ice}}}{\pi N_{\text{ice}}}}. \quad (3.54)$$

Now, the microphysical properties of the contrail can be calculated for its whole life cycle from the initial state right after contrail formation until the end of the contrail life cycle, when either the relative humidity within the contrail is undersaturated and no humidity for ice particles is available or when the ice water content is too small, i.e. the ice particles are a long way away from each other. The initial dimensions of the contrail are determined using the wake vortex calculations by [102]. With the help of the Gaussian plume model, the ice water content can be calculated at every location within the contrail at any time. The ice particle number is estimated according to the expected number of soot particles per unit mass of fuel burn [20]. From this follows, that the aircraft performance influences the contrail microphysical properties. The initial dimensions are a function of aircraft mass  $m$  and true air speed  $v_{\text{TAS}}$  (compare Equation 3.10 for the calculation of the initial circulation influencing the descent speed  $v_s$  during the vortex regime) and the radius  $r$  of the wake vortices during the dissipation regime. Furthermore, the fuel flow  $\dot{m}_f$  influences the number of ice particles. The consequences of this parameters for trajectory optimization on the radiative extinction will be discussed by analyzing the results of this thesis and conclusions will be drawn.

With this last section, the basic requirements for radiative extinction are developed. The new focus will be the development of the contrail radiative forcing model, which will calculate the radiative extinction due to the contrail. The solar radiances and terrestrial irradiances at contrail altitude (calculated with the radiative transfer model libRadtran, assuming a cloud free atmosphere) will now travel through the contrail and will change due to interactions with the ice particles within the contrail. This change defines the radiative forcing of the contrail, because without the contrail, this change would not have happened.

### 3.5 Contrail radiative forcing model

As pointed out in Section 2.2.8, radiative forcing is the imbalance of the energy budget of the Earth-atmosphere system. In other words, radiative forcing considers the amount of energy the contrail prevents from leaving the atmosphere (positive  $RF$ ) and prevents from entering the atmosphere (negative  $RF$ ). As such, both spectra, solar and terrestrial have to be considered. For the calculation of the imbalance, Beer's law (Equation 2.23) is used for a large amount of different directions of incoming photons. Finally, the direction of photons leaving the contrail is evaluated. The extinction coefficient  $\beta_e$  along the way of the photon through the contrail is estimated using the particle number density and particle size from the Gaussian plume model. To consider multiple scattering at various ice particles inside the contrail, a Monte Carlo simulation is used, following a large number of photons through the contrail and saving their original direction  $\Omega$  and their leaving direction  $\Omega'$  one by one. Finally, an integration over all events results in the radiative forcing. The results are combined with the angular dependence of solar radiation provided by libRadtran. Hereby, one is able to treat the contrail as a continuous three-dimensional object and to investigate the influence of both daytime and flight path.

#### 3.5.1 Consideration of multiple scattering using a Monte Carlo simulation

A Monte Carlo simulation tries to constitute a sequence of changes in a model [111]. These degrees of freedom are not strongly predefined [111]. The attempt takes place on a statistical level. Because an integration over all degrees of freedom is too complex, a set of samples is used for integration. The degrees of freedom are described by a large quantity of random numbers, reflecting the specific events. Thereby the order of the events get lost, but an integration over all simulated events often results in a good exposure of the model. A second sequence of random numbers, not equal to the first



one, will result in different findings. The deviation is called statistical error [111]. Its amount depends on the quantity of random numbers and therefore on the amount of considered events. The higher the amount of events, respected for the integration, the smaller the statistical error. This feature causes a large computational effort for such a simulation and the possibilities within the model have to be chosen wisely. Here, the Monte Carlo simulation is used to get an estimation of the multiple scattering process in a contrail. The approach has been published by Rosenow et al. [112] [113].

### 3.5.2 Geometry of the Monte Carlo simulation

To reduce computational effort, a symmetric contrail cross section is assumed, i.e. no wind shear  $s = 0 \text{ s}^{-1}$  and no sheared diffusivities  $D_s = 0 \text{ m}^2\text{s}^{-1}$  are hypothesized. The calculations are done for photons coming from one octant. Because of the mirror symmetry of the contrail, all octants have identical optical properties. Although the photons are entering the contrail from one octant, the whole contrail is included in the simulation and photons are leaving the contrail in all octants. Other directions of incoming photons are considered by reflecting the results of the Monte Carlo simulation in the slice planes to the other octants. In Figure 3.13, one octant is colored, showing the mirror symmetry of the contrail with the symmetric cross section.

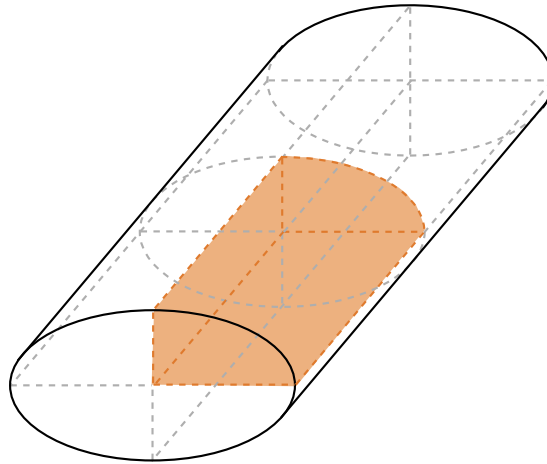


**Figure 3.13:** A contrail section with symmetric cross section. Calculation of angular depending radiative extinction is sufficient for the directions of photons coming from one octant (such as emphasized). The other directions will be considered by reflecting the results of the Monte Carlo simulation in the slice planes to the other octants.

Photons of one direction arrive uniformly distributed along a line with a width  $2w_{\text{in}}$ , which is six times longer, than the width of the contrail cross section. The simulation

starts with the photons distributed along the circular line around the contrail. The simulation of each photon ends either after exiting the circle or being absorbed. Along the x-axis periodic boundary conditions are assumed. Under this condition, photons cannot leave or enter the contrail on its cross section, which is reasonable for infinitely extended contrails, but disruptions due to wind shear or strong local vertical winds can not be considered.

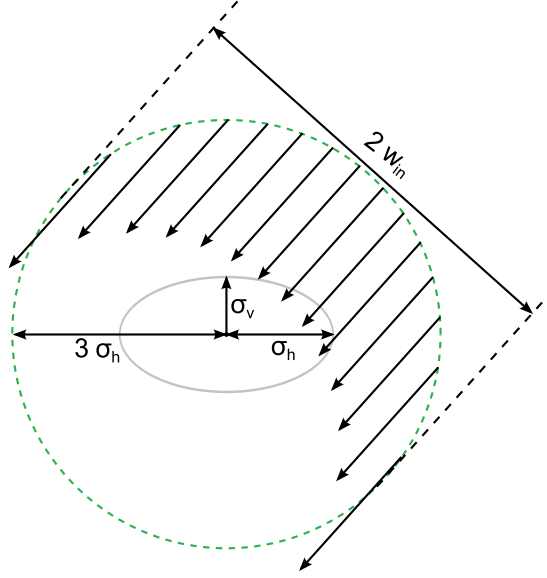


**Figure 3.14:** Geometry of the Monte Carlo simulation. The position of the photons is uniformly distributed along a  $2w_{in} = 6\sigma_h$  long line perpendicular to the direction of arrival. To save computational effort, the simulation of the photons starts along the circular curve with a diameter of  $2w_{in} = 6\sigma_h$  irradiated by photons of the particular direction. The center of the circle (green dotted) is identical with the center of the contrail. Photons leaving the circle are considered as transmitted or scattered depending on the outgoing direction.

### 3.5.3 Interpretation of Beer's law

The fundamental equation describing extinction of radiation, Beers law

$$I_{\lambda}(s_2) = I_{\lambda}(s_1) \exp \left[ - \int_{s_1}^{s_2} \beta_e(s) ds \right]$$

(Equation 2.23) will be applied to calculate radiative extinction due to the existence of the contrail in the atmosphere. For the consideration of multiple scattering, a Monte

Carlo simulation will be used. In the following, the terms of Equation 2.23 will be interpreted for the use within the Monte Carlo simulation. For convenience,  $I_\lambda(s_2)$  will be  $I$  and  $I_\lambda(s_1)$  will be understood as  $I_0$ .

The distance through the contrail is defined by  $ds$ .

The extinction coefficients  $\beta_e(s)$  were derived in Section 2.2.6.

The expression

$$\frac{I}{I_0} = \exp[-\beta_e s] \quad (3.55)$$

is understood as the probability of a photon transmitting through the contrail along the distance  $s$  without being scattered or absorbed. Averaging over a large number of photons, the expression

$$Ext = 1 - \frac{I}{I_0} = 1 - \exp[-\beta_e s] \quad (3.56)$$

denotes the sum of all absorbed and single scattered photons. Remembering the definition of the optical thickness  $\tau$  (Equation 2.24),  $\tau$  is also

$$\tau = -\ln\left(\frac{I}{I_0}\right). \quad (3.57)$$

The optical thickness is a widely used quantity to characterize radiative extinction and will be used for a verification of the model. For a consideration of multiple scattering events, a Monte Carlo simulation over a large number of photons traveling through the contrail is necessary. According to Equation 2.17, the expression 3.55 can be written as

$$\frac{I}{I_0} = \exp[-\beta_s s - \beta_a s]. \quad (3.58)$$

Following Equation 3.58 the averaged sum of all absorbed photons is

$$Abs = 1 - \exp[-\beta_a s] \quad (3.59)$$

and the averaged sum of all scattered photons is

$$Sca = 1 - \exp[-\beta_s s]. \quad (3.60)$$

Furthermore, Equation 3.55 demonstrates the number ratio of photons incident on the contrail and of photons emerging from the contrail in exactly the same direction  $\Omega$  from which they were coming from. For a homogeneous medium with  $\beta_e = \text{const.}$ , Equation 3.55 can be transposed to solve for the required distance  $s$  for an attenuation of radiation from  $I$  to  $I_0$ . Considering a single photon the ratio of  $I$  and  $I_0$  can be understood as the photon's power of endurance until an extinguishing event takes place. In this case, the distance  $s$  is the location of the extinction along a linear path through the contrail. If the location is outside the contrail (the green dotted circle in Figures 3.14 and 3.15), the photon will be transmitted. In the case of inhomogeneous extinction coefficients the inverse of Equation 3.55 is not analytically possible and  $s$  has to be calculated numerically using a Newton iteration. A few examples of extinguishing events and their treatment within the Monte Carlo simulation are shown in Figure 3.15.

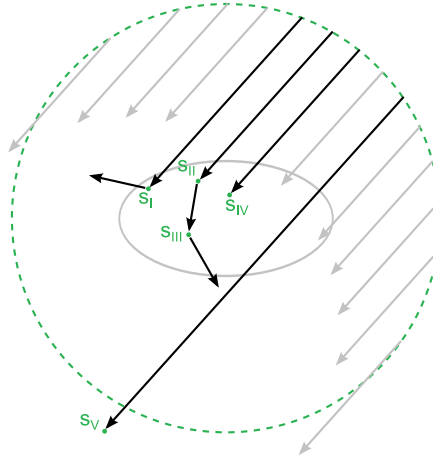


**Figure 3.15:** Some possible extinction events in the contrail. At location  $s_I$  a single scattering event takes place, which redirects the photon's direction, so that it leaves the contrail in the same hemisphere, where it was coming from. At location  $s_{II}$  and  $s_{III}$  a multiple scattering event is shown, the photon is first scattered at  $s_{II}$  and second at location  $s_{III}$ . At location  $s_{IV}$  an absorbing event takes place and the photon disappears from the Monte Carlo simulation. Location  $s_V$  is outside the contrail, the photon has transmitted through the contrail without any extinction. Considering multiple scattering, all combinations of extinguishing events within the contrail are possible.

### 3.5.4 Procedure of the Monte Carlo simulation

For the calculation of the radiative forcing the way of many photons through the contrail needs to be considered. The solution space is divided into above and below the contrail. Hence, the leaving directions of the special events of the Monte Carlo simulation are saved in three counters (one for forward scattered, one for backward scattered and one for absorbed photons). Furthermore, the hemisphere where photons are coming from is important. Photons coming from above the contrail and emerging the contrail into the upper hemisphere (due to scattering events) cool the atmosphere and reduce the radiative forcing, while photons incident from below the contrail and emerging into the lower hemisphere will stay in the Earth-atmosphere system and enhance the radiative forcing. Equally, photons getting absorbed enhance the amount of energy within Earth-atmosphere system, too.

The idea of the Monte Carlo simulation for the estimation of radiative extinction processes through a homogeneous infinitely expanded cloud layer is described by Petty [66]. The application of this idea to an inhomogeneous three-dimensional figure is the core of this thesis and will be described in the following.

An uniformly distributed random number  $Z_s = [0, 1]$  describes the power of endurance (Equation 3.55) and determines the location  $s$  behind the starting point where extinction takes place along a straight path through the contrail. The scattering  $\beta_s$  and absorption coefficient  $\beta_a$  at this place are estimated with the help of the Gaussian plume model. Therefore, the two-dimensional Gaussian distribution function with  $\hat{\sigma}_s(t) = 0 \text{ m}^2 \text{ s}^{-1}$  (for a symmetric cross section)

$$f(x, y, t, D_v, D_h) = \frac{1}{2\pi\sqrt{\det\hat{\sigma}}} \exp \left[ -\frac{1}{2\det\hat{\sigma}} (\hat{\sigma}_v(t)x^2 + \hat{\sigma}_h(t)y^2) \right] \quad (3.61)$$

replaces the number density  $n_p$  in Beer's law (Equation 2.23) considering Equation 2.33

$$I = I_0 \exp \left[ \int_0^{s_e} -Q_e A_p n_p(s) ds \right]$$

the number density  $n_p$  of ice particles at an arbitrary location within the contrail is the total number of ice particles  $N_{ice}$  multiplied with the Gaussian distribution function.

$$I = I_0 \exp \left[ -Q_e \pi r_p^2 \frac{N_{ice}}{2\pi\sqrt{\det\hat{\sigma}}} \int_0^{s_e} \exp \left[ \frac{-1}{2\det\hat{\sigma}} (\hat{\sigma}_v y^2 + \hat{\sigma}_h z^2) \right] ds \right] \quad (3.62)$$

Here,  $y$  and  $z$  are the projections of the photon's straight path on the horizontal ( $y$ -axis) and vertical ( $z$ -axis) plane, respectively:

$$y = y_0 + s \sin \theta \sin \phi \quad (3.63)$$

and

$$z = z_0 + s \cos \theta. \quad (3.64)$$

To interpret Equations 3.63 and 3.64, follow Figures 2.4 and 3.16.

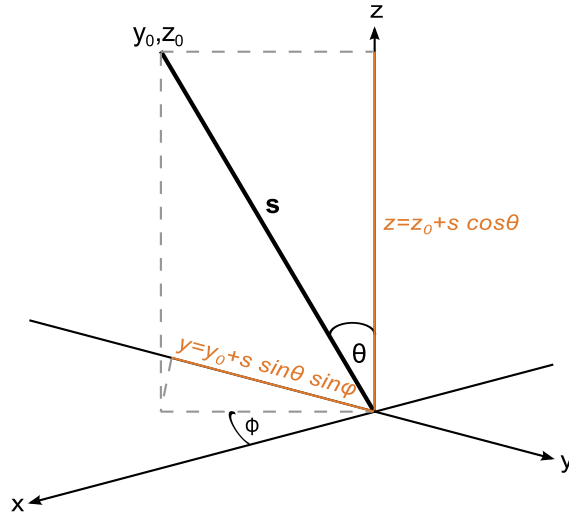


**Figure 3.16:** Transformation of coordinates between polar coordinates described by  $\theta$  and  $\phi$  and Cartesian coordinates  $(x, y, z)$ .

For convenience, the function  $f(s)$  is defined as

$$f(s) = \exp \left[ -\frac{1}{2 \det \hat{\sigma}} (\hat{\sigma}_v y^2 + \hat{\sigma}_h z^2) \right]. \quad (3.65)$$

Furthermore, the function  $g(s)$  is defined as

$$g(s) = \hat{\sigma}_v y^2 + \hat{\sigma}_h z^2 \quad (3.66)$$

and the constant  $C_1$  is defined as

$$C_1 = -Q_e \pi r_p^2 \frac{N_{\text{ice}}}{2\pi \sqrt{\det \hat{\sigma}}}. \quad (3.67)$$

Inserting Equations 3.63 and 3.64 in  $g(s)$  yields

$$\begin{aligned} g(s) = & \hat{\sigma}_v y_0^2 + \hat{\sigma}_v 2s y_0 \sin \theta \sin \phi + \hat{\sigma}_v s^2 \sin^2 \theta \sin^2 \phi \\ & + \hat{\sigma}_h z_0^2 + \hat{\sigma}_h 2s z_0 \cos \theta + \hat{\sigma}_h s^2 \cos^2 \theta \end{aligned} \quad (3.68)$$

or

$$\begin{aligned} g(s) = & s^2 \underbrace{(\hat{\sigma}_v \sin^2 \theta \sin^2 \phi + \hat{\sigma}_h \cos^2 \theta)}_{=a'} \\ & + s \underbrace{(2 \hat{\sigma}_v y_0 \sin \theta \sin \phi + 2 \hat{\sigma}_h z_0 \cos \theta)}_{=b'} \\ & + \underbrace{\hat{\sigma}_v y_0^2 + \hat{\sigma}_h z_0^2}_{=c'} \end{aligned} \quad (3.69)$$

So that  $g(s)$  can be expressed as

$$g(s) = a' s^2 + b' s + c' \quad (3.70)$$

Entering Equation 3.70, 3.65, and 3.67 in Equation 3.62 results in

$$I = I_0 \exp \left[ C_1 \int_0^{s_e} \exp \left[ \frac{-1}{2 \det \hat{\sigma}} (a' s^2 + b' s + c') \right] ds \right] \quad (3.71)$$

and defining

$$a = \frac{1}{2 \det \hat{\sigma}} a' \quad (3.72)$$

$$b = -\frac{1}{2 \det \hat{\sigma}} b' \quad (3.73)$$

$$c = -\frac{1}{2\det\hat{\sigma}}c' \quad (3.74)$$

simplifies Equation 3.71 to

$$I = I_0 \exp \left[ C_1 \int_0^{s_e} \exp [-as^2 + bs + c] ds \right]. \quad (3.75)$$

The special integral

$$\int \exp(-ax^2 + bx + c) dx \quad (3.76)$$

has the solution [114]

$$F(x) = \frac{\sqrt{\pi}}{2\sqrt{a}} \exp \left[ \frac{b^2}{4a} + c \right] \operatorname{Erf} \left( \sqrt{a}x - \frac{b}{2\sqrt{a}} \right) \quad (3.77)$$

with the error function  $\operatorname{Erf}(x)$  for  $x \ll 1$  [114]

$$\operatorname{Erf}(x) = \frac{2}{\sqrt{\pi}} \sum_{n=0}^{\infty} \frac{(-1)^n x^{2n+1}}{(2n+1)n!} \quad (3.78)$$

$\operatorname{Erf}(x)$  is calculated, until the third decimal place of  $\operatorname{Erf}(x)$  is not changing any more.

The distance  $s$  corresponding to the random power of endurance  $Z_s$  is calculated numerically from Equation 3.75 by Newton iteration. For  $s$  being within the contrail (i.e. within the green dotted circle with the radius of  $w_{\text{in}}$  around the contrail center) an extinction event will take place. For a better understanding, compare Figure 3.15.

### Extinction in the Monte Carlo simulation

Now, the theory of the contrail radiative forcing model, is introduced. The photons can start their journey through the contrail. For the decision on the extinguishing event, lots of models and approaches, introduced in this Chapter are now used to find a solution for the calculation of the contrail radiative forcing. Each photon travels individually through the contrail. For each photon the location  $s$  of it's first extinguishing event



is calculated using the random number  $Z_s$ , entered into Equation 3.75 as power of endurance, which is  $I I_0^{-1}$  (compare Section 3.5.3). At the distance  $s$  from starting position  $(y_0, z_0)$  the photon encounters its first extinction event. At this location it has to be decided whether the photon is absorbed or scattered. Equations 3.63 and 3.64 give the position of extinction location in Cartesian coordinates. These coordinates inserted in the Gaussian plume model (Equation 3.39) yield the number density of ice particles  $n_{ice}$  at location  $s$  (compare Section 3.4.2). The ice particle radius  $r_p$  is assumed being constant in the contrail cross section for one time step of the contrail lifetime model, explained in Section 3.4. Following the parameterizations of Wyser et al. [55] and Yang et al. [56], the absorption and scattering efficiency  $Q_a$  and  $Q_s$  can be estimated (compare Section 2.2.6). Hence, using Equations 3.59 and 3.60 the probability of an absorption and a scattering event is defined. A new uniformly distributed random number  $Z_e = [0, 1]$  is generated deciding on the type of extinction (absorption or scattering). The procedure of the decision on the type of extinction is described in the following.

Because the order of consecutively happening events is important, the probability of a particular extinguishing event relates to the sum of the probability of both types of extinction. In other words (compare Equations 3.56, 3.59 and 3.60 for definitions):

$$Ext \neq Abs + Sca, \quad (3.79)$$

but maybe

$$\frac{Sca}{Sca + Abs} = \frac{\beta_s}{\beta_s + \beta_a}. \quad (3.80)$$

Considering the limit

$$\lim_{s \rightarrow 0} \frac{Sca}{Abs} = \lim_{s \rightarrow 0} \frac{1 - \exp[\beta_s s]}{1 - \exp[\beta_a s]} \quad (3.81)$$

and using

$$\lim_{x \rightarrow 0} \frac{f(x)}{g(x)} = \lim_{x \rightarrow 0} \frac{f'(x)}{g'(x)} \quad (3.82)$$

$$\lim_{d \rightarrow 0} \frac{Sca}{Abs} = \lim_{d \rightarrow 0} \frac{\beta_s \exp[\beta_s d]}{\beta_a \exp[\beta_a d]} = \frac{\beta_s}{\beta_a}. \quad (3.83)$$

Hence, Equation 3.80 is satisfied. For the new random number  $Z_e$

$$Z_e > \frac{\beta_s}{\beta_s + \beta_a} \quad (3.84)$$

an absorption event will take place. The absorbed photon disappears from the simulation. Its energy  $E = h\nu$  warms the contrail (compare Equation 2.10). And for

$$Z_e < \frac{\beta_s}{\beta_s + \beta_a} \quad (3.85)$$

a scattering event will happen. After the scattering process, the photon travels with a new direction  $\Omega'$  for a new distance  $s$ . Is the new location  $s$  within the contrail, another extinction event will happen.

The calculation of the new direction  $\Omega$  requires the estimation of the scattering angles  $\vartheta$  and  $\phi$ . Because the particles are randomly orientated within the contrail, the polar scattering angle  $\phi$  around the new propagation direction follows an uniformly distributed random number  $Z_\phi$ . Figure 3.17 exemplifies the consequence of a randomly orientated polar scattering angle  $\phi$  for a scattering event with dominated forward scattering, such as given by the Henyey-Greenstein phase function  $P_{\text{HG}}(\cos \vartheta)$  (Equation 2.40) with  $g_{\text{HG}} = 0.8$ .

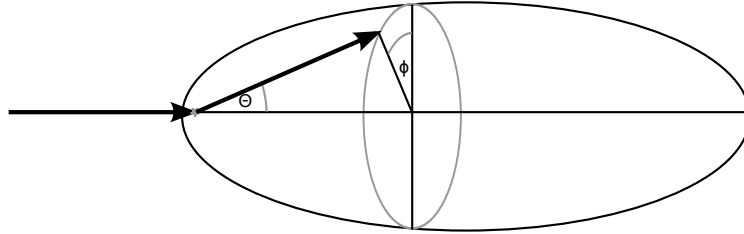


**Figure 3.17:** A scattering event following a Henyey-Greenstein phase function with dominant forward direction ( $g_{\text{HG}} \approx 0.8$ ). Because of randomly orientated particles  $\phi$  is uniformly distributed.

The scattering angle  $\vartheta$  follows the Henyey-Greenstein phase function  $P_{\text{HG}}(\cos \vartheta)$  with the asymmetry parameter  $g_{\text{HG}}$ , estimated by the parameterizations of Wyser et al. [55] and Yang et al. [56]. The inverse transformation method is used for the estimation of a random number following an arbitrary distribution function, i.e. the Henyey-Greenstein phase function. In this method, the phase function  $P_{\text{HG}}(\cos \vartheta)$  is divided into equidistant classes of  $\cos \vartheta$  [115]. A frequency distribution of the classes of  $P_{\text{HG}}(\cos \vartheta)$  allows the estimation of the necessary number of random numbers of each class. The integral of each class  $P_{\text{int}}$

$$P_{\text{int}} = \int_{\vartheta, \text{min}}^{\vartheta, \text{max}} P(\vartheta) d\vartheta \quad (3.86)$$

facilitates the definition of a cumulative frequency  $I(\vartheta)$ ,

$$I(\vartheta) = \sum_i^{\vartheta} P_{\text{int}} \quad (3.87)$$

where each  $I(\vartheta)$  with  $0 \leq I \leq 1$  can be allocated to a single class of  $\vartheta$ . The numerically estimated inverse function  $\vartheta(I)$  enables the allocation of a uniformly distributed random number  $I$  to a scattering angle  $\vartheta$  [115].

After the determination of the new direction  $\Omega'$  in spherical coordinates a transformation of the spherical coordinates into Cartesian coordinates is necessary.

### Calculated quantities during the Monte Carlo simulation

In the end, six quantities are expected. The ratios of photons coming from above the contrail and leaving the simulation space in the upper hemisphere  $V_{\downarrow b}$ <sup>2</sup> and in the lower hemisphere  $V_{\downarrow f}$ <sup>3</sup>. Furthermore, the ratios of photons coming from below the contrail and leaving it in the upper hemisphere  $V_{\uparrow f}$  and in the lower hemisphere  $V_{\uparrow b}$ . And the ratios of absorbed photons coming from below  $V_{\uparrow a}$ <sup>4</sup> and absorbed photons coming from above  $V_{\downarrow a}$ . Table 3.3 gives an overview over the expected quantities of photons. Note, that not all of the six quantities contribute to radiative forcing. For instance, photons coming from below and getting scattered into the upper hemisphere  $V_{\uparrow f}$  and photons coming from above and getting scattered into the lower hemisphere  $V_{\downarrow f}$  constitute the natural way of photons without a barrier. Due to the strong forward peak in the Henyey-Greenstein phase function  $P_{\text{HG}}$ , increased by the expected large asymmetry parameter  $g_{\text{HG}}$ , forward scattering will be very likely and  $V_{\uparrow f}$  and  $V_{\downarrow f}$  will constitute a large amount of the calculated ratios of photons.

Following the achievements of Section 3.5.3, these components are calculated as ratios between the number of incoming photons  $N_{\text{in}}$ , and the number of outgoing or absorbed photons  $N_{\text{out}}$ , derived by the sum of the particular extinction events. The ratio of the numbers of incoming  $N_{\text{in}}$  and outgoing (or absorbed)  $N_{\text{out}}$  photons can be used for

<sup>2</sup>the index b refers to "backscattered"

<sup>3</sup>the index f refers to "forward scattered"

<sup>4</sup>the index a refers to "absorbed"

**Table 3.3:** Components of extinguished photons considering multiple scattering (Monte Carlo simulation). Indices  $a$ ,  $b$  and  $f$  symbolize absorbed, backward scattered and forward scattered, respectively. The arrows indicate the direction of incoming photons.

$V_{\uparrow a}$	absorbed photons coming from below
$V_{\uparrow b}$	photons coming from below, scattered into the lower hemisphere
$V_{\uparrow f}$	photons coming from below, scattered into the upper hemisphere
$V_{\downarrow a}$	absorbed photons coming from above
$V_{\downarrow b}$	photons coming from above, scattered into the upper hemisphere
$V_{\downarrow f}$	photons coming from above, scattered into the lower hemisphere

the calculation of the optical thickness  $\tau$ , for photons traveling through the contrail vertically. Considering Equation 3.57 the optical thickness can be interpreted as

$$\tau = -\ln \left( 1 - \frac{N_{\text{affected}}}{N_{\text{in}}} \right), \quad (3.88)$$

where  $N_{\text{affected}}$  denotes the sum of all extinguished photons. The ratio of the numbers of incoming  $N_{\text{in}}$  and outgoing (or absorbed)  $N_{\text{out}}$  photons must be weighted by the irradiated width ( $2w_{\text{in}}$ ) and the sine on the angle  $\alpha$  between the incoming photons and the x-axes (flight path) as projection of the perpendicular irradiated area on the flight path. This process is very important, because the resultant number of extinguished photons strongly depends on the irradiated width  $2w_{\text{in}}$  and on the angle  $\alpha$  of incidence. The shorter the distance  $2w_{\text{in}}$ , the higher the ratios of photons traveling through the center of the contrail and the higher the probability of extinction. The smaller the angle  $\alpha$  between incoming photons and contrail the larger the irradiated area of the contrail and the smaller the intensity of radiation on a unit area. The angle  $\alpha$  is defined between a unit vector  $\vec{a}$  along the flight path

$$\vec{a} = \begin{pmatrix} 1 \\ 0 \\ 0 \end{pmatrix} \quad (3.89)$$

and a unit vector  $\vec{b}$  along the incident photons (compare Figure 3.16 for the derivation)

$$\vec{b} = \begin{pmatrix} \sin \theta \cos \phi \\ \sin \theta \sin \phi \\ \cos \theta \end{pmatrix} \quad (3.90)$$

Considering the overall definition of the angle between two vectors

$$\cos \alpha = \frac{\vec{a} \cdot \vec{b}}{|\vec{a}| \cdot |\vec{b}|}, \quad (3.91)$$

the angle  $\alpha$  simplifies to

$$\cos \alpha = \sin \theta \cos \phi. \quad (3.92)$$

Figure 3.18 defines the influencing parameters of the contrail. The weighted quantities of Table 3.3 are defined as  $S_i$  [m], getting the same indices as  $V_i$  and are calculated by

$$S_i = \frac{N_{\text{out}}}{N_{\text{in}}} 2w_{\text{in}} \sin \alpha. \quad (3.93)$$

Due to the multiplication of the ratio of numbers  $V_i$  with the irradiated width  $2w_{\text{in}}$  the quantities  $S_i$  have the unit [m].

### 3.5.5 The extinguished power per unit length contrail

To calculate the radiative forcing per unit length of the contrail, the power  $P_i$  [ $\text{W m}^{-1} \text{nm}^{-1}$ ] of the extinguished photons once irradiated on a unit length contrail have to be considered and balanced. Therefore, the solar radiance  $I_0$  [ $\text{mW sr}^{-1} \text{m}^{-2} \text{nm}^{-1}$ ] coming from the particular direction  $\Omega$  [sr], calculated by the radiative transfer model libRadtran has to be weighted by the weighted ratio of numbers of extinguished photons  $S_i$  [m] and the corresponding solid angle  $\Omega$  [sr]. For radiation coming from above and getting scattered into the upper hemisphere the extinguished power  $P_{\downarrow b}$  [ $\text{W m}^{-1} \text{nm}^{-1}$ ] is

$$P_{\downarrow b} = I_0 S_{\downarrow b} \Omega. \quad (3.94)$$

In Figure 3.18 the ratio  $V_{\downarrow b}$  of photons from above and the number of photons scattered into the upper hemisphere is defined exemplarily. Furthermore, the distance  $2w_{in}$  and the incident angle  $\alpha$  influencing  $S_{\downarrow b}$  are demonstrated.

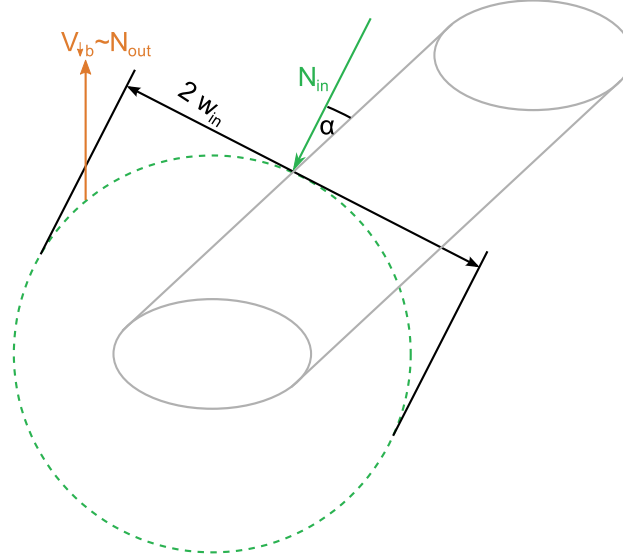


**Figure 3.18:** Visualization of important assumptions during the Monte Carlo simulation. Exemplary depiction of the necessary quantities for the calculation of photons coming from the upper hemisphere and getting scattered back into the upper hemisphere.

Terrestrial irradiances  $F_{up}$  and  $F_{down}$  [ $\text{W m}^{-2} \text{nm}^{-1}$ ], calculated with the Two Stream Approximation are hemispherically averaged irradiances. Furthermore, an integration over the whole terrestrial spectrum is possible due to reduced computational effort by the Two Stream Approximation. To estimate the extinguished power in the terrestrial wavelength spectrum  $F_{up}$  and  $F_{down}$  have to be weighted by the number ratio of extinguished photons. For example:

$$P_{\downarrow b} = F_{down} S_{\downarrow b}. \quad (3.95)$$

The radiative forcing  $RF$  is defined as

$$RF = P_{\downarrow a} + P_{\uparrow b} - P_{\downarrow b}. \quad (3.96)$$

In this thesis, the radiative forcing is calculated for a unit length contrail. Hence, it is a specific radiative forcing. For convenience and to avoid misunderstandings with other studies, capital letters are used in the symbol. According to Equation 3.96 cooling rates

are caused by a negative  $RF$  and heating rates are caused by a positive  $RF$ . Furthermore, the imbalance in the energy budget, caused by solar extinction is calculated in  $[\text{W m}^{-1} \text{nm}^{-1}]$ . Due to the consideration of the whole terrestrial spectrum, terrestrial radiative forcing can be expressed in  $[\text{W m}^{-1}]$ .

Estimating the contribution to the radiative imbalance of the Earth-atmosphere system due to the life time of a single contrail, Schumann et al. [116] defined the energy forcing  $EF$   $[\text{J m}^{-1}]$  of a single contrail as integration of the contrail radiative forcing over the contrail life time. In this thesis, calculation of the contrail energy forcing is possible for the terrestrial wavelength spectrum by balancing the extinguished energies during the contrail life time (compare Section 4.5)

$$EF = E_{\downarrow\uparrow a} + E_{\uparrow b} - E_{\downarrow b}. \quad (3.97)$$

### 3.5.6 Scattering and absorption efficiencies $Q_s$ , $Q_a$ and asymmetry parameters $g_{\text{HG}}$

For the Monte Carlo simulation calculating the contrail radiative forcing, the scattering and absorption efficiencies  $Q_s$ ,  $Q_a$  as well as the asymmetry parameters  $g_{\text{HG}}$  have to be known. These parameters describe the optical properties of the contrail and depend on ice particle radius  $r_p$  and on wavelength  $\lambda$  of the irradiances and radiances in question. The calculation of the scattering and absorption efficiencies  $Q_s$ ,  $Q_a$  is nontrivial and parameterizations have to be used. The background calculations of these parameterizations are explained in the following.

For spherical ice particles up to radii of  $r_p = 6 \mu\text{m}$  scattering and absorption of light due to interactions with spherical particles was developed by Mie [117] in 1908. The Mie theory describes a special solution of Maxwell's equations. The implementation of this theory is nontrivial because the calculation of the required Ricatti-Bessel functions leads to an arithmetic overflow [118]. However, the contrail life cycle model rarely calculates ice particles with radii  $r_p \leq 6 \mu\text{m}$ . Furthermore, the radiative extinction usually grows with increasing particle radius  $r_p$ . For the estimation of the optical properties of a contrail the solution of Mie theory is insufficient, because ice particles in cirrus clouds with  $r_p > 6 \mu\text{m}$  grow non spherically [55], [56], [31], [32], [34], [119]. To account for the non spherical character of large ice particles (large compared to the wavelength), ray-tracing calculations can be used. Such calculations are very demanding in terms of calculation time. Therefore, parameterizations of the results of ray tracing simulations are used in the scope of this work. King et al. [120] identified the ice particle shapes in natural mid latitude cirrus clouds using in situ measurements. Yang et al. estimated their optical properties in the infrared spectrum [56] and Wyser et al. in the

solar wavelength spectrum [55]. For ice particle diameters  $2 \mu\text{m} \leq d_p \leq 70 \mu\text{m}$ , King et al. discovered the composition of ice particle shapes as listed in Table 3.4.

**Table 3.4:** *Estimated ice particle shapes in cirrus clouds for diameters between  $2 \mu\text{m} \leq d_p \leq 70 \mu\text{m}$  discovered by King et al. [120].*

Shape	Ratio [%]
bullet rosettes	50
hollowed columns	25
plates	25

The estimated particle shapes are shown in Figure 3.19.

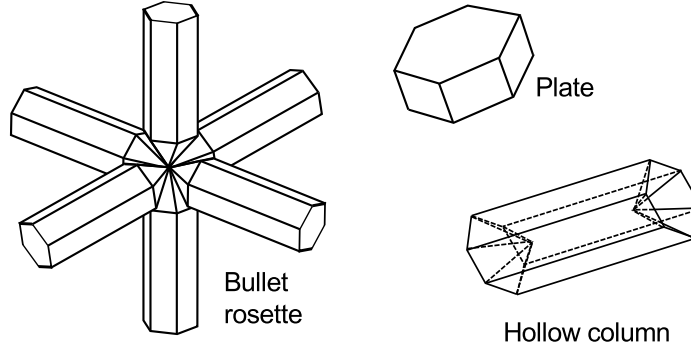


**Figure 3.19:** *Idealized geometry of ice particle shapes (bullet rosettes, plates and hollow columns), estimated in natural midlatitude cirrus clouds by King et al. [120] and used for the parameterization of optical properties of ice particles by Wyser et al. [55] and Yang et al. [56].*

For the sake of simplicity no size distribution, rather a constant particle effective size is assumed. To satisfy a realistic size distribution in condensation trails, a heterogeneous size distribution depending on the position within the contrail cross section would be required. The derivation of such correlation would exceed the scope of this thesis.

For solar wavelengths Wyser et al. [55] calculated the optical properties extinction efficiency  $Q_e$ , single scattering efficiency  $Q_s$  and asymmetry parameter  $g_{HG}$  of the individual randomly orientated ice particle shapes. The results are parameterized depending on maximum dimension  $d_{\max}$  and complex refractive index for several wavelengths. The maximum dimension  $d_{\max}$  is the larger dimension of a non spherical particle. The calculations are done for 56 narrow spectral bands between  $0.2 \mu\text{m} \leq \lambda \leq 5 \mu\text{m}$  for ice particle diameters between  $3 \mu\text{m} \leq d_{\max} \leq 4000 \mu\text{m}$ . The single scattering properties are calculated based on a ray-tracing technique of Takano et al. [121], which



considers the truncation of the forward energy peak in the scattering phase function  $P_{\text{HG}}$  of non spherical ice particles by enhancing the Mie theory by a delta function. The optical properties ( $Q_e$ ,  $Q_s$  and  $g_{\text{HG}}$ ) are parameterized for each particle shape by Wyser et al. [55] for the following wavelengths:  $0.55 \mu\text{m}$ ,  $1.35 \mu\text{m}$ ,  $2.25 \mu\text{m}$ ,  $2.75 \mu\text{m}$ ,  $3.0125 \mu\text{m}$ ,  $3.775 \mu\text{m}$ , and  $4.5 \mu\text{m}$ .

The maximum dimension is also parameterized for each particle shape depending on the radii of the equivalent-volume or equivalent-area spheres. The mean optical properties for the composition of ice particle shapes estimated by King et al. [120] (Table 3.4) are derived by weighting the individual optical properties.

In the terrestrial wavelength spectrum the extinction efficiency  $Q_e$ , single scattering efficiency  $Q_s$  and asymmetry parameter  $g_{\text{HG}}$  are calculated and parameterized by Yang et al. [56] for the mentioned composition of ice particle shapes depending on wavelength and effective particle size  $D_e$  [m], where the effective particle size is assumed as twice of the mean particle radius given in the contrail lifecycle model:  $D_e = 2r_p$ . The calculation are done by Yang et al. [56] for 49 wavelengths between  $3 \leq \lambda \leq 100 \mu\text{m}$  and effective particle sizes between  $2 \leq D_e \leq 10000 \mu\text{m}$ . Therewith, the absorption efficiency  $Q_a$  can be calculated as difference between  $Q_e$  and  $Q_s$ . The radiative transfer is computed from a composite method basing on a combination of a finite difference time domain technique, a T-matrix method, an improved geometrical optics method and Mie theory [56]. Comparisons with Mie theory for spherical ice particles show larger extinction properties for spheres, than for non spherical ice particles [56].

Figure 3.20 shows the extinction and absorption efficiency  $Q_e$  and  $Q_a$ , as well as the asymmetry parameter  $g_{\text{HG}}$  for both parameterizations (solar and terrestrial wavelengths) for a fixed particle radius  $r_p = 10 \mu\text{m}$ . The chosen particle radius is typical for particles, derived in this thesis, calculated with the contrail life cycle model (Section 3.4) using the manipulated model atmosphere with weak ice-supersaturation (compare Figures 3.10 and 3.11). According to Figure 3.20,  $Q_e = 2$  might be an agreeable assumption in the solar spectrum. For example for the maximum solar radiance at  $\lambda = 0.55 \mu\text{m}$   $Q_e = 1.96$ . In contrast,  $Q_a$  is very small, with even negative values in the shortwave spectrum. These negative values show the boundaries of the accuracy of the parameterizations and are set to zero. Because of  $Q_s = Q_e - Q_a$ , the extinction will be finally caused by scattering events, which enhances the probability of multiple scattering. On the other hand, the solar asymmetry parameter shows large values and indicates a strong forward scattering. This means, that the extinction will be weak.

The solar absorption efficiencies have to be considered with care, because Hong et al. [32] estimated the optical properties of small ( $r_p = 0.75 \mu\text{m}$ ) spherical ice particles (using Mie theory) containing soot for two different wavelengths  $\lambda = 0.65 \mu\text{m}$  and  $\lambda = 2.13 \mu\text{m}$ . The results of this study are remarkable, showing differences between pure ice particles and ice particles with a soot core with a volume ratio of 5%. The

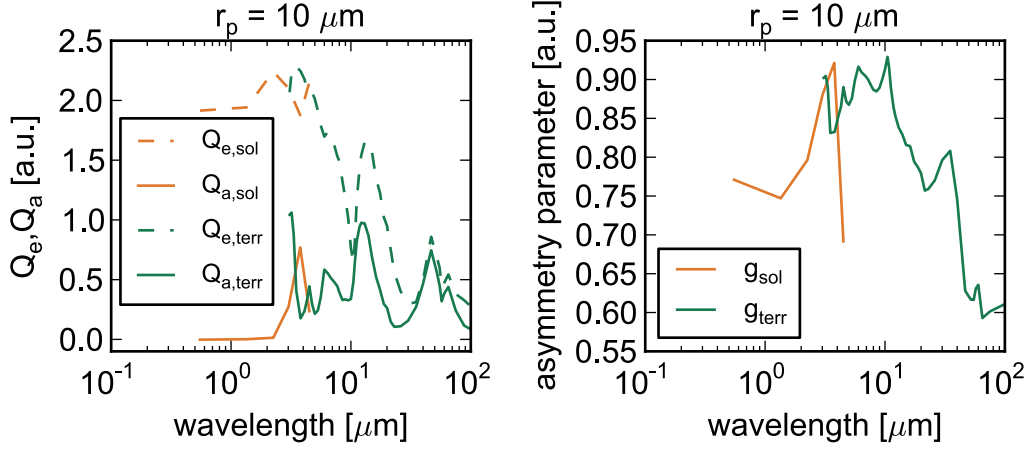


**Figure 3.20:** Extinction  $Q_e$  (dashed) and absorption  $Q_a$  (solid) efficiencies and asymmetry parameter  $g_{HG}$  of a mixture of ice particle shapes following Table 3.4 in the solar (orange) and terrestrial (green) wavelength spectrum for a fixed particle radius  $r_p = 10 \mu\text{m}$  calculated according to Wyser et al. [55] and Yang et al. [56].

differences in absorption efficiency are in the order of  $10^6$  for  $\lambda = 0.65 \mu\text{m}$  and in the order of  $10^2$  for  $\lambda = 2.13 \mu\text{m}$ . Whereas, differences in scattering efficiency are in the order of 1 for  $\lambda = 0.65 \mu\text{m}$  and in the order of  $10^{-2}$  for  $\lambda = 2.13 \mu\text{m}$ , with the smaller values of  $Q_s$  for the soot containing ice spheres. The error in the estimation of the solar absorption efficiency of ice particles containing soot had been only calculated for the special case of very small particles ( $r_p = 0.75 \mu\text{m}$ ) compared to the wavelength ( $\lambda = 0.65 \mu\text{m}$  and  $\lambda = 2.13 \mu\text{m}$ ). As mentioned at the beginning of this Section, the methodology, used for this study (Mie theory) is insufficient for large particles or small wavelengths. Hence, the underestimation of solar extinction efficiencies, considered in this thesis, can not be quantified.

The extinction efficiency of the terrestrial wavelengths in Figure 3.20 for the corresponding radiances (Figure 2.5) decreases with increasing wavelength.

Figure 3.21 demonstrates the results of the parameterizations of the optical properties for two fixed wavelengths  $\lambda = 0.55 \mu\text{m}$  for solar spectrum and  $\lambda = 10.5 \mu\text{m}$  for terrestrial wavelengths. The parameterizations are done for exactly the mixture of particle shapes following Table 3.4. In the terrestrial range,  $Q_e$  and  $Q_a$  increase with increasing particle radius until above  $r_p = 12 \mu\text{m}$  scattering will be very unlikely, because  $Q_e = Q_a$ . However,  $Q_e$  is still much smaller than in the solar wavelength spectrum. The asymmetry parameter  $g_{HG}$  increases with increasing particle radius up to  $g_{HG} = 0.9$  for

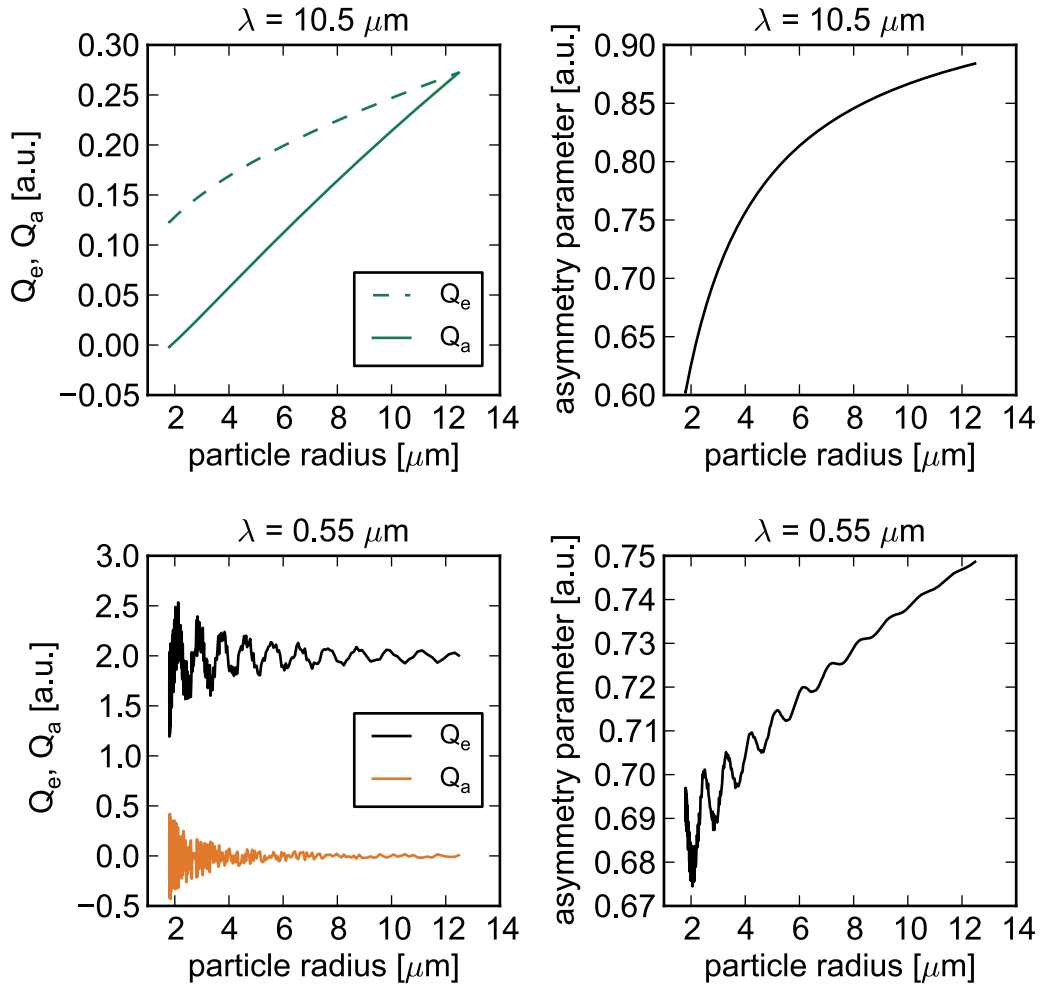


**Figure 3.21:** Extinction  $Q_e$  and absorption  $Q_a$  efficiencies and asymmetry parameter  $g_{\text{HG}}$  depending on particle radius [ $\mu\text{m}$ ] for a mixture of ice particle shapes following Table 3.4 in the terrestrial (top,  $10 \mu\text{m}$ ) and solar (bottom,  $0.55 \mu\text{m}$ ) wavelength spectrum.

$r_p = 12 \mu\text{m}$ . However, scattering is very unlikely ( $Q_s \approx 0$ ). Hence, neither forward nor backward scattering is expected. Summarizing the terrestrial optical properties, it could be noted, although a weak extinction is expected, the contrail will absorb more terrestrial than solar energy.

In the solar wavelength region the differences in the estimated optical properties between solar and terrestrial bands (Figure 3.21) are clear. The "enhanced" Mie theory used for the solar spectrum show the typical fluctuations of Mie theory. Because  $Q_a$  is still very small, no significant absorption is expected. The extinction efficiency fluc-

tuates around  $Q_e = 2$  and indicates a significant scattering efficiency. Hence, multiple scattering will be possible for all particle radii. The asymmetry parameter  $g_{\text{HG}}$  with  $0.67 \leq g_{\text{HG}} \leq 0.75$  does not consequently indicate strong forward scattering for small particles. Hence, a Monte Carlo simulation is necessary, because multiple scattering is possible.

### 3.5.7 Calibration of the Monte Carlo simulation

During the development of the Monte Carlo simulation it has been taken care to reduce the number of parameters to a minimum value. Hence, only three parameters remain. First, the irradiated width of the starting photons  $2w_{\text{in}}$  depending on the larger dimension of the contrail's cross section. Second, the required total number of photons  $N_{\text{eval}}$  and third, the discretization  $\Delta_{\theta, \phi}$  of the angles  $\theta$  and  $\phi$ . In the following, these three parameters will be estimated.

#### The irradiated width $2w_{\text{in}}$ of starting photons

The determination of the required width  $2w_{\text{in}}$  of the contrail irradiated by photons can be done with various Monte Carlo simulations invariably using  $10^7$  photons coming from above  $\theta = 0^\circ$  perpendicular to the horizontal plane between the x- and y-axis for different  $w_{\text{in}}$  as function of the larger dimension of the contrail  $\sigma_h$ . Figure 3.22 shows the ratio of number of affected photons to the total number of photons weighted by the irradiated width  $2w_{\text{in}}$  for different  $w_{\text{in}}$  as a result of the simulations. The calculated quantity corresponds to the weighted number ratio of extinguished photons  $S_{\text{ext}}$  in units of  $[\sigma_h]$  (compare Equation 3.93 with  $\sin \alpha = 1$  for  $\alpha = 90^\circ$ ). The simulations are done for the optical properties of an optically thin contrail in strong turbulence ( $\epsilon = 10^{-4} \text{ m}^2\text{s}^{-3}$ ) after a lifetime of 20 h for photons with a wavelength of  $0.55 \mu\text{m}$  (compare Figures 3.21 and 4.2). The results are underestimated for  $w_{\text{in}} < 3\sigma_h$ , because in this case a significant number of ice particles is not considered. For  $w_{\text{in}} = 3\sigma_h$  the results converge to a constant value. Due to the Gaussian distribution function, describing the contrail, the required irradiated width depends on the number of ice particles which should be considered in the simulation. 99.73 % of the total number of ice particles are distributed within  $3\sigma$  [103]. Hence, to consider a significant number of ice particles in the contrail, a width  $w_{\text{in}} = 3\sigma_h$  is chosen.

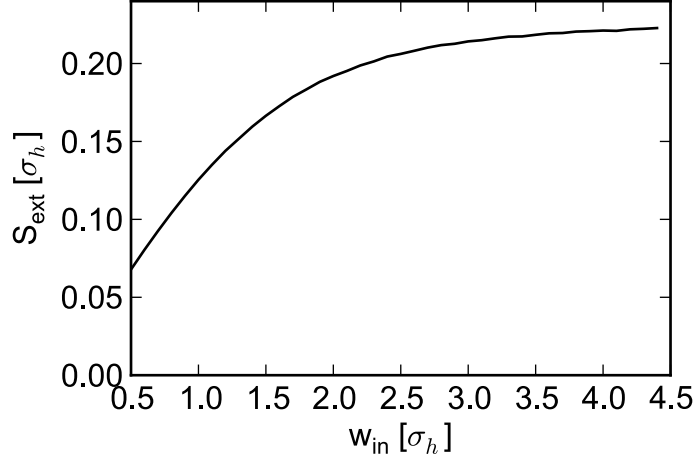


**Figure 3.22:** Influence of the irradiated width  $2w_{in}$  of starting photons (compare Figure 3.14). The ratio of the number of affected photons to the total number of photons is calculated for different  $w_{in}$  as function of the standard deviation  $\sigma_h$ . For  $w_{in} = 3\sigma_h$  the results converge to a constant value.

### The number of photons in the Monte Carlo simulation

The statistical error of a Monte Carlo simulation increases with a decreasing number of considered events. Due to the high probability of transmission, a large number of photons have to be considered assuring a sophisticated number of extinguishing events. For the estimation of the required number of photons, several Monte Carlo simulations with varying total numbers of photons were run for the same conditions as in Figure 3.22. Figure 3.23 shows the ratio of affected photons to the total number of photons for different total numbers of photons and  $w_{in} = 3\sigma_h$ . The result oscillates for an insufficient total number of photons  $N_{eval} \leq 10^7$  showing the effect of the statistical error. For  $N_{eval} = 10^7$  photons (orange marker) the result converges to a constant value. Hence, the Monte Carlo simulation is done with  $N_{eval} = 10^7$  photons.

### The required discretization $\Delta_{\theta,\phi}$ of the angles $\theta$ and $\phi$

Due to the angular variation of solar radiances irradiating the contrail, solar radiances coming from all directions in space have to be considered. To handle this computational effort, the required discretization  $\Delta_{\theta,\phi}$  of the angles  $\theta$  and  $\phi$  describing the direction of the sun has to be estimated. The influence of the maximum step size between the chosen zenith and azimuthal angles  $\theta$  and  $\phi$  of incoming photons can be estimated with the

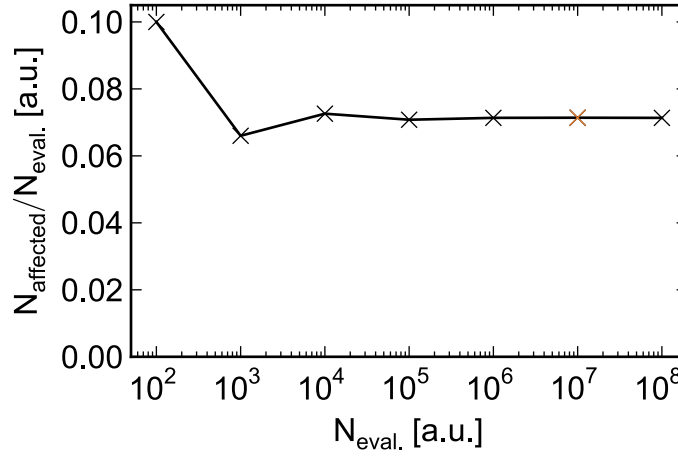


**Figure 3.23:** Influence of the chosen total number of photons for the Monte Carlo simulation. The ratio of the number of affected photons to the total number of photons oscillates for an insufficient total number of photons  $N_{\text{eval}} \leq 10^7$  showing the effect of the statistical error. Using  $N_{\text{eval}} = 10^7$  photons, the result converges to a constant value.

help of the calculated extinguished specific power  $P_e$  [ $\text{W m}^{-1} \text{nm}^{-1}$ ] per meter contrail calculated by combining the number ratios of extinguished photons  $S_i$  [m] of the Monte Carlo simulation with the calculated solar radiances  $I_{\text{dir}}$  and  $I_{\text{diff}}$  [ $\text{mW sr}^{-1} \text{m}^{-2} \text{nm}^{-1}$ ] and terrestrial irradiances  $F_{\text{up}}$  and  $F_{\text{down}}$  [ $\text{mW m}^{-2} \text{nm}^{-1}$ ] of the atmospheric radiative transfer model libRadtran. In Figure 3.24 the influence of the discretization  $\Delta_{\theta, \phi}$  is depicted considering the power  $P_{\downarrow b}$  of photons with a wavelength of  $\lambda = 0.55 \mu\text{m}$  coming from the upper hemisphere and getting scattered back into the upper hemisphere due to a contrail with constant microphysical properties according to Figure 4.2 with a mean turbulence of  $\varepsilon = 5 \cdot 10^{-5} \text{m}^2 \text{s}^{-3}$  and a life time of 20 h. This extinguished power  $P_{\downarrow b}$  is calculated for the diurnal variation of a whole day. Hence, constant contrail properties but changing angular depended irradiances and radiances are chosen. Bin sizes of  $5^\circ$  and  $10^\circ$  are too large. The extinguished power is overestimated at the boundaries of the angle bins and discontinues results in  $P_{\downarrow b}$  are appearing in Figure 3.24. Even for a bin size of  $2^\circ$  small errors at the boundaries of the bins are calculated. The errors are detectible as discontinuances in Figure 3.24. However the computational effort for  $2^\circ$  is already high enough, a Monte Carlo simulation lasts 20 hours per meter contrail and wavelength band on a home computer. Hence,  $2^\circ$  are chosen. In Figure 3.24 the benefit of the angular resolved radiative transfer model is visible. The graphs of  $P_{\downarrow b}$  show the influence of both solar zenith angle  $\theta$  and solar azimuthal angle  $\phi$  of direct solar radiation and the increased solar direct and diffuse radiance at noon. For the calibration of the Monte Carlo simulation, only the discontinuity of the graphs and the

differences between the graphs is important. The shape of the graph will be discussed in section 4.4.1.

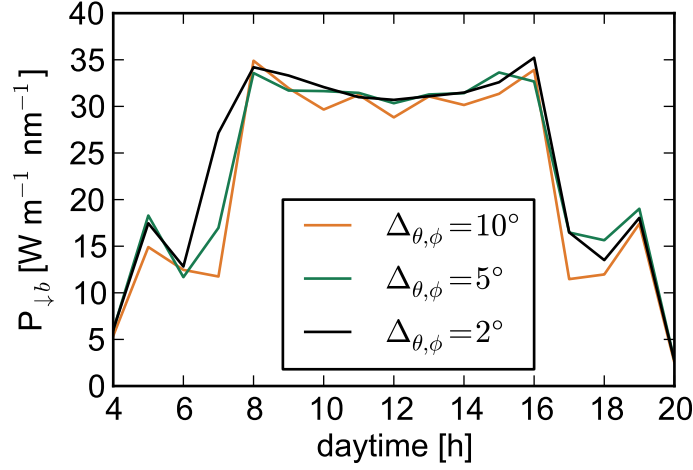


**Figure 3.24:** Influence of the discretization  $\Delta_{\theta,\phi}$  between different zenith and azimuthal angles  $\theta$  and  $\phi$ . The influence is visualized considering the power  $P_{\downarrow b}$  of photons with  $\lambda = 0.55 \mu\text{m}$  contrail properties according to Figure 4.2 after 20 h with a mean turbulence of  $\varepsilon = 5 \cdot 10^{-5} \text{ m}^2\text{s}^{-3}$  calculated for the diurnal variation of a whole day. Bin sizes of  $5^\circ$  and  $10^\circ$  are too large. The extinguished power is overestimated at the boundaries of the angle bins causing discontinuous results.





## 4 Calculations

*This chapter contains the calculation of radiative extinction due to a condensation trail in the Earth-atmosphere system. At first, calculations of the contrail microphysical properties are demonstrated, followed by atmospheric radiative transfer calculations around the contrail. Finally, the results of the Monte Carlo simulation calculating the contrail radiative forcing by combining the contrail microphysical properties with the atmospheric radiative transfer calculations around the contrail are shown and discussed. The influence of the contrail microphysical and atmospheric properties on the extinction of radiation is demonstrated. Hence, decisions can be done, on how to optimize the flight performance with respect to optimal contrail microphysical properties and minimum contrail influence on radiative forcing.*

### 4.1 Contrail properties

First of all, the conditions of contrail formation have to be calculated by applying the Schmidt-Appleman criterion (compare Section 2.3.3) to the flight profile calculated with the flight performance model EJPM. The flight profile is scrutinized for time steps with contrail formation under the conditions of the manipulated standard atmosphere Midlat Winter [52] and the contrail microphysical properties induced by these aircraft performance characteristics will be calculated. The initial contrail horizontal and vertical dimensions  $c_h$  and  $c_v$ , defined at the end of the dissipation regime of the wake vortices, are estimated with the help of the wake vortex model P2P by Holzäpfel et al. [102]. The determination of the contrail life cycle is done by a Gaussian plume model. These estimations yield the development of the required microphysical properties (particle radius  $r_p$  and ice water content  $IWC$ ) during the life cycle of the contrail segment, which is formed during a single time step of the aircraft performance model EJPM. These parameters allow the estimation of the optical parameters scattering and absorption efficiency  $Q_s$  and  $Q_a$  for a dedicated wavelength and for each time step

during the contrail life time.

#### 4.1.1 Conditions of contrail formation

For the identification of time steps with secure contrail formation, the Schmidt-Appleman criterion (compare Section 2.3.3) is applied to the flight profile provided by the EJPM (Section 3.2) and the conditions of the manipulated model atmosphere Midlat Winter [52] (Section 3.1) are used, to estimate altitudes of contrail formation as shown in Figure 4.1. As pointed out in Section 2.3.3, persistent contrails form for an ambient temperature  $T$  colder than the threshold temperature  $T_{LC}$  and an ambient relative humidity with respect to ice  $rh_{ice} \geq 1$ . In the manipulated model atmosphere Midlat Winter, ice saturation takes place above 9.6 km (compare Figure 4.1).

The top plot of Figure 4.1 shows the change of ambient temperature  $T$  and of the threshold temperature  $T_{LC}$  with distance flown by the aircraft in still air. The aircraft performance calculations are done for a single model atmosphere without any influence of changing atmospheric state variables due to changing longitude or latitude. Following Section 2.3.3  $T_{LC}$  depends in the overall propulsion efficiency  $\eta$  (Equation 2.62) and the slope of the mixing line  $G$  (Equation 2.65). Schumann [50] pointed out, that an increase in  $\eta$  causes a stronger slope  $G$  of the mixing line, which enhances the threshold temperature  $T_{LC}$  and reduces the altitude of contrail formation. This phenomena can be seen in Figure 4.1 in comparison with Figure 3.2 between 250 km and 380 km where the thrust is enhanced for a smoother decline with constant fuel flow resulting in an increasing overall efficiency  $\eta$  until a sudden cutback of thrust at 312 km distance in 6100 m altitude, again without any reaction in fuel flow, causes a step change in  $\eta$  and in  $T_{LC}$ . After that major discontinuity in  $T_{LC}$ , the threshold temperature increases again due to increasing ambient pressure  $p$  with falling altitude. The overall shape of the curve of  $T_{LC}$  is characterized by a weak decrease with altitude due to decreasing pressure with height. From Figure 4.1 it gets clear, that the decrease of pressure with height does not compensate the decreasing ambient temperature with altitude. Hence, the higher the aircraft flies the higher the possibility of contrail formation.

The bottom plot of Figure 4.1, the relative humidity with respect to ice shows the manipulated ice saturated layer in the model atmosphere (compare Figure 3.1). Before and behind that ice saturated peak  $rh_{ice}$  decreases with height following the model atmosphere (Figure 3.1).

Within the altitude range of persistent contrail formation, the small period of cruise flight is located. Hence, contrail properties behind a cruising aircraft can be calculated. The flight performance properties taken from the EJPM and considered in the contrail life cycle model are listed in Table 4.1.

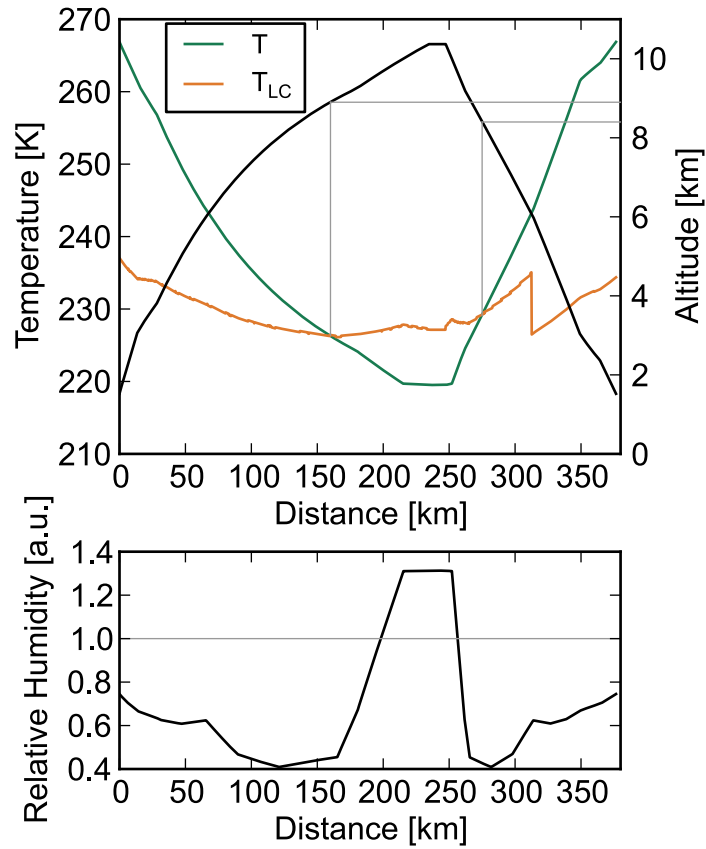


**Figure 4.1:** Application of the Schmidt-Appleman criterion on the flight profile. Top: contrails will form if the ambient temperature  $T$  (green) is smaller than the threshold temperature  $T_{LC}$  (orange). The black line demonstrates the altitude of the flight profile. The grey lines help indicating the altitude of contrail formation, which is 8.9 km during climb and 8.4 km under descent conditions. Bottom: the relative humidity with respect to ice defines the altitudes of persistent contrail formation. Above 9.6 km the atmosphere is saturated with respect to ice and contrails will develop into artificial ice clouds.

#### 4.1.2 Initial dimensions at the end of the dissipation regime

The calculations of the contrail properties are always done for one dedicated time step of the flight profile calculated by Kaiser [81] of an Airbus A320 (compare Section 3.2). The flight performance characteristics are chosen for a time step during cruise flight (compare Figures 3.2 and 4.1), where the Schmidt-Appleman criterion is satisfied, giving the following parameters:

**Table 4.1:** Parameters of the flight profile [81] used for the calculation of the initial state of the contrail.

Altitude	$h = 10500 \text{ m}$
Aircraft mass	$m = 70000 \text{ kg}$
True air speed	$v_{\text{TAS}} = 233 \text{ m s}^{-1}$
Fuel flow	$m_f = 0.314 \text{ kg s}^{-1}$

These properties, together with aircraft specific parameters like a wing span  $l_s = 34.1 \text{ m}$ , allow the following calculations of the wake vortex properties at the end of the dissipation regime using the wake vortex model P2P (compare Section 3.4.1)

**Table 4.2:** Parameters for wake vortex calculations of the initial state of the contrail.

Initial circulation	$\Gamma_0 = m g (\rho b_0 v_{\text{TAS}})^{-1}$	$267 \text{ m}^2 \text{ s}^{-1}$
Initial horizontal vortex spacing	$b_0 = \frac{\pi}{4} l_s$	$26.78 \text{ m}$
Effective horizontal vortex spacing	$b = 0.4 b_0$	$10.7 \text{ m}$
Radius of the vortex core	$r_c = 0.09 l_s$	$3.096 \text{ m}$
Radius of the vortex	$r = 2.53 r_c$	$7.76 \text{ m}$

According to Equation 3.6 the sedimentation speed  $v_s$  of the wake vortices yields

$$v_s = v_{t,0} \left( \exp \left[ \frac{-1.257 b^2}{r_c^2} \right] \right) = 1.73 \text{ m s}^{-1} \quad (4.1)$$

and the initial contrail horizontal extension (compare Figure 3.8 and Equation 3.24) denotes

$$c_h = b_0 + 2r = 33.8 \text{ m}. \quad (4.2)$$

The initial contrail vertical extension depends on turbulence. Due to missing turbulent information, five turbulence classes were defined in Section 3.4.2 considering measurements of eddy dissipation rate with  $10^{-6} \leq \varepsilon \leq 10^{-4} \text{ m}^2 \text{ s}^{-3}$  of Schumann et al. [76].

The definition of the eddy-dissipation  $\varepsilon$  rate allows the estimation of the time  $t$  (Equation 3.11), the wake vortices descent during the dissipation regime, and therewith the

initial vertical contrail extension  $c_v = v_s t + 2r$  (Equation 3.18). The time  $t$  decreases with increasing turbulence resulting in reduced contrail vertical dimension.

**Table 4.3:** Eddy dissipation rate  $\varepsilon$ , sedimentation time  $t$  and initial contrail vertical depth  $c_v$  resulting from wake vortex calculations according to Holzäpfel et al. [53] for flight performance parameters following Table 4.1.

$\varepsilon$ [m <sup>2</sup> s <sup>-3</sup> ]	$t$ [s]	$c_v$ [m]
$1 \cdot 10^{-6}$	58.1	107.5
$5 \cdot 10^{-6}$	55.1	102.3
$1 \cdot 10^{-5}$	51.9	96.9
$5 \cdot 10^{-5}$	44.0	83.1
$1 \cdot 10^{-4}$	40.2	76.6

### 4.1.3 Microphysical properties during the diffusion regime

The development of the contrail properties over its life time is shown in Figure 4.2. Diffusion is driven by differences in concentration. Hence, an accelerated growth is observed in the beginning of the diffusion regime. The fast growth of the contrail cross section at the beginning of the diffusion regime causes a reduction of ice water content  $IWC$  at the beginning, still assuming a constant number of ice particles. With slower growth of the contrail cross section in an ice-supersaturated environment, the ice water content increases. The  $IWC$  plotted in Figure 4.2 is averaged over the contrail cross section and shows a realistic magnitude, compared with simulations [104], [20], [122], [96].

The ice water content in Figure 4.2 shows a boundary of the contrail life cycle model. At the end of the simulation the ice water content reaches lower values for strong turbulence than for all other turbulence classes. This is caused by the determination of the time step depending on the vertical displacement within the previous time step. This causes differences in the conditions of the last time step of the model.

By leaving the ice saturated layer, the ice water content decreases at the end of the life time, as expected.

All simulations ended because of an undersaturated relative humidity with respect to ice within the contrail. In general, strong turbulence ( $\varepsilon = 10^{-4}$  m<sup>2</sup>s<sup>-3</sup>) causes a fast diffusion of the ice particles in the environment and a shorter life time.

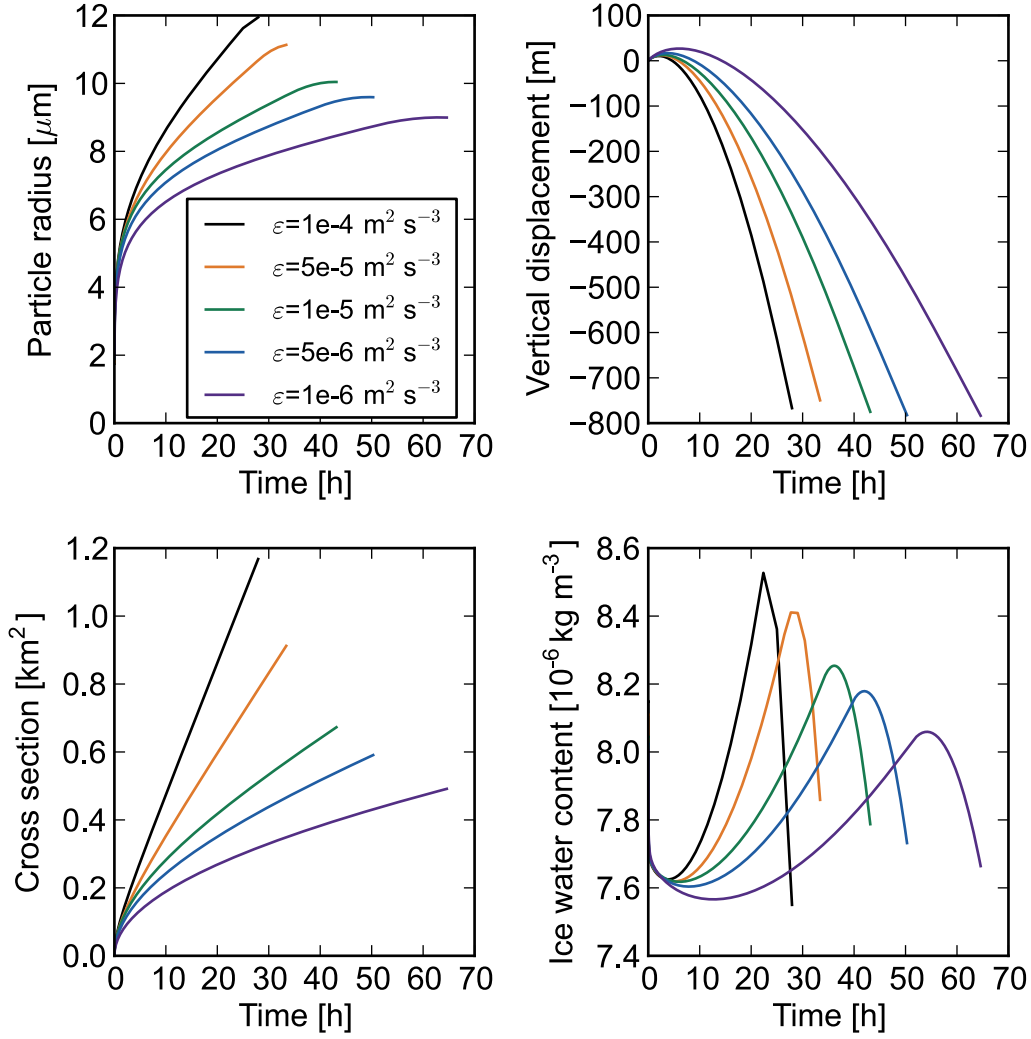


**Figure 4.2:** Development of particle radius, vertical displacement, contrail cross section and ice water content over the whole contrail life. Microphysical properties are calculated for five turbulence classes assuming no wind shear  $s = 0$ , no skewed diffusivity  $D_s = 0$ , a vertical wind drift  $v_z = 0.005 \text{ ms}^{-1}$ , the flight performance parameters depicted in Table 4.1, and the initial dimensions calculated in Section 4.1.2.

ice particles grow until the end, the faster the dilution of the contrail the faster the growth of the ice particles due to more available ice water. In the end, the contrail approaches the boundary of the ice saturated layer and particle growth abates. Strong turbulence enhances the particle growth and yields larger particles and larger contrail cross sections at the end of the contrails life cycle. Due to the fast growth of cross

section and particle, contrails in strong turbulence have a higher ice water content, although they leave the ice saturated layer faster than contrails in weak turbulence. The ice particle radii are in the same magnitude as estimated in measurements and simulations [33], [31], [32], [123], [119].

The calculated life time of the contrail is very long. Due to restrictions regarding neglected wind shear and sheared diffusivity, the contrail surface remains small and decelerates the diffusion of the contrail. However, the symmetrical cross section (resulting in a idealized contrail) is necessary for the radiative forcing model.

Figure 4.3 illustrates the development of the first ten hours of the contrail life cycle for  $\varepsilon = 5 \cdot 10^{-5} \text{ m}^2\text{s}^{-3}$ . A logarithmic time axis is chosen to visualize the fast growth in the first seconds due to large differences in concentration. After only 0.7 s the horizontal standard deviation  $\sigma_h$  exceeds the vertical standard deviation  $\sigma_v$  (not shown in Figure 4.3).

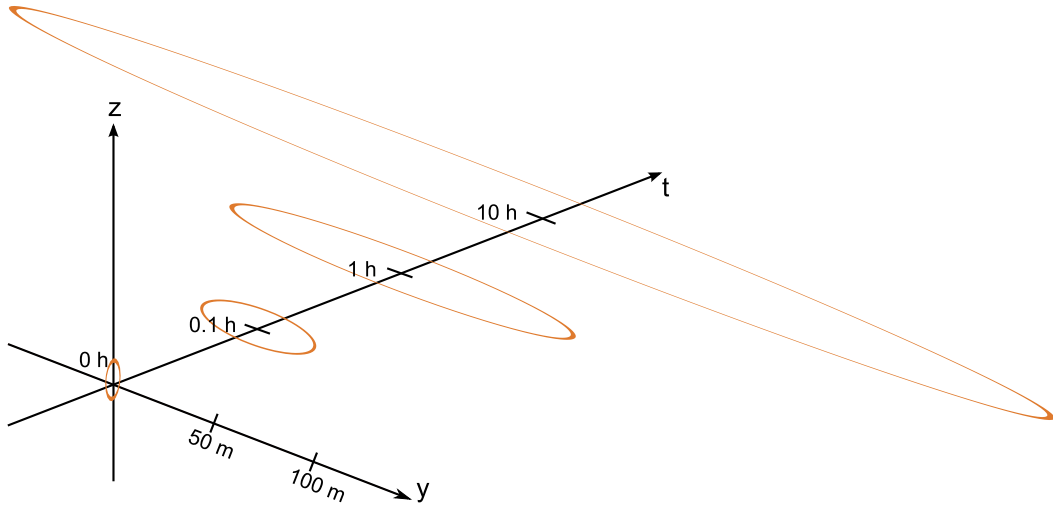


**Figure 4.3:** Development of the horizontal and vertical standard deviations  $\sigma_h$  and  $\sigma_v$  during the first ten hours of the contrail life cycle with mean turbulence  $\varepsilon = 5 \cdot 10^{-5} \text{ m}^2\text{s}^{-3}$ . The dimensions are estimated under the same conditions as described in Figure 4.2.

## 4.2 Radiative transport up to the contrail

After the estimation of both the contrail microphysical properties and the corresponding contrail optical properties depending on location within the contrail and lifetime, the contrail is "prepared" to extinguish radiation. However, the amount of solar radiance and terrestrial irradiances at the position of the contrail are still unknown. Due

to strong extinction by the atmosphere (even without an additional contrail), the spectral radiances and monochromatic irradiances have to be calculated using the DISORT solver and the Two Stream Approximation within the radiative transfer library libRadtran [57], respectively.

### 4.2.1 Solar direct and diffuse radiance

There are two different sources of solar radiation. First, direct solar radiation  $I_{\text{dir}}$ , transmitted through the atmosphere from solid angle  $\Omega$ , defined by solar zenith  $\theta$  and azimuthal angle  $\phi$  (compare Equation 2.11). And second, a small amount of diffuse solar radiation  $I_{\text{diff}}$  originating from  $\Omega$  and scattered by the atmosphere in every direction in space. In Figure 4.4 the direct solar radiation is not plotted, but indicated by arrows, because of the significant differences between diffuse and direct radiances, which otherwise would neglect small differences in diffuse radiation. Two different daytimes, 6 a.m. and 12 a.m., and the corresponding solar azimuthal angles for the respective daytime are plotted for all directions of  $\theta$  for the 21<sup>st</sup> of June 2012 above Berlin (Figure 4.4). Remember, the zenith angle  $\theta$  measures the angle of radiation from the vertical and the azimuthal angle  $\phi$  describes the angle counterclockwise from South on the horizon (compare Section 2.2.2). Calculations with the radiative transfer model libRadtran yield in solar angles  $\theta = 70^\circ$  and  $\phi = 257^\circ$  at 6 a.m. and  $\theta = 29.1^\circ$  and  $\phi = 2.12^\circ$  at 12 a.m..

Figure 4.16 allows an imagination of the diurnal variations of the solar angles for the 21<sup>st</sup> of June, 2012. The radiances in Figure 4.4 are calculated with libRadtran using the radiative transfer solver DISORT for a wavelength of  $\lambda = 0.55 \mu\text{m}$  with an angle discretization of  $\Delta_{\theta,\phi} = 2^\circ$  and the parameterization of absorption is satisfied using the correlated-k method LOWTRAN (compare Section 3.3.3).

Both graphs in Figure 4.4 show an important property of solar diffuse irradiances in raised position (an altitude of 10 km is chosen). The peak at  $\theta = 90^\circ$  is called horizontal brightening, caused by strong scattering from an endless extended atmosphere in the horizontal direction [90], [124]. This is a realistic appearance for a point in the atmosphere in raised position, where the atmosphere is more extended in the horizontal direction than in the vertical direction and can be observed by looking out of the window of a flying aircraft. At 6 a.m. the effect of horizontal brightening is increased by a large amount of solar direct radiation due to a large solar zenith angle  $\theta = 70^\circ$ . The amount of diffuse radiation from above the horizon is smaller than from beneath the horizon, due to a larger reflectance of the Earth's surface than of the atmosphere above an altitude of 10 km. Nevertheless, besides the horizontal brightening effect, at 12 a.m. the diffuse radiation is bigger than at 6 a.m., due to more available direct radiation.



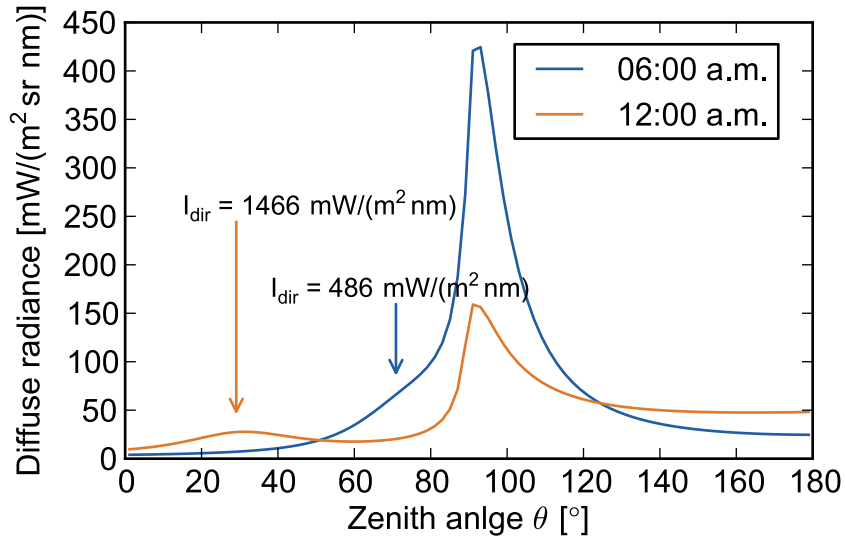


**Figure 4.4:** Direct (arrows) and diffuse radiance of solar radiation with  $\lambda = 0.55 \mu\text{m}$  for different zenith angles  $\theta$ , calculated with the radiative transfer model libRadtran for the 21<sup>st</sup> of June, 2012 in Berlin for 6 a.m. (blue) and 12 a.m. (orange).  $\theta = 0^\circ$  corresponds with radiance coming from above and diffuse radiance from beneath corresponds with  $\theta = 180^\circ$ . The azimuthal angles  $\phi$  are equal to the azimuthal angles of the sun at that time of the day ( $\phi = 257^\circ$  for 6 a.m. and  $\phi = 2.12^\circ$  for 12 a.m.).

#### 4.2.2 Terrestrial irradiance

In the terrestrial spectrum only diffuse irradiance is expected. Due to strong and narrow absorption bands, angular dependent radiances can not be calculated (compare section 3.3). The Two Stream Approximation is used for calculating azimuthally averaged (per hemisphere) irradiances  $F_{\text{up}}$  and  $F_{\text{down}}$ . In Figure 4.5 the Two Stream Approximation is applied to the whole thermal spectrum between  $3 \mu\text{m}$  and  $100 \mu\text{m}$ . Both irradiances,  $F_{\text{up}}$  and  $F_{\text{down}}$  are plotted for an altitude of 10 km in a cloud free atmosphere. The korrelated-k parameterization LOWTRAN is used for the absorption by atmospheric gases (compare Section 3.3.3) and an aerosol model by Shettle [125] is used for background aerosol concentration. Furthermore, the surface library of the International Geosphere Biosphere (IGBP) from the NASA CERES/SARB Surface Properties Project [86] is used for surface reflectivity. Because azimuthally averaged irradiances are calculated, the Two Stream Approximation does not distinguish between latitudes. Neither the day of year or the day time are considered. This uncertainty is tolerable, because the calculated extinction of radiation due to a contrail will be done at mid latitudes. Furthermore, in the mid latitudes the differences of the surface temperature  $T$

between summer and winter are not exceeding 20 K.

Both graphs in Figure 4.5 do not look like Planck's curve due to strong absorption by the atmosphere. The upward irradiances are larger than the downward irradiances, because the Earth's surface is warmer than the atmosphere. There is a strong absorption due to water vapor between  $3\ \mu\text{m}$  and  $8\ \mu\text{m}$ . The upward irradiance is reduced and the downward irradiance is enhanced in this wavelength indicating an emission of radiation which was absorbed by water vapor. Between  $8\ \mu\text{m}$  and  $12\ \mu\text{m}$  the atmospheric window is visible, because the atmosphere does not absorb radiation in this region. Except between  $9\ \mu\text{m}$  and  $10\ \mu\text{m}$ , where ozone absorbs and emits radiation. Hence, the downward radiation is zero in this wavelength spectrum and the diffuse upward irradiance reaches high values. Between  $12\ \mu\text{m}$  and  $18\ \mu\text{m}$  the diffuse downward irradiance is equal to the diffuse upward irradiance, because all radiation is absorbed by carbon dioxide and uniformly emitted in every direction in space.

For the calculation of the extinction of terrestrial radiation by a contrail only two directions of incoming photons have to be considered. This saves computational effort and the whole terrestrial spectrum can be considered.

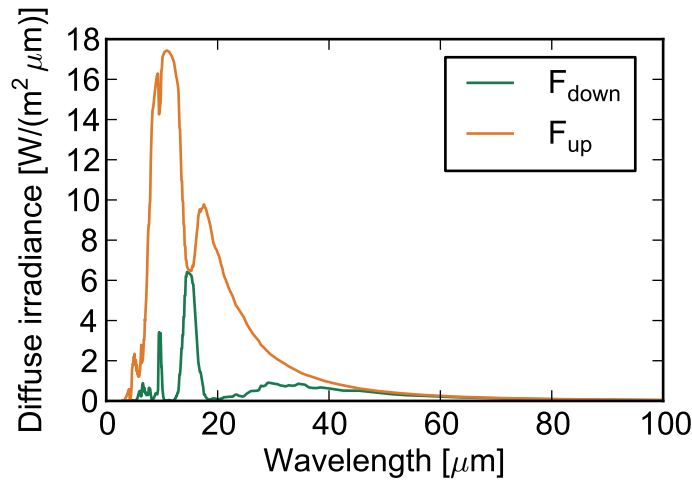


**Figure 4.5:** Irradiances of terrestrial radiation at 10 km altitude coming from the upper ( $F_{\text{down}}$ ) and lower ( $F_{\text{up}}$ ) hemisphere over the terrestrial wavelength spectrum between  $3\ \mu\text{m} \leq \lambda \leq 100\ \mu\text{m}$ .

### 4.3 Scattering and absorption properties of radiation within the contrail

Now, that the optical properties of the contrail and the radiative situation of the atmosphere are estimated, the actual extinction of radiation by the contrail is in focus. First of all, the number ratios of absorbed, forward scattered and backward scattered photons  $S_a$ ,  $S_f$  and  $S_b$  compared to the total number of photons is estimated. For convenience,  $S_i$  denotes all number ratios  $S_a$ ,  $S_f$  and  $S_b$  and will be used for the explanation of effects detectable on all number ratios. For solar extinction, photons are coming from all directions in space and are leaving the contrail in all directions. In the terrestrial spectrum photons are coming from two directions (above and below the contrail) and are leaving the contrail in all directions. Considering the radiative forcing of the contrail, the directions of leaving photons are summarized in two counters for the number of photons leaving the contrail in the upper and in the lower hemisphere. A third counter caches the number of absorbed photons.

#### 4.3.1 Monte Carlo simulation for solar radiation

In the following the angular dependence of photons traveling through a contrail, estimated with the Monte Carlo simulation described in Section 3.5, is shown and discussed. The simulations are done for a contrail after living 20 hours in a weakly turbulent environment of  $\varepsilon = 10^{-4} \text{ m}^2\text{s}^{-3}$  (compare Section 4.1.3). The properties of the contrail for a solar wavelength of  $\lambda = 0.55 \text{ }\mu\text{m}$ , used for the simulation are defined in Table 4.4.

**Table 4.4:** *Contrail properties for the angular dependence of traversing solar radiation.*

Eddy dissipation rate	$\varepsilon = 10^{-4} \text{ m}^2\text{s}^{-3}$
Number of photons	$N_{\text{eval.}} = 10^7$
Width for starting photons	$2w_{\text{in}} = 5094 \text{ m}$
Horizontal standard deviation	$\sigma_h = 1698 \text{ m}$
Vertical standard deviation	$\sigma_v = 74 \text{ m}$
Ice particle radius	$r_p = 10^{-5} \text{ m}$
Solar absorption efficiency	$Q_{a,0.55 \text{ }\mu\text{m}} = 0.009$
Solar scattering efficiency	$Q_{s,0.55 \text{ }\mu\text{m}} = 1.96$
Solar asymmetry parameter	$g_{\text{HG},0.55 \text{ }\mu\text{m}} = 0.74$

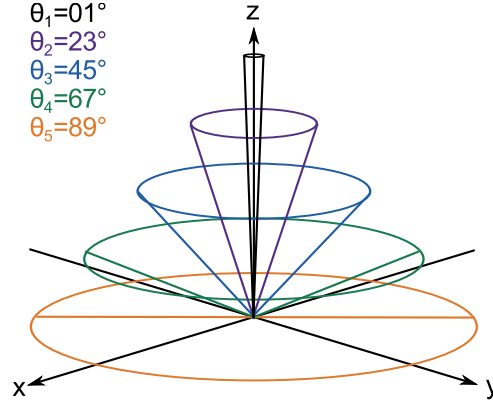


**Figure 4.6:** Geometry of starting photons for the demonstration of the angular dependence of photons traversing a contrail. The results are shown in Figures 4.9 and 4.10 for five uniformly distributed zenith angles  $\theta$  for all azimuthal angles  $\phi$ .

The flight path constitutes the x-axis and the azimuthal angle  $\phi$  is defined as deviation from the contrail axis. The zenith angle  $\theta$  describes the deviation from above, perpendicular to the contrail axis. The geometry is demonstrated in Figure 4.6. Figure 4.9 and Figure 4.10 show the number ratios of backscattered  $S_b$ , forward scattered  $S_f$  and absorbed  $S_a$  photons. Due to the symmetric cross section of the contrail, these quantities are equal for upward and downward incoming photons. These number ratios are weighted by the sine of the angle  $\alpha$  between incoming photons and contrail axis and by the width  $2w_{in}$  where photons are starting from uniformly distributed.

Three main effects can be defined for the interpretation of the results of the Monte Carlo simulation (Figures 4.9 and 4.10). First, all results are influenced by the assumed Gaussian distribution function. The number of extinguished photons depends on the irradiated width of the starting photons, compared to the irradiated width of the contrail in that direction. Because the width of the contrail  $\sigma_h$  is larger than the contrail height  $\sigma_v$ , the extinction will be larger for  $\theta = 1^\circ$  than for  $\theta = 89^\circ$ . This effect has its maximum influence for  $\phi = 89^\circ$  (compare Figure 4.8 top left and bottom right).

The second effect depends on the angle  $\alpha$  (compare Equation 3.92) between incoming photons and the contrail axis influencing the number ratios of extinguished photons  $S_b$ ,  $S_f$  and  $S_a$ . The angle  $\alpha$  constitutes the size of the surface area of the contrail, irradiated by photons. For  $\alpha = 0^\circ$  the photons are traveling along the axes of the contrail. The photons will irradiate the contrail around its cross section, and will have the longest way through the contrail until leaving the model boundaries. For  $\alpha = 90^\circ$  the photons are irradiating perpendicular to the contrail axis. Hence, the photons have the shortest way through the contrail (compare Figure 4.8). At the same time it has to be considered that the number ratios  $S_i$  are weighted by the sine of  $\alpha$ . That's why,  $S_i$  will be Zero if  $\alpha$

converges to Zero.  $\alpha$  converges to  $90^\circ$  (resulting in  $\sin \alpha = 1$ ) for all  $\theta$ , when  $\phi = 90^\circ$ . In contrast to  $\alpha$  converging to  $0^\circ$  (making  $\sin \alpha = 0$ ) for  $\theta = 90^\circ$  for  $\phi = 0^\circ$ .

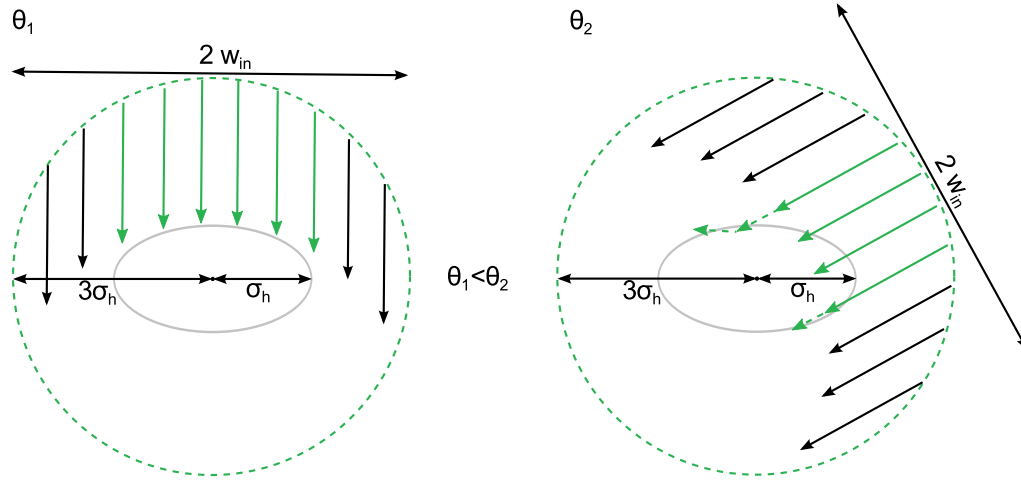


**Figure 4.7:** Influence of the solar zenith angle  $\theta$ . For  $\sigma_h > \sigma_v$ , the larger the angle  $\theta$  the smaller the number of photons, having contact with the contrail. Furthermore, for large angles  $\theta$  the possibility of photons getting scattered out of the contrail right after entering contrail, is high (indicated by dotted arrows).

The third impact on scattering events is caused by the axially symmetrically scattering phase function with dominating forward scattering (compare the Henyey-Greenstein phase function in Section 2.2.6). Hence, for large angles  $\theta$  forward scattering reduces the possibility of significant changes in direction of incident photons. And the axially symmetrical scattering phase function causes equal chances of upward and downward scattering, as also indicated by a dotted arrow in Figure 4.7.

Figure 4.9 shows the weighted number ratios of backward  $S_b$  (right) and forward  $S_f$  (left) scattered photons. Both graphs indicate the dominant forward scattering, especially for small angles  $\theta$ . The weak influence of azimuthal angle  $\phi$  on the extinction for small angles  $\theta$  is also caused by strong forward scattering. For large angles  $\theta$  and  $\phi$  converging to zero, the sine of  $\alpha$  converges to zero and so do the number ratios of scattered photons. With increasing  $\phi$  and large angles  $\theta$  the influence of the Gaussian distribution increases and the number ratios of extinguished photons increase as well.

Absorption is mainly influenced by the distance, the photons pass through the contrail (Figure 4.10). The influence of  $\alpha$  converging to Zero for small angles  $\theta$  is detectable. Discontinuities in the graphs occur due to a small number of absorbed photons, compared to the number of total photons, because of a small absorption efficiency  $Q_{a,0.55 \mu m} = 0.009$  in the shortwave spectrum.

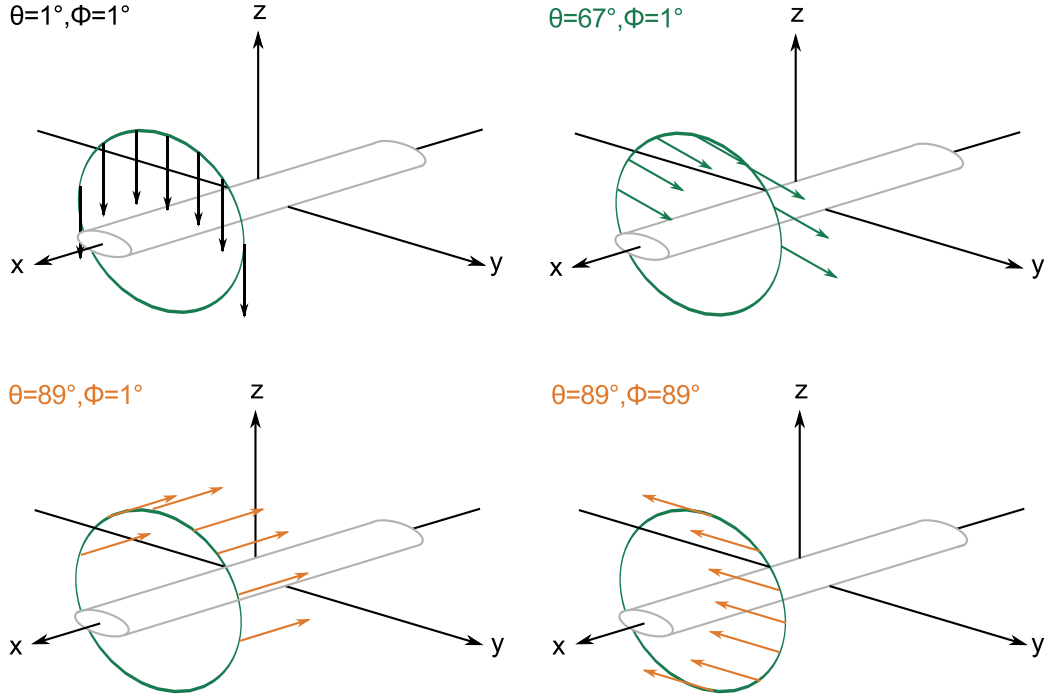


**Figure 4.8:** Demonstration of several directions of photons for different zenith angles  $\theta$  and azimuthal angles  $\phi$ .

### 4.3.2 Monte Carlo simulation for terrestrial irradiances

Due to restrictions in terrestrial radiative transfer simulations to a Two Stream Approximation, the extinction of terrestrial radiation is considered only for two directions of incoming photons. The contrail is irradiated directly from above or beneath resulting in  $\theta = \phi = 0^\circ$ . Figure 4.11 shows the geometry of the Monte Carlo simulation. The microphysical properties of the contrail used in the simulation are the same as for the three-dimensional simulation and can be taken from Table 4.5. Because of the associated reduction of computational effort, the extinction can be calculated for all wavelengths with significant contribution to the energy budget. The simulations are done for 18 wavelengths between  $4.7 \leq \lambda \leq 21.5 \mu\text{m}$ . The absorption and scattering efficiencies  $Q_a$  and  $Q_s$  and the asymmetry parameter  $g_{\text{HG}}$  can be taken from Figure 3.20 using  $Q_s = Q_e - Q_a$ .

Because the photons are coming from a single direction, the calculated number ratios are expected to be proportional to the scattering and absorption efficiencies  $Q_s$  and  $Q_a$  as demonstrated in Figure 3.20. The increased terrestrial absorption efficiency  $Q_{a,10.471 \mu\text{m}} \approx 0.24$  (compared to the solar absorption efficiency  $Q_{a,0.55 \mu\text{m}} \approx 0.009$ ) causes a significant number of absorbed photons (compare Figure 4.12). Due to the strong forward scattering phase function the amount of backward scattered photons is

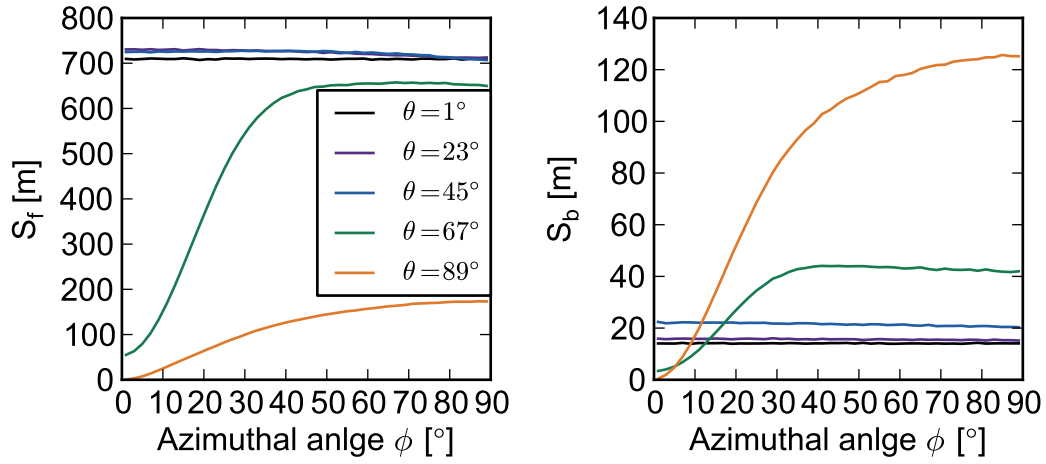


**Figure 4.9:** Number ratios of forward  $S_f$  (left) and backward  $S_b$  (right) scattered photons to the total number of photons ( $N_{\text{eval.}} = 10^7$ ), weighted by the sine of  $\alpha$  between incident photons and contrail axis and by the width  $2w_{\text{in}} = 6 \cdot \sigma_h$  were the photons are starting from. The angular dependent simulation is done for a solar wavelength  $\lambda = 0.55 \mu\text{m}$ .

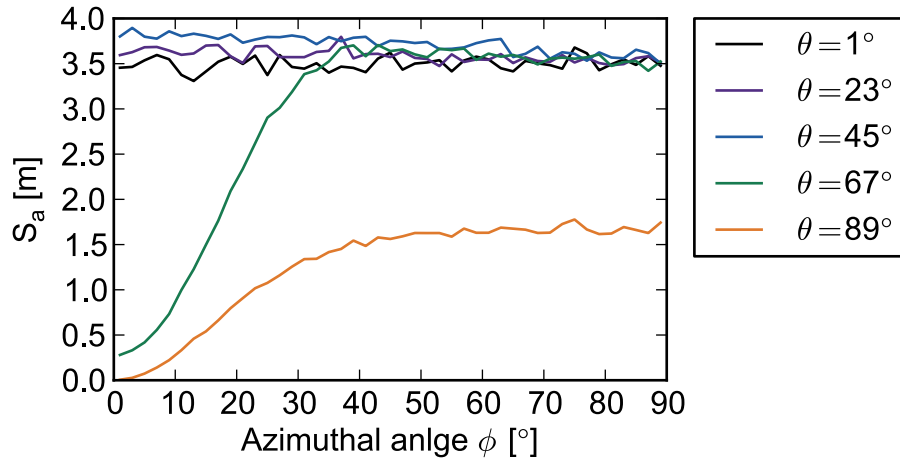


**Figure 4.10:** Number ratio of absorbed photons (originally coming from one hemisphere of the contrail) to the total number of photons ( $N_{\text{eval.}} = 10^7$ ), weighted by the sine of  $\alpha$  between incident photons and contrail axis and by the width  $2w_{\text{in}} = 6 \cdot \sigma_h$  were the photons are starting from. The angular dependent simulation is done for a solar wavelength  $\lambda = 0.55 \mu\text{m}$ .

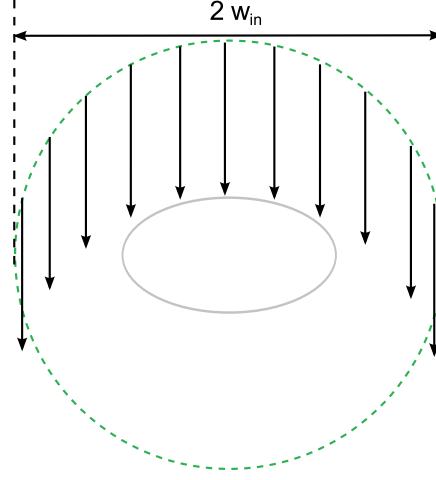


**Figure 4.11:** Geometry of the Monte Carlo simulation for the terrestrial spectrum. Due to hemispherically averaged irradiances, calculated by the Two Stream Approximation, photons are only coming from above (or beneath).

**Table 4.5:** Contrail properties for the Monte Carlo simulation of photons with terrestrial wavelengths.

Eddy dissipation rate	$\varepsilon = 10^{-4} \text{ m}^2\text{s}^{-3}$
Number of photons	$N_{\text{eval.}} = 10^7$
Width of starting photons	$2w_{\text{in}} = 5094 \text{ m}$
Horizontal standard deviation	$\sigma_h = 1698 \text{ m}$
Vertical standard deviation	$\sigma_v = 74 \text{ m}$
Ice particle radius	$r_p = 10^{-5} \text{ m}$

small, compared to the forward scattering and absorption events. Considering a single direction of incoming photons and a symmetrical cross section, the shape of the lines of  $S_f$  and  $S_b$  should be similar but different magnitudes are expected due to strong forward scattering. Differences in the shape occur because of an asymmetry parameter  $g_{\text{HG}}$  depending wavelength and due to the possibility (although very unlikely) of multiple scattering (compare Figure 4.14).

Summarizing the findings of scattering and absorption within the contrail, it should be noted, that the warming effect of the contrail is very likely, compared to the cooling effect, even in broad daylight. This finding can be taken from the strong forward scattering of solar wavelengths, which causes a small amount of backscattered photons (and therewith a small cooling effect) at noon, when solar zenith angle  $\theta$  is small (compare Figure 4.9). Hence, flying in the morning and in the afternoon (with  $\theta \approx 90^\circ$ )



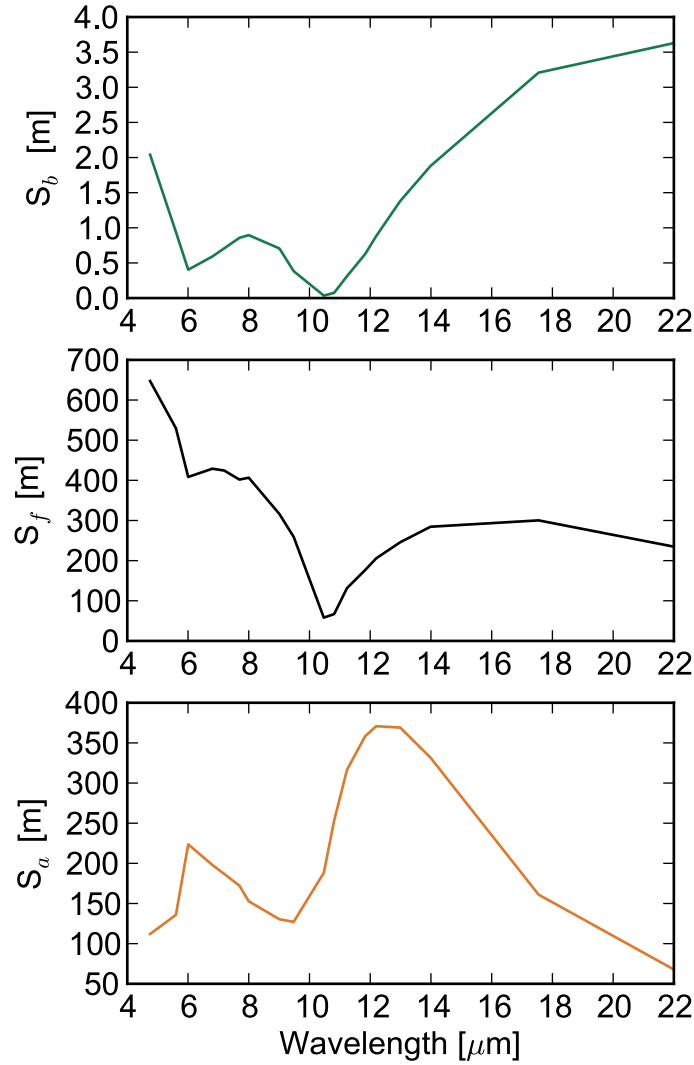


**Figure 4.12:** Number ratios of absorbed  $S_a$  (green, top), forward scattered  $S_f$  (black, middle), and backward scattered  $S_b$  (orange, bottom) photons to the total number of  $10^7$  photons, resulting from one-dimensional Monte Carlo simulations using the parameters listed in Table 4.5 and the efficiencies plotted in Figure 3.20.

and perpendicular to the sun (with  $\phi \approx 90^\circ$ ) would result in a maximum cooling effect, because the number of backscattered photons is maximum. Furthermore, large terrestrial absorption efficiencies  $Q_{a,10.471 \mu\text{m}} \approx 0.24$  (compared to the solar absorption efficiency  $Q_{a,0.55 \mu\text{m}} \approx 0.009$ ) causes a large number of absorbed terrestrial photons (and therewith a warming effect).

### 4.3.3 Relevance of multiple scattering

The possibility of multiple scattering within the contrail causes the requirement of a Monte Carlo simulation. In this section the relevance of multiple scattering on the extinction calculations will be discussed. In the solar wavelength spectrum, the average number of scattering events per scattered photon  $N_{\text{sca}}$  reaches a maximum value of 1.6 (Figure 4.13). This indicates a significant number of multiple scattering events and an enhanced probability of backscattered photons. For large solar angles of direct radiation inducing a long way through the core of the contrail, for example  $\theta = 89^\circ$  and  $\phi = 20^\circ$  (compare also Figure 4.8), a Monte Carlo simulation will be necessary. The shorter the way of direct solar radiation through the contrail the smaller the possibility of multiple scattering and the gain in computational effort by calculating the extinction of radiation directly (using Equation 3.71) must be weighted by the loss in accuracy of the extinction calculation. Nevertheless, the strong forward scattering of the scattering phase function, indicated by the asymmetry parameter  $g_{\text{HG}}$  for ice particles allows the assumption that a few scattering events per scattered photon will not change the result significantly. Figure 4.13 also shows the average number of scattering events in a weak turbulence environment with  $\varepsilon = 10^{-6} \text{ m}^2\text{s}^{-3}$  indicating a smaller contrail cross section and a larger number density of ice particles. Differences in  $N_{\text{sca}}$  for different turbulence classes are small as well, although differences in contrail microphysical properties are significant (compare Figure 4.2).

In the thermal wavelength spectrum the absorption efficiency  $Q_a$  is significantly larger than in the solar spectrum. Anyhow, due to a nearly constant extinction efficiency, the terrestrial scattering efficiency  $Q_s$  is smaller than in the solar spectrum. Hence, the possibility of multiple scattering is much smaller. The average number of scattering events per scattered photon is close to single scattering (Figure 4.14). A direct solution of Beers law combined with Gaussian plume model for the local ice water content (Equation 3.71) should be sufficient.

## 4.4 Radiative extinction

With the number ratios of extinguished photons to the total number of photons  $S_i$  being estimated, these quantities can be combined with the calculated atmospheric radiative transfer situation (compare Section 3.5.5). The outcome of this multiplication will be the influence of a unit length contrail on the energy budget of the Earth-atmosphere system depending on both the number ratios of extinguished photons  $S_i$  [m] and the solar radiances  $I_{\text{dir}}$  and  $I_{\text{diff}}$  [ $\text{mW sr}^{-1} \text{ m}^{-2} \text{ nm}^{-1}$ ] and the terrestrial irradiances  $F_{\text{up}}$  and  $F_{\text{down}}$  transported by the photons. Hence, the solar radiances  $I_{\text{dir}}$  and  $I_{\text{diff}}$  coming from a

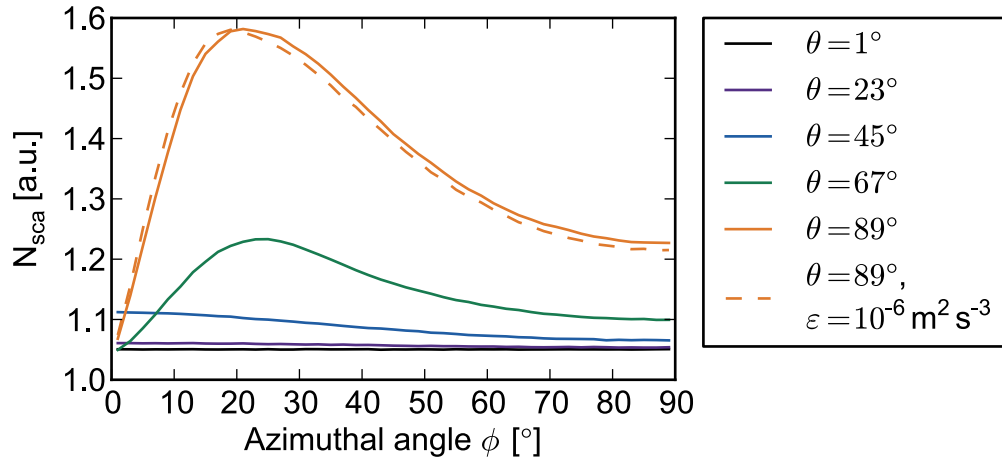


**Figure 4.13:** The average number of scattering events per scattered photon  $N_{\text{sca}}$  for several solar zenith angles  $\theta$  and for all azimuthal angles  $\phi$ . The angular dependent simulation is done for a solar wavelength  $\lambda = 0.55 \mu\text{m}$  and for contrail optical properties after a lifetime of 20 hours and in a strong turbulent environment with  $\varepsilon = 10^{-4} \text{ m}^2\text{s}^{-3}$  (solid lines). The dotted line indicates the number of scattering events for the contrail optical properties in a weak turbulent environment with  $\varepsilon = 10^{-6} \text{ m}^2\text{s}^{-3}$  after a lifetime of 20 hours.

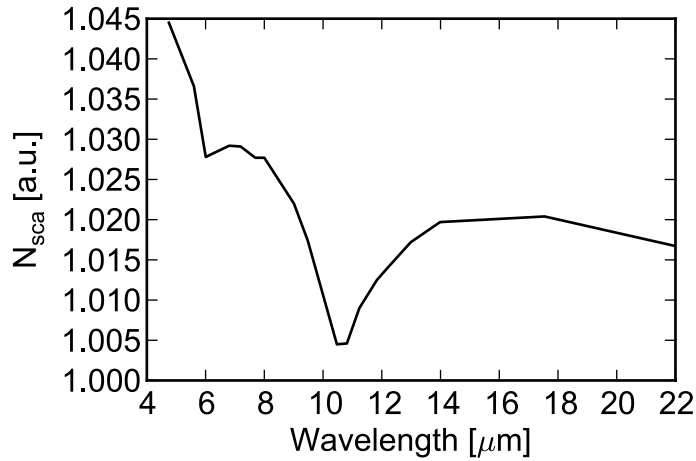


**Figure 4.14:** The average number of scattering events per scattered photon  $N_{\text{sca}}$  in the thermal wavelength spectrum and for contrail optical properties after a lifetime of 20 hours and in a strong turbulent environment with  $\varepsilon = 10^{-4} \text{ m}^2\text{s}^{-3}$ .

particular solid angle  $\Omega$  [sr] has to be weighted by the number ratios  $S_i$  of extinguished photons and by the solid angle  $\Omega$  (Equation 2.11). The radiances  $I_{\text{dir}}$  and  $I_{\text{diff}}$  depend on the location on the Earth's surface (latitude and longitude) and on the day of the year, as well as on the daytime (solar angles  $\theta$  and  $\phi$ ). The following calculations are done for Berlin, 21<sup>st</sup> June, 2012.

#### 4.4.1 Solar zenith and azimuthal angle

In a first step, the influence of the solar zenith angle  $\theta$  and azimuthal angle  $\phi$  on the contrail radiative forcing is estimated considering the diurnal variation of  $\theta$  and  $\phi$  for a whole day. Figure 4.16 qualitatively shows the variation of these angles for Berlin, 21<sup>st</sup> of June, 2012. With this estimation, not only the impact of the daytime, but also the influence of the heading of the flight path on the contrail radiative forcing can be quantified.

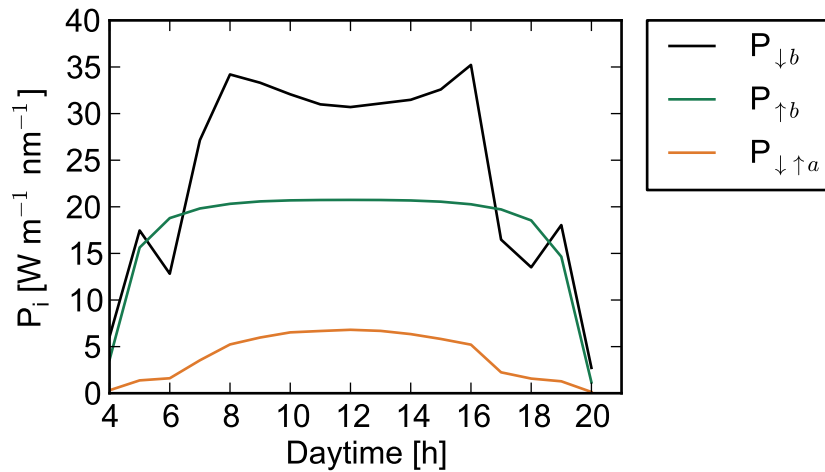


**Figure 4.15:** Backscattered power for diurnal variations of upward ( $P_{\uparrow b}$ ) and downward ( $P_{\downarrow b}$ ) solar radiation ( $\lambda = 0.55 \mu\text{m}$ ) and absorbed power of downward and upward radiation ( $P_{\downarrow \uparrow a}$ ) for constant contrail properties. The contrail constitutes the East-West axis.

In Figure 4.15 the relevant quantities of scattered and absorbed power of solar radiation ( $\lambda = 0.55 \mu\text{m}$ ) are plotted for a whole day (from sunrise at 4 a.m. to sunset at 8 p.m.) considering the diurnal variation of direction and strength of solar direct radiation and solar diffuse radiation. Because libRadtran can not handle solar zenith angles  $\theta > 90^\circ$ , the simulation runs between 4 a.m. and 8 p.m. where solar zenith angles  $\theta < 90^\circ$  are satisfied. Constant contrail properties are assumed avoiding a superposition of different

effects on the results. The contrail properties correspond to a contrail after 20 h of its life time in a strong turbulent environment with  $\varepsilon = 10^{-4} \text{ m}^2 \text{ s}^{-3}$ . The contrail parameters can be taken from Table 4.4. The flight path is along the East-West axis.

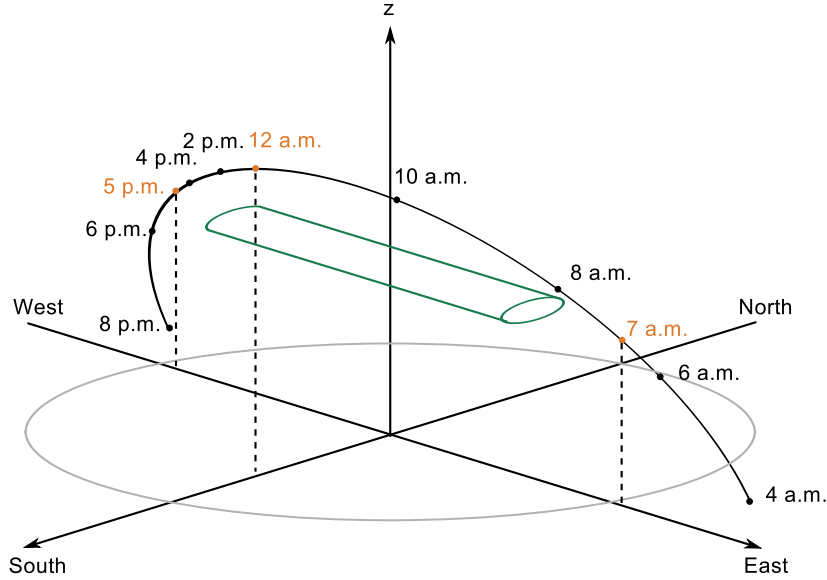


**Figure 4.16:** Qualitative diurnal variation of the direction of direct solar radiation for the longest day of the year, 21<sup>st</sup> of June, 2012 in Berlin and orientation of a contrail along East and West. At 7 a.m. the sun is located to the East and at 5 p.m. the sun has reached the western boundary. Solar zenith and azimuthal angles are calculated with libRadtran.

The absorbed power corresponds to the available radiation, particularly the direct radiation, which increases until 12 a.m.. Due to small solar absorption efficiency  $Q_{a,0.55\mu\text{m}}$ , small values of absorbed power  $P_{\downarrow a}$  are expected. The discontinuity in the absorbed line is caused by the direction of the available direct radiation and gives evidence for the ability of the model, handling horizontal photon transport. Because the contrail is orientated between East and West the main part of radiation is facing the contrail cross section at 7 a.m. and at 5 p.m. when the azimuthal angle  $\phi$  converges to  $\phi \rightarrow 270^\circ$  or  $\phi \rightarrow 90^\circ$  and the solar angle  $\theta$  is still large. This causes small angles of  $\alpha$  (and  $\sin \alpha \rightarrow 0$ ) between incoming photons and the contrail axis and reduces the number of extinguished photons (compare Section 4.3.1). In this case (at 6 a.m. and 6 p.m.), the extinguished quantities  $P_{\downarrow a}$ ,  $P_{\uparrow b}$ , and  $P_{\downarrow b}$  are not converging to Zero, because of the amount of diffuse solar radiances coming from all directions considered in the calculations.

The backscattered power of upward radiation  $P_{\uparrow b}$  is driven by the amount of diffuse radiation. The amount of direct radiation coming from  $\theta > 90^\circ$  up to the contrail is not accounted for, because of the mentioned limitations of the radiative transfer solver

DISORT. The backscattered power of downward radiation  $P_{\downarrow b}$  is strongly influenced by the direction of the available direct radiation and the orientation of the contrail between East and West. After 7 a.m. and before 5 p.m. the amount of direct radiation increases, causing a higher scattered power. At midday the solar zenith angle is minimal, photons are coming from above and the strong forward scattering phase function causes a weak reduction of backscattered photons. The sharp edges especially in the plotted  $P_{\downarrow b}$  are the result of both relatively large time steps of diurnal calculations (two hours), and under- and overestimations of the extinguished power at the boundaries of the chosen bins of solar angles  $\theta$  and  $\phi$  (compare Section 3.5.7).

Considering the question in mind, the radiative forcing of the contrail, a balance between the extinguished powers

$$RF_{0.55 \mu\text{m}} = P_{\downarrow a} + P_{\uparrow b} - P_{\downarrow b} \quad (4.3)$$

gives an idea of the efficiency of the contrail at  $\lambda = 0.55 \mu\text{m}$ . For constant contrail properties (with  $Q_{a,0.55 \mu\text{m}} = 0.009$  and  $Q_{s,0.55 \mu\text{m}} = 1.96$ ) and in a strong turbulent environment the cooling effect (negative  $RF_{0.55 \mu\text{m}}$ ) dominates, except during sunrise and sunset. However, a closer look to Figure 4.15 suggests the assumption of a nearly balanced solar radiative forcing on midday, due to maximum absorption at that time. Here, the terrestrial warming effect is not considered yet.

From Figure 4.15 follows, that flying a few hours after sunrise and a few hours before sunset, here about 8 a.m. and 4 p.m. the cooling effect of the contrail reaches its maximum. Solar direct radiation is coming from above the contrail, but small scattering angles cause a significant amount of upward scattered photons. Due to an azimuthally averaging Two Stream Approximation, the calculation of terrestrial irradiances is not influenced by the time of the day. Hence, the influence of solar angles  $\theta$  and  $\phi$  on the terrestrial spectrum is not evaluated.

#### 4.4.2 Flight path

In the last section, a characteristic of the model was observed, in the case of the Monte Carlo simulation for photons irradiating perpendicular to the contrail cross section (horizontal photon transport). Hence, the influence of the flight path seems significant. Figure 4.17 shows the same results of the Monte Carlo simulation done for the estimation of the influence of the solar angles of direct radiation under the same radiative conditions (Figure 4.15), but the orientation of the contrail is rotated by  $90^\circ$  and the contrail follows the North-South axis (compare Figure 4.18).

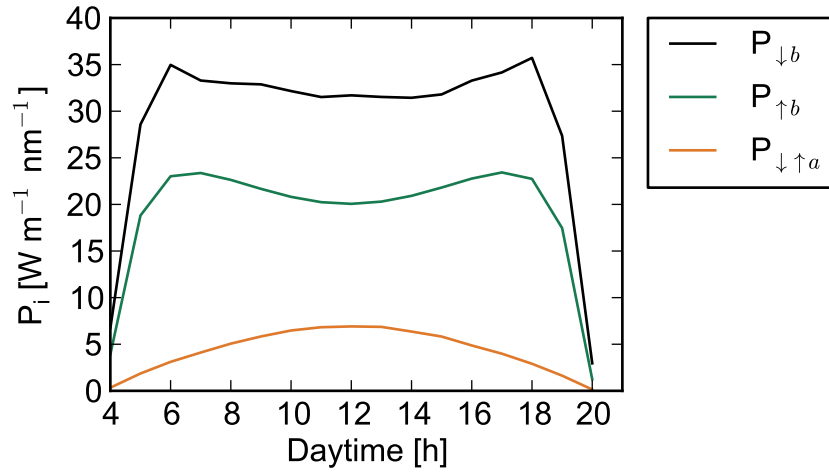


**Figure 4.17:** Backscattered power for diurnal variations of upward ( $P_{\uparrow b}$ ) and downward ( $P_{\downarrow b}$ ) solar radiation ( $\lambda = 0.55 \mu\text{m}$ ) and absorbed power of downward and upward radiation ( $P_{\downarrow\uparrow a}$ ) for constant contrail properties. The contrail constitutes the North-South axis.

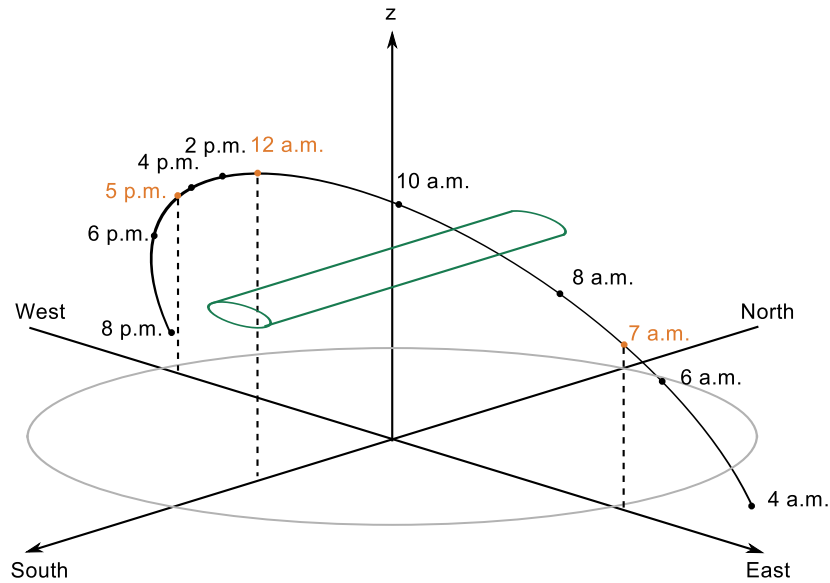


**Figure 4.18:** Qualitative diurnal variation of the direction of direct solar radiation for the longest day of the year, 21<sup>st</sup> June, 2012 in Berlin and orientation of a contrail along North and South. At 7 a.m. the sun is located to the East and at 5 p.m. the sun has reached the western boundary. Solar zenith and azimuthal angles are calculated with libRadtran.

Differences between both orientations allow the estimation of the uncertainty, done during small angles  $\alpha$  between incoming photons and the contrail. In the North-South situation the contrail cross section is irradiated at noon, when the solar zenith angle  $\theta$  is already small enough to avoid a perpendicular irradiation of the contrail cross section (compare Figure 4.18). Hence, the discontinuity observed in Figure 4.15 vanishes. The extinguished powers have the same magnitudes and the phenomena of  $\theta$  (strong forward scattering at midday) are visible. Furthermore, the influence of increasing direct solar radiation until midday (and decreasing  $I_{\text{dir}}$  after midday) is observable.

Because of equal contrail properties between both orientations, on average the solar radiative forcing at  $\lambda = 0.55 \mu\text{m}$  will be negative, with a minimum cooling rate at noon due to strong forward scattering and maximum absorption.

#### 4.4.3 Contrail evolution

The influence of the contrail age on the extinction will be discussed in the following. For this purpose, microphysical properties of every five hours of the contrail life cycle in a mean turbulent environment with  $\varepsilon = 5 \cdot 10^{-5} \text{ m}^2\text{s}^{-3}$  are calculated. The microphysical and solar optical properties for the Monte Carlo simulation of each stage are listed in Table 4.6. The calculated number ratios  $S_i$  are combined with a radiative transfer situation at  $\lambda = 0.55 \mu\text{m}$  in 10.471 km altitude on 21<sup>st</sup> of June, 2012 in Berlin, 12 a.m. (resulting in  $\theta = 29.1^\circ$  and  $\phi = 2.12^\circ$  and  $I_{\text{dir}} = 1460 \text{ mW m}^{-2} \text{ nm}^{-1}$ ). Date and time are chosen because the maximum energy input on the Earth is expected on the longest day of the year at noon.

#### Solar spectrum

The differences in the upward and downward backscattered power  $P_{\downarrow b}$  and  $P_{\uparrow b}$  between a young and an old contrail are significant. Changes up to 100% are possible. Apparently, the effect of growing ice particles during the existence of the contrail on the extinction dominates over the decreasing ice water content and the decreasing number density of ice particles (see Figure 4.19 and compare to Figure 4.2). Due to a small solar zenith angle  $\theta$  at noon, the strong forward scattering phase functions causes a large amount of downward forward scattered photons.

The absorbed power  $P_{\downarrow \uparrow a}$  depends on the method of the estimation of the absorption efficiency  $Q_{a,0.55\mu\text{m}}$  for a single particle radius  $r_p$ . The parameterizations by Wyser et al. [55] used in this thesis are influenced by the oscillations originating from the Mie theory, used for the estimation of the efficiencies, amongst others. These oscillations



**Table 4.6:** Contrail optical properties for  $\lambda = 0.55 \mu\text{m}$  and  $\lambda = 10.471 \mu\text{m}$  of different ages of lifetime. The calculations are done for a mean turbulent environment with  $\varepsilon = 5 \cdot 10^{-5} \text{ m}^2\text{s}^{-3}$ .

Age [h]	5	10	15	20	25	32
$r_p [\mu\text{m}]$	6.8	7.9	8.8	9.6	10.3	11
$\sigma_h [\text{m}]$	778.5	1078.7	1330.3	1529.9	1718.9	1976.7
$\sigma_v [\text{m}]$	44.9	50.2	55.4	59.8	64.3	70.7
$w_{\text{in}} [\text{m}]$	2335.5	3236.1	3990.9	4589.7	5156.7	5930.1
$g_{\text{HG},0.55\mu\text{m}} [\text{a.u.}]$	0.72	0.72	0.73	0.73	0.74	0.74
$Q_{a,0.55\mu\text{m}} [\text{a.u.}]$	0.000	0.029	0.000	0.024	0.003	0.000
$Q_{s,0.55\mu\text{m}} [\text{a.u.}]$	2.03	1.95	2.07	1.96	1.96	2.04
$g_{\text{HG},10.471\mu\text{m}} [\text{a.u.}]$	0.83	0.84	0.85	0.86	0.86	0.87
$Q_{a,10.471\mu\text{m}} [\text{a.u.}]$	0.21	0.22	0.23	0.24	0.25	0.25
$Q_{s,10.471\mu\text{m}} [\text{a.u.}]$	0.13	0.16	0.19	0.20	0.22	0.24

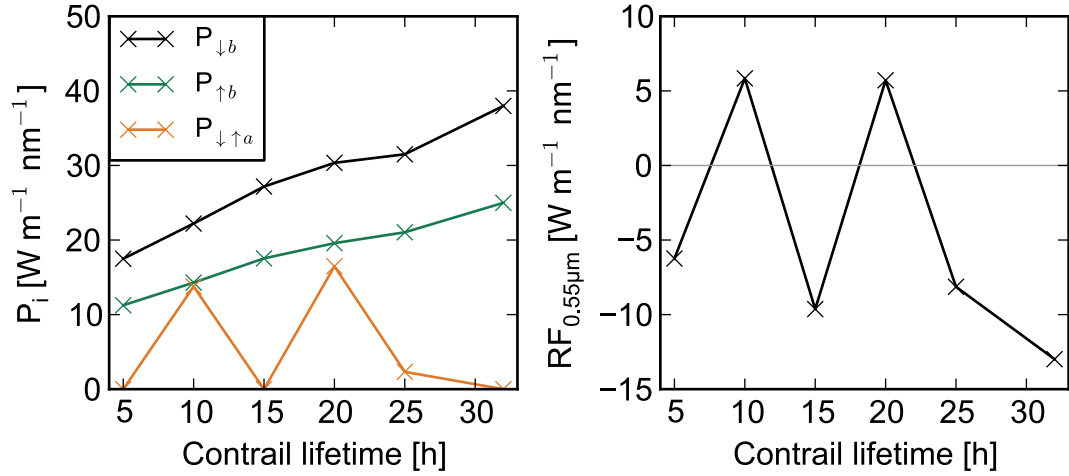


**Figure 4.19:** Left: backscattered power of upward  $P_{\uparrow b}$  and downward  $P_{\downarrow b}$  solar radiation and absorbed power  $P_{\downarrow\uparrow a}$  of solar radiation by a contrail over its whole life time. Right: change of solar radiative forcing  $RF_{0.55\mu\text{m}}$  (compare Equation 4.3) dominated by the differences in absorption efficiency  $Q_{a,0.55\mu\text{m}}$ . The simulations are done for  $\lambda = 0.55 \mu\text{m}$  and for a contrail life cycle in a medium turbulent environment with  $\varepsilon = 5 \cdot 10^{-5} \text{ m}^2\text{s}^{-3}$ . The optical properties of the Monte Carlo simulation are listed in Table 4.6.

could be avoided by averaging the absorption efficiencies of several particle radii using a particle size distribution. It is noteworthy that even small absorption efficiencies can cause a significant value of absorbed power, when direct radiation is coming from above, perpendicular to the contrail axis (compare Figures 4.9 and 4.10).

Remembering the aim of the thesis as calculating the influence of the contrail on the global energy budget, Figure 4.19 shows that the solar radiative forcing can be positive (resulting in heating effects) even on a summers day at midday. The cooling effect of backscattered power  $P_{\downarrow b}$  can be compensated by the sum of absorbed power  $P_{\downarrow a}$  and downward backscattered power  $P_{\uparrow b}$ , which is heating the system (compare Equation 4.3). Even an averaged absorption efficiency  $Q_{a,0.55\mu\text{m}}$  would result in a balanced energy budget. However, the results can not be generalized here, because of a monochromatic calculation of the extinction at a single wavelength  $\lambda = 0.55\mu\text{m}$ . An integration over the whole solar spectrum could result in different conclusions. A consideration of more solar wavelengths for calculations of the whole contrail life cycle exceeds the computational possibilities. Due to the oscillating character of solar absorption efficiency  $Q_{a,0.55\mu\text{m}}$  depending on ice particle radius  $r_p$ , the effect of growing ice particles and reduced number density of ice particles with an ever-aging contrail on the solar contrail radiative forcing, can not be generalized.

### Terrestrial spectrum

The influence of microphysical properties of the contrail on the extinction of terrestrial radiation is estimated for  $\lambda = 10.471\mu\text{m}$  for the exact same contrail and the same atmospheric conditions as the estimations have been done for the solar wavelength spectrum. The efficiencies  $Q_{a,10.471\mu\text{m}}$  and  $Q_{s,10.471\mu\text{m}}$  as well as the asymmetry parameters are listed in Table 4.6. The contrail dimensions  $\sigma_h$  and  $\sigma_v$  and the particle radii  $r_p$  are the same as in Table 4.6.

In the terrestrial wavelength spectrum absorption is expected to dominate the extinction, because of the larger values of absorption efficiency and coexistent small values of extinction efficiency (compare Table 4.6 and Figure 3.20). Absorption exceeds backscattered downward radiation by four orders and backscattered upward radiation even by seven orders of magnitude (note the units of the y-axis in Figure 4.20). Hence, the terrestrial radiative forcing equals the absorption in a first approximation. The different microphysical properties cause changes in extinguished powers  $P_i$  up to 400 %. While  $P_{\downarrow a}$  is increasing almost linearly due to an almost linearly increasing  $Q_{a,10.471\mu\text{m}}$  with increasing particle radius (compare 3.20),  $P_{\downarrow b}$  and  $P_{\uparrow b}$  have a discontinuity between 15 and 20 hours, which is caused by the non linear increasing scattering efficiency with increasing particle radius.

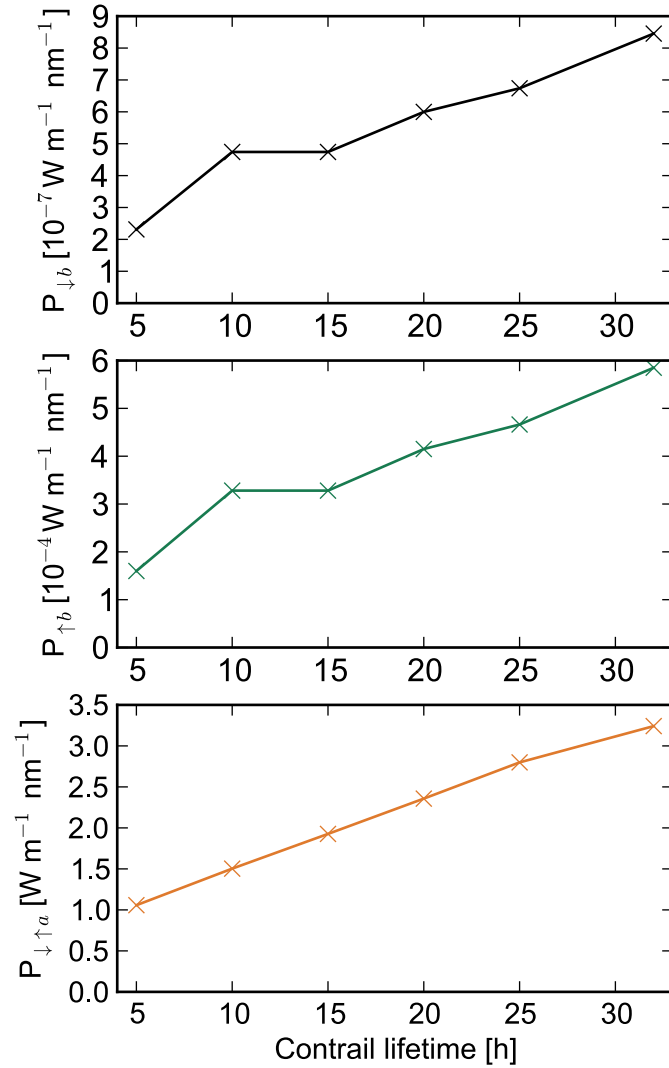


**Figure 4.20:** Backscattered power of upward  $P_{\uparrow b}$  and downward  $P_{\downarrow b}$  terrestrial monochromatic irradiances and absorbed power  $P_{\downarrow \uparrow a}$  of terrestrial radiation by a contrail over its whole life time. The simulations are done for  $\lambda = 10.471 \mu\text{m}$  and for a contrail life cycle in a medium turbulent environment with  $\epsilon = 5 \cdot 10^{-5} \text{ m}^2 \text{ s}^{-3}$ . The optical properties of the Monte Carlo simulation are listed in Table 4.6.

In comparison with solar extinction at the chosen wavelengths, terrestrial extinction is considerably smaller due to markedly smaller extinction efficiencies  $Q_{e,10.471 \mu\text{m}}$  and due to the significant smaller energy input. The terrestrial contribution to the radiative forcing of the contrail will always be heating.

However, the terrestrial heating effects increases with increasing particle radius and increasing contrail age, although the number density of particles decreases with contrail age. From this follows, that decreasing the number of soot particles during flight, maybe by using a more efficient jet engine with reduced fuel flow, would not result in a contrail with reduced impact on climate change, because the few ice particles would be larger (most of the ice water of the ice particles originates from the ambient humidity, not from the water emission in the aircraft exhaust) and would cause an increased terrestrial heating effect. Unfortunately, the soot production within the jet engine and the estimation of the soot properties (soot particle diameter, soot particle density, and soot particle absorption efficiency) is highly complex and still in investigation. Hence, the circumstances of the formation of soot particles with minimum impact on climate change are not fully understood [126], [32], [127], [128].

Due to the acceptable computational effort of the Monte Carlo simulations in the terrestrial wavelength spectrum, the extinction of the whole life cycle has been calculated for the whole terrestrial spectrum. In favor of comparability, the influence of changing contrail properties on the extinction has been first discussed for a monochromic irradiance of  $\lambda = 10.471 \mu\text{m}$ . The consideration of the whole terrestrial spectrum and the whole contrail life cycle will be discussed later in Section 4.5.

#### 4.4.4 Turbulence

Due to missing information about turbulence, the contrail life cycle is calculated for several classes of turbulence within a realistic range represented by the eddy dissipation rate  $\varepsilon$ . The calculations of the contrail life cycle (Section 4.1.3) show larger values of contrail cross section, particle radius and ice water content for strong turbulent environments due to a faster diffusion of the contrail into the ambient atmosphere. Anyhow, the number density of ice particles is constant. The influence of these differences on the extinguished powers  $P_i$  are discussed in the following.

#### Solar spectrum

The influence of turbulence on the solar radiative forcing of a contrail is calculated for all turbulent classes, defined by eddy dissipation rates between  $\varepsilon = 10^{-4} \text{ m}^2\text{s}^{-3}$  and  $\varepsilon = 10^{-6} \text{ m}^2\text{s}^{-3}$  from strong to weak turbulence. A contrail age of 20 hours is chosen, because of maximum differences at this age. For the solar wavelength spectrum ( $\lambda = 0.55 \mu\text{m}$ ) three-dimensional Monte Carlo simulations are done for all turbulence classes. Again, the calculated number ratios are combined with a radiative transfer situation at  $\lambda = 0.55 \mu\text{m}$  in 10.5 km altitude on 21<sup>st</sup> of June, 2012 in Berlin, 12 a.m.

(resulting in  $\theta = 29.1^\circ$  and  $\phi = 2.12^\circ$  and  $I_{\text{dir}} = 1460 \text{ mW m}^{-2} \text{ nm}^{-1}$ ). The parameters, as well as the results can be taken from Table 4.7.

**Table 4.7:** Contrail optical properties in different turbulent environments, after 20 hours. The simulations are done all defined turbulence classes (compare Table 3.2) with eddy dissipation rates between  $\varepsilon = 10^{-4} \text{ m}^2\text{s}^{-3}$  and  $\varepsilon = 10^{-6} \text{ m}^2\text{s}^{-3}$  from strong to weak turbulence. Wavelengths of  $\lambda = 0.55 \mu\text{m}$  and  $\lambda = 10.471 \mu\text{m}$  are chosen for the Monte Carlo simulation and the radiative transfer calculation.

$\varepsilon [\text{m}^2\text{s}^{-3}]$	$10^{-6}$	$5 \cdot 10^{-6}$	$10^{-5}$	$5 \cdot 10^{-5}$	$10^{-4}$
$r_p [\mu\text{m}]$	7.0	8.0	8.5	9.6	10
$\sigma_h [\text{m}]$	848	1123	1342	1530	1698
$\sigma_v [\text{m}]$	49.3	49.6	50	59	74
$w_{\text{in}} [\text{m}]$	2544	3369	4026	4589	5094
$g_{\text{HG},0.55\mu\text{m}} [\text{a.u.}]$	0.72	0.73	0.73	0.73	0.74
$Q_{a,0.55\mu\text{m}} [\text{a.u.}]$	0.000	0.000	0.030	0.024	0.009
$Q_{s,0.55\mu\text{m}} [\text{a.u.}]$	1.98	1.97	1.99	1.96	1.96
$g_{\text{HG},10.471\mu\text{m}} [\text{a.u.}]$	0.83	0.84	0.85	0.86	0.87
$Q_{a,10.471\mu\text{m}} [\text{a.u.}]$	0.21	0.22	0.23	0.24	0.25
$Q_{s,10.471\mu\text{m}} [\text{a.u.}]$	0.14	0.16	0.17	0.20	0.23

Mainly influenced by the particle radius  $r_p$  the differences in the extinguished powers  $P_i$  differ significantly between different turbulence classes. Differences between weak and strong turbulence in scattered powers  $P_{\downarrow b}$  and  $P_{\uparrow b}$  up to 100% are possible (see Figure 4.21). Anyhow, the contrail life time also depends on turbulence. In weak turbulence the contrail lives longer but with less impact on the energy budget per unit time. The differences in absorption are not only forced by turbulence but by the estimation of the absorption efficiency  $Q_a$  for a single particle radius.

### Terrestrial spectrum

The influence of turbulence on the terrestrial wavelength spectrum is calculated with the help of a one-dimensional Monte Carlo simulation with efficiencies listed below (Table 4.7) for a terrestrial wavelength of  $\lambda = 10.471 \mu\text{m}$ .

The number ratios of extinguished photons  $S_i$ , calculated with the Monte Carlo simulation, have been multiplied with the irradiances at  $\lambda = 10.471 \mu\text{m}$  for the estimation

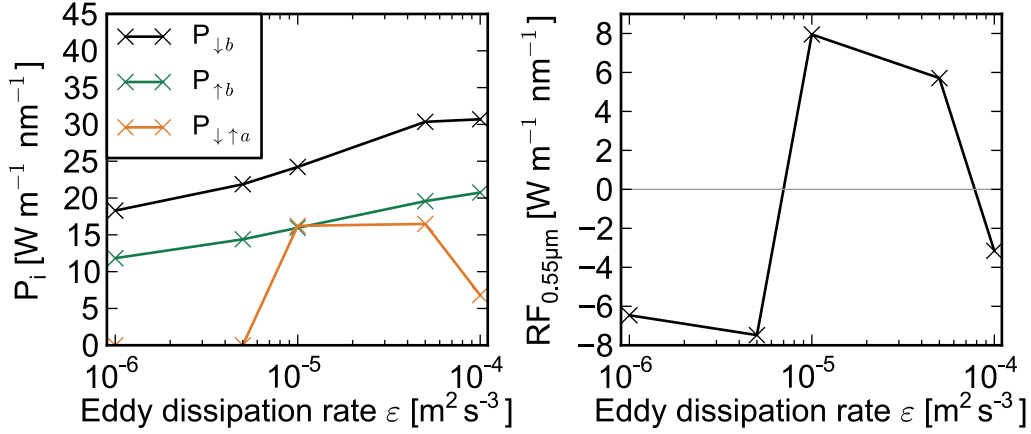


**Figure 4.21:** Left: Backscattered power of upward  $P_{\uparrow b}$  and  $P_{\downarrow b}$  solar radiation and absorbed power  $P_{\downarrow\uparrow a}$  of solar radiation by contrails in different turbulent environments defined by eddy dissipation rates between  $\epsilon = 10^{-4}$  m<sup>2</sup>s<sup>-3</sup> and  $\epsilon = 10^{-6}$  m<sup>2</sup>s<sup>-3</sup> from strong to weak turbulence. The simulations are done for  $\lambda = 0.55$   $\mu$ m and for a contrail age of 20 hours. The optical properties of the Monte Carlo simulation are listed in Table 4.7. Right: change of solar radiative forcing  $RF_{0.55\mu m}$  (compare Equation 4.3) mainly due to differences in absorption efficiency  $Q_{a,0.55\mu m}$ .

of the extinguished powers listed in Table 4.7 and plotted in Figure 4.22. The calculated irradiances at  $\lambda = 10.471$   $\mu$ m are  $F_{up} = 1.73 \cdot 10^{-2}$  Wm<sup>-2</sup>nm<sup>-1</sup> and  $F_{down} = 1.98 \cdot 10^{-5}$  Wm<sup>-2</sup>nm<sup>-1</sup>.

As mentioned in Section 4.1.3, the lower and the upper boundaries of the chosen turbulence classes show some extreme values in the contrail microphysical properties (for example  $r_p$ ), as well as in the extinguished powers  $P_i$ . In general the fast mixing driven by strong turbulence causes large contrail cross sections and ice particle radii resulting in increased extinguished powers. As expected from the extinction efficiencies  $Q_a$  and  $Q_s$  most of the spectral irradiances are extinguished by absorption.

Due to larger upward irradiances than downward irradiances ( $F_{up} > F_{down}$ ) the amounts of backscattered upward irradiances  $P_{\uparrow b}$  exceed the amounts of backscattered downward irradiances  $P_{\downarrow b}$ .

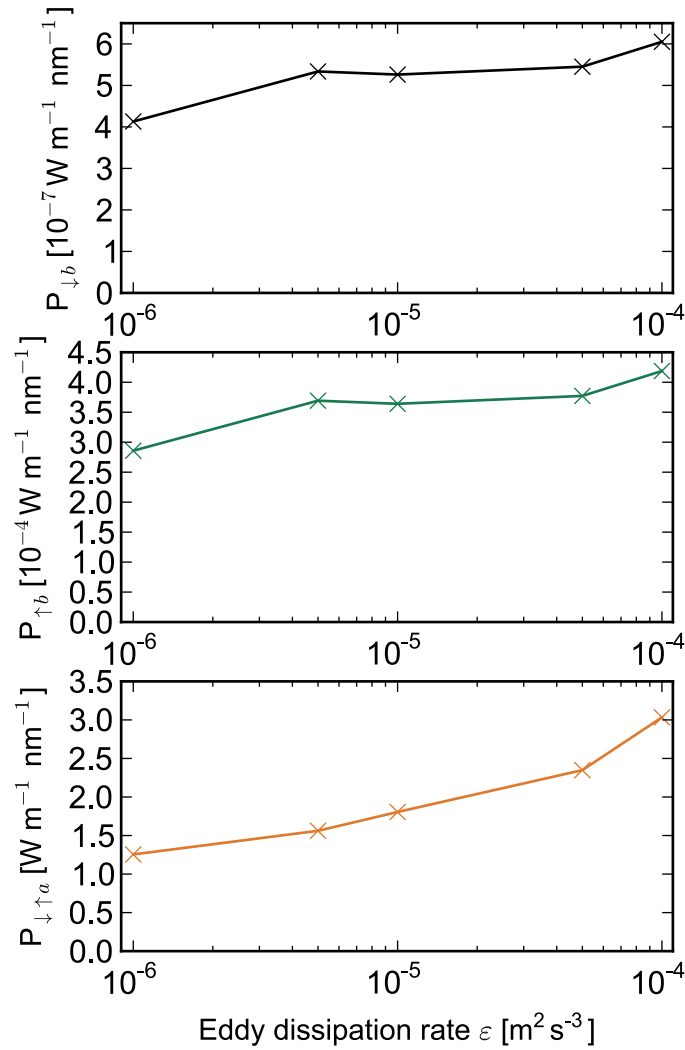


**Figure 4.22:** Backscattered powers of upward  $P_{\uparrow b}$  and downward  $P_{\downarrow b}$  terrestrial irradiances and absorbed power  $P_{\downarrow \uparrow a}$  of terrestrial irradiances by contrails in different turbulent environments defined by eddy dissipation rates between  $\epsilon = 10^{-6} \text{ m}^2 \text{s}^{-3}$  and  $\epsilon = 10^{-4} \text{ m}^2 \text{s}^{-3}$  between weak and strong turbulence, respectively. The simulations are done for  $\lambda = 10.471 \text{ } \mu\text{m}$  and for a contrail age of 20 hours. The optical properties of the Monte Carlo simulation are listed in Table 4.7.

#### 4.4.5 Wavelength specific extinction

Calculations of the optical properties have been done for spectral radiances in the solar wavelength region ( $\lambda = 0.55 \text{ } \mu\text{m}$ ) and for a comparability of spectral irradiances in the

terrestrial wavelength spectrum ( $\lambda = 10.47 \mu\text{m}$ ) so far. In the following, the influence of different wavelengths within each spectrum on the extinguished power will be discussed and conclusions for the calculation of the change of the energy budget will be drawn.

### Solar spectrum

The simulations are done for a mean turbulent environment with  $\varepsilon = 5 \cdot 10^{-5} \text{ m}^2\text{s}^{-3}$  after a contrail lifetime of 20 hours. The microphysical properties of the contrail can be taken from Table 4.7. The calculated number ratios  $S_i$  are combined with a radiative transfer situation of the corresponding wavelengths in 10.5 km altitude on 21<sup>st</sup> of June, 2012 in Berlin, 12 a.m. (resulting in  $\theta = 29.1^\circ$  and  $\phi = 2.12^\circ$ ). The contributions of direct radiation  $I_{\text{dir}}$  and the wavelength dependent efficiencies can be taken from Table 4.8.

Only for these solar wavelength specific calculations, the scattering and absorption efficiencies are calculated according to Key et al. [129] using parameterizations from Yang, because of a high spectral resolution. The parameterizations from Yang yield extinction efficiencies for 21 bands between wavelengths of  $\lambda = 275 \text{ nm}$  and  $\lambda = 2250 \text{ nm}$ .

Although the amount of direct radiances significantly decreases with increasing wavelength (compare Table 4.8) the absorbed power  $P_a$  increases with increasing wavelength (compare Figure 4.23). Hence, even in the solar wavelength spectrum, a heating effect is considerable (see Figure 4.24). However, the extinguished powers with wavelengths larger than  $\lambda > 650 \text{ nm}$  have already have a minor impact on the energy budget (note the logarithmic scale in Figure 4.23). The absorbed power  $P_a$  at  $\lambda > 750 \text{ nm}$  is three orders of magnitude smaller than at  $\lambda > 650 \text{ nm}$ .

Considering both solar diffuse irradiances and solar direct radiances coming from all directions in space, and integrating the wavelength specific radiative forcing [ $\text{W m}^{-1} \text{ nm}^{-1}$ ] shown in Figure 4.24 over the whole solar spectrum, a solar radiative forcing of  $RF = 932.15 \text{ W m}^{-1}$  per meter contrail is calculated. Although the estimation of the real contrail width is impossible (compare Section 3.4.2), the result is divided by the assumed width of the contrail core, which is  $2\sigma_h = 3059.8 \text{ m}$  yielding a solar radiative forcing of  $RF = 0.305 \text{ W m}^{-2}$ . A negative  $RF$  only occurs until  $\lambda < 1050 \text{ nm}$  (compare Figure 4.24). Respecting the whole solar spectrum with relevant contributions of solar radiances results in a positive  $RF$ . For wavelengths  $\lambda > 750 \text{ nm}$ , diffuse upward radiances exceed diffuse downward radiances, probably because atmospheric absorption and reemission is already taking place. The increased absorption for these wavelengths in Figure 4.23 gives evidence for this green house effect. Hence, the amount of downward scattered and absorbed radiation exceeds upward scattered ra-



**Table 4.8:** Contrail optical properties in a mean turbulent environment with an eddy dissipation rate of  $\varepsilon = 5 \cdot 10^{-5} \text{ m}^2\text{s}^{-3}$ , after 20 hours. Additionally, the wavelength specific direct contribution of solar radiances  $I_{\text{dir}}$  is listed in the second column.  $I_{\text{dir}}$  is calculated at 10.5 km altitude on 21<sup>st</sup> of June, 2012 in Berlin, 12 a.m. ( $\theta = 29.1^\circ$ ,  $\phi = 2.12^\circ$ ). The data are used for the wavelength specific simulation of the radiative forcing of a contrail in Section 4.4.5.

Wavelength $\lambda$ [nm]	Direct radiance $I_{\text{dir}}$ [mW m <sup>-2</sup> sr <sup>-2</sup> nm <sup>-2</sup> ]	Asymmetry parameter $g_{\text{HG}}$ [a.u.]	Absorption efficiency $Q_a$ [a.u.]	Scattering efficiency $Q_s$ [a.u.]
275	0	0.761	$3.236 \cdot 10^{-6}$	2.012
350	788.6	0.771	$1.490 \cdot 10^{-6}$	2.019
425	1300	0.772	$9.260 \cdot 10^{-7}$	2.003
475	1700	0.760	$5.942 \cdot 10^{-7}$	1.988
550	1466	0.762	$9.264 \cdot 10^{-7}$	1.997
650	1204	0.756	$3.167 \cdot 10^{-6}$	2.061
750	1047	0.741	$1.188 \cdot 10^{-5}$	1.938
850	742.1	0.738	$3.455 \cdot 10^{-5}$	2.024
950	673.8	0.734	$1.065 \cdot 10^{-4}$	2.000
1050	2.510	0.733	$2.550 \cdot 10^{-4}$	2.029
1150	1.362	0.731	$3.528 \cdot 10^{-4}$	2.034
1250	1.088	0.731	$1.236 \cdot 10^{-3}$	2.044
1350	0.558	0.731	$1.395 \cdot 10^{-3}$	2.001
1450	0.388	0.733	$2.142 \cdot 10^{-2}$	1.991
1575	0.278	0.733	$2.956 \cdot 10^{-2}$	1.967
1720	0.169	0.732	$1.300 \cdot 10^{-2}$	2.003
1850	0.076	0.734	$1.131 \cdot 10^{-2}$	2.015
1925	0.063	0.743	$4.669 \cdot 10^{-2}$	1.950
1975	0.057	0.752	$8.900 \cdot 10^{-2}$	1.912
2050	0.042	0.751	$7.576 \cdot 10^{-2}$	1.899
2150	0.024	0.744	$2.615 \cdot 10^{-2}$	1.971

diances and warm the atmosphere for wavelengths  $\lambda > 950$  nm.

The general white color of a contrail gives evidence of constant scattering properties ( $Q_s = \text{const.}$ ) within the whole visible spectrum between  $\lambda = 0.38 \mu\text{m}$  and  $\lambda = 0.78 \mu\text{m}$ . Hence, considering the contrail optical properties at  $\lambda = 0.55 \mu\text{m}$  and integrating these properties over a range of wavelengths with significant contribution to solar radiation (at least over the visible spectrum) would be sufficient. However, the spectral bandwidth considered in the energy budget has a significant influence on the results. The estimation of the considered bandwidth requires spectral radiative transfer calculations for a wide range of narrow spectral bands (in the order of  $\Delta\lambda = 0.005 \mu\text{m}$ ). The computational costs of these calculations are considered as too high.

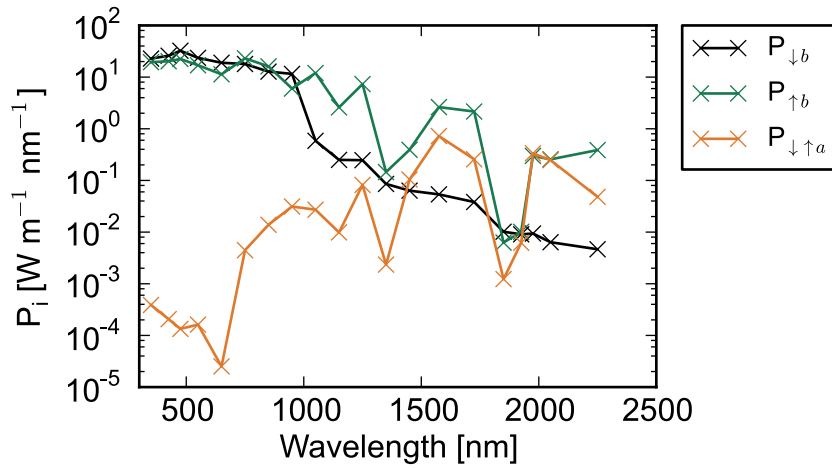


**Figure 4.23:** Backscattered power of upward  $P_{\uparrow b}$  and  $P_{\downarrow b}$  solar radiances and absorbed power  $P_{\downarrow \uparrow}$  of solar radiances. The simulations are done for the whole solar spectrum with significant contribution to the energy budget with wavelengths between  $\lambda = 275$  nm and  $\lambda = 2200$  nm for a contrail age of 20 hours in a medium turbulent environment with  $\varepsilon = 5 \cdot 10^{-5} \text{ m}^2\text{s}^{-3}$ . The optical properties of the Monte Carlo simulation are listed in Table 4.8.

### Terrestrial spectrum

As pointed out in Sections 4.2.2 and 4.3.2, terrestrial radiative transfer calculations and Monte Carlo simulations have been done for the whole terrestrial spectrum. The calculation of terrestrial extinction for contrail properties at 20 hours in a mean turbulence with  $\varepsilon = 5 \cdot 10^{-5} \text{ m}^2\text{s}^{-3}$  at 10.5 km altitude on 21<sup>st</sup> of June, 2012 in Berlin, 12 a.m. are plotted in Figure 4.25.

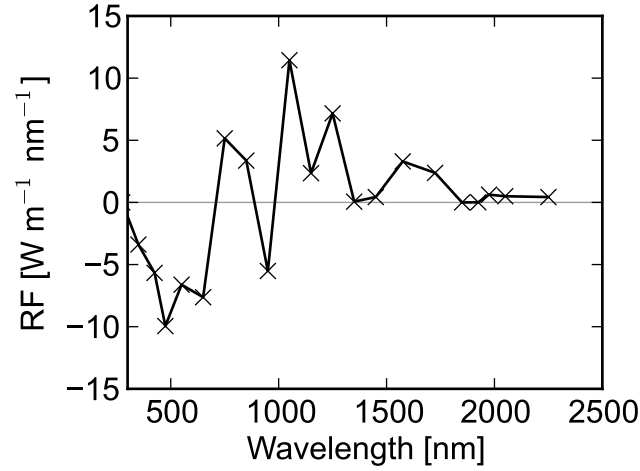


**Figure 4.24:** Solar radiative forcing. The simulations are done for the whole solar spectrum with significant contribution to the energy budget with wavelengths between  $0.55 \mu\text{m} \leq \lambda \leq 4.5 \mu\text{m}$  for a contrail age of 20 hours in a medium turbulent environment with  $\varepsilon = 5 \cdot 10^{-5} \text{ m}^2\text{s}^{-3}$ . The optical properties of the Monte Carlo simulation are listed in Table 4.8.

Differences between Figure 4.25 and the number ratios of extinguished photons for the whole spectrum in Figure 4.12 occur due to wavelength dependent irradiances (compare Figure 4.5) of terrestrial radiation, already extinguished by the atmosphere and calculated by the Two Stream Approximation. Most of the extinction is done by absorption due to large absorption efficiencies  $Q_a$  especially at  $\lambda = 12 \mu\text{m}$ , where the terrestrial irradiances  $F_{\text{up}}$  and  $F_{\text{down}}$  almost reach their maximum values. The local minimum in the scattering efficiency at  $\lambda = 11 \mu\text{m}$  (compare Figure 3.20) is apparent in both the results of the Monte Carlo simulation (Figure 4.12) and the scattered powers  $P_{\uparrow b}$  and  $P_{\downarrow b}$  per unit length contrail (Figure 4.25).

In contrast to the solar wavelength spectrum a consideration of a monochromatic terrestrial extinction efficiency is insufficient for the calculation of the radiative forcing, because of a significant wavelength dependent extinction in the thermal spectrum.

## 4.5 Terrestrial energy forcing of a contrail

In the following, the terrestrial energy forcing of a unit length contrail during its whole lifetime considering the whole terrestrial wavelength spectrum is estimated. As pointed out in Chapter 4 the radiative forcing in the solar wavelength spectrum strongly depends

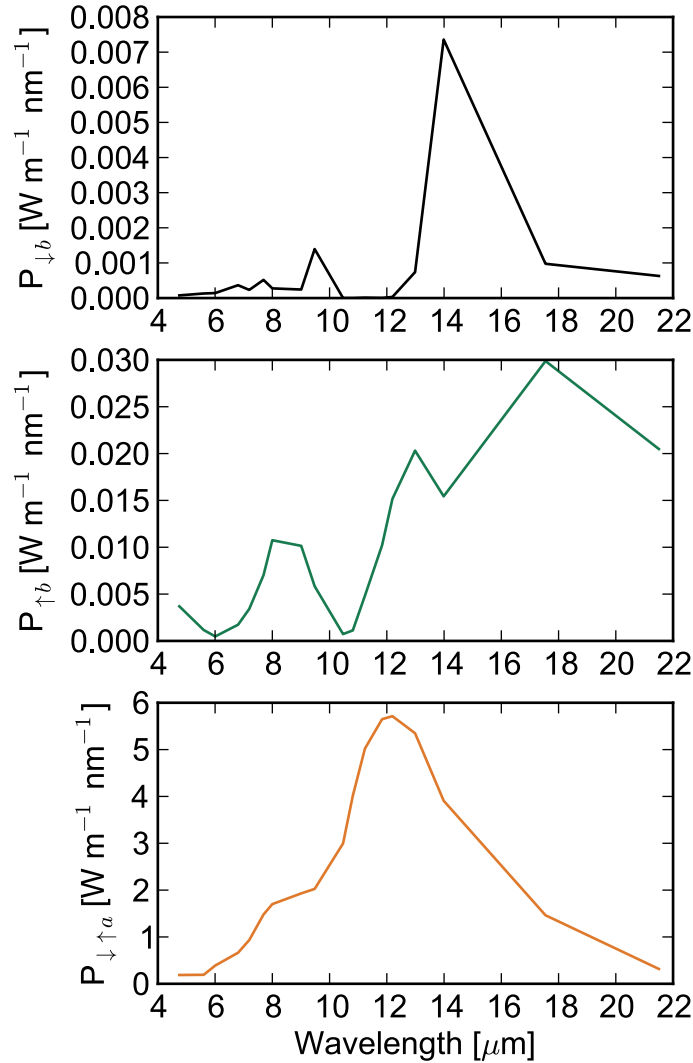


**Figure 4.25:** Backscattered power of upward  $P_{\uparrow b}$  and downward  $P_{\downarrow b}$  terrestrial radiation and absorbed power  $P_{\downarrow \uparrow a}$  of terrestrial radiation. The simulations are done for the whole terrestrial spectrum with significant contribution to the energy budget with wavelengths between  $4.7 \mu\text{m} \leq \lambda \leq 21.5 \mu\text{m}$  for a contrail age of 20 hours in a medium turbulent environment with  $\varepsilon = 5 \cdot 10^{-5} \text{ m}^2 \text{s}^{-3}$ .

on the time of the day, defined by solar zenith and azimuthal angle  $\theta$  and  $\phi$ , respectively. Furthermore, the integration over a solar wavelength spectrum has not been done yet. Hence, the cooling effect, eventually caused by the solar radiative forcing will not be considered. Due to restrictions of the Two Stream Approximation a diurnal variation

of the terrestrial irradiances can not be calculated. Even a seasonal variation is impossible. The errors done by this assumption are acceptable due to relative small differences in surface temperature between night and day and even between summer and winter, compared to approximatively 300 K mean Earth surface temperature. Hence, the terrestrial radiative forcing calculated with the model developed in this theses is constant over daytime and day of year. In Section 4.4.5 (Figure 4.25) the extinguished powers of all contributing terrestrial wavelengths were calculated for one time step (after 20 hours of lifetime). These calculations are repeated for the whole contrail life cycle and integrated over the terrestrial spectrum for each time step.

The heating effect increases nearly linearly with age (Figure 4.26). That's why an integration of the calculated powers over life time is possible. During its whole life time, the contrail absorbs  $E_{\downarrow a} = 4.32 \cdot 10^9 \text{ J m}^{-1}$ . An energy of  $E_{\downarrow b} = 4.60 \cdot 10^6 \text{ J m}^{-1}$  of down coming terrestrial radiation is scattered back to the atmosphere and  $E_{\uparrow b} = 2.75 \cdot 10^7 \text{ J m}^{-1}$  of upcoming terrestrial irradiance is scattered back to the Earth's surface resulting in a terrestrial Energy Forcing  $EF$  of

$$EF = E_{\downarrow a} + E_{\uparrow b} - E_{\downarrow b} = 4.34 \cdot 10^9 \text{ J m}^{-1}. \quad (4.4)$$

This result seems very high. Compared to a mean terrestrial irradiance of  $350 \text{ J s}^{-1} \text{ m}^{-2}$  (note, irradiances are quantified as energy per second and square meter, compare Section 2.2.8), a mean irradiated area per meter contrail of  $\approx 10^4 \text{ m}^2$  and a contrail lifetime of  $1.15 \cdot 10^5$  seconds, the amount of extinguished energy is realistic.

Finally, the terrestrial energy forcing  $EF$  of contrails formed in different turbulent environments is calculated. Considering differences in microphysical properties of these contrails (Figure 4.2) several findings have been made. On the one hand, contrails live longer in weak turbulent environment. On the other hand, estimations in Section 4.4.4 pointed out that extinction of radiation is increased for contrails in high turbulence (for a particular time step of the contrail life cycle simulation). This effect is driven by the enhanced particle radius, contrail cross section, and ice water content. Figure 4.27 shows, that Energy forcing decreases with increasing turbulence. Hence, the effect of increased contrail lifetime outweighs the effect of the particle size.

## 4.6 Verification

To verify the radiative forcing model, a comparison with the results of other publications is done, whenever it is possible. Mostly, the optical thickness  $\tau$  (compare Equations 3.57 and 3.88) is used for the description of optical contrail properties, measured

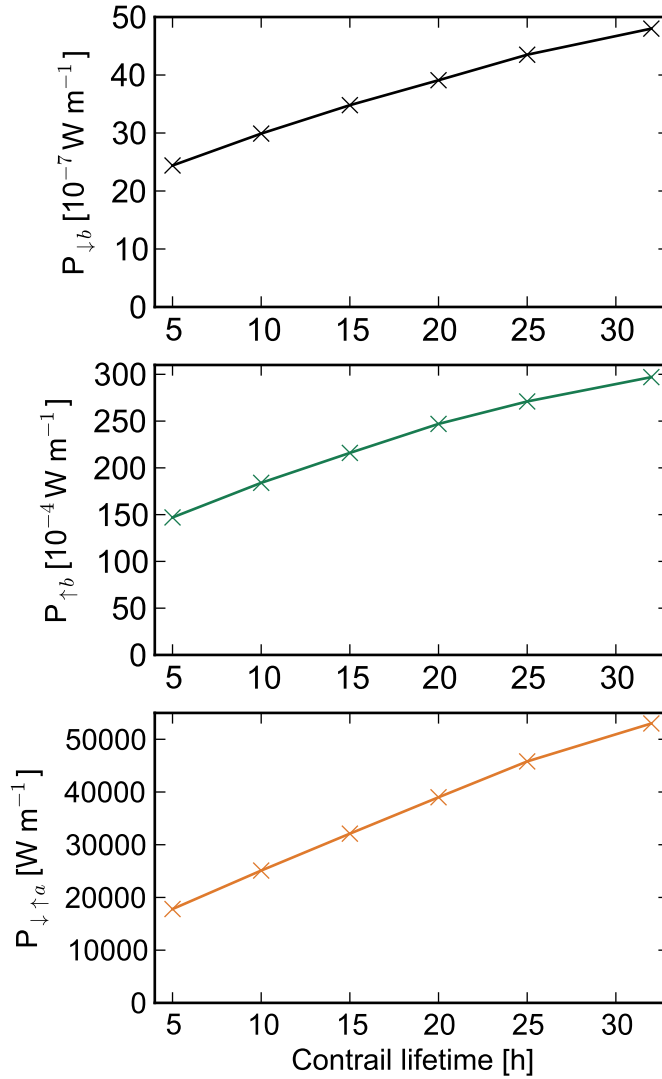


**Figure 4.26:** Change of backscattered power of upward  $P_{\uparrow b}$  and downward  $P_{\downarrow b}$  terrestrial radiation and absorbed power  $P_{\downarrow \uparrow a}$  of terrestrial radiation over the lifecycle of a contrail in a mean turbulent environment with  $\varepsilon = 5 \cdot 10^{-5} \text{ m}^2 \text{s}^{-3}$ . The values of extinguished powers  $P_i$  are integrated over the terrestrial spectrum with significant contribution to the energy budget with wavelengths between  $4.7 \mu\text{m} \leq \lambda \leq 21.5 \mu\text{m}$ .

vertically through the atmosphere. In the present case of treating the contrail by a Gaussian plume without defined boundaries, the optical thickness strongly depends on the contrail irradiated width  $2w_{\text{in}}$ . The larger the irradiated width, the smaller the optical thickness, because the share of photons traveling through the contrail core is reduced.

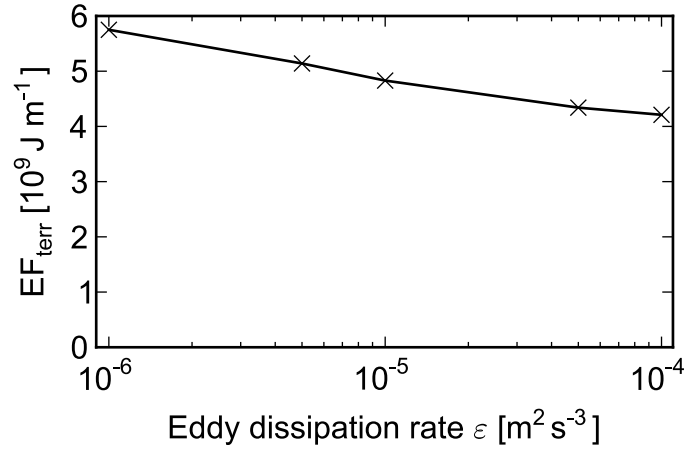


**Figure 4.27:** Energy Forcing  $EF$  [ $\text{J m}^{-1}$ ] of terrestrial radiation integrated over the whole life cycle of contrails in different turbulent atmospheres indicated by eddy dissipation rates  $1 \cdot 10^{-6} \text{ m}^2 \text{s}^{-3} \leq \epsilon \leq 1 \cdot 10^{-4} \text{ m}^2 \text{s}^{-3}$  and integrated over the terrestrial spectrum (with significant contribution to the energy budget with wavelengths between  $4.7 \mu\text{m} \leq \lambda \leq 21.5 \mu\text{m}$ ).

This phenomenon is illustrated in Figure 4.28, where the optical thickness is shown for a contrail with the same optical and microphysical properties as used in Figure 3.22 for vertical photon transport.

However, a few authors [49], [48] and [37] considering single contrails published the corresponding contrail width to the optical thickness. This width can be interpreted as the irradiated width  $2w_{\text{in}}$  used in the present radiative forcing model. Hence, the weighted number ratios of extinguished to evaluated photons  $S_{\text{ext}}$ , which is the sum of  $S_{\downarrow a}$ ,  $S_{\downarrow b}$  and  $S_{\downarrow f}$  (compare Figure 3.22) weighted with the irradiated width can be used for comparison with other publications. In Table 4.9, values of the weighted number ratios  $S_{\text{ext}}$  of a nonsheared contrail in a midlatitude summer atmosphere for several contrail ages derived by Forster et al. [49] are compared with the present weighted number ratios  $S_{\text{ext}}$  at  $\lambda = 0.55 \mu\text{m}$  for the lifetime estimations (compare Figure 4.19 and Table 4.6). Although a different standard atmosphere is used and more ice water content and a longer lifetime are expected in the midlatitude winter atmosphere used in the present study and despite the fact, that Forster et al. integrated the radiative extinction over the whole solar and terrestrial spectrum, the results of the weighted number ratios are in the same order of magnitude.

The influence of the solar zenith angle on radiative extinction can be compared with Gounou et al. [48] as well as with Forster et al. [49]. Here, individual contrails are

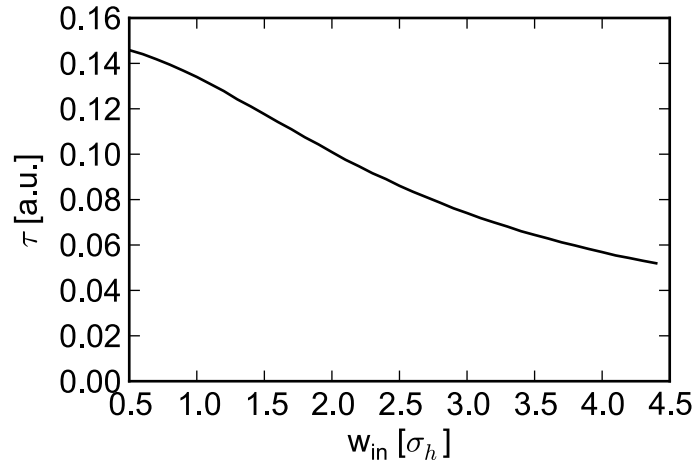


**Figure 4.28:** Optical thickness  $\tau$  for a contrail with the same optical and microphysical properties as used in Figure 3.22 for vertical photon transport.  $\tau$  decreases with increasing irradiated length  $2w_{\text{in}}$  without converging to a constant value. In Figure 3.22 the optical thickness is weighted by the irradiated width resulting in the well discussed quantity  $S$  [m] which converges to a constant value at  $w_{\text{in}} = 3\sigma_h$ .

observed. The results, however, are published as radiative forcing  $RF$  [ $\text{W m}^{-2}$ ] for a dense blanket of contrails and of course, integrated over the whole spectrum. Nevertheless, the shape of the extinction depending on solar zenith angle should be similar to the results observed in the present study treating the individual contrail as a Gaussian plume and considering a single wavelength  $\lambda = 0.55 \mu\text{m}$ . Figure 4.29 shows the typical minimum of radiative forcing at solar zenith angles around  $\theta \approx 70^\circ$  as observed by Gounou et al. [48] and Forster et al. [49].

Vázquez-Navarro et al. [37] tracked contrails over their whole lifetime by using the Automatic Contrail Tracking Algorithm (ACTA) for one year and averaged the optical and microphysical contrail properties. Finally, the time integrated terrestrial and solar energy forcing  $EF$  [ $\text{J m}^{-1}$ ] for this averaged contrail with a mean lifetime of 70 min is comparable with the terrestrial energy forcing calculated in Section 4.5 shown in Figure 4.27. Vázquez-Navarro et al. [37] published a terrestrial energy forcing at day-time of  $EF = 0.267 \text{ GJ m}^{-1}$  (Table 2). The terrestrial energy forcing calculated in Section 4.5 includes values between  $EF = 4.2 \text{ GJ m}^{-1}$  for a lifetime of 29 hours and  $EF = 5.7 \text{ GJ m}^{-1}$  for a 65 hours long living contrail (for lifetime, compare Figure 4.2). Transferring the mean energy forcing of Vázquez-Navarro et al. [37] to a 29 hours long living contrail, the energy forcing would correspond to  $EF = 6.6 \text{ GJ m}^{-1}$ , which is in the range of the values calculated here. The huge differences in lifetime and in en-



**Table 4.9:** Comparison of weighted number ratios  $S_{\text{ext}}$  for  $\lambda = 0.55 \mu\text{m}$  of different ages of lifetime with Forster et al. [49]. The calculations are done for a mean turbulent environment with  $\varepsilon = 5 \cdot 10^{-5} \text{ m}^2\text{s}^{-3}$ .

Study	Age [s]	Contrail width / horizontal standard deviation [m]	$S_{\text{ext}}$ [m]
Forster et al. [49]	1000	960	223.6
	2000	1680	403.2
	3500	2880	720.0
	6500	4320	1036.8
	11000	6000	1020.0
	18000	6480	528.4
present study	18645	778.5	342.5
	35798	1078.5	453.0
	54448	1330.3	585.3
	72011	1539.9	677.5
	90902	1718.9	739.1
	120224	1976.7	889.5

ergy forcing occur due to the assumption of a nonsheared contrail cross section in the present study. Due to wind shear, the horizontal growth of the contrail increases significantly, reducing the contrail lifetime (as shown in Section 3.4.2, Figure 3.10) and optical properties, when measured vertically as done by [37].

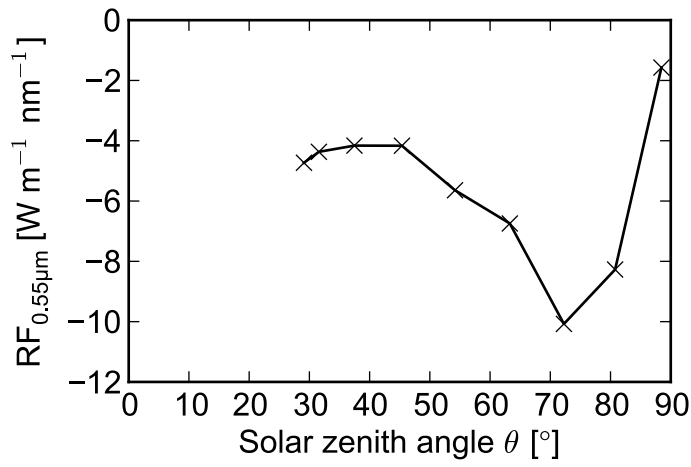


**Figure 4.29:** Radiative forcing at  $\lambda = 0.55 \mu m$  as function of the solar zenith angle  $\theta$  for comparison with other works considering the optical properties of individual contrails depending on solar zenith angle. The shape of the curve is similar to the Figures 3 and 9 of Gounou et al.[48] as well as Figures 5, 6, 10 and 11 of Forster et al. [49].

## 5 Conclusion and outlook

### 5.1 Conclusion

The aim of this thesis was the development of a three-dimensional radiative forcing model of condensation trails considering both the corresponding flight performance properties of the contrail generating aircraft and the state variables of the ambient atmosphere. The results should be used to establish a key performance indicator along the SES Performance Scheme. Therewith, a four-dimensional trajectory can be optimized with respect to minimum influence of a condensation trail on the radiation budget of the Earth-atmosphere system. This optimization might be necessary, if a contrail formation is unavoidable, due to other target functions within the trajectory optimization. With this model the influence of many ambient parameters on the environmental impact of the contrail are estimated and discussed. These are for example time of day or the flight path of the aircraft. Hence, the developed contrail radiative forcing model offers the possibility of optimizing a single flight with given takeoff and landing positions with respect to minimum contrail radiative forcing.

The initial dimensions and microphysical properties of the generated contrail are modeled using an often used wake vortex model, assuming the aircraft emissions being captured in the wake vortices until the circulation is decayed. This approach yields realistic properties. The diffusion of the contrail into the ambient atmosphere is estimated using a recommended Gaussian plume model resulting in realistic macro- and microphysical properties of the contrail. The results are considered to be realistic, although several assumptions regarding the microphysics, which are made because of missing information. For example, a constant number of ice particles during the whole life cycle is assumed, neglecting the break up and the accumulation of ice particles within the contrail. Both processes are taking place in every cloud, but their quantification requires highly complex simulations [61].

The radiative extinction by the contrail is treated separately from the radiative transfer calculations within the atmosphere around the contrail. This approach provides several

new features for three-dimensional radiative transfer calculations: On the one hand, the wavelength specific and angular dependent radiative extinction within the contrail can be investigated in detail. For example, preferred scattering angles can be detected. On the other hand, processes like multiple scattering events and their impact on the radiative transfer can be investigated. The most important benefit of this approach is the possibility of applying the geometrical characteristic of photon transport through the contrail to arbitrary atmospheric conditions, especially to any solar radiance and terrestrial irradiance coming from that particular direction. Hence, the model saves computational effort, during evaluations of the impact of the time of day or of the flight path on radiative extinction, for constant optical properties.

The radiative forcing of a contrail is calculated by balancing the corresponding in- and outgoing energy of the Earth-atmosphere system. On the one side of the balance the power of solar radiation getting scattered back to space cools the Earth-atmosphere system. On the other side the absorbed solar and terrestrial radiation and the power of terrestrial radiation getting scattered back to the Earth are heating the Earth-atmosphere system.

Several major findings were estimated:

Radiative extinction strongly depends on the angle of irradiation. This fact is detectable considering the extinguished radiation depending on the time of the day. Due to strong forward scattering the cooling effect of upward scattered solar radiances will be maximum for large solar zenith angles, unless the incoming photons face the contrail cross section (which happens during sunrise and sunset for an East-West orientated contrail). At noon, when solar radiances are maximum and a significant extinction of radiation is expected, the amount of absorbed power increases as well and nearly completely compensates the cooling effect at wavelengths of  $\lambda = 0.55 \mu\text{m}$ .

Terrestrial irradiance only depends on wavelength, i.e. constant over the whole day, as consequence of the Two Stream Approximation. Hence, the terrestrial ratio of radiative forcing is constant during day and night. Therefore, the solar cooling effect always has to compensate a constant terrestrial heating effect.

Flying at night increases the contrail radiative forcing, independently of the calculation method of atmospheric absorption and re-emission. During the day, the strong forward scattering will be taken into account, when the aircraft flies during sunrise or sunset at best between the North-South axis.

During its life time, the relevant contrail optical properties increase, because of growing ice particles. These changes result in a significantly modified radiative forcing. With increasing particle radius the solar absorption efficiency  $Q_a$  oscillates. Since the amount of absorbed power determines the sign of solar radiative forcing, an absorption

efficiency  $Q_a$ , averaged over a realistic particle size distribution has to be used for radiative transfer calculations. Considering the backscattering of solar radiation, changes up to 100% in backscattered power between a young and an old contrail are possible. In the terrestrial wavelength spectrum differences in absorbed power and in the terrestrial radiative forcing up to 350% are calculated. Due to the non linear dependence of the absorption efficiency on ice particle size, the radiative forcing does not depend linearly on contrail age and can not be accurately calculated by averaging the radiative forcing at the middle of the contrail life time and multiplying this value with the whole life time.

For trajectory optimization it can be summarized, that the size of the ice particles (increasing with increasing contrail age) stronger determines the radiative forcing of the contrail, than the ice particle density (which decreases with increasing contrail age). From this follows the advise to not reduce the number of soot particles during incomplete combustion, but the size of soot particles. Unfortunately, soot formation during the combustion process is a highly complex process, which is still not completely understood.

Atmospheric turbulence influences the contrail life cycle and life time in a non negligible magnitude. Strong turbulence causes a short life time and a fast contrail diffusion. However, the shorter the life time the faster the change in contrail properties. Hence, even in strong turbulence (resulting in a short contrail life time) the assumption of constant contrail properties will underestimate the radiative forcing. Further estimations of the influence of microphysical properties on radiative extinction yield in a minor impact of the number density of ice particles. Considering one particular time step and different contrail cross sections and ice particle sizes, the extinction increases with growing particle radius, regardless of a smaller number density of ice particles within the larger contrail cross section.

Although increased extinction is detected in strong turbulence, the energy forcing of a contrail in weak turbulence exceeds the energy forcing of a contrail in strong turbulence, due to the longer life time. Finally, flying in a turbulent environment, of course only within boundaries given by safety issues, reduces the environmental impact of condensation trails.

Calculating the imbalance in the Earth-atmosphere energy system requires the consideration of the whole wavelength regions with significant contributions to the energy system. Due to high computational costs, this was impossible in the solar wavelength spectrum for the whole contrail life time. First estimations assume satisfying results for calculations of the solar radiative forcing with a shortened solar wavelength spectrum. The terrestrial radiative forcing was calculated for the whole spectrum with significant contribution of irradiance, assuming averaged irradiances over each hemisphere (Two Stream Approximation). Large differences in monochromatic extinction due to

differences in absorption and scattering efficiencies and in available irradiances were estimated resulting in the necessity of considering the whole terrestrial spectrum for the calculation of radiative forcing.

## 5.2 Outlook

The described method for calculating the radiative extinction of a contrail causes high computational costs. Therefore, this method is unsuitable for a fast trajectory optimization. Nevertheless, interesting findings of the scattering properties of single contrails have been made. For the calculation of the total radiative forcing of the whole contrail life time, the following improvements of the model are planned.

The computational costs for considering the strong dependence of the direction of solar direct radiation on the radiative forcing, will be reduced by separating solar direct and diffuse calculations of radiative extinction. The necessary number of bins of angles for the Monte Carlo simulation of diffuse solar radiation is much lower. An additional Monte Carlo simulation for the exact direction of direct solar radiation will consider the main part of radiative extinction more exactly.

The solar radiative extinction will be calculated considering all wavelengths contributing to the energy budget. Significant radiances originate from a narrow wavelength region with maximum contributions at  $\lambda = 0.55 \mu\text{m}$ . Hence, reliable results are expected for calculations of the wavelength region around  $\lambda = 0.55 \mu\text{m}$ .

Furthermore, the calculated number of scattering events especially in the terrestrial wavelength spectrum allows the assumption of single scattering, by directly solving the developed integral (combination of Beer's law and the Gaussian distribution function describing the contrail). The results of these calculations will be compared with the results of the Monte Carlo simulation estimating the error done by neglecting multiple scattering events.

Moreover, a realistic particle size distribution within the contrail is necessary for the improved estimation of realistic absorption efficiencies especially in the solar wavelength spectrum. Schumann et al. [130] already estimated the particle characteristics in young contrails in detail, which will be useful for further investigations. Furthermore, investigations of Petty et al. [131] regarding improvements of the particle size distribution in clouds will be considered.

Finally, uncertainties are expected from the assumption of treating the terrestrial irradiance as hemispherically averaged. Although the Two Stream Approximation seems as

---

the only effortable method of calculating atmospheric absorption, the Monte Carlo simulation for the calculation of terrestrial extinction will be treated three-dimensionally with constant incoming irradiances for each direction per hemisphere. Differences in extinction were found in the solar wavelength spectrum, due to the three-dimensional treatment. Differences are expected in the long wave spectrum as well, although in smaller magnitude, because of the smaller energy input in the terrestrial wavelength region.





# List of Figures

2.1	Saturation vapor pressure curves . . . . .	11
2.2	Atmospheric temperature gradient and pressure gradient defined by the U.S. Standard Atmosphere [60]. . . . .	12
2.3	Meteorologically relevant wavelengths of electromagnetic waves. . . . .	16
2.4	Angles and orientation of polar coordinates. . . . .	18
2.5	Spectral radiance of blackbodies with different temperatures . . . . .	21
2.6	Attenuation of radiation . . . . .	23
2.7	Radiant emittance of a blackbody with a temperature of 5750 K . . . . .	27
2.8	Radiant emittance of a blackbody with a temperature of 288 K . . . . .	28
2.9	Geometry of a scattering event . . . . .	29
2.10	Henye-Greenstein phase function . . . . .	30
2.11	Energy budget of the Earth-atmosphere system . . . . .	33
2.12	Schmidt-Appleman criterion . . . . .	43
3.1	The model atmosphere Mid-Latitude Winter . . . . .	47
3.2	Engine parameters of the short distance flight of an Airbus A320 . . . . .	50
3.3	Geometry of the Two Stream Approximation . . . . .	52
3.4	Geometry of the Discrete Ordinate Radiative Transfer solver . . . . .	53
3.5	Initial vertical contrail extension . . . . .	60
3.6	Geometry of circular velocities . . . . .	61
3.7	Dispersion model of the tangential velocity . . . . .	62
3.8	Contrail horizontal extension . . . . .	63
3.9	Two-dimensional Gaussian plume model . . . . .	64
3.10	Evolution of particle radius for $D_s = 0$ and $D_s = 0.3 \text{ m}^2\text{s}^{-2}$ . . . . .	67
3.11	Influence of the vertical wind drift $v_z$ on particle radius . . . . .	70
3.12	Reynolds number $Re = 2 r_p v_{s,p} v_{\text{kin}}^{-1}$ over a contrail's lifecycle . . . . .	71
3.13	A contrail section with symmetric cross section . . . . .	75
3.14	Geometry of the Monte Carlo simulation . . . . .	76
3.15	Some possibilities of radiative extinction within the contrail . . . . .	78
3.16	Transformation of coordinates between polar coordinates . . . . .	80
3.17	A scattering event following a Henye-Greenstein phase function . . . . .	84
3.18	Important assumptions during the Monte Carlo simulation . . . . .	88
3.19	Idealized geometry of ice particle shapes . . . . .	90

3.20	Extinction $Q_e$ and absorption $Q_a$ efficiencies and asymmetry parameter $g_{\text{HG}}$ . . . . .	92
3.21	Extinction $Q_e$ and absorption $Q_a$ efficiencies and asymmetry parameter $g_{\text{HG}}$ depending on particle radius . . . . .	93
3.22	Influence of the irradiated width $w_{\text{in}}$ of starting photons . . . . .	95
3.23	Influence of the chosen total number of photons . . . . .	96
3.24	Influence of the discretization $\Delta_{\theta,\phi}$ . . . . .	97
4.1	Application of the Schmidt-Appleman criterion . . . . .	101
4.2	Contrail life cycle . . . . .	104
4.3	Development of the horizontal and vertical standard deviations . . . . .	105
4.4	Direct and diffuse radiance of solar radiation . . . . .	107
4.5	Irradiances of terrestrial radiation . . . . .	108
4.6	Geometry of starting photons . . . . .	110
4.7	Influence of the solar zenith angle . . . . .	111
4.8	Demonstration of several directions of photons for different zenith angles $\theta$ and azimuthal angles $\phi$ . . . . .	112
4.9	Number ratios of forward and backward scattered photons to the total number of photons . . . . .	113
4.10	Number ratio of absorbed photons . . . . .	113
4.11	Geometry of the Monte Carlo simulation for the terrestrial spectrum . . . . .	114
4.12	Number ratios of absorbed, forward scattered, and backward scattered photons to the total number of photons . . . . .	115
4.13	The average number of scattering events . . . . .	117
4.14	The average number of scattering events in the thermal wavelength spectrum . . . . .	117
4.15	Extinguished powers for diurnal variations of a contrail along East and West . . . . .	118
4.16	Qualitative diurnal variation of the direction of direct solar radiation of a contrail along East and West . . . . .	119
4.17	Extinguished powers for diurnal variations of a contrail constituting the North-South axis . . . . .	121
4.18	Qualitative diurnal variation of the direction of direct solar radiation of a contrail along North and South . . . . .	121
4.19	Extinguished powers of solar radiation by a contrail over its whole life time . . . . .	123
4.20	Extinguished powers of terrestrial monochromatic irradiances by a contrail over its whole life time . . . . .	125
4.21	Extinguished powers of solar radiation by contrails in different turbulent environments . . . . .	128
4.22	Extinguished powers of terrestrial irradiance by contrails in different turbulent environments . . . . .	129

---

4.23	Extinguished powers of solar radiances with different wavelengths . . .	132
4.24	Solar radiative forcing . . . . .	133
4.25	Extinguished powers of all significant terrestrial irradiances . . . . .	134
4.26	Extinction of terrestrial radiation integrated over the terrestrial spectrum	136
4.27	Energy Forcing $EF$ of terrestrial radiation . . . . .	137
4.28	Optical thickness $\tau$ as function of the irradiated width $2w_{\text{in}}$ . . . . .	138
4.29	Radiative forcing at $\lambda = 0.55 \mu\text{m}$ as function of the solar zenith angle $\theta$ for comparison with other works . . . . .	140



# List of Tables

2.1	Values of the Brunt Väisälä frequency . . . . .	36
3.1	Main characteristics of the aircraft Airbus A320. . . . .	48
3.2	Used measures of turbulence and assumed correlation . . . . .	68
3.3	Components of extinguished photons considering multiple scattering . .	86
3.4	Estimated ice particle shapes in cirrus clouds . . . . .	90
4.1	Parameters of the flight profile [81] used for the calculation of the initial state of the contrail. . . . .	102
4.2	Parameters for wake vortex calculations of the initial state of the contrail.	102
4.3	Eddy dissipation rate, sedimentation time and initial contrail vertical depth . . . . .	103
4.4	Contrail properties for the angular dependence of traversing solar radiance. . . . .	109
4.5	Contrail properties for the Monte Carlo simulation of photons with terrestrial wavelengths. . . . .	114
4.6	Contrail optical properties for $\lambda = 0.55 \mu\text{m}$ and $\lambda = 10.471 \mu\text{m}$ of different ages of lifetime . . . . .	123
4.7	Contrail optical properties in different turbulent environments . . . . .	127
4.8	Optical wavelength specific solar properties for a contrail described in Table4.7 . . . . .	131
4.9	Comparison of the weighted number ratios $S_{\text{ext}}$ for different contrail ages with Forster et al. [49] . . . . .	139



# Abbreviations and Symbols

ACTA	Automatic Contrail Tracking Algorithm
AFGL	Air Force Geophysics Laboratory
ATM	Air Traffic Management
a.u.	arbitrary units
BADA	Base of Aircraft Data
CIRA	Committee on Space Research
CoCiP	Contrail cirrus Prediction tool
DISORT	Discrete Ordinate Radiative Transfer
EJPM	Enhanced Jet Performance Model
ETPM	Enhanced Trajectory Performance Model
ICAO	International Civil Aviation Organization
IGBP	International Geosphere Biosphere
ISA	International Standard Atmosphere
ISO	International Standard Organisation
IR	Infrared
KPI	Key Performance Indicator
libRadtran	Library of Radiative transfer solvers
NASA	National Aeronautics and Space Administration
P2P	Probabilistic Two-Phase Wake Vortex Decay and Transport Model
SES	Single European Sky
SESAR	Single European Sky ATM Research Program
TOA	Top Of the Atmosphere
TSA	Two Stream Approximation
UV	Ultra Violet
VIS	Visible
$A$	Contrail cross section [ $\text{m}^2$ ]
$A_p$	Particle cross section [ $\text{m}^2$ ]

---

$A_{\text{proj.}}$	Projected particle area [ $\text{m}^2$ ]
$a$	Reflectance, albedo [a.u.]
$B_\lambda$	Planck's function [ $\text{W m}^{-2}$ ]
$b$	Effective horizontal vortex spacing [m]
$b_0$	Initial horizontal vortex spacing [m]
$c$	Speed of light in vacuum $c = 2.99 \cdot 10^8 \text{ m s}^{-1}$
$c_h$	Contrail height [m]
$c_v$	Contrail width [m]
$c_p$	Specific heat capacity at constant pressure $c_p = 1004 \text{ J}(\text{kg K})^{-1}$
$D$	Diffusion coefficient [ $\text{m}^2 \text{s}^{-1}$ ]
$D_e$	Effective particle size [m]
$D_h$	Horizontal diffusivity [ $\text{m}^2 \text{s}^{-1}$ ]
$D_s$	Sheared diffusivity [ $\text{m}^2 \text{s}^{-1}$ ]
$D_v$	Vertical diffusivity [ $\text{m}^2 \text{s}^{-1}$ ]
$d_{\text{ice}}$	Ice particle diameter [m]
$d_{\text{max}}$	Maximum dimension of a non spherical ice crystal [m]
$dp$	Particle diameter [m]
$d_{\text{Soot}}$	Soot particle diameter [m]
$ds$	Infinitesimal distance [m]
$E$	Energy [J]
$E_{\downarrow\uparrow a}$	Absorbed energy of photons coming from above and beneath [ $\text{W m}^{-1}$ ]
$E_{\uparrow b}$	Backscattered energy of photons coming from beneath, scattered into the lower hemisphere [ $\text{W m}^{-1}$ ]
$E_{\downarrow b}$	Backscattered energy of photons coming from above, scattered into the upper hemisphere [ $\text{W m}^{-1}$ ]
$EF$	Energy forcing of a single contrail over it's entire life time [ $\text{J m}^{-1}$ ]
$EI_{\text{water}}$	Emission index of water [ $\text{kg kg}^{-1}$ ]
$EI_{\text{water, compl}}$	Emission index of water assuming complete combustion [ $\text{kg kg}^{-1}$ ]
$EI_{\text{Soot}}$	Emission index of soot [ $\text{kg kg}^{-1}$ ]
$e$	Vapor pressure, compare $p_{\text{water}}$ [Pa]
$e_p$	Vapor pressure in the exhaust plume [Pa]
$e^*$	Saturation vapor pressure of water, [Pa]
$e_{\text{ice}}^*$	Saturation vapor pressure above ice, [Pa]
$e_{\text{water}}^*$	Saturation vapor pressure above water, [Pa]
$F$	Thrust [N]
$F_A$	Lifting force [N]
$F_{\text{Atm}}$	Emitted irradiance of the atmosphere [ $\text{W m}^{-2}$ ]
$F_{\text{Earth}}$	Theoretically emitted irradiance of the Earth's surface [ $\text{W m}^{-2}$ ]



$F_{\text{Earth, meas.}}$	Measured emitted irradiance of the Earth's surface [ $\text{W m}^{-2}$ ]
$F_G$	Weight [N]
$F_{G,p}$	Weight of a particle [N]
$F_{\text{down}}$	Downward irradiance [ $\text{W m}^{-2}$ ]
$F_{\text{up}}$	Upward irradiance [ $\text{W m}^{-2}$ ]
$F_{W,p}$	Drag force onto particles [N]
$G$	Slope of the mixing line [ $\text{Pa K}^{-1}$ ]
$g$	Acceleration of gravity $g = 9.81 \text{ m s}^{-1}$
$g_{\text{HG}}$	Asymmetry parameter of the scattering phase function [a.u.]
$h$	Planck's constant $h = 6.626 \cdot 10^{-34} \text{ J s}$
$h$	Specific enthalpy [ $\text{J kg}^{-1}$ ]
$I$	Radiance [ $\text{W m}^{-2} \text{sr}^{-1}$ ]
$I_0$	Original intensity [ $\text{W m}^{-2} \text{sr}^{-1}$ ]
$I_{\text{diff}}$	Diffuse solar radiance [ $\text{W m}^{-2} \text{sr}^{-1} \text{nm}^{-1}$ ]
$I_{\text{dir}}$	Direct solar radiance [ $\text{W m}^{-2} \text{sr}^{-1} \text{nm}^{-1}$ ]
$I_{\text{emit}}$	Emitted intensity [ $\text{W m}^{-2} \text{sr}^{-1} \text{nm}^{-1}$ ]
$I_{\text{ext}}$	Extinguished intensity [ $\text{W m}^{-2} \text{sr}^{-1} \text{nm}^{-1}$ ]
$I_{\text{sca}}$	Scattered intensity [ $\text{W m}^{-2} \text{sr}^{-1} \text{nm}^{-1}$ ]
$IWC$	Ice water content [ $\text{kg m}^{-3}$ ]
$IWC_s$	Ice water content contributing to ice particle size [ $\text{kg m}^{-3}$ ]
$J$	Diffusion flux [ $\text{mol m}^{-2} \text{s}^{-1}$ ]
$k$	Auxiliary function $k(\zeta)$
$k_a$	Mass absorption coefficient [ $\text{m}^2 \text{kg}^{-1}$ ]
$k_B$	Boltzmann's constant $k_B = 1.381 \cdot 10^{-23} \text{ J K}^{-1}$
$k_e$	Mass extinction coefficient [ $\text{m}^2 \text{kg}^{-1}$ ]
$k_s$	Mass scattering coefficient [ $\text{m}^2 \text{kg}^{-1}$ ]
$k_w$	Wien's constant $k_w = 2897 \text{ K}$
$L$	Evaporation heat $L = 2500 \text{ J g}^{-1}$
$l$	External size [m]
$l_s$	Wing span [m]
$\dot{m}_f$	Fuel flow [ $\text{kg s}^{-1}$ ]
$m_p$	Mass per particle [kg]
$m_{\text{ice}}$	Mass of available ice within the contrail [kg]
$m^*$	Saturation mixing ratio [a.u.]
$N$	Brunt Väisälä frequency [ $\text{s}^{-1}$ ]
$N_n$	Normalized Brunt Väisälä frequency [ $\text{s}^{-1}$ ]
$N_{\text{affected}}$	Number of affected photons [a.u.]
$N_{\text{eval}}$	Total number of simulated photons [a.u.]

$N_{\text{in}}$	Number of incoming photons [a.u.]
$N_{\text{soot}}$	Number of emitted soot particles [ $\text{s}^{-3}$ ]
$N_{\text{out}}$	Number of outgoing photons [a.u.]
$N_{\text{sca}}$	Number of scattering events [a.u.]
$N_{\tilde{\nu}}$	Number of wavenumbers $\tilde{\nu}_i$ [a.u.]
$n$	Number of moles [ $\text{m}^{-3}$ ]
$n$	Number of streams [a.u.]
$n_i$	Partial number of moles [ $\text{m}^{-3}$ ]
$n_p$	Number of particles [ $\text{m}^{-3}$ ]
$P_{\text{HG}}$	Heney-Greenstein phase function
$P_e$	Extinguished power [ $\text{W m}^{-1} \text{nm}^{-1}$ ]
$P_i$	$P_{\uparrow a}$ , $P_{\uparrow b}$ and $P_{\downarrow b}$ in their entirety
$P_{\text{int}}$	Integral over all scattering angles per class [a.u.]
$P_{\downarrow \uparrow a}$	Absorbed power of photons coming from above and beneath [ $\text{W m}^{-1} \text{nm}^{-1}$ ]
$P_{\uparrow b}$	Backscattered power of photons coming from beneath, scattered into the lower hemisphere [ $\text{W m}^{-1} \text{nm}^{-1}$ ]
$P_{\downarrow b}$	Backscattered power of photons coming from above, scattered into the upper hemisphere [ $\text{W m}^{-1} \text{nm}^{-1}$ ]
$p$	Pressure [Pa]
$p_0$	Pressure at reference level [Pa]
$p_i$	Partial pressure [Pa]
$p_{\text{water}}$	Partial pressure of water vapor, compare $e$ [Pa]
$Q$	Combustion heat [ $\text{J kg}^{-1}$ ]
$Q_a$	Absorption efficiency [a.u.]
$Q_e$	Extinction efficiency [a.u.]
$Q_s$	Scattering efficiency [a.u.]
$R_L$	Individual gas constant of dry air $R_L = 287 \text{ J}(\text{kg K})^{-1}$
$R_v$	Specific gas constant of water vapor $R_L = 461.5 \text{ J}(\text{kg K})^{-1}$
$Re$	Reynold's number [a.u.]
$Re_{\text{turb}}$	Turbulent Reynold's number [a.u.]
$RF$	Radiative forcing [ $\text{W m}^{-2}$ ]
$r$	Radius of the vortex [m]
$r$	Distance between Earth and Sun $r = 149 \cdot 10^6 \text{ m}$
$r_c$	Core radius of the vortex [m]
$r_{\text{Earth}}$	Radius of the Earth [m]
$r_p$	Particle radius [m]
$rH$	Relative Humidity [a.u.]
$rH_{\text{ice}}$	Relative Humidity with respect to ice [a.u.]

---

$rH_{\text{water}}$	Relative Humidity with respect to water [a.u.]
$S_0$	Solar constant [ $\text{Wm}^{-2}$ ]
$S_i$	$S_{\uparrow a}$ , $S_{\downarrow a}$ , $S_{\uparrow b}$ and $S_{\downarrow b}$ in their entirety
$S_{\uparrow a}$	Weighted number ratios of absorbed photons coming from beneath [m]
$S_{\uparrow b}$	Weighted number ratios of photons coming from beneath, scattered into the lower hemisphere [m]
$S_{\downarrow a}$	Weighted number ratios of absorbed photons coming from above [m]
$S_{\downarrow b}$	Weighted number ratios of photons coming from above, scattered into the upper hemisphere [m]
$S_{\text{ext}}$	Weighted number ratios of extinguished photons [m]
$s$	Distance [m]
$s$	Wind shear [ $\text{s}^{-1}$ ]
$T(v)$	Transmittance [a.u.]
$T$	Temperature [K]
$T_{\text{Earth}}$	Earth's surface temperature [K]
$T_{\text{Sun}}$	Sun's surface temperature [K]
$T_{\text{LC}}$	Threshold temperature of contrail formation [K]
$T_{\text{LM}}$	Threshold temperature of contrail formation for $rH_{\text{water}} = 1$ [K]
$T_e$	Temperature of the environment [K]
$T_p$	Temperature of the plume [K]
$T_{\Theta}$	Potential temperature [K]
$t$	Time [s]
$u$	Mean velocity [ $\text{ms}^{-1}$ ]
$u'$	Fluctuation in flow velocity [ $\text{ms}^{-1}$ ]
$V$	Volume [ $\text{m}^3$ ]
$V_i$	Partial volume [ $\text{m}^3$ ]
$V_p$	Particle volume [ $\text{m}^3$ ]
$V_{\uparrow a}$	Number ratios of absorbed photons coming from beneath [a.u.]
$V_{\uparrow b}$	Number ratios of photons coming from beneath, scattered into the lower hemisphere [a.u.]
$V_{\uparrow f}$	Number ratios of photons coming from beneath, scattered into the upper hemisphere [a.u.]
$V_{\downarrow a}$	Number ratios of absorbed photons coming from above [a.u.]
$V_{\downarrow b}$	Number ratios of photons coming from above, scattered into the upper hemisphere [a.u.]
$V_{\downarrow f}$	Number ratios of photons coming from above, scattered into the lower hemisphere [a.u.]
$v$	Velocity [ $\text{ms}^{-1}$ ]

$v_s$	Descent speed of wake vortices during the vortex regime [ $\text{m s}^{-1}$ ]
$v_{s,p}$	Sedimentation speed of particles [ $\text{m s}^{-1}$ ]
$v_{t,0}$	Initial tangential velocity [ $\text{m s}^{-1}$ ]
$v_{\text{TAS}}$	True air speed [ $\text{m s}^{-1}$ ]
$v_\infty$	Free stream velocity [ $\text{m s}^{-1}$ ]
$W_{\text{Sun}}$	Energy production of the Sun $W_{\text{Sun}} = 3.8 \cdot 10^{23} \text{ kW}$
$w_{\text{in}}$	Half contrail maximum width [m]
$\vec{x}$	Position vector
$Z_s$	Random number of power of endurance [a.u.]
$Z_e$	Random number of extinction [a.u.]
$Z_\Phi$	Random number of polar scattering angle $\Phi$ [a.u.]
$z$	Height [m]
$z_0$	Reference level [m]
$\alpha$	Angle between incident photons and contrail axis [rad]
$\alpha_\lambda$	Absorption capacity [a.u.]
$\beta_a$	Volume absorption coefficient [ $\text{m}^{-1}$ ]
$\beta_e$	Volume extinction coefficient [ $\text{m}^{-1}$ ]
$\beta_s$	Volume scattering coefficient [ $\text{m}^{-1}$ ]
$\Gamma_0$	Initial circulation [ $\text{m}^2 \text{s}^{-1}$ ]
$\gamma_d$	Dry adiabatic lapse rate [ $\text{K m}^{-1}$ ]
$\gamma_s$	Saturated adiabatic lapse rate [ $\text{K m}^{-1}$ ]
$\Delta u$	Change in mean flow velocity $u$ over distance $l$ [ $\text{m s}^{-1}$ ]
$\Delta\theta, \phi$	Size of the bins between two different angles $\theta$ or $\phi$
$\varepsilon$	Eddy dissipation rate [ $\text{m}^2 \text{s}^{-3}$ ]
$\varepsilon_{\text{mol}}$	Ratio between molar masses of dry air and water vapor [a.u.]
$\varepsilon_n$	Normalized eddy dissipation rate [ $\text{m}^2 \text{s}^{-3}$ ]
$\varepsilon_\lambda$	Emission capacity [a.u.]
$\eta$	Overall propulsion efficiency [a.u.]
$\eta_{\text{dyn}}$	Dynamical viscosity [ $\text{kg m}^{-1} \text{s}^{-1}$ ]
$\vartheta$	Scattering angle [rad]
$\theta$	Solar zenith angle [rad]
$\lambda$	Wavelength [ $\mu\text{m}$ ]
$\lambda_{\text{max}}$	Wavelength of maximum peak of Planck's function [ $\mu\text{m}$ ]
$\lambda_{\text{max,Sun}}$	Wavelength of maximum peak of Planck's function of the sun [ $\mu\text{m}$ ]
$\lambda_{\text{turb}}$	Size of a particular turbulent element [m]
$\nu$	Frequency [ $\text{s}^{-1}$ ]
$\tilde{\nu}$	Wavenumber [ $\text{cm}^{-1}$ ]

---

$\nu_{\text{kin}}$	Kinematic viscosity [ $\text{m}^2\text{s}^{-1}$ ]
$\nu_{\text{turb}}$	Turbulent viscosity [ $\text{m}^2\text{s}^{-1}$ ]
$\rho$	Density [ $\text{kg m}^{-3}$ ]
$\rho_p$	Density of particles [ $\text{kg m}^{-3}$ ]
$\rho_{\text{ice}}$	Density of ice [ $\text{kg m}^{-3}$ ]
$\rho_{\text{Soot}}$	Density of soot [ $\text{kg m}^{-3}$ ]
$\sigma$	Stefan Boltzmann constant $\sigma = 5.67 \cdot 10^{-8} \text{ J m}^{-2}\text{K}^{-4}$
$\sigma_a$	Absorption cross section [ $\text{m}^2$ ]
$\sigma_e$	Extinction cross section [ $\text{m}^2$ ]
$\sigma_h$	Horizontal standard deviation [m]
$\sigma_s$	Scattering cross section [ $\text{m}^2$ ]
$\sigma_v$	Vertical standard deviation [m]
$\hat{\sigma}(t)$	Variance of the standard deviation [ $\text{m}^2$ ]
$\zeta$	Auxiliary variable for the replacement of the integration over $T(v)$ in the auxiliary function $k(\zeta)$
$\tau$	Optical depth [a.u.]
$v$	Finite mass path [ $\text{kg m}^{-2}$ ]
$v'$	reduced mass path between two boundaries of math path $v$ [ $\text{kg m}^{-2}$ ]
$\varphi$	Polar scattering angle [rad]
$\phi$	Solar azimuthal angle [rad]
$\Omega$	Unit vector [a.u.]
$\Omega'$	Changed unit vector [a.u.]
$\omega$	Solid angle [sr]
$\tilde{\omega}$	Single scatter albedo [a.u.]
$\vec{\omega}$	angular velocity [ $\text{m s}^{-1}$ ]



# Glossary

## **Absorption**

Conversion of photons into intrinsic energy.

## **Advection**

Horizontal air movements and convective heat transport in the vicinity of the ground.

## **Agglomeration**

Accumulation of ice particles in clouds.

## **Air traffic management**

A system to ensure safe and efficient air traffic during all phases of the aircraft operations.

## **Asymmetry parameter**

$g_{HG}$  is the cosine of the scattering angle, averaged over a large number of scattering events. It is a measure of the scattering properties of the material.

## **Atmospheric radiative transfer model**

A model, calculating spectral diffuse and direct radiances and spectral irradiances at any altitude coming from an arbitrary direction in space. The model considers radiative extinction due to interactions of the photons with the ingredients of the atmosphere, e.g. a model atmosphere, where the altitude dependent composition of the atmosphere is defined. In this thesis, the radiative transfer package libRadtran is used as atmospheric radiative transfer model, providing several solvers for different applications.

## **Azimuthal angle**

$\phi$  measures the angle of radiation in the horizontal plane.

## **Band model**

Model to calculate broadband radiances and irradiances by an analytical treatment of the absorption spectrum by replacing the original spectrum with an analytically solvable function.

**Band width**

The width of the interval in a frequency spectrum, where are the dominant frequency components of a signal, which is to be transmitted.

**Beer's law**

A fundamental model for calculating radiative extinction.

**Brunt Väisälä frequency**

$N$  is a measure of atmospheric stability and denotes the buoyancy frequency and represents the frequency of oscillation of an air parcel around its equilibrium level.

**Circulation**

$\Gamma$  is the integral of the velocity along a circular path around a closed curve. In a flow,  $\Gamma$  is the measure of the vorticity in the area enclosed by the path.

**Condensation**

The transition of a substance from the gaseous to the liquid state. Ice particles are formed through condensation and subsequent freezing of water vapor on soot particles.

**Condensation trail**

Ice particles at flight level developed from condensed water vapor emitted by an aircraft.

**Contrail**

Short for condensation trail.

**Contrail life cycle model**

A model calculating the change of microphysical properties over the whole contrail life cycle. Therefore, a model atmosphere and a flight performance model are required. The microphysical properties are: horizontal and vertical dimensions, ice particle number density, ice particle radius and ice water content. From this information, the optical contrail properties can be estimated for the contrail radiative forcing model.

**Contrail radiative forcing model**

A model calculating the radiative forcing of an individual condensation trail considering the flight performance of the aircraft flying ahead of the condensation trail. Furthermore, a model atmosphere and an atmospheric radiative transfer model providing the angle dependent direct and diffuse radiances and irradiances



are considered. The results of the contrail life cycle model are also used in the contrail radiative forcing model.

**Convection**

The movement of molecules within fluids due to advection or diffusion or both.

**Descent speed**

During the vortex regime, the wake vortices descent with descent speed  $v_s$  due to the strong circulation within the vortices.

**Diffuse solar radiation**

Electromagnetic radiation originating from the sun and redirected by the atmosphere. Diffuse solar radiation  $I_{\text{diff}}$  is expected from all directions in space, is defined in  $[\text{Wm}^{-2}\text{nm}^{-1}\text{sr}^{-1}]$  and is integrated over the respective solid angle  $d\omega$ .

**Diffusion**

Transport caused by a concentration gradient.

**Diffusion coefficient**

$D_v$  and  $D_h$  are the measures of the proper motion of particles in vertical and horizontal direction, depending on material, pressure and temperature.

**Direct solar radiation**

Electromagnetic radiation originating from the sun and NOT redirected by the atmosphere. Direct solar radiation  $I_{\text{dir}}$  is considered as direct beam coming from a single direction, such as described by the unit vector  $\Omega$ .  $I_{\text{dir}}$  is defined in  $[\text{Wm}^{-2}\text{nm}^{-1}]$ .

**Dissipation**

Conversion of kinetic energy due to molecular friction per unit mass and per time into thermal energy.

**Dissociation**

Division of a chemical compound into two or more molecules, atoms or ions.

**Eddy dissipation rate**

$\varepsilon$  is a measure of atmospheric turbulence and defines the conversion of kinetic energy due to molecular friction per unit mass and per time into thermal energy.

**Emission**

Conversion of intrinsic energy into photons.

**Energy forcing**

$EF$  is the integration of the contrail radiative forcing over the contrail life time.

**Evaporation**

The transition of a substance from the liquid to the gaseous state.

**Exitance**

Irradiance emerging from a surface.

**Extinction cross section**

$\sigma_e$  is the ratio of the volume extinction coefficient  $\beta_e$  and the number density of particles and describes radiation extinction.

**Extinction efficiency**

$Q_e$  is the ratio of the scattering cross section  $\sigma_e$  and the geometrical cross section of the particle, extinguishing electromagnetic waves.

**Flight Performance Model**

A model defining the flight performance indicators of an aircraft during a virtual flight and providing the necessary information about Thrust  $F$ , fuel flow  $\dot{m}_f$ , and true air speed  $v_{TAS}$  for each time step of a flight path from origin to destination.

**Henyey-Greenstein phase function**

$P_{HG}(\cos \vartheta)$  is a scattering phase function.  $P_{HG}(\cos \vartheta)$  defines the probability of a photon getting scattered by the angle  $\vartheta$  relative to the original direction  $\Omega$ .

**Hydrostatic equilibrium**

Equilibrium between the gravity that pulls down a solid body, and the buoyancy that tries to lift the body upwards from the liquid.

**Ice water content**

$IWC$  is the total amount of ice mass per volume contrail and is expressed in  $[\text{kg m}^{-3}]$ .

**Ice-supersaturated**

A relative humidity over a flat ice surface larger than necessary for saturation:  $rH_{\text{ice}} > 100\%$ .

**Irradiance**

$F_{\text{up}}$ ,  $F_{\text{down}}$  describe the transport of energy either by photons or electromagnetic waves in units of Joule per second (because radiation is a continuous flow) and unit area (for the distribution of radiation)  $[\text{W m}^{-2} \text{nm}^{-1}]$ .

**Lapse rate**

The temperature gradient with height in the Earth's atmosphere.

**Mass extinction coefficient**

$k_e$  describes radiation extinction per mass of extinguishing material.

**Meridian convergence**

A phenomenon in polar coordinates, where lines of equal azimuthal angle  $\phi$  converge at the pole.

**Model atmosphere**

A model describing the change of the state variables temperature, pressure, density of the atmosphere with altitude.

**Multiple scattering**

A single photon is scattered more than once on its way through the contrail.

**Newton iteration**

A standard method for the numerical solution of nonlinear equations and systems of equations.

**Optical depth**

A dimensionless measure of the spectral atmospheric transmissivity and the extinction coefficient in Beer's law.

**Optical thickness**

A dimensionless measure of the spectral atmospheric transmissivity measured vertically through the atmosphere.

**Photon**

Light quanta (or particles) transporting energy through space [65].

**Plane parallel**

Two planes are considered plane parallel, if they have common points, even if they were extended to infinity.

**Plume**

The accumulation of exhaust gases in the atmosphere. "Plume" is used for the treatment of the aircraft exhaust gases before the conditions of contrail formation are defined. Furthermore, the Gaussian plume model is used in the diffusion regime of the contrail.

**Potential temperature**

$T_{\Theta}$  is the temperature, that an air parcel would reach, if it is adiabatically moved from an arbitrary altitude to the Earth's surface.

**Pressure broadening**

The spreading of frequencies of a spectral line due to interactions between the molecules.

**Radiance**

$I$  is the transport of energy either by photons or electromagnetic waves in units of Joule per second, unit area and steradian [ $\text{Wm}^{-2}\text{nm}^{-1}\text{sr}^{-1}$ ]. It contains both the strength and the direction of radiation.

**Radiation**

Particles (photons) or electromagnetic waves propagating through space and transporting energy.

**Radiative forcing**

$RF$  is the imbalance of the energy budget of the Earth-atmosphere system.  $RF$  considers the amount of energy the contrail prevents from leaving the atmosphere (positive  $RF$ ) and prevents from entering the atmosphere (negative  $RF$ ).

**Radiative transfer equation**

The RTE calculates the depletion of radiation due to atmospheric extinction for a single wavelength and a single direction.

**Reflection**

Special case of scattering, i.e. backscattering.

**Saturation vapor pressure**

Maximum value of partial pressure of water vapor in an equilibrium system over a plane surface.

**Scattering**

Redirection of radiation without a change of the intrinsic energy.

**Schmidt-Appleman criterion**

The thermodynamical formulation of conditions of contrail formation. The Schmidt-Appleman criterion defines the threshold temperature  $T_{LC}$  of the atmosphere. Under atmospheric conditions below  $T_{LC}$ , the atmosphere is cold enough for contrail formation.

**Sedimentation speed**

$v_{s,p}$  characterizes the downward movement of the ice particles according to Stoke's law.

**Single scattering**

A single photon is scattered only once at an ice particle while passing through the contrail.

**Solid angle**

A partial surface of a sphere, divided by the square of the radius of the sphere in units of [sr].

**Soot particle**

Particles of black carbon, formed during incomplete combustion processes in the combustion chamber of a jet engine. Soot particles act as condensation nuclei within the exhaust plume. Water vapor originating from the exhaust and from the atmosphere condense at these soot particles and form ice particles.

**Spectral band**

Sub-ranges or parts of the electromagnetic spectrum.

**Spectrum**

All electromagnetic waves of different wavelengths.

**Stability**

A measure of atmospheric turbulence and defines the ability of an air parcel to move vertically within the atmosphere.

**Steradian**

Unit of the solid angle.

**Stratosphere**

The stratosphere is the layer of the atmosphere located between the troposphere and the mesosphere.

**Sublimation**

The transition of a substance from the solid to the gaseous state.

**Tangential velocity**

The cross product of the angular velocity and the radius of the circle.

**Thermodynamic equilibrium**

All properties of a small volume in the atmosphere are equal to their thermodynamic equilibrium values at the local values of temperature and pressure.

**Transmission**

A measure of the permeability of a medium for waves such as sound waves or electromagnetic waves.

**Tropopause**

A boundary in the Earth's atmosphere between the troposphere and the stratosphere.

**Troposphere**

The lowest layer of the Earth's atmosphere.

**Turbulence**

An irregular movement of air parcels around a mean state. These movements are called turbulent elements or eddies. They have dimensions between millimeters and kilometers and lifetimes between seconds and days. Turbulent elements are able to transport energy by their proper motion over a large distance.

**Turbulent Reynolds number**

The turbulent Reynolds number  $Re_{\text{turb}}$  characterizes turbulence by describing the change of the mean flow velocity  $\Delta u$  within a distance  $l$  for a given kinematic viscosity.

**Two Stream Approximation**

TSA is a simple solver of the radiative transfer equation and is characterized by an azimuthally averaged radiative transfer equation.

**Vapor pressure**

Partial pressure of water vapor in a gas.

**Volume extinction coefficient**

$\beta_e$  is measure of radiation extinction after passing a given distance.

**Wake vortex**

Vortices developed at the end of each aircraft wing due to differences in air density between the upper and the lower side of the wing (as consequence of the induced drag).

**Wavelength**

$\lambda$  is the smallest distance between two points of the same phase of a wave. Two points have the same phase when they have the same deflection and the same direction of movement in the timing.

**Wind shear**

Local change in the amount of wind velocity perpendicular to the wind direction. Wind shear is caused by friction between individual air parcels, moving with varying speeds.

**Zenith angle**

$\theta$  measures the angle of radiation in the vertical plane.





# Bibliography

- [1] M. T. Cicero. "De divinatione", (44 BC).
- [2] L. da Vinci. "Codice sul volo degli uccelli", (1505).
- [3] G. Myhre, D. Shindell, F.-M. Bréon, W. Collins, J. Fuglestad, J. Huang, D. Koch, J.-F. Lamarque, D. Lee, B. Mendoza, T. Nakajima, A. Robock, G. Stephens, T. Takemura, and H. Zhang. "Anthropogenic and Natural Radiative Forcing. In: Climate Change 2013: The Physical Science Basis. Contribution of Working Group I to the Fifth Assessment Report of the Intergovernmental Panel on Climate Change". *Cambridge University Press* (2013).
- [4] SES Single european Sky. "Verordnung (eg) Nr. 549/2004 des europäischen Parlaments und des Rates vom 10. März 2004 zur Festlegung des Rahmens für die Schaffung eines einheitlichen europäischen Luftraums". *Rahmenverordnung* (2004).
- [5] Generaldirektion Energie Europäische Kommission, Generaldirektion Mobilität und Verkehr. "SESAR Modernisierung des Flugverkehrsmanagements in Europa". (2008).
- [6] SESAR Consortium. "The Roadmap for Sustainable Air Traffic Management - European ATM Master Plan". *EUROCONTROL 2* (2012).
- [7] H. Fricke, C. Seiß, and R. Herrmann. "A Fuel and Energy Benchmark Analysis of Continuous Descent Operations". In *ATM-Seminar 2015, June 2015, Lisbon, Portugal* (2015).
- [8] ICAO. "Continuous Descent Operations (CDO) Manual – Doc 9931/AN/476". *Montreal 1* (2010).
- [9] T. Guenther and H. Fricke. "Impact of trajectory restrictions onto fuel and time-related cost efficiency". In *International Conference on Research in Air Transportation (ICRAT)*, Istanbul (2014).
- [10] M. Kaiser, M. Schultz, and H. Fricke. "Automated 4D descent path optimization using the Enhanced trajectory Prediction Model (EJPM)". In *Proceedings of the International Conference on Research in Air Transportation (ICRAT)* (2012).

- [11] M. Kaiser, J. Rosenow, H. Fricke, and M. Schultz. "Tradeoff between optimum altitude and contrail layer to ensure maximum ecological en-route performance using the Enhanced Trajectory Prediction Model (ETPM)". In *2nd International Conference on Application and Theory of Automation in Command and Control Systems (ATACCS)*, London (2012).
- [12] R. Sausen, K. Gierens, M. Ponater, and U. Schumann. "A Diagnostic Study of the Global Distribution of Contrails Part I: Present Day Climate". *Theoretical and Applied Climatology* **61**, 127–141 (1998).
- [13] C. Fichter, S. Marquart, R. Sausen, and D. Lee. "The impact of cruise altitudes on contrails and related radiative forcing". *Meteorologische Zeitschrift* **14**, 563–572 (2005).
- [14] V. Williams, R. B. Noland, and R. Toumi. "Reducing the climate change impacts of aviation by restricting cruise altitudes". *Transportation Research Part D* **7**, 451–464 (2002).
- [15] V. Williams and R. B. Noland. "Air Transport Cruise Altitudes Restrictions to Minimize Contrail Formation". *Centre for Transport Studies, Dept. Of Civil & Environmental Engineering, Imperial College of Science, Technology & Medicine, London, Paper submitted for Presentation to the 82nd Annual Meeting of the Transportation Research Board* (2002).
- [16] H. Mannstein, P. Spichtinger, and K. Gierens. "A note on how to avoid contrail cirrus". *Transportation Research Part D* **10**, 421–426 (2005).
- [17] U. Schumann. "Formation, properties and climatic effects of contrails". *C.R. Physique* **6**, 549–565 (2005).
- [18] E. Schmidt. "Die Entstehung von Eisnebel aus den Auspuffgasen von Flugmotoren". *Schriften der Deutschen Akademie der Luftfahrtforschung, Verlag R. Oldenbourg, München/Berlin* **44**, 1–15 (1941).
- [19] H. Appleman. "The formation of exhaust condensation trails by jet aircraft". *Bulletin of the American Meteorological Society* **34**, 14–20 (1953).
- [20] R. Sussmann and K. M. Gierens. "Differences in early contrail evolution of two-engine versus four-engine aircraft: Lidar measurements and numerical simulations". *Journal of Geophysical Research* **106**, 4899–4911 (2001).
- [21] A. W. Brewer. "Condensation trails". *Weather* **1**, 34–40 (1946).
- [22] U. Schumann. "On conditions for Contrail formation from aircraft exhaust". *Meteorologische Zeitschrift* **5**, 4–23 (1996).

- [23] R. Meerkötter, U. Schumann, P. Minnis, D. R. Doelling, T. Nakajima, and Y. Tsushima. "Radiative forcing by contrails". *Journal of Geophysical Research* **17**, 1080–1094 (1999).
- [24] D. S. Lee, D. W. Fahey, P. M. Forster, P. J. Newton, R. C.N. Witt, L. L. Lim, B. Owen, and R. Sausen. "Aviation and global climate change in the 21st century". *Atmospheric Environment* **43**, 3520–3537 (2009).
- [25] P. Minnis, U. Schumann, D. R. Doelling, K. M. Gierens, and D. W. Fahey. "Global distribution of contrail radiative forcing". *Geophysical Research Letters* **26**, 1853–1856 (1999).
- [26] R. Sausen, I. Isaksen, V. Grewe, D. Hauglustaine, D. S. Lee, G. Myhre, M.O. Köhler, G. Pitari, U. Schumann, F. Stordal, and C. Zerefos. "Aviation radiative forcing in 2000: An update on IPCC (1999)". *Meteorologische Zeitschrift* **14**, 555–561 (2005).
- [27] U. Burkhardt and B. Kärcher. "Global radiative forcing from contrail cirrus". *Nature Climate Change* **1**, 54–58 (2011).
- [28] V. Freudentaler, F. Homburg, and H. Jäger. "Optical parameters of contrails from lidar measurements: linear depolarization". *Geophysical Research Letters* **23**, 3715–3718 (1996).
- [29] G. Febvre, J. F. Gayet, A. Minikin, H. Schlager, V. Shcherbakov, O. Jourdan, R. Busen, M. Fiebig, B. Kärcher, and U. Schumann. "On optical and microphysical characteristics of contrails and cirrus". *Journal of Geophysical Research* **114**, D02204 (2009).
- [30] K. Sassen. "Contrail-Cirrus and Their Potential for Regional Climate Change". *Bulletin of the American Meteorological Society* **78**, 1885–1903 (1997).
- [31] B. A. Baum, A. J. Heymsfield, P. Yang, and S. T. Bedka. "Bulk scattering properties for the remote sensing of ice clouds. Part I: Microphysical data and models". *Journal of Applied Meteorology* **44**, 1885–1895 (2005).
- [32] G. Hong, Q. Feng, P. Yang, G. Kattawar, P. Minnis, and Y. X. Hu. "Optical properties of ice particles in young contrails". *Journal of Quantitative Spectroscopy and Radiative Transfer* **109**, 2635–2647 (2008).
- [33] P. Yang, B. A. Baum, A. J. Heymsfield, Y. X. Hu, H.-L. Huang, S.-C. Tsay, and S. Ackerman. "Single-scattering properties of droxtals". *Journal of Quantitative Spectroscopy and Radiative Transfer* **79**, 1159–1169 (2000).

- [34] A. Heymsfield, D. Baumgardner, P. DeMott, P. Forster, K. Gierens, and B. Kärcher (2010). "Contrail microphysics". *Bulletin of the American Meteorological Society* **91**, 456–472 (2010).
- [35] K. Graf, U. Schumann, H. Mannstein, and B. Mayer. "Aviation induced diurnal North Atlantik cirrus cover cycle". *Geophysical Research Letters* **39**, L16804 (2012).
- [36] U. Schumann and K. Graf. "Aviation-induced cirrus and radiation changes at diurnal timescales". *Journal of Geophysical Research* **118**, 1–18 (2013).
- [37] M. Vázquez-Navarro, H. Mannstein, and S. Kox. "Contrail life cycle and properties from one year of MSG/SEVIRI rapid-scan images". *Atmospheric Chemistry and Physics Discussions* **15**, 7019–7055 (2015).
- [38] J. E. Hansen, M. Sato, and R. Ruedy. "Radiative forcing and climate response". *Journal of Geophysical Research* **102**, 6831–6684 (1997).
- [39] J. E. Hansen et al. "Efficacy of climate forcing". *Journal of Geophysical Research* **110**, D18104 (2005).
- [40] G. Myhre and F. Stordal. "On the tradeoff of the solar and thermal infrared impact of contrails". *Geophysical Research Letters* **28**, 3119–3122 (2001).
- [41] G. W. Petty. "Area-Average Solar Radiative Transfer in Three-Dimensionally Inhomogeneous Clouds: The Independently Scattering Cloudlet Model". *Journal of the Atmospheric Science* **59**, 2910–2929 (2002).
- [42] S. Marquart. "Klimawirkung von Kondensstreifen: Untersuchungen mit einem globalen Zirkulationsmodell". Dissertation, University of Munich, Department of Physics (2003).
- [43] M. Ponater, S. Pechtl, R. Sausen, U. Schumann, and G. Hüttig. "Potential of cyroplane technology to reduce aircraft climate impact: A state-of-the-art assessment". *Atmospheric Environment* **40**, 6928–6944 (2006).
- [44] S. Solomon, D. Quin, M. Manning, M. Marquis, K. Averyt, M. M. B. Tignor, H. L. Miller Jr., and Z. Chen. "Climate change 2007: The Physical Science Basis". Cambridge University Press (2007).
- [45] T. Corti and T. Peter. "A simple model for cloud radiative forcing". *Atmospheric Chemistry and Physics* **9**, 5751–5758 (2009).
- [46] U. Schumann, B. Mayer, K. Graf, and H. Mannstein. "A Parametric radiative forcing model for contrail cirrus". *American Meteorological Society* **51**, 1391–1405 (2012).

- [47] J. Schultz. "On the effect of cloud inhomogeneity on area averaged radiative properties of contrails". *Geophysical Research Letters* **25**, 1427–1430 (1997).
- [48] A. Gounou and R. J. Hogan. "A sensitivity study of the effect of horizontal photon transport on the radiative forcing of contrails". *Journal of Atmospheric Sciences* **64**, 1706–1716 (2007).
- [49] L. Forster, C. Emde, B. Mayer, and S. Unterstrasser. "Effects of Three-Dimensional Photon Transport on the Radiative Forcing of Realistic Contrails". *American Meteorological Society*, 2243–2255 (2011).
- [50] U. Schumann. "Influence of propulsion efficiency on contrail formation". *Aerospace Science and Technology* **4**, 391–401 (2000).
- [51] P. Jeßberger, C. Voigt, U. Schumann, I. Sölch, H. Schlager, S. Kaufmann, A. Petzold, D. Schäuble, and F. G. Gayet. "Aircraft type influence on contrail properties". *Atmospheric Chemistry and Physics* **13**, 11965–11984 (2013).
- [52] G. Anderson, S. Clough, F. Kneizys, J. Chetwynd, and E. Shettle. "AFGL atmospheric constituent profiles (0-120 km)". Technical report afgl-tr-86-0110, Air Force Geophys. Lab., Hanscom Air Force Base, (1986).
- [53] F. Holzäpfel. "Probabilistic Two-Phase Wake Vortex Decay and Transport Model". *Journal of Aircraft* **40** (323-331) (2003).
- [54] U. Schumann. "A contrail cirrus prediction tool". In *Intern. Conf. on transport, Atmosphere and Climate, DLR/EUR, Aachen and Maastricht, 22-25 June* (2009).
- [55] K. Wyser D. Mitchell P. Yang, K. N. Liou. "Parameterization of the scattering and absorption properties of individual ice crystals". *Journal of Geophysical Research* **105**, 4699–4718 (2000).
- [56] P. Yang, H. Wei, H.-L. Huang, B. A. Baum, Y. X. Hu, G. W. Kattawar, M. I. Mishchenko, and Q. Fu. "Scattering and absorption property database for non-spherical ice particles in the near- through far-infrared spectral region". *Applied Optics* **44**, 5512–5523 (2005).
- [57] B. Mayer, A. Kylling, C. Emde, U. Hamann, and R. Buras. "libRadtran user's guide". Technical report, Technische Universität München, (2011).
- [58] H. Kraus. "Die Atmosphäre der Erde". Springer-Verlag Berlin Heidelberg (2001).
- [59] D. Sonntag. "Advancements in Field Hygrometry, Review Article". *Meteorologische Zeitschrift* **3**, 51–66 (1994).

- 
- [60] NASA. "U. S. Standardatmosphere". *National Aeronautics & Space Administration* **VA 22161** (ADA 035728), 227 (1976).
- [61] W. Roedel. "Physik unserer Umwelt, die Atmosphäre". Springer-Verlag Berlin Heidelberg (2000).
- [62] ICAO, Doc 7488-CD. "Manual of the ICAO Standard Atmosphere (extended to 80 kilometres (262 500 feet))", third edition, (1993).
- [63] W. Demtröder. "Experimentalphysik 2 Elektrizität und Optik". Springer, Berlin (2002).
- [64] J. C. Maxwell. "A Dynamical Theory of the Electromagnetic Field". *Royal Society Transactions* **155**, 459–512 (1865).
- [65] A. Einstein. "Über einen die Erzeugung und Verwandlung des Lichtes betreffenden heuristischen Gesichtspunkt". *Annalen der Physik* **17**, 132–148 (1905).
- [66] G. W. Petty. "A first course in Atmospheric Radiation". Sundog Publishing (2006).
- [67] M. Planck. "Über das Gesetz der Energieverteilung im Normalspektrum". *Annalen der Physik* **309**, 553–563 (1901).
- [68] H. D. Baehr and K. Stephan. "Wärme- und Stoffübertragung". Springer-Verlag Berlin Heidelberg (2010).
- [69] M. Wild, D. Folini, Ch. Schär, N. Loeb, E. G. Dutton, and G. König-Langlo. "The global energy balance from a surface perspective". *Climate Dynamics* **14**, 3107–3134 (2013).
- [70] H. Malberg. "Meteorologie und Klimatologie". Springer-Verlag Berlin Heidelberg (2007).
- [71] G. E. Thomas and K. Stamnes. "Radiative Transfer in the Atmosphere and Ocean". Cambridge University Press (2002).
- [72] J. T. Kiehl and K. E. Trenberth. "Earth's Annual Global Mean Energy Budget". *Bulletin of the American Meteorological Society* **78**, 197–208 (1997).
- [73] D. Etling. "Theoretische Meteorologie". Springer-Verlag Berlin Heidelberg (2008).
- [74] L.A. Landau and E.M. Lifschitz. "Lehrbuch der theoretischen Physik, Band VI: Hydrodynamik". Akademie-Verlag Berlin (1991).

- [75] T. Foken. "Angewandte Meteorologie". Springer-Verlag Berlin Heidelberg (2006).
- [76] U. Schumann, P. Konopka, R. Baumann, R. Busen, T. Gerz, D. Schlager, P. Schulte, and H. Volkert. "Estimate of diffusion parameters of aircraft exhaust plumes near the tropopause from nitric oxide and turbulence measurements". *Journal of Geophysical Research* **100**, 14147–14162 (1995).
- [77] G. D. Nastrom and F. D. Eaton. "Turbulence eddy dissipation rates from radar observations at 5-20 km at white Sands Missile Range, New Mexico". *Journal of Geophysical Research* **102**, 19495–19505 (1997).
- [78] A. Fick. "Über Diffusion". *Annalen der Physik* **95**, 59–86 (1855).
- [79] C. Kittel and H. Krömer. "Thermodynamik". Oldenburg Verlag München, Wien (2001).
- [80] P. Spichtinger. "Eisübersättigte Regionen". Dissertation, University of Munich, Department of Physics Mai 2004.
- [81] M. Kaiser. "Optimierung von Flugtrajektorien strahlgetriebener Verkehrsflugzeuge bei konkurrierenden SESAR Zielfunktionen mittels Entwicklung eines hochpräzisen Flugleistungsmodells". Dissertation, Technische Universität Dresden (2014).
- [82] AIRBUS S.A.S. "A320/A320NEO Aircraft Characteristics, Airport and Maintenance planning". Technical report, AIRBUS S.A.S Customer Services Technical Data Support and Service, (May 2014).
- [83] M. Kaiser, M. Schultz, and H. Fricke. "Enhanced Jet Performance Model". In *Proceedings of the 2nd International Conference on Application and Theory of Automation in Command and Control Systems (ATACCS)* (2011).
- [84] Eurocontrol Experimental Center. "Coverage of European Air Traffic by Base of Aircraft Data (BADA)", revision 3.6 edition, (2004).
- [85] B. Mayer and A. Kylling. "Technical note: The libRadtran software package for radiative transfer calculations description and examples of use". *Atmospheric Chemistry and Physics* **5**, 1855–1877 (2005).
- [86] A. Belward and T. Loveland. "The DIS 1-km land cover data set". *GLOBAL CHANGE, The IGBP Newsletter* **27** (1996).
- [87] A. Kylling, K. Stamnes, and S.-C. Tsay. "A Reliable and Efficient Two-Stream Algorithm for Spherical Radiative Transfer: Documentation of Accuracy in Realistic Layered Media". *Journal of Atmospheric Chemistry* **21** (115-150) (1995).



- [88] K. Stamnes, S.-C. Tsay, W. Wiscombe, and K. Jayaweera. "Numerically stable algorithm for discrete-ordinate-method radiative transfer in multiple scattering and emitting layered media". *Applied Optics* **27**, 2502–2509 (1988).
- [89] A. Dahlback and K. Stamnes. "A new spherical model for computing the radiation field available for photolysis and heating at twilight". *Planetary and Space Science* **39**, 671–683 (1991).
- [90] K. Stamnes, S.-C. Tsay, W. Wiscombe, and I. Laszlo. "DISORT, a General-Purpose Fortran Program for Discrete-Ordinate-Method Radiative Transfer in Scattering and Emitting Layered Media: Documentation of Methodology". Technical report, Technical Report Dept. of Physics and Engineering Physics, Stephens Institute of Technology, Hoboken, NJ 07030, (2000).
- [91] S. Kato, T. P. Ackerman, J. H. Mather, and E. Clothiaux. "The k-distribution method and correlated-k approximation for a shortwave radiative transfer model". *Journal of Quantitative Spectroscopy & Radiative Transfer* **62**, 109–121 (1999).
- [92] Q. Fu and K. Liou. "On the correlated k-distribution method for radiative transfer in nonhomogeneous atmospheres". *Journal of Atmospheric Sciences* **49** (2139–2156) (1992).
- [93] D. P. Kratz and P. Varanasi. "The correlated k-distribution technique as applied to the AVHRR channels". *Journal of Quantitative Spectroscopy & Radiative Transfer* **53** (501–517) (1995).
- [94] P. Ricchiazzi, S. Yang, C. Gautier, and D. Sowle. "SBDART: A research and Teaching software tool for plane-parallel radiative transfer in the Earth's atmosphere". *Bulletin of the American Meteorological Society* **79** (2101–2114) (1998).
- [95] J. Rosenow, M. Kaiser, and H. Fricke. "Modeling Contrail life cycles based on highly precise flight profile data of modern aircraft". In *Proceedings of the International Conference on Research in Airport Transportation (ICRAT)* (2012).
- [96] R. Paugam, R. Paoli, and D. Cariolle. "Influence of vortex dynamics and atmospheric turbulence on the early evolution of a contrail". *Atmospheric Chemistry and Physics* **10** (8), 3933–3952 (2010).
- [97] A. Betz. "Verhalten von Wirbelsystemen". *Zeitschrift für angewandte Mathematik und Mechanik* **12** (3) (1932).
- [98] H. Glauert. "Die Grundlagen der Tragflügel- und Luftschraubentheorie". Springer-Verlag New York Inc., softcover reprint of the original 1st ed. 1929 edition (2013).



- 
- [99] J. D. Anderson. "Introduction to flight". McGraw-Hill, NY (1989).
- [100] T. Sarpkaya. "A new model for vortex decay in the atmosphere". *Journal of Aircraft* **37** (1), 53–61 (2000).
- [101] D. C. Burnham and J. N. Hallock. "Chicago monostatic acoustic vortex sensor system". *Report No. DOT-TSC-FAA-79-103.IV* (1982).
- [102] F. Holzäpfel, T. Gerz, and R. Baumann. "The turbulent decay of trailing vortex pairs in stably stratified environments". *Aerospace Science and Technology* **5**, 95–108 (2001).
- [103] G. Merziger, G. Mühlbach, D. Wille, and T. Wirth. "Formeln + Hilfen zur Höheren Mathematik". Binomi Verlag Hannover (2001).
- [104] R. Sussmann and K. M. Gierens. "Lidar and numerical studies on the different evolution of vortex pair and secondary wake in young contrails". *J. Geophys. Res.* **104**, 2131–2142 (1999).
- [105] A. D. Naiman, S. K. Lele, and M. Z. Jacobson. "Large eddy simulations of contrail development: Sensitivity to initial and ambient conditions over first twenty minutes". *Journal of Geophysical Research* **116**, D21208 (2011).
- [106] A. Chlond. "Large-Eddy Simulation of Contrails". *Journal of Atmospheric Sciences* **55**, 796–819 (1997).
- [107] W. Sutherland. "The viscosity of gases and molecular force". *Philosophical Magazine* **5**, 507–531 (1893).
- [108] A. Döplheuer and M. Lecht. "Influence of engine performance on emission characteristic". *RTO MP-14. Lisabon, Portugal* (1998).
- [109] U. Schumann, J. Ström, R. Busen, R. Baumann, K. Gierens, M. Krautschunk, F. P. Schröder, and J. Stringl. "In situ observations of particles in jet aircraft exhausts and contrails for different sulfur containing fuels". *Journal of Geophysical Research* **101**, 6853–6869 (1996).
- [110] R. I. Smith-Johannsen. "Ice Crystal Agglomeration: T Formation". *Journal of the Atmospheric Science* **26**, 532–534 (1969).
- [111] D. P. Landau and K. Binder. "A Guide to Monte Carlo Simulations in Statistical Physics". Cambridge University Press (2009).
- [112] J. Rosenow and H. Fricke. "Angle dependent extinction of solar radiation by individual condensation trails". In *4th International Conference on Transport, Atmosphere and Climate (TAC-4)*, Bad Kohlburg (2015).

- [113] J. Rosenow and H. Fricke. "Condensation trails affecting the thermal energy budget of the Earth-atmosphere system". *Transportation Research Part D: Transport and Environment*, (submitted) (2016).
- [114] I. S. Gradshteyn and I.M. Ryzhik. "Tables of integrals, series and products". Academic Press, seventh edition edition (2007).
- [115] L. Devroye. "Non-Uniform Random Variante Generation". Springer-Verlag New York Inc. (1986).
- [116] U. Schumann, K. Graf, H. Mannstein, and B. Mayer. "Atmospheric physics". Springer-Verlag Berlin Heidelberg (2012).
- [117] G. Mie. "Beiträge zur Optik trüber Medien, speziell kolloidialer Metallösungen". *Annalen der Physik* **330**, 377–445 (1908).
- [118] H. Du. "Mie-scattering calculation". *Applied Optics* **43**, 1951–1956 (2004).
- [119] U. Schumann, B. Mayer, K. Gierens, S. Unterstrasser, P. Jeßberger, A. Petzold, C. Voigt, and F. G. Gayet. "Effective radius of ice particles in cirrus and contrails". *Journal of Atmospheric Sciences* **68**, 300–321 (2011).
- [120] M. D. King, S. Platnick, P. Yang, G. T. Arnold, M. A. Gray, J. C. Riedi, S. A. Ackerman, and K. N. Liou. "Remote sensing of liquid water and ice cloud optical thickness, and effective radius in the arctic: application of air-borne multispectral MAS data". *Journal of Atmospheric Oceanic Technology* **21**, 857–875 (2004).
- [121] Y. Takano and K. N. Liou. "Solar radiative transfer in cirrus clouds I, single scattering and optical properties of hexagonal ice crystals". *Journal of Atmospheric Sciences* **46**, 3–19 (1989).
- [122] S. Unterstrasser and K. Gierens. "Simulation of Contrails in the vortex regime - Examination of the microphysical properties". In *Proceedings of the TAC-Conference, June 26 to 29. 2006, Oxford, UK* (2006).
- [123] P. Yang, G. Hong, A. E. Dessler, S. S. C. Ou, K.-N. Liou, P. Minnis, and Harshvardhan. "Contrails and Induced Cirrus: Optics and Radiation". *Bulletin of the American Meteorological Society* **91**, 473–478 (2010).
- [124] M. Huber, M. Blumthaler, J. Schreder, B. Schallhart, and J. Lenoble. "Effect of inhomogenous surface albedo on diffuse UV-sky radiance at high-altitude site". *Journal of Geophysical Research* **109**, 1–7 (2004).
- [125] E. Shettle. "Models of aerosols, clouds and precipitation for atmospheric propagation studies". In *Atmospheric propagation in the uv, visible, ir and mm-region and related system aspects*, number 454. AGARD Conference Proceedings (1989).

- 
- [126] A. Sorokin, X. Vancassel, and P. Mirabel. "Emission of ions and charged soot particle by aircraft engines". *Atmospheric Chemistry and Physics* **3**, 325–334 (2003).
- [127] H. W. Wong and R. C. Miake-Lye. "Parametric studies of contrail ice particle formation in jet regime using microphysical parcel modeling". *Atmospheric Chemistry and Physics* **12**, 3261–3272 (2010).
- [128] D. S. Lee, G. Pitari, V. Grewe, K. Gierens, J. E. Penner, A. Petzold, M. J. Prather, U. Schumann, A. Bais, T. Berntsen, D. Iachetti, L. L. Lim, and R. Sausen. "Transport impacts on atmosphere and climate: Aviation". *Atmospheric Environment* **44**, 4678–4734 (2010).
- [129] J. Key, P. Yang, B. A. Baum, and S. L. Nasiri. "Parameterization of shortwave ice cloud optical properties for various particle habits". *Journal of Geophysical Research* **107** (2002).
- [130] U. Schumann, P. Jeßberger, and C. Voigt. "Contrail ice particles in aircraft wakes and their climatic importance". *Geophysical Research Letters* **40**, 2867–2872 (2013).
- [131] G. W. Petty and W. Huang. "The Modified Gamma Size Distribution Applied to Inhomogeneous and Nonspherical Particles: Key Relationships and Conversions". *Journal of the Atmospheric Science* **68**, 1460–1473 (2011).



# Acknowledgements

Hereby, I would like to thank those people, without whose help I would have never been able to reach my ambitious goal. In the first place, I would like to express my gratitude to my thesis supervisor, **Prof. Dr.-Ing. Hartmut Fricke** for trusting me since our first meeting and for always helping me to get on the right track. Not less, I would like to thank my second supervisor, **Prof. Dr. Ulrich Schumann**, for the prompt willingness to supervise me during the entire process time. Thank you for many helpful advises, bibliographies, and positive food for thought.

Very special thanks goes to my husband, **Thomas**, for many hours of programming support, for a thousand advises and for your patience. I thank you, as well as **Leopold** and **Penelope** for all your love and understanding. I promise, I will give you back all the time you gave me for this phase in my life.

I would like to thank my **colleagues** at the Institute of Logistics and Aviation for countless helpful information about the air traffic system and for many encouraging words during coffee breaks and team meetings. Especially **Bernd** and **Micha** for virtual hugs and smiles.

Many thanks go to my **parents**, who support me, trust me and believe in me since I was born. Further, I thank both **Anne** and **Anne** for always giving ear to me and my problems.

I'm also indebted to **C. Kolumbus**, for thoughtfully bringing the cocoa bean from America to Europe. Without him, I would have never come this far.